Multi-Purpose Pattern-Fitting System RIETAN-FP

Fujio IZUMI[1]

Graduate School of Engineering, Kyoto University

December 16, 2021

[1]E-mail: fizumi3776@gmail.com

Chapter 1

WHAT CAN WE DO USING RIETAN-FP?

Written in Fortran 90, RIETAN-FP [1, 2] is a successor program to RIETAN [3], RIETAN-94 [4], RIETAN-98 [5], and RIETAN-2000 [5–8]. RIETAN-FP is applicable to the following four main purposes:

1. pattern decomposition by the Le Bail method [9],
2. refinement of lattice and structure parameters by the Rietveld method [10] ,
3. whole-pattern fitting based on the maximum-entropy method (MEM) [11–17],
4. local pattern decomposition by individual profile fitting [18] (a rather outdated and impractical technique).

Figure 1.1 illustrates the above four purposes to be achieved by RIETAN-FP. In pattern fitting 1−4, a premier and robust engine for nonlinear least squares by Gauss-Newton, Fletcher's modified Marquardt, and Powell's conjugate-direction methods can be utilized, permitting stable convergence in most refinements. The use of the conjugate-direction method, also known as the direction set method in multi-dimensions, often makes it possible to escape from local minima easily and automatically. It is relatively slow but excels at analyzing complex structures such as (a) organic compounds having relatively large unit cells and molecular weights and (b) micro-porous materials in final stages.

The Rietveld method is used to refine lattice and structure parameters from X-ray and neutron powder diffraction data, from which structural information such as fractional coordinates, occupancies, and atomic displacement parameters can be extracted as much as possible. Since it is now very popular, its explanation is unnecessary here. For details of Rietveld analysis using RIETAN-FP, read Chap. 2.

The Le Bail method provides us with the opportunity for estimation of integrated intensities in the absence of any structural model with a simple procedure proposed by Rietveld. The resulting integrated intensities serve for *ab initio* structure analysis by the heavy-atom (Patterson), direct, and Monte Carlo, simulated-annealing, and genetic-algorithm methods. RIETAN-FP is capable of outputting files for (a) improving integrated intensities for overlapping reflections and

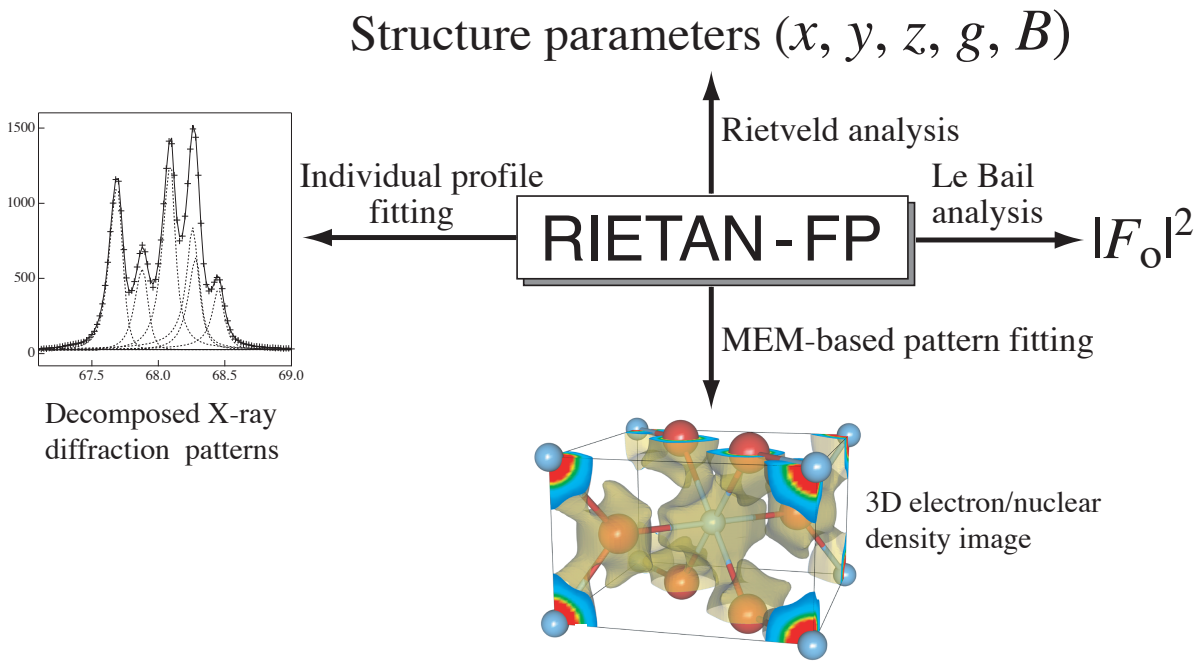

Figure 1.1: Four main purposes of RIETAN-FP

determining three-dimensional (3D) Patterson functions by the maximum-entropy Patterson (MEP) method [19] with ALBA [20,21] and (b) construction of structural models with EXPO[1] [22]. To refine lattice parameters, this method excels the Rietveld method when the effect of preferred orientation or coarse particles is pronounced. This is a newborn function that needs to be tested and improved further. Nevertheless, we confirmed that RIETAN-FP usually yields smaller reliability indices than EXPO, particularly, on the use of hybrid pattern decomposition, where Le Bail analysis is followed by individual profile fitting by the conjugate-direction method (see Chap. 11).

RIETAN-FP offers a state-of-the-art structure-refinement technique alternative to the classical Rietveld method: MEM-based Pattern Fitting (MPF). The revolutionary MPF technology was implemented in RIETAN-FP to overcome limitations of conventional Rietveld analysis. RIETAN-FP is distinguished from other programs for classical Rietveld analysis by this elegant methodology. We have been distributing Dysnomia [17,23], which is the successor to PRIMA [13], for MEM analysis in cooperation with RIETAN-FP.

Whole-pattern fitting and MEM analysis are alternately repeated in an iterative procedure called REMEDY cycles, where the bias imposed by a structural model upon final electron/nuclear densities is minimized. During the REMEDY cycles, the total number of electrons, $F(000)$ (X-ray diffraction), or the total coherent-scattering lengths (neutron diffraction) [24] in the unit cell is fixed at that input by the user. Electron/nuclear-density distribution changes noticeably with dramatic decreases in reliability indices based on integrated intensities during the REMEDY cycles, which is a strong piece of evidence for the reduction in the bias of the structural model. Consequently, crystal structures are virtually represented not by structure parameters but by 3D

[1] http://wwwba.ic.cnr.it/content/software

electron/nuclear densities within the unit cell.

Individual profile fitting deals with a local powder-diffraction pattern within a limited 2θ range. No constraints are imposed upon peak positions and integrated intensities of reflections in that range. Both of them are directly refined by a method of nonlinear least squares together with profile parameters.

A definite advantage of RIETAN-FP over other Rietveld-analysis programs is close cooperation with a powerful 3D visualization system VESTA[2] [25, 26], which enables quick evaluation of results obtained by Rietveld and MPF analyses. VESTA fully utilizes the OpenGL Application Programming Interface (API). Video cards equipped with GPUs supporting hardware acceleration for OpenGL are desired to rotate, expand, shrink, and translate objects fast in three dimensions. Personal computers with Windows, macOS, and Linux as operating systems allow us to run VESTA swiftly and smoothly. With VESTA, graphics workstations are no longer necessary!

VESTA bears the bell in 3D visualization, rendering, and, consequently, graphic manipulation of crystal structures and various physical quantities such as electron/nuclear densities determined not only by X-ray and neutron diffraction but by electronic-structure calculations. It also supports the 3D visualization of electrostatic potentials and wave functions that have both positive and negative values, which allows us to obtain additional information about chemical bonding. Thus, VESTA may be able to prevent phase separation between experimental and theoretical approaches. We must understand crystal structures, electron/nuclear-density distribution, and electronic states not two-dimensionally but three-dimensionally!

The removal of both absolute paths and (period + extensions) from names of most files input and output by RIETAN-FP gives a common string, *e.g.*, 'Fapatite' in the case of files contained in folder Fapatite included under folder RIETAN_VENUS_examples in the distribution files. In what follows, 'hoge' is the metasyntactic variable that should be replaced by the common string consisting of 62 alphanumeric characters (A–Z, a–z, and 0–9) plus '_' (underscore). For example, hoge.ins is a user input file, hoge.int is an intensity data file, and hoge.lst is a standard-output file.

[2] http://jp-minerals.org/vesta/en/

Chapter 2

FUNDAMENTALS OF RIETVELD ANALYSIS

> "When you can measure what you are speaking about and express it in numbers, you know something about it; but when you cannot express it in numbers, your knowledge is of a meagre and unsatisfactory kind; it may be the beginning of knowledge, but you have scarcely in your thoughts advanced to the state of science, whatever the matter may be."
>
> Lord Kelvin

2.1 Raison D'être of the Rietveld Method

The Rietveld method is a technique for refining structure and lattice parameters directly from whole X-ray or neutron powder-diffraction patterns without separating overlapped reflections contained in them. In contrast with single-crystal diffraction, the projection of the 3D reciprocal lattice onto the single dimension of a powder-diffraction pattern leads to a serious loss of structural information. Solving phase problems in compounds with unknown structures is, therefore, very difficult with powder-diffraction data unless the compounds have fairly high symmetry and contain few atoms in their asymmetric units. However, once structural models can be constructed by some means, the Rietveld method is available as a most powerful procedure for structure refinements.

Many scientists, including even crystallographers, still have a preconceived idea that the Rietveld method should be applied only when single crystals cannot be grown or when twins are inevitably formed during crystallization processes and phase transitions. Such an idea is judged to be too superficial from the standpoint of materials science. Most metal and inorganic materials, *e.g.*, intermetallic compounds, metal hydrides, solid-state ionics, superconductors, zeolites, catalysts, inorganic ion exchangers, and ceramics, are polycrystals. The crystal (defect) structures of single crystals may differ to some extent from those of polycrystalline materials. As described above, the powder method always suffers from the disadvantage that an appreciable amount of structural information is lost owing to the overlaps of reflections. Nevertheless, it possesses several advantages over the single-crystal method:

1. easy preparation of polycrystalline samples,

2. simple procedures for measurements,

3. the ease of in situ diffraction experiments in special sample environments (high/low temperature, high pressure, gas atmosphere, *etc.*),

4. negligible secondary-extinction effects.

The starting point of all studies on crystalline materials is to learn their crystal structures and chemical compositions accurately, and also the relationships between them. Synchrotron X-ray powder diffraction [27, 28] is particularly useful for the analysis of complex structures because of its extremely high resolution. Rietveld analysis can be regarded as the method for a kind of state analysis by which the positions, atomic displacements, and occupancies of atomic sites in crystalline materials are quantitatively determined. The principle of the Rietveld method can be applied not only to elastic powder diffraction but to other spectroscopic techniques that produce complex spectra containing overlapping reflections. Furthermore, precise determination of compositional ratios in mixtures is possible with this method. The introduction of basic information on the Rietveld method is, therefore, important for scientists and students in research areas other than crystallography.

2.2 Amazing Ability of the Rietveld Method

The Rietveld method substantially contains the following data-processing procedures:

1. indexing of reflections,

2. separation of overlapping reflections in diffraction patterns,

3. separation of $K\alpha_1$ and $K\alpha_2$ reflections when using characteristic X rays,

4. background subtraction,

5. refinement of lattice parameters,

6. refinement of crystal-structure parameters (fractional coordinates, occupancies, and atomic displacement parameters),

7. refinement of magnetic-structure parameters (magnitudes and directions of magnetic moments),

8. correction for preferred orientation,

9. identification of impurity reflections,

10. quantitative analysis of mixtures,

11. determination of integrated intensities,[1] full-widths at half-maximum intensities (FWHM), and peak positions,

[1]Throughout this document, the integrated intensity for a reflection is defined as the area surrounded by its diffraction profile and the background intensity.

12. determination of crystallite sizes and microstrains.

The Rietveld method, in which these complex calculations are executed simultaneously, is an exquisite technique worthy of being the ultimate method for the analysis of powder-diffraction data. It owes its dramatic development to the spread and improvement of computers in recent years.

The Rietveld method is widely applicable to metals, inorganic compounds, and organic compounds of low molecular weights provided that they are crystalline enough. Conventional X-ray powder diffractometers using characteristic X rays are changed into high-performance machines with which both structure and lattice parameters can be refined accurately by the Rietveld method. The combination of X-ray powder diffraction and Rietveld refinement can provide us with much more reliable information about average structures than the direct observation of crystal structures by high-resolution transmission electron microscopy (HRTEM) and analysis of X-ray absorption fine structures (XAFS). High-resolution powder diffraction data obtained from synchrotron or neutron sources yield structure parameters with accuracy and precision which are comparable to those obtained by the single-crystal X-ray method using four-circle goniometers.

2.3 Principle

Before the appearance of the Rietveld method, structure parameters were refined from diffraction data using integrated intensities of respective reflections obtained by the nonlinear least-squares fitting of diffraction patterns. This procedure is effective when dealing with those compounds of high symmetry and simple structures that display relatively few reflections. However, it is no longer useful when reflections overlap so heavily in the small-d region that they cannot be separated by curve fitting.

In Rietveld analysis from angle-dispersive powder-diffraction data, a set of variable parameters, $\boldsymbol{x}$ $(x_1, x_2, x_3, \cdots x_n)$, that represent powder-diffraction patterns is refined by fitting the calculated powder pattern to the observed one by a nonlinear least-squares method. In other words, the sum of weighted squares of residuals

$$S(\boldsymbol{x}) = \sum_{i=1}^{N} w_i \left[y_i - f_i(\boldsymbol{x})\right]^2 \tag{2.1}$$

is minimized by refining $\boldsymbol{x}$ successively. In the above equation, i is the step number, N is the total number of data points, w_i is the statistical weight based on counting statistics, y_i is the observed intensity, and $f_i(\boldsymbol{x}) \equiv f(2\theta_i; x_1, x_2, x_3, \cdots x_n)$ is the calculated intensity at a diffraction angle of $2\theta_i$.

Strictly speaking, each observation should be assigned a statistical weight

$$w_i = \frac{1}{\sigma^2(y_i) + \sigma^2(B_i)}, \tag{2.2}$$

where σ^2 is the variance of each physical quantity, and B_i is the observed background intensity [29]. Since B_i cannot be determined from some experimental values, $\sigma^2(B_i)$ is usually set arbitrarily at zero:

$$w_i = \frac{1}{\sigma^2(y_i)}. \tag{2.3}$$

This rough approximation may cause some problems in Rietveld refinement from synchrotron X-ray powder diffraction data measured by the Debye–Scherrer method using glass capillaries owing to the high background with humps arising from short-range order in the amorphous material.

In addition to y_i, its error, $\sigma(y_i)$, is supposed to be determined on use of one-dimensional and two-dimensional detectors to collect diffraction intensities at different points simultaneously. Nevertheless, only y_i's are usually recorded in files where diffraction data are recorded because of difficulties in estimating $\sigma(y_i)$'s. In such cases, we are obliged to evaluate $\sigma(y_i)$ from y_i by a simple equation,

$$\sigma(y_i) = \sqrt{y_i}, \tag{2.4}$$

which is, however, suitable only for a single detector such as a scintillation counter. The use of Eq. (2.4) inevitably leads to the underestimation of $\sigma(y_i)$ and thus the overestimation of w_i because of error propagation and systematic errors, influencing results of Rietveld refinement more or less.

When two or more counts are recorded at the same angle, as is the case where n detectors are employed, we use the mean count with a variance of y_i/n. The weight to be multiplied in this case is $w_i \approx n/y_i$.

The model function $f_i(\boldsymbol{x})$ contains lattice and structure parameters as a part of independent variables, $\boldsymbol{x}$; details of this very complex function will be described in 2.5. Because lattice and structure parameters are refined from the whole diffraction pattern in the least-squares calculation, maximum structural information can be directly extracted from the powder pattern without any pre-processing.

Figure 2.1 exemplifies the result of a Rietveld refinement for $Sr_9In(PO_4)_7$ (space group: $R3c$; $a = 10.439$ Å and $c = 37.375$ Å) from synchrotron X-ray powder diffraction data ($n = 20504$) measured at a wavelength, λ, of 0.85001 Å [30]. The solid line is calculated intensities, and small crosses superimposed on it are observed intensities. Differences between observed and calculated intensities are shown by a line appearing at the bottom. Tick marks below the profile indicate the peak positions of all allowed Bragg reflections. The number of possible Bragg reflection that appeared between 2.5° and 64° was as many as 2627, and that of refinable parameters including 2 lattice and 88 structure parameters was 116.

All the Rietveld-refinement programs including RIETAN-FP are capable of calculating only $f_i(\boldsymbol{x})$'s ($i = 1, 2, 3, \cdots n$) and output a text file to plot the resulting powder-diffraction pattern; such a feature is called simulation of powder-diffraction patterns.

2.4 Development and Spread of the Rietveld Method

The above idea is very simple but was a creative achievement that seemed impossible until it was actually tried and confirmed to be effective by Rietveld [31] in 1967. He originally devised it for the analysis of constant-wavelength neutron-powder data (he was a researcher at a reactor center at Petten in the Netherlands). Since then, many neutron-diffraction data have been measured using reactor neutron sources and analyzed with a Fortran program developed by Rietveld, and

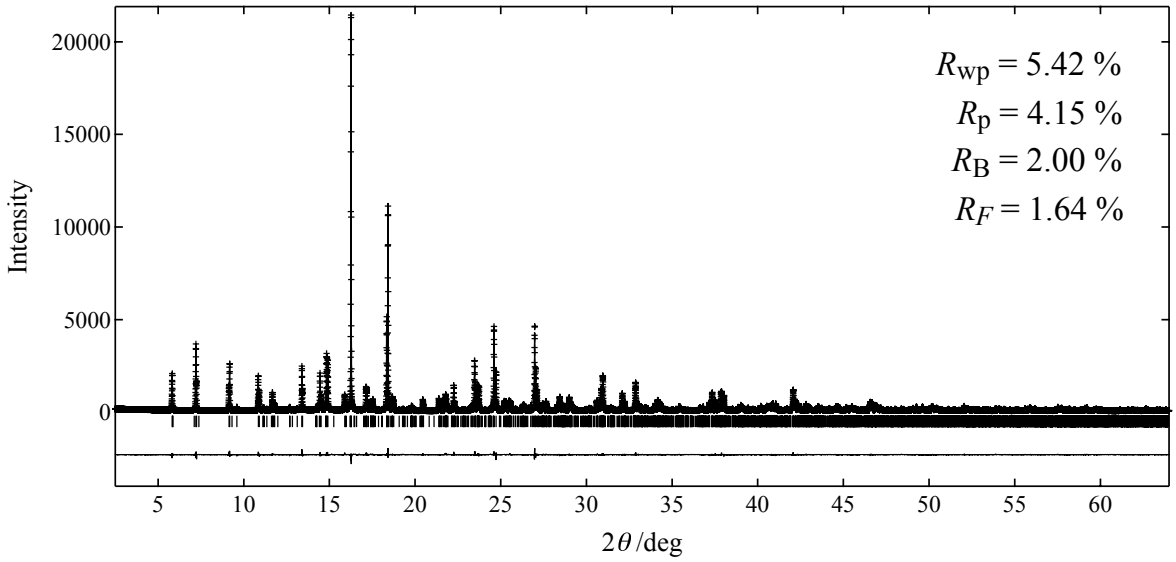

Figure 2.1: Observed, calculated and difference patterns resulting from Rietveld analysis from synchrotron X-ray powder diffraction data of $Sr_9In(PO_4)_7$

its extended version enabling us to refine anisotropic atomic displacement parameters. Up to 1977 the number of crystal and magnetic structures analyzed by this method reached as high as 172 [32]. In that year, Malmros and Thomas [33] first applied the Rietveld method to the analysis of X-ray diffraction data. Many researchers made this pioneer work an occasion to start studying Rietveld analysis from X-ray powder-diffraction data.

The so-called two-stage method proposed by Will [34] may be an alternative to the Rietveld method. This methodology generally gives more reliable standard uncertainties of structure parameters (see 4.2) and more meaningful reliability indices (see 4.3) than Rietveld analysis. However, as its name implies, structure refinement comprising (a) the determination of observed integrated intensities and (b) refinement of structure parameters from the resulting observed integrated intensities are more troublesome than the single stage method (Rietveld method). In fact, Will's method is no longer used widely.

The structural information that can be extracted from powder-diffraction data increases markedly as the resolution is enhanced because the overlapping of reflections is diminished. In any experimental system with a high intrinsic resolution, it is always possible to trade intensity for resolution. Synchrotron radiation facilities and pulsed-spallation-neutron sources built in several countries made it possible to collect high-resolution powder-diffraction data over relatively short periods, and opened paths to structure refinements as good as those by the single-crystal method.

Structure refinement according to the procedure that Rietveld developed had been referred to as several different terms such as profile refinement, profile fitting, and pattern-fitting structure refinement (PFSR). In 1982, the International Union of Crystallography (IUCr) adopted Rietveld analysis/method/refinement as the formal technical terms [35]. These names should be used when reporting the results obtained by this method.

2.5 Model Function

In angle-dispersive powder diffraction, the observed intensity, y_i, at a particular step, i, is modeled by the calculated intensity, $f_i(\boldsymbol{x})$, which is the sum of contributions from Bragg reflections plus background correction $y_\mathrm{b}(2\theta_i)$:

$$f_i(\boldsymbol{x}) = S_\mathrm{R}(\theta_i)A(\theta_i)D(\theta_i)s\sum_K m_K|F(\boldsymbol{h}_K)|^2P_KL(\theta_K)G(\Delta 2\theta_{iK}) + y_\mathrm{b}(2\theta_i), \tag{2.5}$$

where $S_\mathrm{R}(\theta_i)$ = correction factor for surface roughness, $A(\theta_i)$ = absorption factor (transmission coefficient), $D(\theta_i)$ = correction factor for the constant irradiation width, s = scale factor for the particular phase, K = reflection number, m_K = multiplicity, $F(\boldsymbol{h}_K)$ = structure factor, $\boldsymbol{h}_K$ = reflection indices hkl, P_K = correction factor for preferred orientation, $L(\theta_K)$ = Lorentz and polarization factors (the polarization factor is unnecessary in neutron diffraction), θ_K = Bragg angle, and $G(\Delta 2\theta_{iK}) \equiv G(2\theta_i - 2\theta_K)$ = profile function. The sum with respect to K in Eq. (2.5) must be carried out over all the Bragg reflections contributing to the net intensity at the ith step.

For convenience, Eq. (2.5) was formulated for a pure sample containing no impurities. When dealing with multi-phase samples, different scale factors have to be assigned to all the crystalline phases. Accordingly, $s\sum_K m_K|F(\boldsymbol{h}_K)|^2P_KL(\theta_K)G(\Delta 2\theta_{iK})$ in the first term of the right-hand side of Eq. (2.5) must be further summed up with respect to all the phases (j = 1, 2, ...) while $S_\mathrm{R}(\theta_i)A(\theta_i)D(\theta_i)$ and $y_\mathrm{b}(2\theta_i)$ are independent on all the phases:

$$f_i(\boldsymbol{x}) = S_\mathrm{R}(\theta_i)A(\theta_i)D(\theta_i)\sum_j s_j\sum_K m_{jK}|F_j(\boldsymbol{h}_K)|^2P_{jK}L(\theta_K)G_j(\Delta 2\theta_{iK}) + y_\mathrm{b}(2\theta_i). \tag{2.6}$$

The multiplicity, m_{jK}, contains subscript j because a different set of multiplicities is given to each Laue class [36]. Note that the Lorentz–polarization factor, $L(\theta_K)$, is simply a function of θ_K.

If microabsorption is negligible, mass fractions of constituent phases can be determined from final scale factors, s_j, refined in Rietveld analysis, using a simple equation, Eq. (7.1), linear with respect to the scale factors [37, 38] (see Chap. 7). The content of amorphous components is obtainable by addition of a crystalline internal standard material (see 7.3). Thus, the Rietveld method is now widely used as an important means for quantitative analysis by X-ray and neutron powder diffraction. One of the most important industrial applications is compositional analyses of clinker minerals in cement companies.

While lattice parameters are contained in θ_K, structure parameters are included in $F(\boldsymbol{h}_K)$. $F(\boldsymbol{h}_K)$ consists of two parts: the crystal-structure factor (see 3.5), $F(\boldsymbol{h}_K, \mathrm{cryst.})$, and the magnetic-structure factor (see 3.6), $F(\boldsymbol{h}_K, \mathrm{magn.})$:

$$|F(\boldsymbol{h}_K)|^2 = |F(\boldsymbol{h}_K, \mathrm{cryst.})|^2 + |F(\boldsymbol{h}_K, \mathrm{magn.})|^2. \tag{2.7}$$

The second term in the right-hand side of this equation is required in neutron diffraction only when compounds containing magnetic atoms such as Cr, Mn, Fe, Co, and Ni exhibit magnetic scattering in addition to nuclear scattering. It should be pointed out that neutron diffraction is the only experimental means to determine the direction and magnitude of a magnetic moment

for each magnetic-atom site. With RIETAN-FP, collinear magnetic structures can be analyzed relatively easily.

The profile shapes of individual Bragg reflections need to be approximated by appropriate profile functions $G(\Delta 2\theta_{iK})$. The profile function is primarily a function symmetric with respect to the peak position (see 3.9). The symmetric profile function is made asymmetric according to some procedures (see 3.10). RITEAN-FP supports an original feature of partial profile relaxation whereby the fit between observed and calculated patterns is improved more or less; this elaborate and effective technique will be described in 4.4.

Details of functions and factors contained in the right side of the model function (2.5) will be described in detail in Chap. 3, where subscript j for multi-phase samples are omitted for simplicity.

The reliability of results for Rietveld analysis depends on how $f_i(\boldsymbol{x})$ can approach observed intensities; a reasonable structural model, good fits between observed and calculated diffraction patterns and backgrounds, and negligible effects of preferred orientation and coarse particles are required to acquire reliable results.

Chapter 3

FUNCTIONS AND FACTORS IN THE MODEL FUNCTION

3.1 X-Ray Wavelengths

In this chapter, wavelengths of characteristic X rays will be first described since they are indispensable for evaluation of Bragg angles, θ_K, lattice-plane spacings, d_K, and other physical quantities. **Table 3.1** lists experimentally measured wavelengths of K-emission lines for six characteristic X rays [39] used in RIETAN-FP. For the Cu $K\beta$ radiation ($K\beta_1 + K\beta_3$), a single wavelength of 1.392 234 Å is given [39, 40]. It should be noted that peak positions in the line position and line shape standard reference material, SRM 640e (silicon powder), were computed with the wavelength of 1.540 592 9 Å (see the certificate of SRM 640e). Unfortunately, parts of Rietveld-analysis programs adopt obsolete values of wavelengths, which necessarily gives less-accurate lattice parameters refined in whole-pattern fitting.

Table 3.1: Wavelengths, λ/Å, of K-emission lines for representative characteristic X rays

Symbol	$K\alpha_1$	$K\alpha_2$	$K\beta$
Ag	0.559 421 78	0.563 813 1	
Mo	0.709 317 15	0.713 607	
Cu	1.540 592 9	1.544 427 4	1.392 234
Co	1.788 996	1.792 835	
Fe	1.936 041	1.939 973	
Cr	2.289 726	2.293 651	

3.2 Surface-Roughness Factor

In the Bragg–Brentano geometry, the surface of a flat-plate sample must be flat enough; otherwise, the sample itself absorbs parts of diffracted X-ray beams. As can be understood intuitively, this effect becomes more pronounced with increasing linear attenuation coefficient, μ, (see 3.3) and decreasing 2θ. Needless to say, the surface-roughness factor is not required for neutron powder diffraction and synchrotron X-ray powder diffraction. In parallel-beam optics including

those used in synchrotron X-ray powder diffraction, surface roughness does not affect observed intensities.

The following five surface-roughness factors, where p, q, r_s, t, and S are surface-roughness parameters to be refined by a least-squares method, were built into RIETAN-FP.

Combination model [41]

$$S_\mathrm{R}(\theta_i) = (1 - r_\mathrm{s})\left[1 - t\left(\theta_i - \frac{\pi}{2}\right)\right] + r_\mathrm{s}\left[1 - p\exp(-q) + p\exp\left(-\frac{q}{\sin\theta_i}\right)\right], \tag{3.1}$$

which is a linear combination of Eqs. (3.2) and (3.3) in a $(1 - r_\mathrm{s})$:r_s ratio.

Model of Sparks *et al.* [42]

$$S_\mathrm{R}(\theta_i) = 1 - t\left(\theta_i - \frac{\pi}{2}\right). \tag{3.2}$$

Model of Suortti [43]

$$S_\mathrm{R}(\theta_i) = 1 - p\exp(-q) + p\exp\left(-\frac{q}{\sin\theta_i}\right). \tag{3.3}$$

This straight-line model is valid only for the simplest cases where the intensity reduction at low angles is less than 1–2 %.

Model of Pitschke *et al.* [44, 45]

$$S_\mathrm{R}(\theta_i) = 1 - pq(1 - q) - \frac{pq}{\sin\theta_i}\left(1 - \frac{q}{\sin\theta_i}\right). \tag{3.4}$$

Model of Sidey [46]

$$\begin{aligned} S_\mathrm{R}(\theta_i) &= \left(\frac{\theta_i}{90}\right)^{S/\theta_i} \\ &= \exp\left[\frac{S}{\theta_i}\ln\left(\frac{\theta_i}{90}\right)\right], \end{aligned} \tag{3.5}$$

where θ_i is given in degrees. Equation (3.5) serves as a practical replacement for Eqs. (3.1), (3.3), and (3.4), with which procedures of Rietveld analysis become very complicated as a result of high correlations between the refinable parameters, p and q, in addition to correlations with the scale factor, atomic displacement parameters, and occupancies [46].

In an input file, hoge.ins, of RIETAN-FP, four parameters, q_0–q_3, are input as follows:

1. Combination model [41]: $q_0 = p$, $q_1 = q$, $q_2 = r_\mathrm{s}$, and $q_3 = t$.
2. Model of Sparks [42]: $q_0 = q_1 = q_2 = 0$ and $q_3 = t$.
3. Model of Suortti [43]: $q_0 = p$, $q_1 = q$, and $q_2 = q_3 = 0$.
4. Model of Pitschke *et al.* [44, 45]: $q_0 = p$, $q_1 = q$, and $q_2 = q_3 = 0$.
5. Model of Sidey [46]: $q_0 = q_1 = q_2 = 0$ and $q_3 = S$.

Of course, refinement identifiers, ID(I), of parameters fixed at 0 must be 0.

The reasonable range of S is $0 \leqslant S \leqslant 0.15$. If $S = 0$ then $S_\mathrm{R}(\theta_i) = 1$ over the whole 2θ range. If $S = 0.15$, the intensity reduction at $\theta = 2^\circ$ is *ca.* 25 %.

3.3 Absorption Factor

The reduction in the intensity of a reflection from a uniform beam owing to absorption is given by the absorption factor (transmission coefficient)

$$A(\theta_i) = \frac{1}{V}\int \exp(-\mu T)\,\mathrm{d}V, \tag{3.6}$$

where μ is the linear attenuation coefficient, T is the sum of the path lengths for the incident and diffracted beams, and the integration is over the volume, V, of the crystal [47].

3.3.1 Bragg–Brentano geometry

No absorption factor is required in Bragg–Brentano-type X-ray powder diffraction using flat-plate samples. The parafocusing geometry has a merit that $A(\theta_i)$ is inversely proportional to only μ. That is,

$$A(\theta_i) = \frac{1}{2\mu} \tag{3.7}$$

regardless of $2\theta_i$ because plate samples are used which are at the same angle to the incident and diffracted beams.

3.3.2 Debye–Scherrer geometry

The Debye–Scherrer geometry is usually adopted in synchrotron X-ray and neutron powder diffraction experiments using glass capillary tubes and cylindrical containers (usually vanadium), respectively. Both of them are regarded as cylinders, whose $A(\theta_i)$ values are tabulated in Table 6.3.3.2 [47]. Ida [48] proposed a highly efficient method for numerical calculation of $A(\theta_i)$ for cylinders. In his method, the Gauss–Legendre quadrature is applied to a formula proposed by Thorkildsen and Larsen [49, 50]:

$$A(\mu r, \theta_i) = \frac{2}{\pi \sin 2\theta_i}\int_0^{2\theta_i}\!\!\int_0^{\pi-2\theta_i} \exp\left[-\frac{2\mu r \sin x \cos(y-\theta_i)}{\cos\theta_i}\right]\sin(x+y)\sin(x-y+2\theta_i)\mathrm{d}x\,\mathrm{d}y. \tag{3.8}$$

$A(\theta_i)$ calculated from μ, the radius, r, of the cylinder, and θ_i by Ida's procedure using 12×12 terms in the numerical integration gives results with relative errors less than 10^{-6}. Another approach, which uses Simpson's method in conjunction with a formula proposed by Dwiggins [51], proved to be far less efficient than that of Thorkildsen and Larsen.

3.3.3 Transmission specimen method

In this method, *e.g.*, using a Guinier diffractometer, $A(\theta_i)$ is

$$A(\theta_i) = \frac{t}{\cos\theta_i}\exp\left(-\frac{s_\mathrm{a}}{\cos\theta_i}\right), \tag{3.9}$$

where t is the powder thickness, and s_a is the sum of the products of the absorption coefficients and thicknesses of the powder and the substrate [52]. The thickness, t, is absorbed into the scale factor, s, while s_a can be obtained just by measuring the direct beam intensity with and without a sample. Including this correction allows us to obtain more reliable atomic displacement parameters.

3.4 Factor to Correct for the Constant Irradiation Width

$D(\theta_i)$ has to be included in Eq. (2.5) on the use of the Bragg–Brentano geometry where the irradiation width is kept constant at l_s (mm) by changing the width of the divergence slit. Let ω be the divergence angle (°) at the lowest diffraction angle, and R_g the radius (mm) of the goniometer circle, then $D(\theta_i)$ is expressed as

$$D(\theta_i) = \frac{2\tan\theta_i}{\omega}\left\{\left[\left(\frac{R_\mathrm{g}}{l_\mathrm{s}\cos\theta_i}\right)^2 + 1\right]^{\frac{1}{2}} - \frac{R_\mathrm{g}}{l_\mathrm{s}\cos\theta_i}\right\} \tag{3.10}$$

[53]. In other optics, $D(\theta_i)$ is set at unity.

3.5 Crystal-Structure Factor

If the fractional coordinate of jth atom in the unit cell is (x_j, y_j, z_j), its position vector is given by

$$\boldsymbol{r}_j = x_j\boldsymbol{a} + y_j\boldsymbol{b} + z_j\boldsymbol{c}. \tag{3.11}$$

Let g_j be the occupancy (population factor or occupation factor), f_j the atomic form factor, and T_j the Debye–Waller factor (commonly called the temperature factor). From Eqs. (A.17) and (3.11), we obtain

$$\boldsymbol{s}_K \cdot \boldsymbol{r}_j = hx_j + ky_j + lz_j. \tag{3.12}$$

Then, $F(\boldsymbol{h}_K, \mathrm{cryst.})$ is formulated as

$$\begin{aligned} F(\boldsymbol{h}_K, \mathrm{cryst.}) &= \sum_j g_j f_j T_j \exp\left(2\pi\mathrm{i}\boldsymbol{s}_K \cdot \boldsymbol{r}_j\right) \\ &= \sum_j g_j f_j T_j \exp\left[2\pi\mathrm{i}\left(hx_j + ky_j + lz_j\right)\right]. \end{aligned} \tag{3.13}$$

The summation is formally carried out over all the atoms in the unit cell. However, parts of the summation are actually skipped by full use of space-group symmetry (see 3.5.3), which accelerates the calculation of structure factors particularly in centrosymmetric space groups and complex lattices.

Equation (3.13) has to be rewritten to derive actual equations to calculate $F(\boldsymbol{h}_K, \mathrm{cryst.})$ and partial derivatives of $|F(\boldsymbol{h}_K, \mathrm{cryst.})|$ with respect to crystal-structure parameters; for details, see ref. [54].

3.5.1 Atomic form factor

The atomic form factor is the scattering power of the atom. X rays are scattered by electrons, and neutrons virtually by atomic nuclei.

Equation to approximate the atomic scattering factor

Let $\rho(\boldsymbol{r})$ be the electron density at the position $\boldsymbol{r}$ from the origin, $\boldsymbol{k}_0$ the wave number vector of the incident wave, and $\boldsymbol{k}$ that of the scattered wave. If electron-density distribution is spherical,

$f_0(\sin\theta/\lambda)$ is expressed as a function of $\boldsymbol{k} - \boldsymbol{k}_0$:

$$f_0\left(\frac{\sin\theta}{\lambda}\right) = \int_{\text{atom}} \rho(\boldsymbol{r}) \exp\left[2\pi \mathrm{i}\,(\boldsymbol{k} - \boldsymbol{k}_0)\cdot\boldsymbol{r}\right] \mathrm{d}v. \tag{3.14}$$

That is, $f_0(\sin\theta/\lambda)$ is the Fourier transform of the density of free electrons. It is a fundamental quantity (dimensionless) in X-ray diffraction. In RIETAN-FP, $f_0(\sin\theta/\lambda)$ is approximated by an equation containing eleven coefficients, a_i, b_i, and c [55]:

$$f_0\left(\frac{\sin\theta}{\lambda}\right) = \sum_{i=1}^{5} a_i \exp\left[-b_i\left(\frac{\sin\theta}{\lambda}\right)^2\right] + c. \tag{3.15}$$

These coefficients for 288 neutral atoms and ions are stored in a text file, asfdc (see Table 17.1), in the RIETAN_VENUS folder. Equation (3.15) is valid for the full range of $\sin\theta/\lambda$ from 0 to 6. Sets of nine coefficients compiled in "International Tables for Crystallography," Vol. C [56] are no longer utilized because they are unsuitable for approximating $f_0(\sin\theta/\lambda)$ in a high-angle region of $2\ \text{Å}^{-1} < \sin\theta/\lambda < 6\ \text{Å}^{-1}$. Refer to Table 17.3 when names of chemical species to be input in hoge.ins are required.

In **Fig. 3.1**, atomic scattering factors of V, V^{2+}, V^{3+}, and V^{5+} are plotted against $\sin\theta/\lambda$. It really helps to remember that $f_0(0)$ is equal to the number of electrons in the atomic species. Because differences in $f_0(\sin\theta/\lambda)$ among these four chemical species are appreciable only in a low-angle region, selection of chemical species is not very important in the absence of large-d reflections.

X-ray dispersion corrections

The absorption edge is located at wavelengths (energies) where the energy of an absorbed photon corresponds to an electronic transition or ionization potential. When the quantum energy of

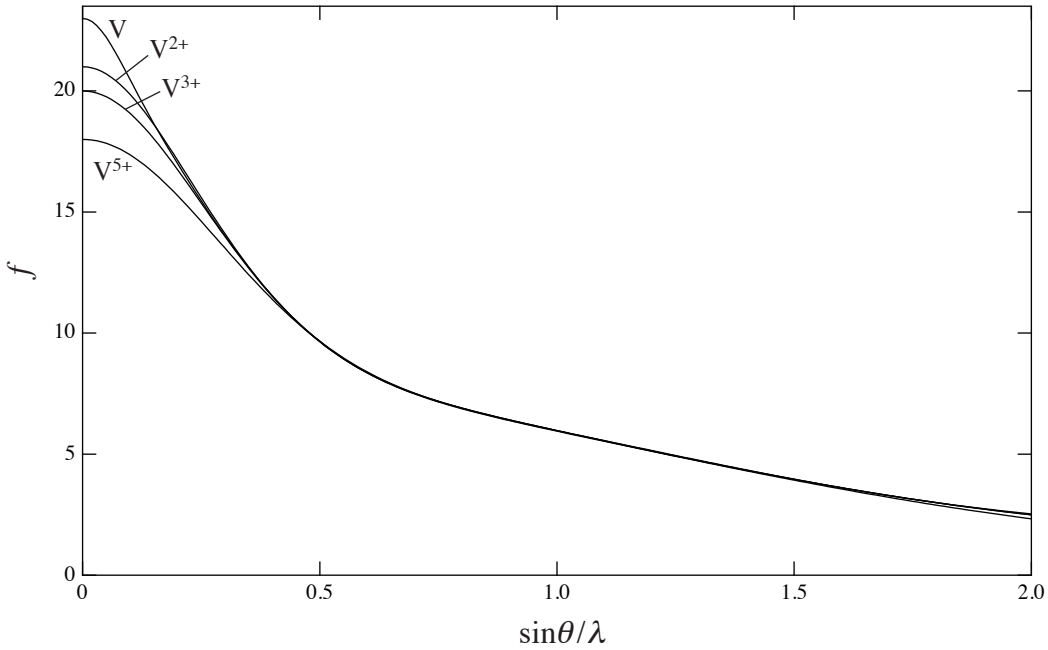

Figure 3.1: Atomic scattering factors of vanadium with four different oxidation states

the incident radiation becomes smaller than the work required to eject an electron from one or other quantum states in the absorbing atom, the incident radiation is no longer absorbed by that state. As λ approaches the absorption edge, λ_e, of an atom, the atomic form factor, f, changes with λ because of the interaction between the incident beam and the atom, *i.e.*, the resonant excitation of core electrons. This phenomenon is referred to as X-ray dispersion. The technical term 'anomalous dispersion,' which often appears in the literature, is never used in this manual because there is nothing 'anomalous' about these corrections [57]. In fact, the X-ray dispersion is totally predictable.

The atomic form factor in the presence of X-ray dispersion consists of the atomic scattering factor, $f_0(\sin\theta/\lambda)$, the real and imaginary parts, $f' + \mathrm{i}f''$, of the dispersion correction, and the nuclear Thomson correction [58], f_{NT}:

$$f = f_0\left(\frac{\sin\theta}{\lambda}\right) + f' + \mathrm{i}f'' + f_{\mathrm{NT}} \tag{3.16}$$

with

$$f' = f_1 + f_{\mathrm{rel}} - Z, \tag{3.17}$$

where f_1 is the real part of the angle-independent atomic-scattering-factor components for forward scattering, f_{rel} is the relativistic correction, and Z is the atomic number [59]. The nuclear Thomson scattering is small and negative in phase relative to the electric form factor: $f_0(\sin\theta/\lambda) + f'$.

The dispersion corrections, f' and f'', of all the elements for characteristic X rays (Ag $K\alpha$, Mo $K\alpha$, Cu $K\alpha$, Co $K\alpha$, Fe $K\alpha$, and Cr $K\alpha$ radiations) [60] are input from a text file, asfdc (see Table 17.1), by RIETAN-FP. Nuclear Thomson scattering is neglected on use of the above six characteristic X-ray radiations.

For Cu $K\beta$ radiation (λ = 1.39223 Å) and synchrotron X rays, f' and f'' are either input by the user or calculated by RIETAN-FP (see 17.3.10). The Cu $K\beta$ radiation is sometimes used instead of Cu $K\alpha_1$ at the expense of diffraction intensities since it is obtained by use of a relatively cheap curved graphite monochromator. The f_1 and f_2 (= f'') values of all the elements up to uranium (Z = 92) were tabulated as a function of the photon energy (E = 10–30000 eV) by Henke *et al.* [61] and have been updated at intervals. The latest tables of Henke *et al.* are believed to be the most reliable source of f_1 and f_2.

Further, Chantler [59] compiled f_{NT} and two kinds of f_{rel}: H82 (following the computation procedure of Cromer–Liberman [62] but omitting the Jensen energy-dependent correction) and 3/5CL (3/5ths of the Cromer–Liberman value). These f_{NT} and f_{rel} (3/5CL) values are worthy of being used by RIETAN-FP.

The f_1, f_2, f_{rel} (3/5CL), and f_{NT} values (in electrons/atom) of the elements with $Z \leqslant 92$ are recorded together with Z in a binary file, xdc.bin (see Table 17.1), which is placed in the RIETAN_VENUS folder. On calculation of f' and f'', xdc.bin is read by RIETAN-FP, and f_1 and f_2 at an arbitrary wavelength, λ, are determined by interpolating the f_1 and f_2 data in xdc.bin. For convenience, f_{NT}, which is usually neglected in X-ray structure analysis, is included in f'. Nevertheless, the user may input $f_1 + f_{\mathrm{rel}} - Z$ as f' in hoge.ins, referring to hoge.lst (see

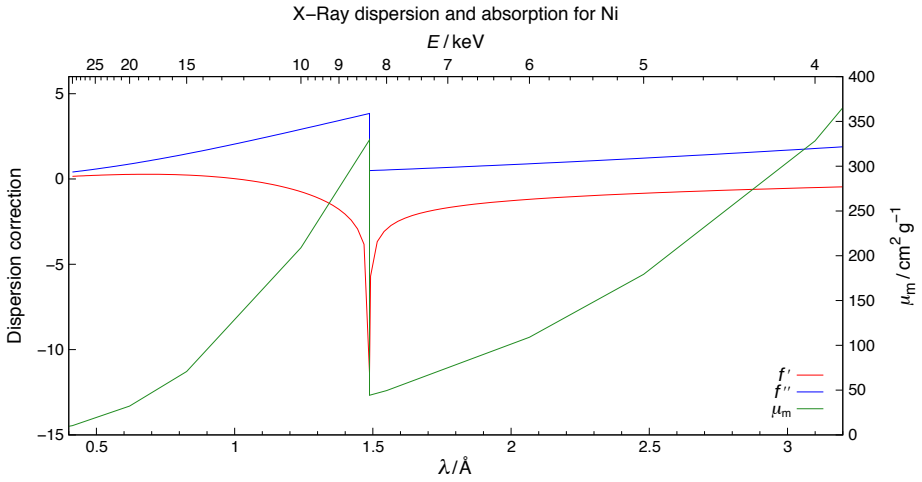

Figure 3.2: The dependence of f', f'', and $\mu_{\rm m}$ on the wavelength, λ, in Ni. E is the photon energy.

17.8.1). As described above, tables recorded in xdc.bin cover only a photon-energy region up to 30 000 eV ($\lambda = 0.413281$ Å). If synchrotron X-ray powder diffraction data are measured at a larger photon energy (a shorter wavelength), please refer to other references such as "International Tables for Crystallography," Vol. C [60].

The phase of the imaginary term deviates by +90° from that of the real one. Near the absorption edge, the real term, f', changes like a very steep valley, and the imaginary term, f'', stepwise, as **Fig. 3.2** illustrates for Ni. This figure was drawn by gnuplot [63] with an xdc macro of the RIETAN-FP–VENUS assistance environment from data in (1) xdc.gpd, which is output on specification of NPRINT = 2 in hoge.ins, and (2) mac.tbl (see 17.1). The K absorption edge of Ni proves to lie at 1.4879 Å = 8.3328 keV by viewing a Web page of the University of Washington.[1]

Thus, f can be considerably changed by the dispersion effect if the wavelength is set near an absorption edge in contrast with conventional sources. This phenomenon is utilized to enhance the contrast of a particular element in synchrotron X-ray diffraction. In general, dispersion corrections do not depend on 2θ and tend to increase with increasing atomic number and wavelength.

In addition to f' and f'', mass attenuation coefficients, $\mu/\rho = \mu_{\rm m}$, are input from mac.tbl (see Table 17.1) and plotted against λ in Fig. 3.2, which demonstrates that absorption of X rays increases rapidly in a region of λ slightly smaller than λ at the absorption edge. Fluorescent X rays also increase in that region. Hence, a graph such as Fig. 3.2 is very useful to estimate levels of X-ray absorption and fluorescent X rays at certain wavelengths.

Inserting a pair of commands, `set table` and `unset table`, into a gnuplot script file, xdc.plt (see Table 17.1), is useful to obtain a text file, xdc.tbl, storing f', f'', and $\mu_{\rm m}$ *vs.* λ:

```
set table "xdc.tbl"
plot 'element.dat' \
   every :::0::0 using 1:3 title "{/:Italic=16 f}&{/=8 |}{/=16 \342\200\262}" \
```

[1] http://skuld.bmsc.washington.edu/scatter/AS_periodic.html

```
   with lines linetype 11 linecolor rgbcolor "red", \
'' every :::0::0 using 1:4 title "{/:Italic=16 f}&{/=8 |}{/=16 \342\200\263}" \
   with lines linetype 11 linecolor rgbcolor "blue", \
'' every :::1::1 using (0.0123984/$1):2 title "{/:Italic=15 \316\274}_{/=13 m}" axes x1y2 \
   with lines linetype 11 linecolor     rgbcolor "forest-green"
unset table
```

Dispersion corrections can be not fixed (as in RIETAN-FP) but refined in an in-house version of RIETAN-2000 by Xiao [64]. This feature will be useful on the use of a wavelength near the absorption edge of an element.

Friedel pairs

Friedel's law holds in centrosymmetric space groups:

$$|F(\boldsymbol{h})| = |F(\bar{\boldsymbol{h}})|, \tag{3.18}$$

where $F(\boldsymbol{h}) \equiv F(\boldsymbol{h}_K, \text{cryst.})$, and $\bar{\boldsymbol{h}}$ denotes reflection $\bar{h}\bar{k}\bar{l}$. As **Fig. 3.3** illustrates, compounds belonging to noncentrosymmetric space groups have different $|F(\boldsymbol{h})|$ values for hkl and $\bar{h}\bar{k}\bar{l}$ reflections (Friedel pair) because of the X-ray dispersion effect [65]. For example, in the case of orthorhombic space group $P222$ (No. 16), reflections belonging to a pair of reflection groups,

1. hkl, $h\overline{k}l$, $\overline{h}k\overline{l}$, and $\overline{hk}l$,
2. $\overline{hk}\overline{l}$, $hk\overline{l}$, $h\overline{k}l$, and $\overline{h}kl$,

have $|F(\bar{\boldsymbol{h}})|$'s slightly different from each other. These differences are particularly appreciable in compounds containing heavy atoms. When dealing with such a compound with RIETAN-FP, the multiplicity, m_K, generated by LAZY PULVERIX [66] is divided by 2, and the $|F(\boldsymbol{h}_K, \text{cryst.})|$'s of hkl and $\bar{h}\bar{k}\bar{l}$ reflections are individually calculated to raise the accuracy of crystal-structure factors.

$$|F(\boldsymbol{h})| \neq |F(\bar{\boldsymbol{h}})|. \tag{3.19}$$

If the dispersion effect were included in $F_\mathrm{o}(\boldsymbol{h}_K)$, electron densities, ρ, resulting from Fourier synthesis or MEM analysis would become meaningless complex numbers. Then, contributions of X-ray dispersion, *viz.* $\Delta F(\boldsymbol{h})$ (red lines) in Fig. 3.3, must be subtracted from observed structure factors to calculate ρ's correctly [67].

Further attention must be paid to the origin in parts of noncentrosymmetric space groups where no origin is assigned to a definite position; refer to item 11 in 17.3.14 for details.

Coherent scattering length

Scattering of neutrons by the atomic nucleus is regarded as that by a point with a negligible size because the size of the atomic nucleus has an order of 1 fm, which is much smaller than the wavelength, λ, of neutrons (*ca.* 10^5 fm). The scattered wave is, therefore, a spherical one with the atomic nucleus at the center, having the wave function φ:

$$\varphi(r) = -\frac{b_\mathrm{c}}{r} \exp\left(\frac{2\pi \mathrm{i} r}{\lambda}\right), \tag{3.20}$$

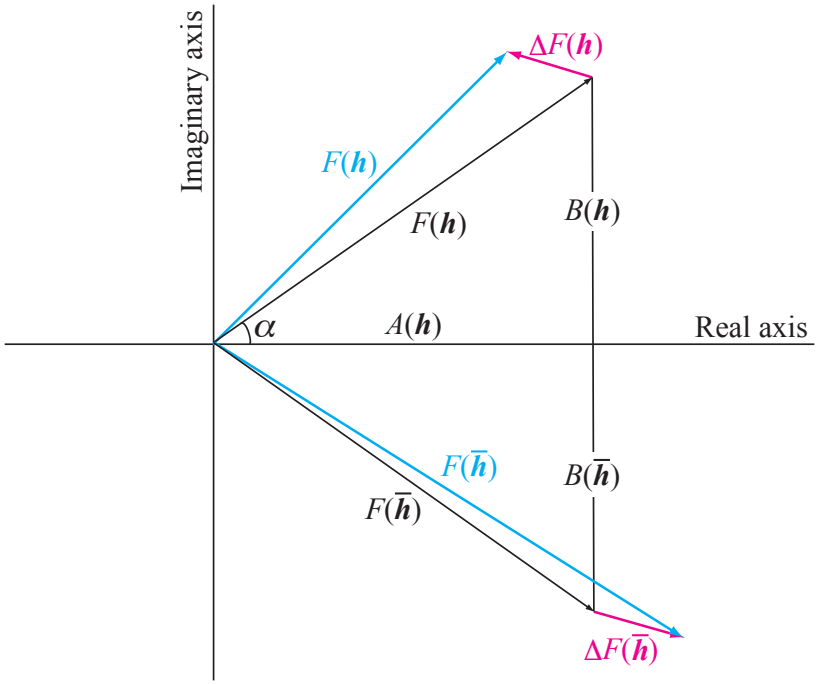

Figure 3.3: The relationship between different components of the structure amplitude in a Friedel pair when there are anomalously scattering atoms in the crystal structure. $A(\boldsymbol{h})$: the real part of the structure factor $F(\boldsymbol{h})$, $B(\boldsymbol{h})$: the imaginary part of $F(\boldsymbol{h})$, α: phase angle

where r is the distance from the atomic nucleus, and b_c is the coherent scattering length which corresponds to $f_0(\sin\theta/\lambda)$ in X-ray diffraction.

Differences in scattering power between X rays and neutrons

The difference in the mechanism of elastic scattering described above leads to the following differences in scattering power between the atomic form factor, $f_0(\sin\theta/\lambda)$, for X rays and the coherent-scattering length, b_c, for neutrons [24] :

1. As the number of electrons for an atom or an ion is increased, $f_0(\sin\theta/\lambda)$ increases monotonously. On the other hand, b_c changes irregularly and takes positive or negative values, depending on the atomic nucleus (isotope), as illustrated in **Fig. 3.4**.

2. In X-ray diffraction, $f_0(\sin\theta/\lambda)$ decreases monotonously with increasing $\sin\theta/\lambda$ whereas in neutron diffraction b_c remains constant, regardless of $\sin\theta/\lambda$.

3. Absorption of X rays is generally far higher than that of neutrons with absorption coefficients 10^4–10^5 times as much as those for neutrons. Excitations with much higher absorption of neutrons include shielding materials B (as B_4C), Cd, and Gd (as Gd_2O_3).

In general, inner shell electrons contribute to $f_0(\sin\theta/\lambda)$ over all the $\sin\theta/\lambda$ region whereas outer shell electrons contribute only in a small $\sin\theta/\lambda$ region. The invariant b_c value arises from

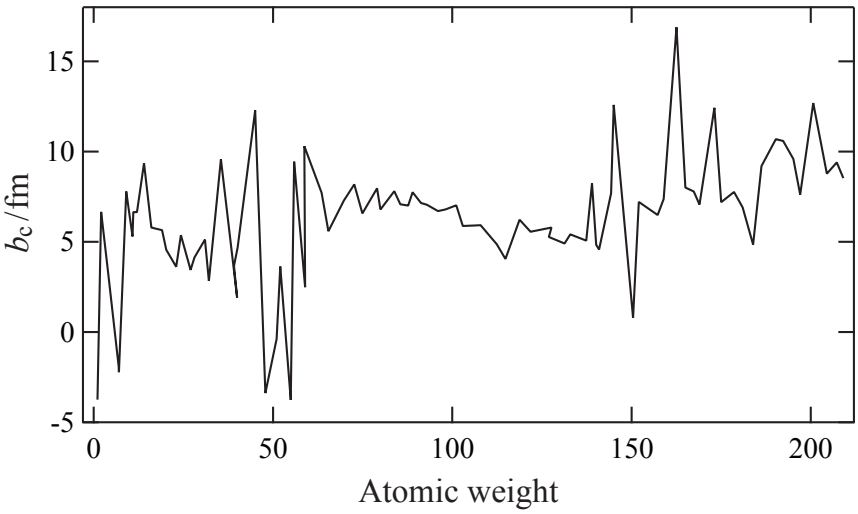

Figure 3.4: Coherent atomic scattering lengths for thermal neutrons plotted as a function of atomic weight

the fact that it is the Fourier transform of the nuclear density whose distribution is similar to a δ function (spot-like). The intensities of reflections with large Q (small d) are relatively higher in neutron diffraction than in X-ray diffraction because of the constancy of b_c. This tendency is favorable for collecting information about those atoms with small atomic numbers because they display marked thermal motion and their $f_0(\sin\theta/\lambda)$ values decrease considerably in high-Q regions.

The first characteristic of neutron diffraction is utilized for the analysis of compounds with a combination of constituent atoms which is not suitable for X-ray diffraction; that is,

1. O (atomic No.: 8, $b_c = 5.803$ fm) has a b_c value 70 % as large as that of Bi (atomic No.: 83, $b_c = 8.532$ fm); the b_c values of H ($b_c = -3.7390$ fm), Li ($b_c = -1.90$ fm), Ti ($b_c = -3.370$ fm), and Mn ($b_c = -3.750$ fm) are negative; b_c changes irregularly with increasing atomic weight.

2. Evidently, neutron diffraction is very useful for refinement of the structure parameters for light elements (*e.g.*, D, Li, N, and O) in compounds containing heavy elements as principal constituents and for distinguishing elements (*e.g.*, N and O, Mn and Fe, Co and Ni, and Ba and La) with comparable atomic weights.

3. Two atoms with b_c values close to each other may have considerably different $f_0(\sin\theta/\lambda)$ values, *e.g.*, O and Ba.

Bear in mind that asfdc contains data for three popular isotopes: ^{2}H (‘`D`’), ^{7}Li (‘`Li7`’), and ^{11}B (‘`B11`’), where the strings in the parentheses denote names of the real chemical species (see 17.3.9). Compounds containing these isotopes are often used in neutron diffraction experiments to minimize absorption of neutrons.

3.5.2 Two thermal-vibration models

Let B_j and U_j be two types of isotropic atomic displacement parameters, and $\boldsymbol{\beta}_j$ the anisotropic atomic displacement tensor defined as

$$\boldsymbol{\beta}_j = \begin{pmatrix} \beta_{11j} & \beta_{12j} & \beta_{13j} \\ \beta_{12j} & \beta_{22j} & \beta_{23j} \\ \beta_{13j} & \beta_{23j} & \beta_{33j} \end{pmatrix}. \tag{3.21}$$

Then, the thermal displacement of atom j is formulated in two different ways, that is,

$$\begin{aligned} T_j &= \exp\left[-B_j\left(\frac{\sin\theta_K}{\lambda}\right)^2\right] \\ &= \exp\left[-8\pi^2 U_j\left(\frac{\sin\theta_K}{\lambda}\right)^2\right] \end{aligned} \tag{3.22}$$

for isotropic thermal motion and

$$T_j = \exp\left(-\widetilde{\boldsymbol{h}}\cdot\boldsymbol{\beta}_j\cdot\boldsymbol{h}\right) \tag{3.23}$$

with

$$\widetilde{\boldsymbol{h}} = \begin{pmatrix} h & k & l \end{pmatrix} \tag{3.24}$$

and

$$\boldsymbol{h} = \begin{pmatrix} h \\ k \\ l \end{pmatrix}; \tag{3.25}$$

hereinafter, the tilde denotes the transposed matrix.

Because $\widetilde{\boldsymbol{h}}\cdot\boldsymbol{\beta}_j\cdot\boldsymbol{h} > 0$ for all $\boldsymbol{h}$, the following conditions have to be satisfied among β_{11j}, β_{22j}, $\cdots$ after Rietveld refinement:

$$\beta_{11j} > 0, \tag{3.26}$$

$$\beta_{22j} > 0, \tag{3.27}$$

$$\beta_{33j} > 0, \tag{3.28}$$

$$\beta_{11j}\beta_{22j} + \beta_{22j}\beta_{33j} + \beta_{33j}\beta_{11j} - \beta_{12j}^2 - \beta_{13j}^2 - \beta_{23j}^2 > 0, \tag{3.29}$$

$$\det\boldsymbol{\beta} > 0, \tag{3.30}$$

where det denotes the determinant. Unless anisotropic atomic displacement parameters satisfy them because of low-quality diffraction data, isotropic ones should be refined. In general, the refinement of anisotropic atomic displacement parameters from X-ray powder-diffraction data is fairly difficult because of rapid decreases in $f_0(\sin\theta/\lambda)$ with increasing $\sin\theta/\lambda$.

B_j and U_j are related to the mean square displacement, $\langle u_j^2\rangle$, along the direction perpendicular to the reflection plane with

$$\begin{aligned} B_j &= 8\pi^2 U_j \\ &= 8\pi^2\langle u_j^2\rangle. \end{aligned} \tag{3.31}$$

Figure 3.5 gives isotropic temperature factors, T, plotted against $\sin\theta/\lambda$ for five different

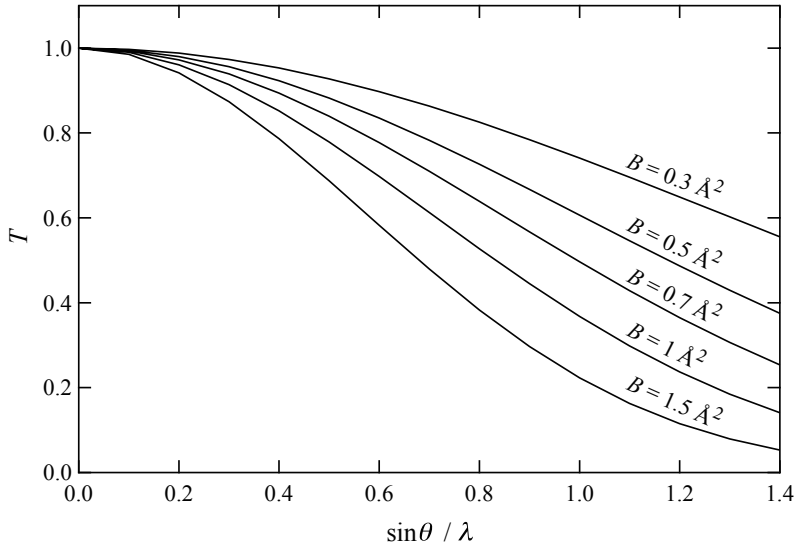

Figure 3.5: Isotropic temperature factor *versus* $\sin/\lambda$ for five different B parameters

isotropic atomic displacement parameters, B. T decreases more rapidly with increasing B. The order of $\sqrt{U}$ lies between 0.05 Å and 0.2 Å (B lying between 0.2 and 3.16 Å^2) in typical inorganic compounds whereas it reaches 0.5 Å ($B \approx 20$ Å^2) for some organic crystals [68]. The consequence of this is to make the electron or nuclear density of the atom more diffuse, reducing the ability for scattering X rays or neutrons with increasing values of $\sin\theta/\lambda$.

Since $\widetilde{\boldsymbol{h}} \cdot \boldsymbol{\beta}_j \cdot \boldsymbol{h}$ is expressed as

$$\widetilde{\boldsymbol{h}} \cdot \boldsymbol{\beta}_j \cdot \boldsymbol{h} = \begin{pmatrix} h & k & l \end{pmatrix} \begin{pmatrix} \beta_{11j} & \beta_{12j} & \beta_{13j} \\ \beta_{12j} & \beta_{22j} & \beta_{23j} \\ \beta_{13j} & \beta_{23j} & \beta_{33j} \end{pmatrix} \begin{pmatrix} h \\ k \\ l \end{pmatrix}, \tag{3.32}$$

Eq. (3.23) is rewritten as

$$T_j = \exp\left[-\left(h^2\beta_{11j} + k^2\beta_{22j} + l^2\beta_{33j} + 2hk\beta_{12j} + 2hl\beta_{13j} + 2kl\beta_{23j}\right)\right], \tag{3.33}$$

which is the simplest expression of T_j. Other two representations of T_j,

$$T_j = \exp\left[-2\pi^2\left(h^2a^{*2}U_{11j} + k^2b^{*2}U_{22j} + l^2c^{*2}U_{33j} + 2hka^*b^*U_{12j} + 2hla^*c^*U_{13j} + 2klb^*c^*U_{23j}\right)\right], \tag{3.34}$$

$$T_j = \exp\left[-\frac{1}{4}\left(h^2a^{*2}B_{11j} + k^2b^{*2}B_{22j} + l^2c^{*2}B_{33j} + 2hka^*b^*B_{12j} + 2hla^*c^*B_{13j} + 2klb^*c^*B_{23j}\right)\right], \tag{3.35}$$

may also be used. Equations (3.33), (3.34), and (3.35) contain the following three sets of anisotropic atomic displacement parameters, respectively [69]:

1. β_{11j}, β_{22j}, β_{33j}, β_{12j}, β_{13j}, and β_{23j},
2. U_{11j}, U_{22j}, U_{33j}, U_{12j}, U_{13j}, and U_{23j},
3. B_{11j}, B_{22j}, B_{33j}, B_{12j}, B_{13j}, and B_{23j}.

The β parameters are dimensionless whereas the U and B parameters have a dimensional formula of L^2. The U parameters are related to the corresponding B ones in a similar way as Eq. (3.31) for isotropic thermal motion. It is the elements of the atomic displacement tensor, β_{11j}, β_{22j}, $\cdots$, that are actually input, refined, and output in RIETAN-FP due to the conciseness of Eq. (3.33). Nevertheless, the other set of anisotropic atomic displacement parameters, U_{11j}, U_{22j}, , U_{33j}, $\cdots$, should be described in papers, review articles, reports, CIFs (Crystallographic Information File), *etc.* because U_{11j}, U_{22j}, and U_{33j} are mean square displacements along a, b, and c axes, respectively; the shape of each displacement ellipsoid can directly be understood with them. Further, description of U_j is likewise preferred to that of B_j on the use of an isotropic thermal-vibration model.

On refinements of anisotropic atomic displacement parameters, $\boldsymbol{\beta}_j$, certain parameters will be constant or linearly related to others, which depends on site symmetry. Note that symmetry conditions described in Ref. [70, 71] are valid only for the first equivalent positions described in "International Tables for Crystallography," Vol. A [72] and that a center of symmetry must be placed at the origin if any.

On the refinement of β_{11j}, β_{22j}, $\cdots$, equivalent isotropic atomic displacement parameters, B_{eq} and U_{eq} are calculated from them, a^*, b^*, c^*, and the metric tensor, $\boldsymbol{G}$, of the direct cell (see Appendix A) [73, 74]:

$$B_{\mathrm{eq}} = 8\pi^2 U_{\mathrm{eq}} \tag{3.36}$$

with

$$\begin{aligned} U_{\mathrm{eq}} &= \frac{1}{3}\sum_i\sum_j U_{ij}a_i^*a_j^*\boldsymbol{a}_i\cdot\boldsymbol{a}_j \\ &= \frac{1}{3}\big[U_{11}\left(aa^*\right)^2 + U_{22}\left(bb^*\right)^2 + U_{33}\left(cc^*\right)^2 \\ &\quad + 2U_{12}a^*b^*ab\cos\gamma + 2U_{13}a^*c^*ac\cos\beta + 2U_{23}b^*c^*bc\cos\alpha\big]. \end{aligned} \tag{3.37}$$

Since $a^* = 1/a$, $b^* = 1/b$, and $c^* = 1/c$ in orthogonal systems (orthorhombic, tetragonal, and cubic), it follows that

$$U_{\mathrm{eq}} = \frac{1}{3}\big(U_{11} + U_{22} + U_{33}\big). \tag{3.38}$$

RIETAN-FP outputs all of the above atomic displacement parameters after a list of final structure parameters with their standard uncertainties.

3.5.3 How to deal with equivalent positions

A text file, spgra, (see 17.1) contains coordinates of equivalent positions of 230 space groups; those of inverted positions (an inversion center at the origin) and translated ones (complex lattices) are not included in spgra. These coordinates for the space group of a compound to be analyzed in Rietveld refinement are used on calculation of structure factors.

The summations $\sum_j$ in Eqs. (3.13) and (3.49) are actually not carried out straightforwardly in RIETAN-FP. Only fractional coordinates, $\boldsymbol{x}_j$ (j: site number), of atoms in the asymmetric unit need to be input in RIETAN-FP, which reads in coordinates of equivalent positions from

spgra (see 17.1), converts them into corresponding symmetry operations, *i.e.*, rotation matrices $\boldsymbol{R}_s$ and translation vector $\boldsymbol{t}_s$. Then, sth equivalent position, $\boldsymbol{x}_{js}$, is given by

$$\boldsymbol{x}_s = \boldsymbol{R}_s \cdot \boldsymbol{x}_j + \boldsymbol{t}_s; \tag{3.39}$$

that is,

$$\begin{aligned} \begin{pmatrix} x_{js} \\ y_{js} \\ z_{js} \end{pmatrix} &= \begin{pmatrix} R_{11s} & R_{12s} & R_{13s} \\ R_{21s} & R_{22s} & R_{23s} \\ R_{31s} & R_{32s} & R_{33s} \end{pmatrix} \begin{pmatrix} x_j \\ y_j \\ z_j \end{pmatrix} + \begin{pmatrix} t_{1s} \\ t_{2s} \\ t_{3s} \end{pmatrix} \\ &= \begin{pmatrix} R_{11s}x_j + R_{12s}y_j + R_{13s}z_j + t_{1s} \\ R_{21s}x_j + R_{22s}y_j + R_{23s}z_j + t_{2s} \\ R_{31s}x_j + R_{32s}y_j + R_{33s}z_j + t_{3s} \end{pmatrix}. \end{aligned} \tag{3.40}$$

Components in $\boldsymbol{R}_s$ are all 0 or ± 1 while those in $\boldsymbol{t}_s$ are 0, $n/2$, $n/4$, and $n/6$ (n: integer) with $0 \leqslant t_s < 1$. All the off-diagonal terms are zero in orthorhombic, monoclinic, and triclinic systems. The fractional coordinates of (part of) atoms outside the asymmetric unit are evaluated by applying these symmetry operations to those of the atoms inside the asymmetric unit. That is, the coordinates, x_{js}, y_{js}, and z_{js}, of the sth equivalent position are related to those of the atoms in the asymmetric unit: x_j, y_j, and z_j. Inverted positions are not included in the above calculations in the case of centrosymmetric space groups.

In actual calculation of the structure factor, $F(\boldsymbol{h}_K)$, and the partial derivatives of $F(\boldsymbol{h}_K)$ with respect to structure parameters, the cosine term,

$$C_{sj\boldsymbol{h}} = \cos 2\pi\big(\widetilde{\boldsymbol{h}}_s \cdot \boldsymbol{x}_j + t_s\big), \tag{3.41}$$

and the sine term,

$$S_{sj\boldsymbol{h}} = \sin 2\pi\big(\widetilde{\boldsymbol{h}}_s \cdot \boldsymbol{x}_j + t_s\big), \tag{3.42}$$

with

$$\begin{aligned} \boldsymbol{h}_s &\equiv \boldsymbol{h} \cdot \boldsymbol{R}_s \\ &= \widetilde{\boldsymbol{R}}_s \cdot \boldsymbol{h} \end{aligned} \tag{3.43}$$

and

$$t_s = \widetilde{\boldsymbol{t}}_s \cdot \boldsymbol{h} \tag{3.44}$$

are used to accelerate calculation of fractional coordinates for equivalent positions at the expense of tiny memory consumption [54]. Further, overlaps of equivalent positions are checked in advance from initial fractional coordinates so that only one of overlapped atoms may be included in the calculation of $F(\boldsymbol{h}_K)$ and its derivatives with respect to structure parameters.

After calculating the partial structure factor in the above way, it is further multiplied by a coefficient in **Table 3.2** in space groups with complex lattices and/or inversion centers at the origin (centrosymmetric) [54].

A point, j, on a symmetry element containing no translation is referred to as a special position. For special positions, part of structure parameters may be fixed, and linear equality constraints may be imposed between part of them (see 17.3.16). For example, the following rules hold for fractional coordinates in structure refinement:

Table 3.2: Lattice types and coefficients for structure factors

	P	A, B, C, I	F	R
Centrosymmetric	2	4	8	6
Noncentrosymmetric	1	2	4	3

- For an atoms on the center of symmetry, all the coordinates are fixed.
- For an atom on a rotation axis, only coordinates along the axis are variable.
- For an atom on a mirror plane, only two coordinates on the plane are variable.

The number of equivalent positions, *i.e.*, the site multiplicity, for a special potion is equal to that of general equivalent positions divided by an integer, n_j. Not g_j but $g_j/n_j = g_j \times$(site multiplicity)/(number of general equivalent positions) is usually refined in many structure-refinement programs only to keep them simple. For example, the multiplicity of the general equivalent position in space group $Fd\bar{3}m$ (No. 227) is 192. Then, $n_j = 2$ for the 96h site (0, y, $\bar{y}$), $n_j = 6$ for the 32e site (x, x, x), and $n_j = 24$ for the 8a (1/8, 1/8, 1/8) site in the case of origin choice 2 with the center of symmetry at the origin.

RIETAN-FP adopts a more sophisticated approach to the refinement of g_j. After the overlap of equivalent positions has been checked for every site, only one of overlapped positions is arbitrarily selected to minimize the time to calculate Eq. (3.13), particularly in space groups where the numbers of equivalent positions are relatively large. Consequently, g_j, can be refined straightforwardly.

3.6 Magnetic-Structure Factor

Magnetic scattering is caused by interaction between the magnetic moment of atoms with unpaired electrons in 3d, 4d, 4f, and 5f orbitals and that of the neutron. Neutron diffraction is the only means of determining the direction and magnitude of a magnetic moment for each magnetic-atom site and, hence, have a firm footing in experimental research in magnetism [75, 76]. RIETAN-FP allows us to analyze simple collinear magnetic structures where the magnetic moments of all the magnetic-atom sites are aligned along the same direction with Shirane's equations [77].

3.6.1 Magnetic-structure parameters

Let us define the magnetic interaction vector, $\boldsymbol{q}$, as

$$\begin{aligned} \boldsymbol{q} &= \hat{\boldsymbol{\kappa}} \times (\hat{\boldsymbol{\mu}} \times \hat{\boldsymbol{\kappa}}) \\ &= \hat{\boldsymbol{\mu}} - (\hat{\boldsymbol{\kappa}} \cdot \hat{\boldsymbol{\mu}})\hat{\boldsymbol{\kappa}} \end{aligned} \tag{3.45}$$

with

$$|q| = \sin\alpha, \tag{3.46}$$

where $\hat{\boldsymbol{\mu}}$ and $\hat{\boldsymbol{\kappa}}$ are, respectively, unit vectors parallel to the scattering vector and the magnetic

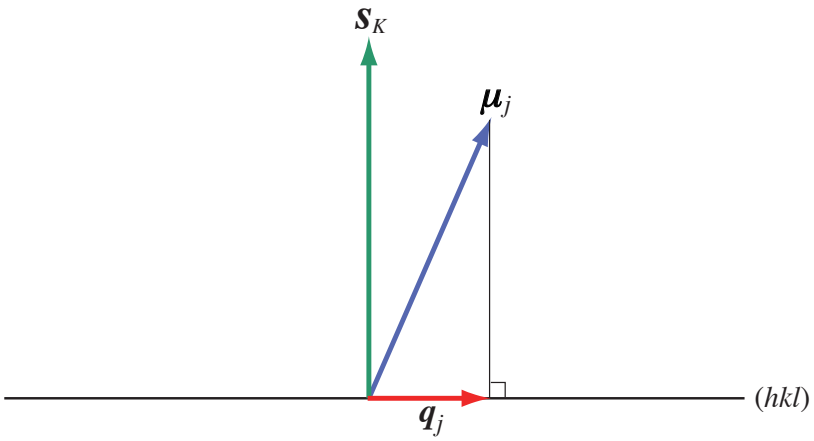

Figure 3.6: The magnetic interaction vector, $\boldsymbol{q}_j$, which is the component of $\boldsymbol{\mu}_j$ perpendicular to the reciprocal-lattice vector, $\boldsymbol{s}_K$

moment, and α is the angle between $\hat{\boldsymbol{\mu}}$ and $\hat{\boldsymbol{\kappa}}$ [78]. A red arrow in **Fig. 3.6** on the (hkl) plane is the magnetic interaction vector of a magnetic atom at site j.

In the nuclear-scattering case, the structure amplitude, $F(\boldsymbol{h}_K, \text{cryst.})$, is computed by summing up the contributions from all the atoms in the unit cell as formulated in Eq. (3.13). When coherent magnetic scattering occurs, the magnetic structure amplitude, $\boldsymbol{F}(\boldsymbol{h}_K, \text{magn.})$, is likewise represented as a vector γ is $\mu_\text{n}/\mu_\text{N}$ = (magnetic moment of the neutron)/(nuclear magneton), e is the elementary charge,

$$\boldsymbol{F}(\boldsymbol{h}_K, \text{magn.}) = \sum_j g_j p_j \boldsymbol{q}_j T_j \exp\left[2\pi\mathrm{i}\left(hx_j + ky_j + lz_j\right)\right] \tag{3.47}$$

with

$$p_j = \left(\frac{\gamma e^2}{2m_\text{e}c^2}\right) g J f_j(\text{magn.}), \tag{3.48}$$

where p_j is the magnetic scattering length, m_e is the electron mass, c is the light speed, g is the Landé splitting factor (see 3.6.3), J is the total angular momentum quantum number, and $f_j(\text{magn.})$ is the magnetic form factor for unpaired electrons (see 3.6.3) [79]. The summation, Σ_j, in Eq. (3.47) is carried out over all the magnetic atoms in the unit cell. The intensity of the magnetic contribution to the hkl reflection is proportional to $|\boldsymbol{F}(\boldsymbol{h}_K, \text{magn.})|^2$ as expressed in Eq. (2.7).

Let $\cos\eta$ be the direction cosine between the scattering vector (see A.3) , $\boldsymbol{Q}_K$, and magnetic moment, s_j the magnitude of the magnetic moment $\boldsymbol{\mu}_j$, then $|F(\boldsymbol{h}_K, \text{magn.})|$ for the collinear magnetic structure is greatly simplified in comparison with the generalized form of $\boldsymbol{F}(\boldsymbol{h}_K, \text{magn.})$, *i.e.*, Eq. (3.47):

$$|F(\boldsymbol{h}_K, \text{magn.})| = \frac{\gamma e^2}{2m_\text{e}c^2}\sqrt{1 - \left\langle\cos^2\eta\right\rangle}\left|\sum_j g_j s_j f_j(\text{magn.}) T_j \exp\left[2\pi\mathrm{i}\left(hx_j + ky_j + lz_j\right)\right]\right|, \tag{3.49}$$

where $\left\langle\cos^2\eta\right\rangle$ is the average of $\cos^2\eta$ values for all the equivalent (hkl) planes, and s_j has either a positive or negative value, depending on the direction of $\boldsymbol{\mu}_j$.

Table 3.3: Values of $\langle \cos^2 \eta \rangle$ in collinear magnetic structures

Crystal system	$\langle \cos^2 \eta \rangle$
Cubic	$\frac{1}{3}$
Hexagonal	$\left[\frac{1}{2}\left(h^2+k^2+hk\right)a^{*2}\sin^2\varphi + l^2c^{*2}\cos^2\varphi\right]d^2$ φ: angle between $\boldsymbol{\mu}_j$ and the c axis
Rhombohedral	$\left[2(n-r)\left(1-\cos\alpha^*\right)\sin^2\varphi + (n+2r)\left(1+2\cos\alpha^*\right)\cos^2\varphi\right]\frac{1}{3}a^{*2}d^2$ $n = h^2+k^2+l^2$ $r = hk+kl+lh$ φ: angle between $\boldsymbol{\mu}_j$ and the [111] axis
Tetragonal	$\left[\frac{1}{2}\left(h^2+k^2\right)a^{*2}\sin^2\varphi + l^2c^{*2}\cos^2\varphi\right]d^2$ φ: angle between $\boldsymbol{\mu}_j$ and the c axis
Orthorhombic	$\left(h^2a^{*2}\cos^2\varphi_a + k^2b^{*2}\cos^2\varphi_b + l^2c^{*2}\cos^2\varphi_c\right)d^2$ φ_a: angle between $\boldsymbol{\mu}_j$ and the a axis φ_b: angle between $\boldsymbol{\mu}_j$ and the b axis φ_c: angle between $\boldsymbol{\mu}_j$ and the c axis
Monoclinic	$\left[\left(ha^*\cos\varphi_{a*} + lc^*\cos\varphi_{c*}\right)^2 + \left(kb^*\cos\varphi_{b*}\right)^2\right]d^2$ φ_{a*}: angle between $\boldsymbol{\mu}_j$ and the a^* axis φ_{b*}: angle between $\boldsymbol{\mu}_j$ and the b^* axis φ_{c*}: angle between $\boldsymbol{\mu}_j$ and the c^* axis
Triclinic	$\left(ha^*\cos\varphi_{a*} + kb^*\cos\varphi_{b*} + lc^*\cos\varphi_{c*}\right)^2 d^2$ φ_{a*}: angle between $\boldsymbol{\mu}_j$ and the a^* axis φ_{b*}: angle between $\boldsymbol{\mu}_j$ and the b^* axis φ_{c*}: angle between $\boldsymbol{\mu}_j$ and the c^* axis

Table 3.3 lists equations to calculate $\langle \cos^2 \eta \rangle$ for seven crystal systems. Equations for the cubic, hexagonal, rhombohedral, tetragonal, and orthorhombic systems were derived by Shirane [77] while those for the monoclinic and triclinic systems by N. Yamada [80] (see Appendix B).

Magnetic-structure parameters refined in Rietveld analysis are s_j and

1. φ (hexagonal, rhombohedral, and tetragonal),
2. φ_a, φ_b, and φ_c (orthorhombic),
3. φ_{a*}, φ_{b*}, and φ_{c*} (monoclinic and triclinic).

The Rietveld analysis of a magnetic material from neutron powder-diffraction data necessarily leads to the partial loss of its magnetic crystal structure. For example, we can obtain no information on the direction of the magnetic moment in the cubic system where $\langle \cos^2 \eta \rangle = 1/3$;

on the other hand, components along the a, b, and c axes can be determined in the orthorhombic system.

Before starting to refine magnetic-structure parameters, trial and error concerning the direction and magnitude of $\boldsymbol{\mu}_j$ in the simulation mode (`NMODE = 2`) is highly recommended. In the simulation of powder diffraction patterns, pay attention to the fact that only the component of $\boldsymbol{\mu}_j$ perpendicular to the reciprocal-lattice vector, $\boldsymbol{s}_K$, contributes to magnetic scattering, as illustrated in Fig. 3.6. In other words, magnetic scattering disappear when the direction of the magnetic moment coincide with that of the scattering vector.

3.6.2 Limitations on the analysis of magnetic structures

If crystallographically equivalent sites of magnetic atoms are nonequivalent to each other when taking spin directions into consideration, special treatment is required. For example, an antiferromagnetic oxide $LaMnO_3$ (space group: *Pbnm*) shows reflections such as 001 and 003, which are absent in its X-ray diffraction pattern. Then, we must select a space group consistent with the symmetry of the magnetic structure and impose constraints on appropriate crystal-structure parameters.

We must sometimes analyze collinear magnetic structures whose symmetry cannot be represented by crystallographic space groups. Such a case is not rare in view of the fact that even in ferromagnets, magnetic-symmetry groups are as many as 275, which is larger than 230 for crystallographic space groups. A sophisticated technique to overcome such a difficulty is to regard that the magnetic material consists of two virtual phases: a nonmagnetic phase with a crystallographic unit cell and a metallic phase with a magnetic unit cell. Details in this procedure will be described separately in Chap. 8.

3.6.3 Analytical approximations to the magnetic form factor

An outstanding characteristic of magnetic scattering is its strong dependence on the diffraction angle, 2θ (lattice-plane spacing, d). Because the magnetic scattering of neutron is caused by outer electrons such as 3d, 4f, and 5d electrons, the forward scattering is much stronger than the back-scattering. Interference effects within individual atoms give rise to a magnetic form factor analogous to the atomic scattering factor in X-ray diffraction.

The form factors used in the calculations of the cross sections for magnetic scattering of neutrons are defined as

$$\left\langle j_l(k) \right\rangle = \int_0^\infty U^2(r) j_l(kr) 4\pi r^2 \mathrm{d}r, \tag{3.50}$$

in which $U(r)$ is the radial wavefunction for the unpaired electrons in the atoms, k is the length of the scattering vector, and $j_l(kr)$ is the lth-order Bessel function. RIETAN-FP uses $\left\langle j_l(s) \right\rangle$ ($l = 0$ and 2) as magnetic form factors f_j(magn.) [81]. The $\left\langle j_0 \right\rangle$ magnetic form factor is calculated from seven coefficients (A, a, B, b, C, c, and D) in an analytical approximation to $\left\langle j_0(s) \right\rangle$ as a function of s ($= \sin\theta/\lambda$):

$$\left\langle j_0(s) \right\rangle = A \exp\left(-as^2\right) + B \exp\left(-bs^2\right) + C \exp\left(-cs^2\right) + D. \tag{3.51}$$

On the other hand, the $\langle j_2 \rangle$ magnetic form factor is approximated with another type of Bessel equation:

$$\begin{aligned} \langle j_2(s) \rangle &= As^2 \exp\left(-as^2\right) + Bs^2 \exp\left(-bs^2\right) + Cs^2 \exp\left(-cs^2\right) + Ds^2 \\ &= s^2 \left[A \exp\left(-as^2\right) + B \exp\left(-bs^2\right) + C \exp\left(-cs^2\right) + D\right]. \end{aligned} \tag{3.52}$$

The coefficients, A, a, B, b, C, c, and D, in Eqs. (3.51) and (3.52) are tabulated for the $3d$ and $4d$ transition series, the $4f$ electrons of lanthanoid ions, and the $5f$ electrons of some actinoid ions [81].

In the so-called dipole approximation, only the lowest-order spherical harmonics describing the shape of the ion are used; the electron density is treated spherical. Within the dipole approximation, the magnetic form factor is given by

$$f_j(\text{magn.}) = \langle j_0(s) \rangle + \left(\frac{2}{g} - 1\right) \langle j_2(s) \rangle. \tag{3.53}$$

Beware of incorrect Eq. (6.1.2.17) in ref. [82]. Let S the spin angular momentum, and L the orbital angular momentum, then g is given by [78]

$$g = 1 + \frac{J(J+1) + S(S+1) - L(L+1)}{2J(J+1)}. \tag{3.54}$$

Intensities of reflections due to magnetic scattering decay rapidly with increasing Q because of the extreme decrease in $f_j(\text{magn.})$ with Q, which is explained in terms of magnetic scattering of neutrons by outer shell electrons [78].

3.7 Preferred-Orientation Functions

Preferred orientation should be corrected with a function, P_K, which is independent of the diffraction geometry and applicable to both plate and needle-shaped crystallites. However, a perfect preferred orientation function applicable to any samples does not exist particularly when the preferred orientation effect is very marked. The best way to tackle this problem is to reduce the preferred-orientation effect by preparing the specimen properly.

In general, preferred orientation is negligible when the crystallite size is less than about 3 µm. Then, the so-called ω (ϵ) scan [83] is recommended to check whether or not coarse particles are included in the specimen.

3.7.1 March–Dollase function

Dollase [84] tested several preferred-orientation functions and selected a special case from the more general description by March [85] as the best preferred-orientation correction. This March-Dollase function has been implemented in most Rietveld-refinement program as a preferred-orientation function:

$$P_K = \sum_{j=1}^{m_K} \frac{1}{m_K} \left(r^2 \cos^2 \alpha_j + r^{-1} \sin^2 \alpha_j\right)^{-\frac{3}{2}}, \tag{3.55}$$

where r is an adjustable parameter, and α_j is the angle between the preferred-orientation vector, $h_\mathrm{p}\boldsymbol{a}^* + k_\mathrm{p}\boldsymbol{b}^* + l_\mathrm{p}\boldsymbol{c}^*$, and the reciprocal-lattice vector, $\boldsymbol{s}_K$, for the jth member of the symmetry-equivalent set of m_K diffraction planes. The summation over m_K planes and averaging in Eq.

(3.55) is required only when the symmetry is cubic, or the preferred-orientation axis is not parallel to a unique axis. Nevertheless, the summation is alway carried out in RIETAN-FP regardless of crystal systems or preferred-orientation axes for simplicity.

The March-Dollase function (3.55) displays overall performance good enough for most structural studies. It conserves scattering matter, thereby allowing its use in the quantitative analysis of mixtures.

The refinable parameter, r, represents the effective sample compression or extension due to preferred orientation. Its value depends on both the diffraction geometry and the crystallite shape:

(a) Cylindrical sample (*e.g.*, neutron powder diffraction using vanadium cells)

Plate crystallite	$r > 1$
Needle-shaped crystallite	$r < 1$

(b) Flat-plate sample (*e.g.*, Bragg-Brentano geometry)

Plate crystallite	$r < 1$
Needle-shaped crystallite	$r > 1$

For samples exhibiting no preferred orientation, r is equal to one (not zero!).

3.7.2 Modified March–Dollase function

To deal with up to three different preferred-orientation vectors, we added a modified March–Dollase function [86, 87], P'_K, which is a linear combination of Eq. (3.55):

$$P'_K = f_1 P_K(r_1) + f_2 P_K(r_2) + f_3 P_K(r_3) \tag{3.56}$$

with

$$f_1 + f_2 + f_3 = 1.$$

This equation is a special case of a preferred-orientation function described by Pecharsky and Zavalij [88]: $k_0 = 0$ and $N_a = 3$ in Eq. (2.80) of their book.

Let n_p be the number of preferred-orientation vectors. In the input file, hoge.ins, of RIETAN-FP, preferred-orientation vectors should be input in the following ways:

$$n_\mathrm{p} = 1 : \ h_\mathrm{p} = k_\mathrm{p} = l_\mathrm{p} = 0 \text{ for the second and third vectors}$$
$$n_\mathrm{p} = 2 : \ h_\mathrm{p} = k_\mathrm{p} = l_\mathrm{p} = 0 \text{ for the third vector}$$

The six preferred-orientation parameters, f_1, r_1, f_2, r_2, f_3, and r_3, must alway be input in this order. Then, the following linear constraints are imposed on f_1, f_2, and f_3:

$$n_\mathrm{p} = 1 : \ f_1 = 1,$$
$$n_\mathrm{p} = 2 : \ f_2 = 1 - f_1,$$
$$n_\mathrm{p} = 3 : \ f_3 = 1 - f_1 - f_2.$$

Hence, no linear constraints corresponding to them are required in hoge.ins. Further, f_2, r_2, f_3 and r_3 should be set at 0 when $n_\mathrm{p} = 1$ while f_3 and r_3 should be set at 0 when $n_\mathrm{p} = 2$. Of course, their ID(I)'s are also set at 0.

3.7.3 Spherical-harmonics approach

Ahtee *et al.* [89] and Järvinen [90] proposed preferred-orientation functions where the preferred-orientation effect is modeled by expanding the orientation distribution in spherical harmonics. They implemented the model in their Rietveld-refinement program where the Voigt function was used as the profile function. In tests using samples with textures known from pole-figure measurements, they found that the corrections obtained from the refinement agreed very closely with the measured values.

If satisfactory results could not be obtained with the March-Dollase approach, this more complex but, in principle, more powerful approach would be worth trying. However, such multiparameter descriptions may allow pole-density profiles that are physically unrealistic [91], which is the reason why RIETAN-FP does not support this feature.

3.8 Lorentz and Polarization Factors

The Lorentz and polarization factors are represented by

$$L(\theta_K) = \frac{1 - u + u\cos^2 2\theta_\mathrm{M} \cos^2 2\theta_K}{2\sin^2 \theta_K \cos\theta_K}, \tag{3.57}$$

where θ_M denotes the Bragg angle of the crystal monochromator. In the Bragg–Brentano and Debye–Scherrer optics, u is 0.5 (characteristic X-ray diffraction), *ca.* 0.1 (synchrotron X-ray diffraction; ask an instrument scientist for its exact value), and 0 (neutron diffraction).

3.9 Symmetric Profile Functions

3.9.1 Representative symmetric profile functions

Typical symmetric profile functions that have been used to approximate the profile shape of reflections observed in angle-dispersive powder diffraction are given below:

$$G(\Delta 2\theta_{iK}) = \frac{2}{\pi H_K}\left[1 + 4\left(\frac{\Delta 2\theta_{iK}}{H_K}\right)^2\right]^{-1}, \tag{3.58}$$

$$G(\Delta 2\theta_{iK}) = \frac{2\sqrt{\ln 2}}{\sqrt{\pi} H_K}\exp\left[-4\ln 2\left(\frac{\Delta 2\theta_{iK}}{H_K}\right)^2\right], \tag{3.59}$$

$$G(\Delta 2\theta_{iK}) = \frac{4\sqrt{2^{1/2} - 1}}{\pi H_K}\left[1 + 4\left(\sqrt{2} - 1\right)\left(\frac{\Delta 2\theta_{iK}}{H_K}\right)^2\right]^{-2}, \tag{3.60}$$

$$G(\Delta 2\theta_{iK}) = \frac{\sqrt{2^{2/3} - 1}}{H_K}\left[1 + 4\left(2^{2/3} - 1\right)\left(\frac{\Delta 2\theta_{iK}}{H_K}\right)^2\right]^{-\frac{3}{2}}, \tag{3.61}$$

$$G(\Delta 2\theta_{iK}) = \eta\frac{2}{\pi H_K}\left[1 + 4\left(\frac{\Delta 2\theta_{iK}}{H_K}\right)^2\right]^{-1} + (1 - \eta)\frac{2\sqrt{\ln 2}}{\sqrt{\pi} H_K}\exp\left[-4\ln 2\left(\frac{\Delta 2\theta_{iK}}{H_K}\right)^2\right], \tag{3.62}$$

$$G(\Delta 2\theta_{iK}) = \frac{2\sqrt{2^{1/m} - 1}\,\Gamma(m)}{\sqrt{\pi}\,\Gamma(m - 0.5) H_K}\left[1 + 4\left(2^{1/m} - 1\right)\left(\frac{\Delta 2\theta_{iK}}{H_K}\right)^2\right]^{-m}, \tag{3.63}$$

$$G(\Delta 2\theta_{iK}) = \frac{1}{\beta_{\mathrm{G}}} \mathrm{Re}\left[\omega\left(\frac{\sqrt{\pi}\Delta 2\theta_{iK}}{\beta_{\mathrm{G}}} + \mathrm{i}\frac{\beta_{\mathrm{L}}}{\sqrt{\pi}\beta_{\mathrm{G}}}\right)\right], \tag{3.64}$$

where H_K is the full-widths at the half-maximum intensity (FWHM), η is the Lorentzian fraction, m is the decay parameter, Γ is the Γ function, β_{G} and β_{L} are respectively the integral-breadths of Gaussian and Lorentzian components, Re is the real part of the function, and ω is the complex error function. All the functions are normalized in such a way that integrals from $-\infty$ to ∞ are equal to unity.

Simple Lorentz (3.58) or Gauss (3.59) functions do not satisfactorily fit to profile shapes, even though the profiles are symmetric except at low scattering angles. In general, poor fitting of profiles strongly affects occupancies and atomic displacement parameters whereas fractional coordinates are not significantly influenced by the choice of profile functions [92].

The profile function implemented in all the modern Rietveld-refinement programs for angle-dispersive X-ray and neutron diffraction as well as energy-dispersive X-ray diffraction is the pseudo-Voigt function (3.62), which is a linear combination of the Lorentz and Gauss functions in a $\eta : 1-\eta$ ratio. The Pearson VII function (3.63) [93] is sometimes adopted as an optional profile function. The Gauss function ($\eta = 0$ or $m = \infty$) and the Lorentz function ($\eta = 1$ or $m = 1$) are the two extremes of these two profile-shape functions as regards the degree of decay from peak tops to tails. In X-ray powder diffraction, the Gauss function is usually too broad near the peak and too narrow at the tails, whereas the Lorentz function is unsatisfactory in the opposite way. Both the pseudo-Voigt and Pearson VII functions can be varied from Gaussian to Lorentzian by changing the mixing parameter, η (**Fig. 3.7**), and the exponent m. Diffraction profiles in angle-dispersive neutron diffraction can be approximated fairly satisfactorily by the Gauss function.

Both of the pseudo-Voigt and Pearson VII functions fit powder-diffraction data equally well. Nevertheless, the pseudo-Voigt function is generally preferred to the Pearson VII function for Rietveld analysis because it can offer physical insight into the origin of the profile shape, *e.g.*, profile broadening due to crystallite-size and microstrain effects (see Chap. 13).

The Voigt function (3.64), which is the convolution of the Gauss and Lorentz functions, is also built into some Rietveld analysis programs [89, 94]. It is, however, not very popular owing to the inclusion of the complex error function whose calculation is very time-consuming. Because the Voigt function (3.64) can be approximated by the pseudo-Voigt function (3.62) within a maximum error of $\pm 1\,\%$ of the peak height, the pseudo-Voigt function is widely used in place of the Voigt function.

3.9.2 Primary and secondary profile parameters

To build in the profile functions, Eqs. (3.62) and (3.63), the dependence of η and H_K (pseudo-Voigt) and that of m and H_K on the Bragg angle, θ_K, must be investigated in detail experimentally and theoretically. Hereafter, such parameters will be referred to as primary profile parameters (PPP). For example, H_K is often approximated by the equation of Caglioti *et al.* [95]:

$$H_K = \left(U\tan^2\theta_K + V\tan\theta_K + W\right)^{\frac{1}{2}}. \tag{3.65}$$

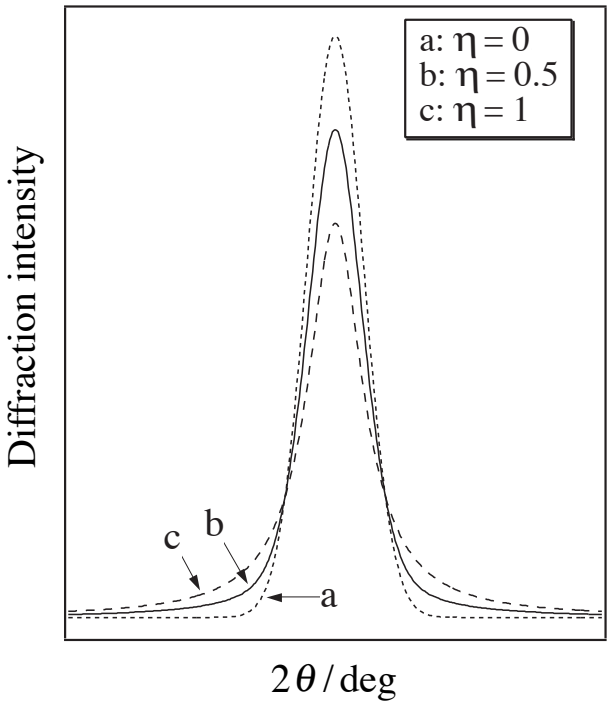

Figure 3.7: Pseudo-Voigt function with an equal integrated intensity and an equal FWHM; (a) $\eta = 0$ (Gauss), (b) $\eta = 0.5$, and (c) $\eta = 1$ (Lorentz)

Parameters such as U, V, and W, in the right-hand side of an equation representing the dependence of a PPP on θ_K are called secondary profile parameters (SPP), which are common to the whole 2θ (d) range. It is not local PPPs but global SPPs that are refined in Rietveld analysis. Our original technique called partial profile relaxation where PPPs are refined in part of reflections is described in detail in 4.4.

3.9.3 Pseudo-Voigt function of Thompson, Cox, and Hastings

Thompson, Cox, and Hastings [96] derived a series expansion relating the Lorentzian fraction in the pseudo-Voigt function to H_K and the FWHM's of the Lorentzian component, H_{KL}, for the Voigt function as:

$$\eta = 1.36603\left(\frac{H_{KL}}{H_K}\right) - 0.47719\left(\frac{H_{KL}}{H_K}\right)^2 + 0.11116\left(\frac{H_{KL}}{H_K}\right)^3. \tag{3.66}$$

They also used a set of numerically convoluted profiles to obtain the series approximation for the FWHM of the pseudo-Voigt profile:

$$\begin{aligned} H_K = \big(&H_{KG}^5 + 2.69269H_{KG}^4H_{KL} + 2.42843H_{KG}^3H_{KL}^2 + 4.47163H_{KG}^2H_{KL}^3 \\ &+ 0.07842H_{KG}H_{KL}^4 + H_{KL}^5\big)^{\frac{1}{5}}, \end{aligned} \tag{3.67}$$

where the Gaussian FWHM, H_{KG}, for the Voigt function is related to the variance of the Gaussian component σ by the relation

$$H_{KG} = \sqrt{8\sigma^2 \ln 2}. \tag{3.68}$$

Separate refinement of H_{KG} and H_{KL} is preferred when they are used to account for the crystallite-size and microstrain effects, respectively, on profile broadening. In general, size broadening is Lorentzian in shape whereas microstrain broadening is Gaussian. Convolution of these two with the profile-shape functions of well-crystallized samples of adequate crystallite sizes affords profiles for actual samples displaying microstrain and size broadening. Atomic displacement parameters and occupancies are strongly influenced by crystallite size and microstrain, which must therefore be included in the profile-shape function.

Here, expressions adopted by Larson and Von Dreele in their GSAS program [87] will be introduced instead of simpler ones given by Thompson and coworkers [96] because they enable one to model anisotropic profile broadening. The variance of the Gaussian component, σ^2, varies with θ_K as

$$\sigma^2 = \left(U + \sigma_a^2 d_K^4\right) \tan^2 \theta_K + V \tan \theta_K + W + P \sec^2 \theta_K, \tag{3.69}$$

where σ_a is the anisotropic Gaussian broadening caused by microstrain [87,97], and d_K is the lattice-plane spacing. The angular dependence of σ is thus a function of the three parameters U, V, and W, the Scherrer coefficient, P, for Gaussian broadening, and σ_a. From Eqs. (3.68) and (3.69), we obtain

$$H_{KG} = \left\{8 \ln 2 \left[\left(U + \sigma_a^2 d_K^4\right) \tan^2 \theta_K + V \tan \theta_K + W + P \sec^2 \theta_K\right]\right\}^{\frac{1}{2}}. \tag{3.70}$$

Next, let ψ_K be the direction cosine between the reciprocal lattice vectors of reflection K and reflection $h_a k_a l_a$ where anisotropic profile broadening is the most marked. Then, H_{KL} varies with θ_K as

$$H_{KL} = (X + X_e \cos \psi_K) \sec \theta_K + \left(Y + Y_e \cos \psi_K + \gamma_a d_K^2\right) \tan \theta_K, \tag{3.71}$$

where X_e and Y_e are anisotropy coefficients, and γ_a is the anisotropic Lorentzian broadening arising from microstrain [87,97]. Chapter 13 will describe the determination of crystallite sizes and microstrains from the profile parameters, U, X, and Y.

The two contributions to the Gaussian and Lorentian broadening, σ_a^2 and γ_a, are obtainable from the action of the mixing coefficient, ζ, for mixing a Lorentzian contribution to the anisotropic microstain broadening, Γ_a, by

$$\sigma_a = (1 - \zeta)\Gamma_a \tag{3.72}$$

and

$$\gamma_a = \zeta \Gamma_a. \tag{3.73}$$

Stephens [97] expressed Γ_a in a semi-empirical form:

$$\Gamma_a = \left(\sum_{HKL} S_{HKL} h^H k^K l^L\right)^{\frac{1}{2}}, \tag{3.74}$$

where S_{HKL} are refinable coefficients, and H, K, and L represent permutations of nonnegative integers restricted to $H + K + L = 4$ (see Appendix C); beware that H, K, and L differ from diffraction indices hkl. Thus, ζ and S_{HKL} coefficients are refined in Rietveld analysis. Appendix

C gives equations to represent $\Gamma_{\rm a}^2$ as functions of S_{HKL} for all the standard Laue classes while Table S-6 lists S_{HKL} terms to be refined (vacant) or fixed (zero) in whole-pattern fitting such as Rietveld and Le Bail analyses.

The pseudo-Voigt function of Thompson *et al.* contains the following refinable parameters (SPPs): U, V, W, P, X, $X_{\rm e}$, Y, $X_{\rm e}$, ζ, and S_{HKL}'s. The number of S_{HKL} coefficients depends on Laue symmetry, ranging from 2 (cubic) to 15 (triclinic). Interpretations of these coefficients are described in the manual of GSAS.

U, V, and W tend to be highly correlated, with a result that various combinations of quite different values can lead to essentially the same variance, σ^2. These three parameters, therefore, do not converge in a stable manner when refined simultaneously. In particular, refining P in addition to U, V, and W almost certainly affords a singular (non-positive definite) coefficient matrix. Of the four profile parameters in Eq. (3.68), V and W depend not on specimens but only on instruments. Then, these two instrumental parameters may well be fixed at values obtained by the Rietveld refinement of a well-crystallized sample where profile broadening is negligible, *i.e.*, $P = 0$.

3.10 How to Introduce Asymmetry into Profile Functions

A variety of instrumental and sample effects, such as axial divergence of the X-ray beam and sample transparency, cause marked asymmetry in the observed profile shape, especially at low diffraction angles. Four methods have been proposed to make symmetric profile functions asymmetric.

3.10.1 Asymmetry function

In the first method, the symmetric profile-shape function $G(\Delta 2\theta_{iK})$ is modified for profile asymmetry by multiplying $G(\Delta 2\theta_{iK})$ and an asymmetric function, $a(\Delta 2\theta_{iK})$, together [10, 98]. For example, Rietveld [10] proposed the following asymmetric function containing the asymmetry parameter A:

$$a(\Delta 2\theta_{iK}) = 1 - A \cot\theta_K \Delta 2\theta_{iK} |\Delta 2\theta_{iK}|. \tag{3.75}$$

3.10.2 Superposition method

The second method introduces profile asymmetry by overlapping some symmetric profile functions with different peak positions and integrated intensities. Will *et al.* reported a profile function where $2\theta_K$ of the Lorentz function was shifted toward the low 2θ side to match the asymmetry of the experimental profiles and added the Gauss function. Howard [99] employed the multi-term Simpson's rule integration, where n symmetric profile-shape functions with different Simpson's coefficients for weights, g_j, and shifts, j_j, are positioned asymmetrically and superimposed with each other:

$$G'(\Delta 2\theta_{iK}) = \frac{1}{3(n \pm 1)} \sum_{j=1}^{n} g_j G(\Delta 2\theta'_{iK}) \tag{3.76}$$

with

$$\Delta 2\theta'_{iK} = \Delta 2\theta_{iK} + f_j A_\mathrm{s} \cot 2\theta_K. \tag{3.77}$$

Here, $G'(\Delta 2\theta_{iK})$ is the asymmetric pseudo-Voigt function, and $\Delta 2\theta'_{iK}$ is the 2θ difference modified for profile asymmetry with the refinable asymmetry parameter, A_s. The corresponding Simpson's coefficients are:

$$\begin{aligned}
&n = 3: \ g_1 = g_3 = 1; \ g_2 = 4 \\
&n = 5: \ g_1 = g_5 = 1; \ g_2 = g_4 = 4; \ g_3 = 2 \\
&n = 7: \ g_1 = g_7 = 1; \ g_2 = g_4 = g_6 = 4; \ g_3 = g_5 = 2 \\
&n = 9: \ g_1 = g_9 = 1; \ g_2 = g_4 = g_6 = g_8 = 4; \ g_3 = g_5 = g_7 = 2 \\
&f_j = \left(\frac{j-1}{n-1}\right)^2.
\end{aligned}$$

The number of terms, n (= 3, 5, 7, or 9), in Eq. (3.76) is either automatically adjusted for each reflection using its FWHM and A_s or fixed at 3 in X-ray powder diffraction using characteristic X rays (NBEAM = 1). The value of A_s must be positive to give reasonable tendencies of profile asymmetry.

This method of making the profile shape asymmetric gives better fits to asymmetric profiles than the simple one using Eq. (3.75), showing less correlation with lattice parameters. It may, however, fail to fit strongly asymmetric profiles at very low scattering angles. In fact, the Simpson's rule integration can break up into multiple reflections for very strong asymmetry. It is not very suitable for analyzing high-resolution powder-diffraction data.

3.10.3 Modeling of axial divergence with geometrical parameters

Finger, Cox, and Jephcoat [100] proposed a method to represent profile asymmetry as a function of the sample height, h_s, the detector height, h_d, and the distance, l_sd, between the sample and detector (goniometer radius). Their approach, which is an implementation of the asymmetric profile function described by van Laar and Yelon [101], offers physical insight into the origin of the asymmetry because it is based explicitly upon axial divergence.

In RIETAN-FP, a profile function adopting the procedure of Finger *et al.* is formed by a convolution of the pseudo-Voigt function of Thompson, Cox, and Hastings [96] with the intersection of the diffraction cone at $2\theta_K$ and a finite-height slit positioned below $2\theta_K$ by τ. The slit intercept function is

$$D(\tau) = \frac{l_\mathrm{sd}^2 \sin 2\theta_K}{4 h_\mathrm{s} h_\mathrm{d} h(\tau) \cos(2\theta_K - \tau)} \cdot W(\tau) \tag{3.78}$$

with

$$h(\tau) = l_\mathrm{sd} \left[\frac{\cos^2(2\theta_K - \tau)}{\cos^2 2\theta_K} - 1\right]^{\frac{1}{2}} \tag{3.79}$$

and

$$W(\tau) = \begin{cases} h_\mathrm{s} + h_\mathrm{d} - h(\tau) & \text{for } \tau_\mathrm{infl} \leqslant \tau \leqslant \tau_\mathrm{min} \\ 2 \min(h_\mathrm{s}, h_\mathrm{d}) & \text{for } 0 \leqslant \tau \leqslant \tau_\mathrm{infl} \\ 0 & \text{elsewhere} \end{cases}.$$

The inflection point at which the entire slit sees the sample is found by

$$\tau_{\mathrm{infl}} = 2\theta_K - \cos^{-1}\left[\cos 2\theta_K \sqrt{\left(\frac{h_\mathrm{s} - h_\mathrm{d}}{l_\mathrm{sd}}\right)^2 + 1}\right] \tag{3.80}$$

while the point of the first contact between the slit and Debye–Scherrer cone is given by

$$\tau_{\mathrm{min}} = 2\theta_K - \cos^{-1}\left[\cos 2\theta_K \sqrt{\left(\frac{h_\mathrm{s} + h_\mathrm{d}}{l_\mathrm{sd}}\right)^2 + 1}\right]. \tag{3.81}$$

The convolution of $D(\tau)$ and the pseudo-Voigt function, $G(\Delta 2\theta)$, is

$$\begin{aligned} H(\Delta 2\theta) &= \int G(\Delta 2\theta - \tau) D(\tau) \mathrm{d}\tau \\ &= \frac{l_\mathrm{sd}^2 \sin 2\theta_K}{4 h_\mathrm{s} h_\mathrm{d}} \int_0^{\tau_\mathrm{min}} \frac{W(\tau) G(\Delta 2\theta - \tau)}{h(\tau) \cos(2\theta_K - \tau)} \mathrm{d}\tau. \end{aligned} \tag{3.82}$$

Because $H(\Delta 2\theta)$ cannot be integrated analytically, a Gauss-Legendre quadrature is calculated instead:

$$\begin{aligned} H(\Delta 2\theta) &= \frac{l_\mathrm{sd}^2 \sin 2\theta_K}{4 h_\mathrm{s} h_\mathrm{d}} \cdot \frac{\sum_{i=M}^{N} w_i \left[\frac{W(\delta_i) G(\Delta 2\theta - \delta_i)}{h(\delta_i) \cos \delta_i}\right]}{\sum_{i=M}^{N} w_i \left[\frac{W(\delta_i)}{h(\delta_i) \cos \delta_i}\right]} \\ &= \frac{\sin 2\theta_K}{4 r_\mathrm{s} r_\mathrm{d}} \cdot \frac{\sum_{i=M}^{N} w_i \left[\frac{W(\delta_i) G(\Delta 2\theta - \delta_i)}{h(\delta_i) \cos \delta_i}\right]}{\sum_{i=M}^{N} w_i \left[\frac{W(\delta_i)}{h(\delta_i) \cos \delta_i}\right]}. \end{aligned} \tag{3.83}$$

In Eq. (3.83), δ_i and w_i are the displacements and weights for the points included in the summations; $r_\mathrm{s} = h_\mathrm{s}/l_\mathrm{sd}$; $r_\mathrm{d} = h_\mathrm{d}/l_\mathrm{sd}$; i ranges from $M = N/2 + 1$ to N where N is chosen to give the number of intervals needed to obtain a sufficiently accurate integration. The range of N lies between 10 and 100, depending on τ_min.

Equation (3.83) is described only by two parameters, r_s and r_d, which can be specified exactly from the diffractometer geometry. These two parameters can be measured experimentally or refined when Bragg reflections in a very low-2θ region are included in powder-diffraction data. Because refinement of r_s and r_d requires some skill, Papoular [102] proposed a procedure for their automatic estimation.

This approach takes only axial divergence into account while neglecting several other effects responsible for profile asymmetry. Because this method is not optimized for all the optics, fits between observed and calculated patterns may sometimes be inadequate with it, particularly, in a very low 2θ region.

3.10.4 Split profile functions

Asymmetric profiles can also be approximated by a split profile-shape function where two independent sets of profile-shape parameters are assigned to the low- and high-angle sides of

each Bragg reflection. Toraya [103] proposed two split profile functions, *i.e.*, a split pseudo-Voigt function

$$G(\Delta 2\theta_{iK}) = \frac{(1+A)\left[\eta_{\mathrm{H}} + \sqrt{\pi \ln 2}\,(1-\eta_{\mathrm{H}})\right]}{\eta_{\mathrm{L}} + \sqrt{\pi \ln 2}\,(1-\eta_{\mathrm{L}}) + A\left[\eta_{\mathrm{H}} + \sqrt{\pi \ln 2}\,(1-\eta_{\mathrm{H}})\right]} \times$$
$$\left\{ \eta_{\mathrm{L}} \frac{2}{\pi H_K} \left[1 + F(A) \left(\frac{\Delta 2\theta_{iK}}{H_K} \right)^2 \right]^{-1} + (1-\eta_{\mathrm{L}}) \left(\frac{\ln 2}{\pi} \right)^{\frac{1}{2}} \frac{2}{H_K} \exp\left[-\ln 2 \cdot F(A) \left(\frac{\Delta 2\theta_{iK}}{H_K} \right)^2 \right] \right\} \tag{3.84}$$

and a split Pearson VII function

$$G(\Delta 2\theta_{iK}) = \frac{2\,(1+A)}{\sqrt{\pi} H_K} \left[\frac{A\Gamma(m_{\mathrm{L}} - 1/2)}{\sqrt{2^{1/m_{\mathrm{L}}} - 1}\,\Gamma(m_{\mathrm{L}})} + \frac{\Gamma(m_{\mathrm{H}} - 1/2)}{\sqrt{2^{1/m_{\mathrm{H}}} - 1}\,\Gamma(m_{\mathrm{H}})} \right]^{-1} \times$$
$$\left[1 + (2^{1/m_{\mathrm{L}}} - 1) F(A) \left(\frac{\Delta 2\theta_{iK}}{H_K} \right)^2 \right]^{-m_{\mathrm{L}}} \tag{3.85}$$

with

$$F(A) = \left(\frac{1+A}{A} \right)^2. \tag{3.86}$$

In Eqs. (3.84) and (3.85), A is the asymmetry parameter, and subscripts L and H are the regions of 2θ lower and higher than the peak position, respectively. Both equations are effective in a region $\Delta 2\theta_{iK} < 0$. For $\Delta 2\theta_{iK} > 0$, subscripts L and H should be replaced with each other, and A with $1/A$. The dependence of PPPs other than H_K in Eqs. (3.84) and (3.85) on θ_K is represented in the forms

$$A = a_0 + a_1 \left(\sqrt{2} - \frac{1}{\sin\theta_K} \right) + a_2 \left(2 - \frac{1}{\sin^2\theta_K} \right), \tag{3.87}$$

$$\eta = \eta_0 + \eta_1(2\theta_K), \tag{3.88}$$

$$m = -1.517 + 0.980\left[m_0 + m_1(2\theta_K) \right] + \frac{1.578}{m_0 + m_1(2\theta_K)}, \tag{3.89}$$

where a_0, a_1, a_2, η_0, η_1, m_0, and m_1 are SPPs refined by a least-squares method. Two sets of PPPs are assigned to the low- and high-angle sides of the diffraction profile. Toraya used Eq. (3.65) to represent the dependence of H_K on θ_K. On the other hand, we adopted a more complex equation

$$H_K = \left[\left(U + U_{\mathrm{e}} \cos^2\psi_K \right) \tan^2\theta_K + V \tan\theta_K + W + P_{\mathrm{e}} \left(\cos\psi_K \sec\theta_K \right)^2 \right]^{\frac{1}{2}} \tag{3.90}$$

containing U_{e} and P_{e} to represent anisotropic broadening arising from effects of microstrain and crystallite sizes, respectively; ψ_K is just the same as in Eq. (3.71). Although the main problem with the split profile function is the difficulty in assigning a physical meaning to the functional form, both Eqs. (3.84) and (3.85) are flexible enough to fit observed diffraction profiles fairly well.

3.11 Shifts in Peak Positions

3.11.1 Pseudo-Voigt function of Thompson, Cox, and Hastings

In the Bragg–Brentano geometry, the specimen-displacement and specimen-transparency effects shift peak positions of Bragg reflections [52].

Let d_s be the displacement of the specimen surface from the goniometer axis, R_g the radius of the goniometer, and D_s the specimen displacement parameter, then $2\theta_K$ is shifted from the ideal position by

$$\begin{aligned}\Delta 2\theta_K &= -\frac{2d_\mathrm{s}}{R_\mathrm{g}}\cos\theta_K \\ &= D_\mathrm{s}\cos\theta_K.\end{aligned} \tag{3.91}$$

On the other hand, the peak shift due to penetration of X rays into the sample is represented as

$$\begin{aligned}\Delta 2\theta_K &= -\frac{1}{2\mu R_\mathrm{g}}\sin 2\theta_K \\ &= T_\mathrm{s}\sin 2\theta_K,\end{aligned} \tag{3.92}$$

where T_s is the specimen-transparency parameter. The introduction of T_s is indispensable when dealing with X-ray data of compounds with small linear attenuation coefficients, μ, which is the case in various organic compounds. In general, specimens containing only light elements with small mass attenuation coefficients,

$$\mu_\mathrm{m} = \mu/\rho, \tag{3.93}$$

have large values of T_s and, in turn, $\Delta 2\theta_K$.

In the Debye–Scherrer geometry, the specimen displacement from the central position and decentering along the incident beams give $\Delta 2\theta_K$ proportional to $\cos\theta_K$ and $\sin 2\theta_K$, respectively. $\Delta 2\theta_K$ arising from absorption of X rays by the sample is also proportional to $\cos\theta_K$. $\Delta 2\theta_K$ is, therefore, represented as the sum of terms proportional to $\cos\theta_K$ and $\sin 2\theta_K$ in both the Bragg–Brentano and Debye–Scherrer optics. Then, $\Delta 2\theta_K$ equals the sum of the zero-point shift, Z, Eq. (3.91), and Eq. (3.92):

$$\Delta 2\theta_K = Z + D_\mathrm{s}\cos\theta_K + T_\mathrm{s}\sin 2\theta_K. \tag{3.94}$$

This equation and the pseudo-Voigt function of Thompson, Cox, and Hastings [96] (see 3.9.3) are combined in RIETAN-FP.

3.11.2 Split profile functions

Toraya [103] represented the dependence of $\Delta 2\theta_K$ on θ_K in the split profile functions (3.84) and (3.85) by three linear equations containing four peak-shift parameters, t_0, t_1, t_2, and t_3:

$$\Delta 2\theta_K = t_0 + t_1\cos 2\theta_K + t_2\sin 2\theta_K + t_3\tan\theta_K, \tag{3.95}$$

$$\Delta 2\theta_K = t_0 + t_1(2\theta_K) + t_2(2\theta_K)^2 + t_3(2\theta_K)^3, \tag{3.96}$$

$$\Delta 2\theta_K = t_0 + t_1 \tan\theta_K + t_2 \tan^2\theta_K + t_3 \tan^3\theta_K. \tag{3.97}$$

To minimize correlations among the peak-shift parameters in Eq. (3.96), we approximated $\Delta 2\theta_K$ by a finite sum of Legendre polynomials, $F_j(q_K)$, orthogonal relative to integration over the interval $[-1, 1]$:

$$\Delta 2\theta_K = \sum_{j=0}^{3} t_j F_j(q_K) \tag{3.98}$$

with q_K being the diffraction angle, $2\theta_K$, normalized between -1 and 1

$$q_K = \frac{2\theta_K - \theta_{\max} - \theta_{\min}}{\theta_{\max} - \theta_{\min}}, \tag{3.99}$$

and

$$F_j(q_K) = \left(\frac{2j-1}{j}\right) q_K F_{j-1}(q_K) - \left(\frac{j-1}{j}\right) F_{j-2}(q_K), \tag{3.100}$$

where $\theta_{\max}$ and $\theta_{\min}$ are, respectively, the maximum and minimum diffraction angles (θ), $F_0(q_K) = 1$, and $F_1(q_K) = q_K$. Equation (3.97) is likewise modified as

$$\Delta 2\theta_K = \sum_{j=0}^{3} t_j F_j(t_K) \tag{3.101}$$

with

$$t_K = \frac{2\tan\theta_K - \tan\theta_{\max} - \tan\theta_{\min}}{\tan\theta_{\max} - \tan\theta_{\min}} \tag{3.102}$$

and

$$F_j(t_K) = \left(\frac{2j-1}{j}\right) t_K F_{j-1}(t_K) - \left(\frac{j-1}{j}\right) F_{j-2}(t_K). \tag{3.103}$$

3.11.3 Correction for peak positions with an internal standard material

Equations (3.95)–(3.97) and parameters t_0–t_3 to represent the angular dependence of shifts in peak positions have no physical meanings. Because t_0–t_3 and lattice parameters are highly correlated with each other, refinement of them in addition to lattice parameters should be carried out very carefully, *e.g.*, by mixing standard reference materials such as Si (SRM 640d) in samples. Part of peak-shift parameters sometimes need to be fixed at values refined from intensity data of a standard reference material by fixing its lattice parameters at a certificated value.

For example, on the use of the split profile functions, the lattice parameters of a standard sample (mixed as an internal standard or only itself) are fixed, and $t_0 - t_3$ (or part of them) are refined in Rietveld analysis. The four peak-shift parameters, $t_0 - t_3$, should be determined with a standard sample having a similar absorption coefficient, and only the zero-point shift, t_0, is refined in actual structure refinement. Ideally, two separate measurements with and without an internal standard are preferable, which is, however, impossible in many cases because of high prices of standard samples and/or demands to keep samples pure.

3.12 Background Functions

RIETAN-FP supports four types of background functions: `NRANGE` = `0`–`3`. When `NRANGE` > `0`, 2θ and background pairs are read in from file hoge.bkg (see 17.5).

3.12.1 NRANGE = 0

Background parameters (b_j; $j = 0{-}11$) are refined by a method of least squares. Let q_i be the diffraction angle, $2\theta_i$, normalized between -1 and 1, $\theta_{\max}$ the maximum 2θ, and $\theta_{\min}$ the minimum 2θ, then q_i is obtained by

$$q_i = \frac{2\theta_i - \theta_{\max} - \theta_{\min}}{\theta_{\max} - \theta_{\min}}. \tag{3.104}$$

The background, $y_{\rm b}(2\theta_i)$, at step i is approximated by a finite sum of Legendre polynomials, $F_j(q_K)$, orthogonal relative to integration over the interval $[-1, 1]$:

$$y_{\rm b}(2\theta_i) = \sum_{j=0}^{11} b_j F_j(q_i) \tag{3.105}$$

with

$$F_j(q_i) = \left(\frac{2j-1}{j}\right) q_i F_{j-1}(q_i) - \left(\frac{j-1}{j}\right) F_{j-2}(q_i). \tag{3.106}$$

Correlation coefficients between background parameters can be somewhat reduced with this background function. Even "humps" due to amorphous or poorly crystallized compounds may be fit well by increasing the number of refinable background parameters. However, be careful not to vary too many background parameters when dealing with a diffraction pattern whose background has simple dependence on 2θ; refining six background parameters would be adequate in such a case.

3.12.2 NRANGE = 1

Background intensities at (interpolated) values at specified 2θ's are fixed in this mode. If a background is zero, it is set at a smoothed value at that data point. Backgrounds at other data points are fixed at interpolated values. Such a manner is useful for the analysis of diffraction patterns where the number of reflections are relatively small and the background curve is complex, for example, having "humps." For the format of a file, hoge.bkg, storing background intensities, see 17.5.2.

Note that all data points farther than the profile cutoffs of the nearest Bragg reflection are excluded in least-squares fitting.

3.12.3 NRANGE = 2

Backgrounds of all the points are fixed at values recorded in hoge.bkg, from which 2θ and background pairs are input. Their total number should be equal to that of observed diffraction intensities in file hoge.int.

All data points farther than the profile cutoffs of the nearest Bragg reflection are excluded in least-squares fitting as with `NRANGE = 1`.

Measuring diffraction data of capillary tubes

We sometimes measure X-ray diffraction data of empty capillary tubes under experimental conditions (*e.g.*, temperature and wavelength) similar to those of measuring diffraction intensities

of samples, smooth them, and record the resulting data in hoge.bkg. Program PowderX [104] is very convenient to smooth these data [105]. This method is ineffective when the shape of background intensities in a sample differs considerably from that of diffraction intensities in the capillary tube.

Sonneveld–Visser method

An alternative to the above method in samples showing relatively simple patterns is to determine background intensities in diffraction data of samples with a simple procedure of Sonneveld and Visser [106] using PowderX or RIETAN-FP (see 11.2). The use of RIETAN-FP is recommended because somewhat troublesome procedures are required in PowderX. For two different formats of hoge.bkg, see 17.5.2.

Conversion of hoge.bgr into hoge.bkg

The third method of creating hoge.bkg utilizes a graphic tool for powder diffraction, WinPLOTR[2] [107], or FOX[3] for *ab initio* crystal-structure solution [108]. With these two applications, hoge.bgr, where discrete background intensities are recorded, are produced directly or indirectly. If the following three conditions,

1. `NRANGE` is set at `2` or `3` in hoge.ins.
2. A file, hoge.bkg, storing backgrounds of all the data points does not exist in the current folder.
3. The current folder contains hoge.bgr.

are all satisfied, RIETAN-FP automatically converts hoge.bgr into hoge.bkg by interpolating the discrete backgrounds,

WinPLOTR makes it possible to determine discrete background intensities, delete parts of them, add more appropriate backgrounds, and output the resultant full points of backgrounds to a file, hoge.bgr, which is also the case with `NRANGE = 3` (see 3.12.4). Note that hoge.bgr may consist of two or more blocks, *i.e.*, lines from '`! Data file :`' to the last pair of $2\theta_i$ and $y_\mathrm{b}(2\theta_i)$ and that RIETAN-FP inputs only the last block when dealing with multi-block hoge.bgr. For details in cooperation between RIETAN-FP and WinPLOTR, refer to an opened note (in Japanese) of Evernote.[4]

On the other hand, FOX has an advanced feature of estimating the background in a powder diffraction pattern by a robust Bayesian analysis proposed by David and Sivia [109]. A text file, hoge.pcr, exported by FOX for FullProf [110] contains lines of $2\theta_i$, $y_\mathrm{b}(2\theta_i)$, and 0.0 sandwiched between two comment lines: '`!2Theta Background for .....`' and '`!`'. *The part of background intensities in hoge.pcr can be directly input by RIETAN-FP in the same way as hoge.bgr exported by WinPLOTR.*

[2] http://www.cdifx.univ-rennes1.fr/winplotr/winplotr.htm
[3] https://github.com/vincefn/objcryst/releases
[4] http://urx.mobi/BqUY

Alternatively, a macro called pcr2bgr of the integrated assistance environment for RIETAN-FP–VENUS (see Chap. 16) enables us to convert hoge.pcr into hoge.bgr consisting of $2\theta_i$ and $y_\mathrm{b}(2\theta_i)$ values without any comment lines. The resulting file, hoge.bgr, can be edited with an editor and then imported by by pressing the Object button and selecting "Import" in FOX. As described above, hoge.bgr can be converted into hoge.bkg by RIETAN-FP if the three conditions are satisfied. An advantage of FOX over WinPLOTR is that both Windows and macOS versions of FOX are available.

3.12.4 NRANGE = 3

The background is represented by

$$\begin{aligned} y_\mathrm{b}(2\theta_i) &= y'_\mathrm{b}(2\theta_i) \sum_{j=0}^{11} b_j F_j(q_i) \\ &= y'_\mathrm{b}(2\theta_i) \sum_{j=0}^{11} b_j \left[\left(\frac{2j-1}{j} \right) q_i F_{j-1}\left(q_i\right) - \left(\frac{j-1}{j} \right) F_{j-2}\left(q_i\right) \right], \end{aligned} \tag{3.107}$$

where $y'_\mathrm{b}(2\theta_i)$ is the approximate background input from hoge.bkg [105], which is just the same as with `NRANGE = 2`.

This composite background function is particularly useful for the Debye–Scherrer geometry where samples are charged in capillary tubes, which makes the background rather complex and high because of short-range order in glass.

3.13 Classification of Refinable Parameters

In summary, the calculated intensity, $f_i(\boldsymbol{x})$, contains the following five kinds of parameters, $\boldsymbol{x}$ (functions in brackets are those containing each parameter).

1. Parameters to adjust integrated intensities
   Scale factor, s
   Preferred-orientation parameters $[P_K]$

2. Parameters related to peak positions of Bragg reflections
   Lattice parameters $[\theta_K]$
   Parameters related to shifts in peak positions $[\theta_K]$

3. Profile parameters
   Parameters to express the dependence of FWHM on θ_K $[G(\Delta 2\theta_{iK})]$
   Parameters to approximate the dependence of the rate of decay on θ_K $[G(\Delta 2\theta_{iK})]$
   Parameters to represent profile asymmetry due to axial divergence, sample transparency, *etc.* $[G(\Delta 2\theta_{iK})]$

4. Crystal-structure parameters
   Parameters, x_j, y_j, z_j, g_j, B_j, β_{11j}, β_{22j}, β_{33j}, β_{12j}, β_{13j}, and β_{23j}, by which crystal structures are represented $[F(\boldsymbol{h}_K, \mathrm{cryst.})]$

5. Magnetic-structure parameters
   Parameters to describe the magnetic moments (directions and magnitudes of spins) of magnetic atoms [$F(\boldsymbol{h}_K, \text{magn.})$]

6. Background parameters
   Parameters to describe the background [$y_{\text{b}}(2\theta_i)$]

The most important purpose of Rietveld analysis is to refine crystal-structure parameters as well as lattice parameters. In addition, the qualitative analysis of mixtures from scale factors of phases contained in them are now widely used to identify industrial products (Chap. 7). Recent progress in highly-sensitive detectors for laboratory X-ray powder diffraction has made this technique more and more practical.

The zero-point shift and background parameters are global parameters independent of phases contained in a sample whereas all the other parameters are phase-dependent. Nevertheless, profile parameters are sometimes made common to all the phases with linear equality constraints (see 17.3.16) to decrease the total number of profile parameters.

Only commensurate and collinear magnetic structure can be analyzed with RIETAN-FP (see 3.6 and Chap. 8) in view of the fact that most magnetic materials investigated by neutron powder diffraction have such simple magnetic structures.

Chapter 4

OTHER DETAILS RELATED TO RIETVELD ANALYSIS

4.1 Nonlinear Least-Squares Methods

Almost all computer programs for Rietveld refinement employ some form of the Gauss-Newton algorithm to find parameters which minimize $S(\boldsymbol{x})$ apart from XRS-84 and MINREF adopting a variable metric method. However, when applied to Rietveld analysis, the Gauss-Newton method suffers a disadvantage that the range of convergence is rather narrow, and the refinements often converge to local minima rather than the global minimum. Since none of algorithms has proved to be so superior that it can be classified as a panacea for nonlinear least-squares solutions, it is advantageous to have more than one method available on call.

In RIETAN-FP, three different techniques for nonlinear least-squares fitting are adopted: the Gauss-Newton method, a modified Marquardt method, and the conjugate-direction method. All of them are designed to give stable convergence. RIETAN-FP also has the very convenient features of incremental and combined refinements. The algorithms implemented in RIETAN-FP will be introduced shortly.

4.1.1 Gauss–Newton method

In this algorithm, changes in n variable parameters at each iterative step, $\Delta\boldsymbol{x}$, are calculated by setting up a normal equation

$$\boldsymbol{M} \cdot \Delta\boldsymbol{x} = \boldsymbol{N}, \tag{4.1}$$

where $\boldsymbol{M}$ is the coefficient matrix with n rows and n columns, and both $\Delta\boldsymbol{x}$ and $\boldsymbol{N}$ are $n \times 1$ column matrices (n: number of refined parameters). On linear approximation of $\boldsymbol{M}$ to reduces the time required to calculate $\boldsymbol{M}$, each element in $\boldsymbol{M}$ is simply represented as

$$M_{jk} = \sum_i w_i \frac{\partial f_i(\boldsymbol{x})}{\partial x_j} \cdot \frac{\partial f_i(\boldsymbol{x})}{\partial x_k}, \tag{4.2}$$

where the summation with respect to i is carried out over all the diffraction steps. The jth element of $\boldsymbol{N}$ is obtained by

$$N_j = \sum_i w_i \left[y_i - f_i(\boldsymbol{x}) \right] \frac{\partial f_i(\boldsymbol{x})}{\partial x_j}. \tag{4.3}$$

In RIETAN-FP, both $\boldsymbol{M}$ and $\boldsymbol{N}$ are declared as double precision to raise computation accuracy, and only a lower triangle of the positive-definite symmetric matrix $\boldsymbol{M}$ is kept in a one-dimensional array to save storage.

Although $\Delta\boldsymbol{x}$ is evaluated from $\boldsymbol{M}^{-1} \cdot \boldsymbol{N}$ in most structure-refinement programs, there is little to recommend such an old-fashioned technique because of the long computation time and low precision. Accordingly, Choleski decomposition of $\boldsymbol{M}$ and forward- and back-substitutions for the solution of consistent sets of linear equations [111] are carried out in RIETAN-FP. A new set of $\boldsymbol{x}$ and $\boldsymbol{x}'$ is readily calculated by

$$\boldsymbol{x}' = \boldsymbol{x} + \alpha\Delta\boldsymbol{x} \tag{4.4}$$

with

$$\alpha = 2^{-m} \qquad (m = 0 - 4).$$

The value of α is appropriately adjusted, according to the rule adopted in SALS [112]. The variable damping factor, α, is initially set at 1 ($m = 0$). If the current set of $\boldsymbol{x}'$ gives *physically or mathematically meaningless variables* (*e.g.*, divergence of SPPs and s_K) or $S(\boldsymbol{x}') > S(\boldsymbol{x})$, α is halved, and $\boldsymbol{x}'$ is calculated again with Eq. (4.4). In the next step of iterations, α is doubled if $\alpha \leqslant 1/2$. Such a procedure decreases α in the case of high non-linearity and increases α with increasing linearity near the solution.

4.1.2 Modified Marquardt method

The Marquardt method [113] also calculates $\boldsymbol{M}$ and $\boldsymbol{N}$ but adds $\lambda \cdot \mathrm{diag}(\boldsymbol{M})$ (λ: Marquardt parameter; diag: diagonal matrix) to $\boldsymbol{M}$ to stabilize the convergence to the minimum:

$$[\boldsymbol{M} + \lambda \cdot \mathrm{diag}(\boldsymbol{M})] \cdot \Delta\boldsymbol{x} = \boldsymbol{N}. \tag{4.5}$$

Then, $\Delta\boldsymbol{x}$ tends towards the steepest descent direction as λ increases, while the Gauss-Newton solution is obtained when λ becomes negligible. In other words, λ is increased in a high non-linearity region far from the solution but decreased in a high linearity region near the solution. Even if $\boldsymbol{M}$ is not positive definite, it can be made computationally positive definite by choosing λ to be large enough.

The value of λ is automatically adjusted during a series of iterations using a most efficient method developed by Fletcher [112, 114]. The motivation for his strategy is that if the ratio of (actual reduction in $S(\boldsymbol{x})$)/(predicted reduction in $S(\boldsymbol{x})$) is near 1, then λ ought to be reduced, and if the ratio is near to or less than 0, then λ ought to be increased.

Let ΔS be the change in the sum of weighted squares of residuals,

$$\Delta S = S(\boldsymbol{x} + \Delta\boldsymbol{x}) - S(\boldsymbol{x}), \tag{4.6}$$

and $\Delta\bar{S}$ be the corresponding change in a linearized model. In Fletcher's algorithm, the ratio of ΔS to $\Delta\bar{S}$,

$$r = \frac{\Delta S}{\Delta\bar{S}}, \tag{4.7}$$

which is regarded as a measure of non-linearity, is used to adjust λ according to the following scheme:

1. $r \geqslant 0.75$ Nearly as expected; λ is halved.
2. $0.75 > r > 0.25$ A little disappointing; λ remains unchanged.
3. $0.25 \geqslant r \geqslant 0$ Because of high non-linearity, λ is increased.
4. $r < 0$ $\Delta S > 0$; λ is increased to recalculate $\Delta \boldsymbol{x}$.

In cases 1–3, x is replaced with $\boldsymbol{x} + \Delta x$, and $\boldsymbol{M} + \lambda \cdot \mathrm{diag}(\boldsymbol{M})$ is calculated to proceed to the next step. A factor, u, to be multiplied by r in cases 3 and 4 ranges from 2 to 10:

$$u = \max\left(2, \min(2 - r, 10)\right). \tag{4.8}$$

The critical value of λ, λ_c, is determined from

$$\lambda_\mathrm{c} = \frac{1}{\mathrm{trace}\left(\boldsymbol{M}^{-1}\right)} \tag{4.9}$$

as a λ value that halves the norm of $\Delta \boldsymbol{x}$.

Fletcher's elaborate algorithm improves the performance of the Marquardt method in certain circumstances, yet requires negligible extra computer time and storage. The modified Marquardt method is very effective for dealing with highly nonlinear model functions, $f(\boldsymbol{x})$, or problems in which starting values for refinable parameters differ markedly from the true ones. In the same way as with Gauss–Newton method, λ *is increased if the current set of* $\boldsymbol{x}'$ *give physically or mathematically meaningless variables.*

4.1.3 Conjugate-direction method

Powell's conjugate-direction method [115–118] is one of the most efficient algorithms for minimizing objective functions without calculating partial derivatives. Powell's method is essentially based on the idea that if the following two conditions,

1. The minimum of the quadratic function is found along each of p conjugate directions ($p < n$; n: number of refined parameters) in one stage of the search.
2. A step is accordingly made in each direction.

are satisfied, the overall step from the start to the pth step is conjugate to all the p subdirections of search [117].

In the case of Rietveld analysis, the sum of weighted squares of residuals, *i.e.*, $S(\boldsymbol{x})$ in Eq. (2.1), corresponds to the objective function. The hessian matrix, $\boldsymbol{H}(\boldsymbol{x})$, of $S(\boldsymbol{x})$ to be minimized by the conjugate-direction method is defined as the square matrix of the second partial derivatives of $S(\boldsymbol{x})$:

$$\begin{aligned} \boldsymbol{H}(\boldsymbol{x}) &= \boldsymbol{\nabla}^2 S(\boldsymbol{x}) \\ &= \begin{pmatrix} \dfrac{\partial^2 S(\boldsymbol{x})}{\partial x_1^2} & \dfrac{\partial^2 S(\boldsymbol{x})}{\partial x_1 \partial x_2} & \cdots & \dfrac{\partial^2 S(\boldsymbol{x})}{\partial x_1 \partial x_n} \\ \dfrac{\partial^2 S(\boldsymbol{x})}{\partial x_2 \partial x_1} & \dfrac{\partial^2 S(\boldsymbol{x})}{\partial x_2^2} & \cdots & \dfrac{\partial^2 S(\boldsymbol{x})}{\partial x_2 \partial x_n} \\ \cdots & \cdots & \cdots & \cdots \\ \dfrac{\partial^2 S(\boldsymbol{x})}{\partial x_n \partial x_1} & \dfrac{\partial^2 S(\boldsymbol{x})}{\partial x_n \partial x_2} & \cdots & \dfrac{\partial^2 S(\boldsymbol{x})}{\partial x_n^2} \end{pmatrix}. \end{aligned} \tag{4.10}$$

$\boldsymbol{H}(\boldsymbol{x})$ is a positive-definite square matrix. Two directions of search, $\boldsymbol{s}_j$ and $\boldsymbol{s}_i$, which are column vectors indicating the direction of search, are said to be conjutate if

$$\begin{aligned} (\boldsymbol{s}_j)^T \boldsymbol{\nabla}^2 S(\boldsymbol{x}^{(k)}) \boldsymbol{s}_i &= 0, \qquad i \neq j \\ (\boldsymbol{s}_j)^T \boldsymbol{\nabla}^2 S(\boldsymbol{x}^{(k)}) \boldsymbol{s}_i &\geqslant 0, \qquad i = j \end{aligned} \tag{4.11}$$

where superscript T denotes the transpose of a vector, superscripts, $k = 0, 1, \ldots$, in parentheses are the stages of the search, and subscripts are used to distinguish among the vectors on one stage.

The transition from a starting point $\boldsymbol{x}_0^{(k)}$ to a point $\boldsymbol{x}_m^{(k)}$ is formulated as

$$\boldsymbol{x}_m^{(k)} = \boldsymbol{x}_0^{(k)} + \sum_{i=0}^{m-1} \lambda_i^{(k)} \boldsymbol{s}_i^{(k)}, \tag{4.12}$$

where $\lambda^{(k)}$ is the step length to minimize $S(\boldsymbol{x})$ in the direction of search. The essence of the procedure is as follows [117]. At a vector $\boldsymbol{x}_0^{(0)}$ in the n-dimensional euclidean space, E^n, the initial $\boldsymbol{s}_1^{(0)}, \ldots, \boldsymbol{s}_n^{(0)}$ are taken to be parallel to the coordinate axis of E^n. A first step is taken in the $\boldsymbol{s}_n^{(0)}$ direction; that is, $S(\boldsymbol{x}_0^{(0)} + \lambda \boldsymbol{s}_n^{(0)})$ is minimized by a unidimensional search with respect to λ to evaluate $\lambda_0^{(0)}$, with a result that $\boldsymbol{x}_1^{(0)} = \boldsymbol{x}_0^{(0)} + \lambda_0^{(0)} \boldsymbol{s}_n^{(0)}$. Next, for each of the n directions $\boldsymbol{s}_i^{(0)}$, $i = 1, \ldots, n$, in turn $S(\boldsymbol{x}_i^{(0)} + \lambda \boldsymbol{s}_i^{(0)})$ is minimized to find $\lambda_i^{(0)}$, and Eq. (4.12) is applied to calculate new values of $\boldsymbol{x}_i^{(0)}$ successively.

The following theorem for quadratic objective funcitions [117] serves to understand how conjugate diretions are involved in Powell's algorithm:

> **Theorem**
> if, starting at $\boldsymbol{x}^{(0)}$, the point $\boldsymbol{x}^{(a)}$ is located in the direction $\boldsymbol{s}$ at the minimum of $S(\boldsymbol{x})$, and if, starting from the point $\boldsymbol{x}^{(1)} \neq \boldsymbol{x}^{(0)}$, the point $\boldsymbol{x}^{(b)}$ is located in the same direction $\boldsymbol{s}$ at the minimum of $S(\boldsymbol{x})$, then, if $S(\boldsymbol{x}^{(b)}) < S(\boldsymbol{x}^{(a)})$, the direction $(\boldsymbol{x}^{(b)} - \boldsymbol{x}^{(a)})$ is conjugate to $\boldsymbol{s}$.

For further details in Powell's method, refer to Ref. [117].

In RIETAN-FP, a combination of Davies–Swann–Campey and Powell algorithms [117], which is better than either of the individual algorithms, is adopted as a method of unidimensional minimization. $S(\boldsymbol{x})$ is set at an unusually large value if the current set of $\boldsymbol{x}'$ give physically or mathematically meaningless variables, which leads to stable convergence to the solution while avoiding divergence. Standard uncertainties of refinable parameters are obtained by calculating $\boldsymbol{M}$ and inverting it (see 4.2) after convergence to the solution.

Since the directions for minimization are determined solely from successive evaluations of the objective function, $S(\boldsymbol{x})$, this procedure is much slower than the two least-squares methods with derivatives: the Gauss–Newton and modified Marquardt methods. It is, however, capable of solving ill-conditioned problems in which very high correlations exist between parameters. Because the conjugate-direction method is very fast in any nearly quadratic region near a minimum, it is mainly used in the late stages of refinement to test the prospect of a local minimum being the global minimum or to escape from a local minimum by using sufficiently large

step sizes in line searches. On the other hand, someone using the Gauss-Newton and Marquardt algorithms can check the convergence to the global minimum simply by using different starting vectors. In our experience, the conjugate-direction method has been most effective to get out of local minima where the solution obtained by the Gauss–Newton or modified Marquardt method was trapped on the analysis of compounds, *e.g.*, organic compounds and zeolites, containing many atoms in the asymmetric unit.

4.1.4 Auxiliary techniques for stable convergence

We usually proceed in steps in Rietveld analysis, first refining only one or two parameters and then gradually letting more and more of the parameters be adjusted in the successive least-squares refinement cycles. RIETAN-FP requires only a single input to refine parameters incrementally; that is, variable parameters in each cycle can be pre-designated by the user or selected appropriately by the program when using the Gauss-Newton and modified Marquardt methods (incremental refinements). Repetition of batch jobs is, hence, unnecessary in most Rietveld refinements. For example, linear parameters (background parameters and a scale factor) are refined in the first cycle, lattice parameters in the second cycle, profile parameters in the third cycle, and subsequently all the parameters simultaneously. Even if initial parameters are far from the true solution, incremental refinements coupled with the appropriate adjustment of d (Gauss-Newton method) or λ (modified Marquardt method), enable very stable convergence to an optimum solution in most cases.

Combined refinements (`NAUTO = 3`) are also possible in which the parameters obtained by the incremental refinements described above are further adjusted by the conjugate-direction method to ensure that there are no lower minima in the vicinity of the one found by the initial refinement.

In general, the most important notice in nonlinear least-squares fitting is to provide sufficiently good initial estimates of refined parameters, which is certainly the case in Rietveld analysis. In particular, starting values for the lattice parameters should be close enough to the true ones to ensure that the calculated diffraction profiles adequately overlap with the corresponding observed ones. If the lattice parameters are in error by say 1 %, then the refinement will diverge almost certainly.

4.2 Standard Uncertainties

Let $\boldsymbol{M}$ be the diagonal element of the inverse coefficient matrix in the normal equation, n the number of refinable parameters, and C the number of constraints applied, then the standard uncertainty, σ_j, for the jth parameter, x_j, is usually evaluated as

$$\sigma_j = \left[\frac{\boldsymbol{M}_{jj}^{-1} S(\boldsymbol{x})}{N - n + C} \right]^{\frac{1}{2}}. \tag{4.13}$$

In recent years, much discussion has appeared in the literature about the reliability of σ_j in Rietveld refinements [119]. The σ_j's calculated with Eq. (4.13) are correct, provided there are no

unaccounted systematic errors. However, in most Rietveld refinements, systematic errors result from the preferred orientation, inadequate profile shape and structure models, poor background fit, inclusion of unknown impurities, *etc.*, which causes serial correlation among neighboring residuals. If there are systematic errors unaccounted for, the calculated σ_j is no longer a valid measure of uncertainty. Under these conditions, σ_j's calculated by Rietveld refinement may be significantly smaller than those obtained by the integrated-intensity refinement of the same data set.

Scott [120] proposed a method of adjusting σ_j's in Rietveld analysis to provide comparability with integrated-intensity refinement:

$$\sigma_j = \left\{ \boldsymbol{M}_{jj}^{-1} \left[1 + \frac{S(\boldsymbol{x}) - N - n_\mathrm{p}}{N_\mathrm{B} - n_\mathrm{c}} \right] \right\}^{\frac{1}{2}}, \tag{4.14}$$

where n_p is the number of parameters describing the profile (all those parameters in the model that do not directly affect the integrated intensities), N_B is the number of Bragg reflections, and n_c is the number of structure parameters. Because this equation is based on the assumption that only the integrated intensities are subject to model errors, it should be applied only to structure parameters. The adjustments calculated above are only approximations because they assume that Bragg reflections are completely resolved and that the model for the profile shape is good, which are both seldom true. Nevertheless, this procedure imposes reasonable restraints on the uncritical use of σ_j's generated by Rietveld refinements as measures of the accuracy of the refined structure parameters.

4.3 Reliability Indices

Numerical criteria used to measure the agreement between observed and calculated intensities and the progress of Rietveld refinement fall into three classes described in what follows. The method to estimated observed integrated intensities will also be described in 4.3.3 in connection with two reliability indices based on integrated intensities.

4.3.1 Reliability indices based on observed and calculated intensities

The most significant reliability index is R_wp (R-weighted pattern) because its numerator is the quantity that is actually minimized in the least-squares refinement procedure:

$$R_\mathrm{wp} = \left\{ \frac{\sum_{i=1}^{N} w_i \left[y_i - f_i(\boldsymbol{x}) \right]^2}{\sum_{i=1}^{N} w_i y_i^2} \right\}^{\frac{1}{2}}. \tag{4.15}$$

R_p (R-pattern) defined as

$$R_\mathrm{p} = \frac{\sum_{i=1}^{N} \left| y_i - f_i(\boldsymbol{x}) \right|}{\sum_{i=1}^{N} y_i} \tag{4.16}$$

is also reported frequently. A variation of R_{p} is R_{R} (R-Rietveld) defined by Rietveld [10] as

$$R_{\mathrm{R}} = \frac{\sum_{i=1}^{N} \left| y_i - f_i(\boldsymbol{x}) \right|}{\sum_{i=1}^{N} \left| y_i - y_{\mathrm{b}}(2\theta_i) \right|}. \tag{4.17}$$

Both R_{wp} and R_{p} are influenced mostly by the intensity of the diffraction line as well as the background level because the sum of the observed intensities is used in the denominator of these reliability indices. It is obvious that R_{wp}, for example, will be decreased as the background level is increased (the S/N level decreased) because it is easier to get a good fit to a function that varies slowly and near to monotonically with angle, as the background does, than to one that has many sharp maxima along the way, as the pattern of the Bragg reflections does. Experienced users, therefore, do not expect to judge the relative quality of Rietveld refinements carried out with different data sets and even different materials by the relative R_{wp} or R_{p} values. Those indices are, however, good indicators of the progress of a particular refinement.

To judge the quality of the fit, the final R_{wp} value should be compared to the expected R_{wp}, R_{e} (R-expected), which is derived from the statistical error associated with the measured intensities:

$$R_{\mathrm{e}} = \left[(N - n) \Big/ \sum_{i=1}^{N} w_i y_i^2 \right]^{\frac{1}{2}}. \tag{4.18}$$

Thus, the goodness-of-fit indicator,

$$\begin{aligned} S &= \frac{R_{\mathrm{wp}}}{R_{\mathrm{e}}} \\ &= \left\{ \sum_{i=1}^{N} w_i \left[y_i - f_i(\boldsymbol{x}) \right]^2 \Big/ (N - n) \right\}^{\frac{1}{2}}, \end{aligned} \tag{4.19}$$

is often used as a measure of the fit between observed and calculated patterns [121]. An S value of unity indicates that the refinement is complete; it can get no better statistically. An S value of 1.3 or less is usually considered to be quite satisfactory. S includes the number of variables, nP, undergoing refinement. It may, therefore, help in determining whether or not a change in n significantly decreases the residual error.

The goodness-of-fit, GofF [122],

$$\begin{aligned} \mathrm{GofF} &= S^2 \\ &= \sum_{i=1}^{N} w_i \left[y_i - f_i(\boldsymbol{x}) \right]^2 \Big/ (N - n) \end{aligned} \tag{4.20}$$

is as important as R_{wp} because its numerator is the quantity to be minimized by a method of least squares.

Integrating-type detectors such as imaging plates sometimes give too high intensities, *e.g.*, more than 1 000 000, which may give unreasonably large S values. In such case, raw intensities have to be adjusted by multiplying a factor to obtain acceptable S values.

4.3.2 Reliability indices based on integrated intensities

R_{B} (R-Bragg factor; also denoted by R_I), R_F (R-structure factor), and R_{F^2}, which are respectively defined as

$$R_{\mathrm{B}} = \frac{\sum_K \left| I_{\mathrm{o}}(\boldsymbol{h}_K) - I(\boldsymbol{h}_K) \right|}{\sum_K I_{\mathrm{o}}(\boldsymbol{h}_K)}, \tag{4.21}$$

$$R_F = \frac{\sum_K \left| |F_{\mathrm{o}}(\boldsymbol{h}_K)| - |F(\boldsymbol{h}_K)| \right|}{\sum_K |F_{\mathrm{o}}(\boldsymbol{h}_K)|}, \tag{4.22}$$

$$R_{F^2} = \frac{\sum_K \left| \left[F_{\mathrm{o}}(\boldsymbol{h}_K)\right]^2 - \left[F(\boldsymbol{h}_K)\right]^2 \right|}{\sum_K \left[F_{\mathrm{o}}(\boldsymbol{h}_K)\right]^2} \tag{4.23}$$

are exceptional in the point that they are not calculated from residuals $y_i - f_i(\boldsymbol{x})$. $I_{\mathrm{o}}(\boldsymbol{h}_K)$ and $I(\boldsymbol{h}_K)$ in Eq. (4.21) are, respectively, the observed and calculated integrated intensities for reflection K, and $F_{\mathrm{o}}(\boldsymbol{h}_K)$ in Eq. (4.22) is the observed structure factor. R_F is the closest equivalent to the R factor quoted in single-crystal studies.

4.3.3 Estimation of observed integrated intensities

Neglecting $S_{\mathrm{R}}(\theta_i)$, $A(\theta_i)$, and $D(\theta_i)$ in Eq. (2.5), we can represent $I(\boldsymbol{h}_K)$ as

$$I(\boldsymbol{h}_K) = s m_K |F(\boldsymbol{h}_K)|^2 P_K L(\theta_K). \tag{4.24}$$

$I_{\mathrm{o}}(\boldsymbol{h}_K)$ and, in turn, $|F_{\mathrm{o}}(\boldsymbol{h}_K)|$ for an overlapped reflection are actually not observed but estimated after Rietveld analysis from observed diffraction data and final refinable parameters with the following approximation method proposed by Rietveld [10].

Let us suppose that some reflections overlap each other at step i. The observed intensity, $y_{i\mathrm{B}}$, for overlapped Bragg reflections is equal to the difference between the observed intensity and the background function:

$$y_{i\mathrm{B}} = y_i - y_{\mathrm{b}}(2\theta_i). \tag{4.25}$$

$I_{\mathrm{o}}(\boldsymbol{h}_K)$ is approximated by calculating the profile intensity, Y_{ij}, of each overlapped reflection from final refinable parameters after Rietveld analysis and apportioning y_{iB} in proportion to Y_{ij} [10]:

$$I_{\mathrm{o}}(\boldsymbol{h}_K) = \Delta 2\theta \sum_i y_{i\mathrm{B}} \frac{Y_{iK}}{\sum_j Y_{ij}}, \tag{4.26}$$

where $\Delta 2\theta$ is the step width in radians, Y_{iK} is the calculated intensity of Bragg reflection K, $\sum_i$ is the summation over all the diffraction points contributing to $I(\boldsymbol{h}_K)$, and $\sum_j$ is the summation over all the reflections contributing to $y_{i\mathrm{B}}$.

Figure 4.1 shows the observed intensity, y_{iB}, for overlapped Bragg reflections, the calculated intensity, Y_{i1}, for the 21$\underline{1}$3 reflection ($K = 1$), and the calculated intensity, Y_{i1}, for the 20$\underline{1}$6

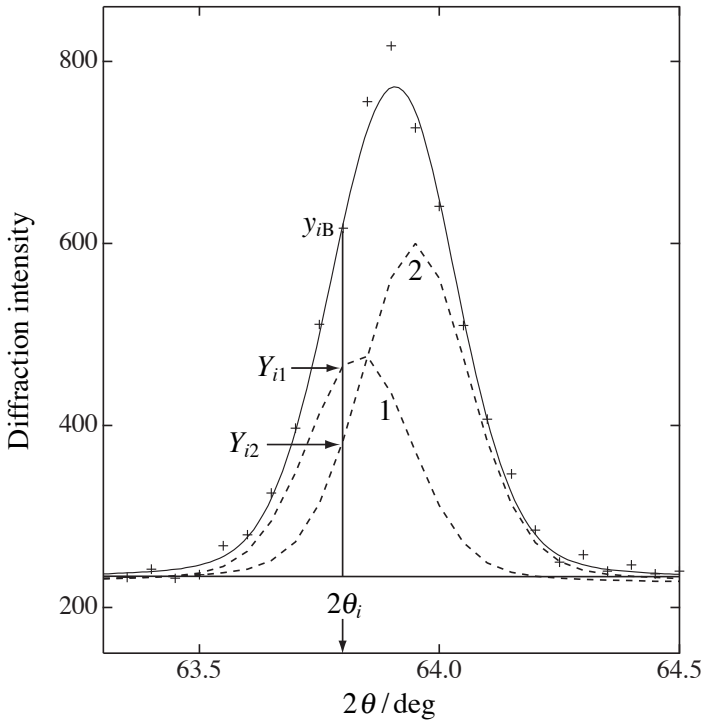

Figure 4.1: Partition of observed Bragg intensities into contributions of two overlapped reflections in $Tl_2(Ba_{0.8}Sr_{0.2})_2Ca_2Cu_3O_{10-\delta}$

($K = 2$) reflection in neutron powder diffraction data ($\lambda = 1.5401$ Å) of a high-T_c superconductor $Tl_2(Ba_{0.8}Sr_{0.2})_2Ca_2Cu_3O_{10-\delta}$ [123]. In this example of the two overlapped reflections, $y_{iB} = Y_{i1} + Y_{i2}$ at the ith step.

From Eq. (2.5), we can derive

$$Y_{iK} = sm_K|F(\boldsymbol{h}_K)|^2 P_K L(\theta_K) G(\Delta 2\theta_{iK}). \tag{4.27}$$

Replacing K with j in this equation affords Y_{ij}. $|F_o(\boldsymbol{h}_K)|$ in Eq. (4.22) is readily calculated from $I_o(\boldsymbol{h}_K)$

$$|F_o(\boldsymbol{h}_K)| = \left[\frac{I_o(\boldsymbol{h}_K)}{sm_K P_K L(\theta_K)}\right]^{\frac{1}{2}}. \tag{4.28}$$

In the case of an isolated reflection ($j = K$), $Y_{iK}/\sum_j Y_{ij}$ is equal to unity; thus Eq. (4.26) is reduced to

$$I_o(\boldsymbol{h}_K) = \Delta 2\theta \sum_i y_{iB}. \tag{4.29}$$

This equation contains no calculated structure factor, $F(\boldsymbol{h}_K)$. Accordingly, accurate observed integrated intensities can be obtained for the isolated reflections provided that intensity data of high counting statistics are measured with negligible effects of coarse particles and preferred orientation. On the other hand, Y_{iK} contains $F(\boldsymbol{h}_K)$. Consequently, the $I_o(\boldsymbol{h}_K)$'s and $|F_o(\boldsymbol{h}_K)|$'s of overlapped reflections are heavily biased by the structural model in Rietveld analysis and tend to be too optimistic.

R_{B} and R_F are nevertheless valuable indicators because they depend more strongly on the fit of the structure parameters than do the other agreement indices. It should be pointed out that R_F closely resembles the reliability index widely used in single-crystal X-ray analysis. Some workers find this useful in *ab initio* structure analysis.

4.3.4 Durbin–Watson statistics

The Durbin–Watson statistics, d_{DW}, in the weighted form [124]

$$d_{\mathrm{DW}} = \frac{\sum_{i=2}^{N} \left[\frac{y_i - f_i(\boldsymbol{x})}{\sigma_i} - \frac{y_{i-1} - f_{i-1}(\boldsymbol{x})}{\sigma_{i-1}} \right]^2}{\sum_{i=1}^{N} \left[\frac{y_i - f_i(\boldsymbol{x})}{\sigma_i} \right]^2} \tag{4.30}$$

and in the unweighted form [125]

$$d_{\mathrm{DW}} = \frac{\sum_{i=2}^{N} \Big\{ [y_i - f_i(\boldsymbol{x})] - [y_{i-1} - f_{i-1}(\boldsymbol{x})] \Big\}^2}{\sum_{i=1}^{N} [y_i - f_i(\boldsymbol{x})]^2} \tag{4.31}$$

are very useful for assessing the reliability of standard uncertainties in Rietveld analysis, by providing quantitative information about serial correlation in the residuals. Moreover, d_{DW} is a sensitive measure of the progress of a refinement, and is still discriminating even when other indices fail. The unweighted form is preferred by some statisticians over the weighted one proposed by Hill and Flack [124].

This d_{DW}-statistic is sensitive to the misfit of the calculated and observed reflection profiles, both because their areas may differ as well as their positions and, importantly, because their shapes may be inherently different. Consider, for example, how d_{DW} would be small for a symmetric calculated Lorentzian profile used to fit a symmetric Gaussian experimental profile even if the two profiles had the same peak positions, peak heights and areas.

In the absence of serial correlation, a d_{DW} value close to 2 is expected. For positive serial correlations, adjacent residuals tend to have the same sign, and d_{DW} will be smaller than 2. On the other hand, d_{DW} is expected to be larger than 2 and smaller than 4 for negative serial correlation (alternating signs of adjacent residuals).

The Durbin–Watson statistics, d_{DW}, in the weighted form may be tested against the 0.1 per cent significance point using the formula:

$$Q = 2 \left[(N-1)(N-n) - \frac{3.0902}{\sqrt{N+2}} \right], \tag{4.32}$$

where $Q < d_{\mathrm{DW}} < 4 - Q$ if consecutive terms tend to have uncorrelated, if $d_{\mathrm{DW}} < Q$ or $d_{\mathrm{DW}} > 4 - Q$, consecutive terms tend to have positive or negative serial correlation [126]. The Durbin–Watson statistics suggest that an optimum value of the step width lies between one-fifth and one-half of the minimum FWHM of well-resolved reflections.

4.3.5 Other points to remember on assessment of refinement results

Almost all users may find interesting the paper of Cox and Papoular [127] on reliability indices, errors, and significance tests. Although 'Synchrotron Data' is a part of the title, its content has much wider potential applicability.

In addition to the above agreement indices, the reliability of the refinement must be checked on the basis of final structure and lattice parameters. Occupancies and atomic displacement parameters need to be physically meaningful values; interatomic distances and bond angles should be reasonable from a crystal-chemical point of view.

4.4 Partial Profile Relaxation

4.4.1 Principle

As described above, we refine not PPPs but SPPs in the least-squares fitting of whole powder patterns. Equations, such as Eq. (3.65), impose a kind of equality constraints on PPPs, sometimes failing to express relations between PPPs and θ_K satisfactorily. As a PPP deviates from an equation relating it to θ_K, the fit between observed and calculated profiles gets worse and worse.

We devised a new technique called partial profile relaxation, where the PPPs of (nearly) isolated reflections specified by the user are locally refined independently of SPPs for structure refinement from time-of-flight (TOF) neutron powder diffraction data [128, 129]. That is, PPPs are included in variable parameters, $\boldsymbol{x}$, in Eq. (2.1). Later, we applied this technology to angle-dispersive X-ray and neutron powder-diffraction data [5]. In Rietveld refinement with partial profile relaxation, PPPs of these reflections are all or partially freed from equations relating PPPs to θ_K and diffraction indices, hkl. On the other hand, peak positions and integrated intensities for the relaxed reflections are, respectively, calculated from lattice and structure parameters in the same fashion as those for the other reflections; Refinement of peak positions would lead to excessive degrees of freedom in least-squares fitting.

As required, part of PPPs may be constrained by the equations applied to reflections not to be relaxed. Though the profiles of only low-angle reflections can be substantially relaxed except for very simple structures, better fits in this region lead to improvements in fits in a high-angle region.

Partial profile relaxation is especially suitable for samples showing anisotropic profile broadening. This technique is sound and powerful in the point that neither assumption nor approximation is required in regard to the dependence of PPPs on θ_K. We can even apply more flexible profile functions to relaxed reflections to improve the fit between observed and calculated patterns. In principle, the profile relaxation technology can be introduced not only into Rietveld refinements but into Pawley [130] and Le Bail [9] refinements.

Profile functions used for partial profile relaxation

In RIETAN-FP, we combined the technique of partial profile relaxation with the two split-type pseudo-Voigt and Pearson VII profile functions formulated by Toraya [103] (see p. 37). We

further implemented a modified split pseudo-Voigt function

$$G(\Delta 2\theta_{iK}) = \frac{(1+A)\left[\eta_{\rm H} + \sqrt{\pi \ln 2}\,(1-\eta_{\rm H})\right]}{\eta_{\rm L} + \sqrt{\pi \ln 2}\,(1-\eta_{\rm L}) + A\left[\eta_{\rm H} + \sqrt{\pi \ln 2}\,(1-\eta_{\rm H})\right]} \times$$
$$\left\{\eta_{\rm L}\frac{2}{\pi H_1}\left[1 + F(A)\left(\frac{\Delta 2\theta_{iK}}{H_1}\right)^2\right]^{-1} + (1-\eta_{\rm L})\left(\frac{\ln 2}{\pi}\right)^{\frac{1}{2}}\frac{2}{H_2}\exp\left[-\ln 2 \cdot F(A)\left(\frac{\Delta 2\theta_{iK}}{H_2}\right)^2\right]\right\}, \tag{4.33}$$

where H_1 is the FWHM of the Lorentzian component, H_2 is the FWHM of the Gaussian components, and subscripts L and H are the regions of 2θ lower and higher than the peak position, respectively; $F(A)$ has been defined in Eq. (3.86). Equation (4.33) is effective in the region $\Delta 2\theta_{iK} < 0$. For $\Delta 2\theta_{iK} > 0$, subscripts L and H should be replaced with each other, and A with $1/A$. In Eq. (4.33), The FWHM's of the Lorentzian and Gaussian components may be different from each other. The split-type pseudo-Voigt function, Eq. (3.84), of Toraya corresponds to a special case of Eq. (4.33): $H = H_1 = H_2$.

Equation (4.33) may be fit to observed profiles of only relaxed reflections. That is, Eq. (4.33) cannot be applied to reflections in the whole 2θ region whereas Eq. (3.84) is applied to all the other reflections.

Using partial profile relaxation and the combination of these two pseudo-Voigt functions, (3.84) and (4.33), we have been successfully analyzing the crystal structures of various compounds exhibiting reflections in 2θ regions lower than 20° (Cu $K\alpha$ radiation). Profile relaxation with Eqs. (3.84) and (4.33) usually gives better fits between observed and calculated diffraction patterns.

4.4.2 Applications

In the Rietveld analysis of $Sr_9In(PO_4)_7$ from the synchrotron X-ray powder-diffraction data (see 2.3), Eq. (4.33) was used as a profile function. Partial profile relaxation was applied to four reflections where fits between observed and calculated patterns are relatively poor. The combination of partial profile relaxation and Eq. (4.33) is responsible for the ultimate goodness-of-fit demonstrated in Fig. 2.1.

Figure 4.2 is a Rietveld-refinement plot for $Sr_{9.08}Ni_{1.04}K_{0.76}(PO_4)_7$ with a β-$Ca_3(PO_4)_2$-type structure [131]. X-Ray powder diffraction data were measured at room temperature on a Siemens D500 powder diffractometer equipped with an incident-beam quartz monochromator to obtain Cu $K\alpha_1$ radiation and a Braun position-sensitive detector. Equation (3.84) was fit to each reflection profile with partial profile relaxation applied to 012, 104, 110, 122, 214, 300, 02$\underline{1}$0, and 220 reflections to improve fits in these reflections at the last stages of the structure refinements. Reliability indices were $R_{\rm wp} = 4.86\,\%$ ($S = 1.97$), $R_{\rm p} = 3.53\,\%$, $R_{\rm B} = 1.50\,\%$, and $R_F = 0.70\,\%$. As Fig. 4.2 illustrates, a very excellent fit could be achieved between observed and calculated patterns by use of partial profile relaxation.

Using the technique of partial profile relaxation, we have also been analyzing the crystal structures of various zeolites and related compounds showing reflections in 2θ regions lower than 20°. Equation (4.33) proved to be flexible enough to fit highly asymmetric profiles in low-2θ regions by refining PPPs.

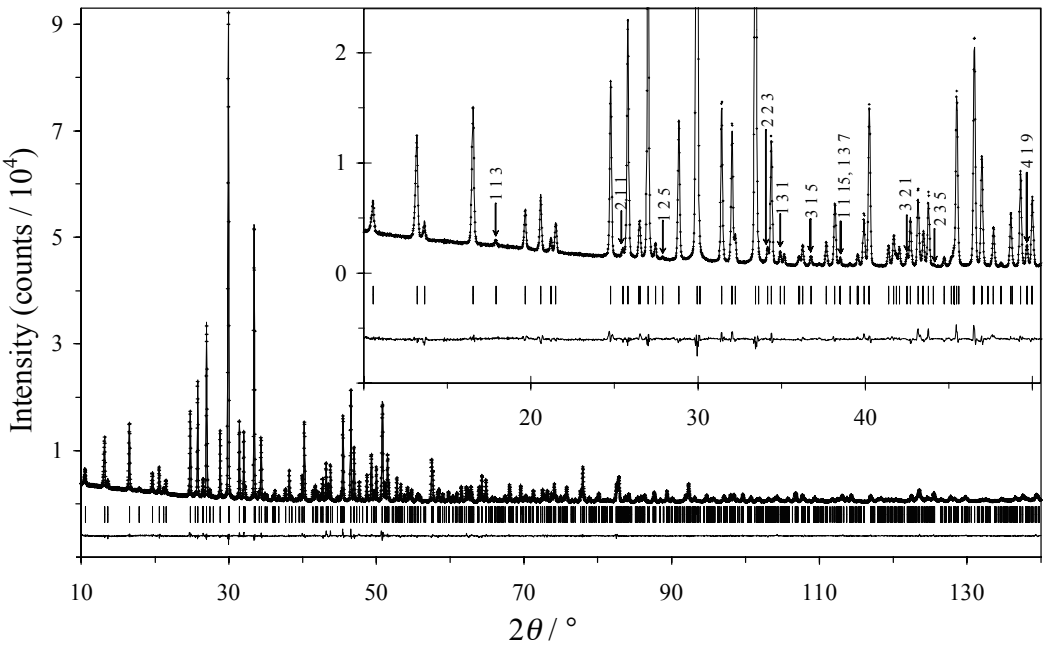

Figure 4.2: Observed (plus marks), calculated (solid line), and difference (bottom) patterns of $Sr_{9.08}Ni_{1.04}K_{0.76}(PO_4)_7$. The insets show an X-ray diffraction pattern in a 2θ range from 10° to 50.5°. Reflections with odd indices, l, are attached with hkl.

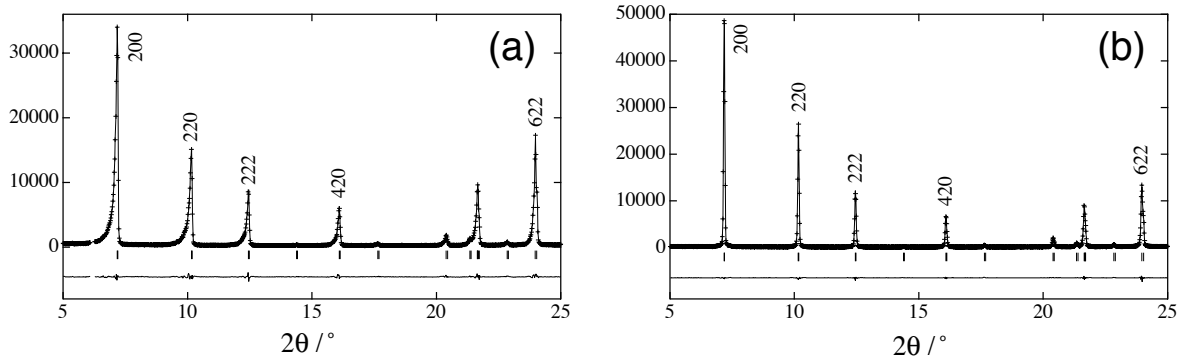

Figure 4.3: Observed (plus marks), calculated (solid line), and difference (bottom) patterns of hydrated Na-LTA in a low-2θ region

Figure 4.3 exemplifies low-2θ parts of Rietveld-refinement patterns for a zeolite, hydrated Na-LTA (Linde Type A), with a lattice parameter a as large as 24.61 Å [5]. Its X-ray powder-diffraction data were measured with Cu $K\alpha$ radiation and two different goniometers equipped with a pair of Soller slits having angular apertures of (a) 5° and (b) 1°. PPPs of reflections with their indices attached were relaxed in this 2θ region. On combination with the technique of partial profile relaxation, Eq. (4.33) was satisfactorily fit to (a) the extremely asymmetric profiles measured with a conventional X-ray powder diffractometer and (b) fairly symmetric ones taken on a vertical θ:θ diffractometer equipped with a pair of long horizontal Soller slits.

Chapter 5

IMPOSING RESTRAINTS ON GEOMETRICAL PARAMETERS

Although high-resolution synchrotron X-ray and neutron powder data can be measured almost routinely at present, the amount of information in these data is still limited in comparison with that in corresponding single-crystal data. Rietveld refinements generally converge more slowly, and it is not possible to refine all parameters together from the start. It is essential to have a good initial structural model and to proceed with Rietveld refinements slowly and carefully. The chances of finding false minima increase particularly if the lattice parameters are not initially well known.

Parameters cannot be refined with small standard uncertainties, in particular when dealing with compounds showing complex diffraction patterns or severe profile broadening. In such cases, reflections overlap heavily with each other, the weighted sum of squares, $S(\boldsymbol{x})$, does not decrease sharply near the minimum (flat minimum), and there can be quite a number of false (local) minima around the global minimum, in particular in compounds containing many atoms in the asymmetric unit. When the positions of sites for light elements are poorly defined because of the coexistence of heavy and light elements, the calculated interatomic distances and bond angles often deviate from crystal-chemically reasonable values.

5.1 Introduction of Pseudo-Observations into Rietveld Analysis

Introduction of *a priori* geometric and chemical relationships into Rietveld analysis is often very effective for overcoming the above problems, and needs only the addition of the relationships and their estimated uncertainties to the observed intensity data [132]. The dependence of bond lengths on dopant concentrations in solid solutions often serve for estimating occupancies of the dopant, particularly when the ionic radii of elements occupying the same site are considerably different from each other [133]. In the case of aluminosilicates, where (Si,Al)−O bond lengths can be estimated fairly reliably from Al/(Al+Si) amount-of-substance ratios, restraints can be imposed on the (Si,Al)−O bond lengths [134].

These 'pseudo-observations', referred to as restraints (soft/slack constraints), include expected structural features such as interatomic distances, bond angles, relationships between atomic displacement parameters, and those between occupancies. Mathematically, there is no difference

between the pseudo-observations and the X-ray or neutron diffraction data. The weighted sum of squares, $F(\boldsymbol{x})$, can be calculated in a similar fashion [135]:

$$F(\boldsymbol{x}) = S(\boldsymbol{x}) + \sum_j \left[\frac{z_j - g_j(\boldsymbol{x})}{\sigma_j}\right]^2, \tag{5.1}$$

where z_j and $g_j(\boldsymbol{x})$ are respectively observed and calculated relationships between parameters, and σ_j is the estimated error for z_j. Such a function including a penalty term is referred to as the augmented objective function in the field of nonlinear optimization. Thus, the restraints supplement the powder-diffraction data, increasing the substantial number of observations significantly. Such a method is referred to as a penalty function method by regarding the second term in the right-hand side of Eq. (5.1) as penalty.

Rietveld analysis under restraints leads to a prompt and sure convergence, makes it possible to refine more structural parameters than conventional analysis, and reduces the possibility of trapping into a false minimum.

5.2 Penalty Function Method

In RIETAN-FP, nonlinear restraints are imposed on (a) interatomic distances, l_{12}, for atoms 1 and 2, (b) bond angles, ϕ_{123}, for atoms 1, 2, and 3 with atom 2 as the apex, and (c) dihedral angles, ω_{1234}, for atoms 1, 2, 3, and 4. The definition of ω_{1234} will be described in 5.4. The augmented objective function, $F(\boldsymbol{x})$, to be minimized by a nonlinear least-squares method is the sum of $S(\boldsymbol{x})$ and three penalty terms, $P_l(\boldsymbol{x})$ for interatomic distances, $P_\phi(\boldsymbol{x})$ for bond angles, and $P_\omega(\boldsymbol{x})$ for dihedral angles, multiplied by the penalty parameter, $t^{(J)}$ $(J = 0, 1, 2, \cdots)$, in the Jth stage of unconstrained minimization:

$$F(\boldsymbol{x}) = S(\boldsymbol{x}) + t^{(J)}\big[P_l(\boldsymbol{x}) + P_\phi(\boldsymbol{x}) + P_\omega(\boldsymbol{x})\big] \tag{5.2}$$

with

$$P_l(\boldsymbol{x}) = \sum_j w(l_{12j})\Big\{\min\big[0, \Delta l_{12j}(\boldsymbol{x}) - \big|l_{12j}(\boldsymbol{x}) - l_{12j}(\mathrm{exp})\big|\big]\Big\}^2, \tag{5.3}$$

$$P_\phi(\boldsymbol{x}) = \sum_k w(\phi_{123k})\Big\{\min\big[0, \Delta\phi_{123k}(\boldsymbol{x}) - \big|\phi_{123k}(\boldsymbol{x}) - \phi_{123k}(\mathrm{exp})\big|\big]\Big\}^2, \tag{5.4}$$

$$P_\omega(\boldsymbol{x}) = \sum_l w(\omega_{1234l})\Big\{\min\big[0, \Delta\omega_{1234l}(\boldsymbol{x}) - \big|\omega_{1234l}(\boldsymbol{x}) - \omega_{1234l}(\mathrm{exp})\big|\big]\Big\}^2. \tag{5.5}$$

In Eqs. (5.3)–(5.5), $w(l_{12j})$ is the weight for the jth atom pair, $l_{12j}(\boldsymbol{x})$ is l_{12j} calculated from the current structure and lattice parameters for the same pair, $l_{12j}(\mathrm{exp})$ is l_{12j} expected for the same pair, $\Delta l_{12j}(\boldsymbol{x})$ is the allowance for $l_{12j}(\boldsymbol{x})$, $w(\phi_{123k})$ is the weight for the kth atom trio, $\phi_{123k}(\boldsymbol{x})$ is ϕ_{123k} calculated from the current structure and lattice parameters for the same trio, $\phi_{123k}(\mathrm{exp})$ is ϕ_{123k} expected for the same trio, $\Delta\phi_{123k}(\boldsymbol{x})$ is the allowance for ϕ_{123k}, $w(\omega_{1234l})$ is the weight for the lth atom quartet, $\omega_{1234l}(\boldsymbol{x})$ is ω_{1234l} calculated from the current structure and lattice parameters for the same quartet, $\omega_{1234l}(\mathrm{exp})$ is ω_{1234l} expected for the same quartet, and $\Delta\omega_{1234l}(\boldsymbol{x})$ is the allowance for ω_{1234l}. Interatomic distances lying in the range $l_{12j}(\mathrm{exp}) \pm \Delta l_{12j}(\boldsymbol{x})$ are never penalized because of their reasonable values. Likewise, no

penalties are imposed on bond angles within the range $\phi_{123k}(\mathrm{exp}) \pm \Delta\phi_{123k}(\boldsymbol{x})$ or on dihedral angles within the range $\omega_{1234l}(\mathrm{exp}) \pm \Delta\omega_{1234l}(\boldsymbol{x})$.

In Eqs. (5.3), (5.4), and (5.5), penalties for l_{12j}, ϕ_{123k}, and ω_{1234l} are respectively multiplied by $w(l_{12j})$, $w(\phi_{123k})$, and $w(\omega_{1234l})$ to deal with l_{12j}, ϕ_{123k}, and ω_{1234l} having a wide range of values nearly evenly. Weights $w(l_{12j})$ and $w(\phi_{123k})$ set at null (default value) in hoge.ins are respectively calculated as

$$w(l_{12j}) = \frac{1}{l_{12j}(\boldsymbol{x})} \tag{5.6}$$

and

$$w(\phi_{123k}) = \frac{1}{\phi_{123k}(\boldsymbol{x})}. \tag{5.7}$$

Note that weights must directly be input for dihedral angles because they may be (nearly) equal to 0°. In general, $w(\omega_{1234l})$ must be small enough to bring a balance between penalties for dihedral angles and other two kinds of penalties; trial-and-error determination of $w(\omega_{1234l})$ is required to obtain an optimum value.

If $t^{(J)}$ is so small as to give penalty terms much smaller than $S(\boldsymbol{x})$, restraints are not well satisfied. On the other hand, if $t^{(J)}$ is too large, nonlinear least-squares calculations becomes ill-conditioned for stable convergence, which may lead to the divergence of the solution. In our experience, Rietveld analysis under nonlinear restraints converge steadily provided that penalty terms lie in between several % and 10 % of $S(\boldsymbol{x})$.

Because the three terms in the right-hand side of Eqs. (5.3), (5.4), and (5.5) all have forms of the sum of squares, conventional methods of nonlinear least squares can be used to refine $\boldsymbol{x}$. When imposing restraints on geometrical parameters such as l_{12j}, ϕ_{123k}, and ω_{1234l} with the above technique, $F(\boldsymbol{x})$ becomes steeper near the global minimum than $S(\boldsymbol{x})$, increasing the probability of convergence to the global minimum.

The algorithm of the penalty function method consists of the following four steps:

1. Set J at 0. Give the initial values of $\boldsymbol{x}$ and $t^{(0)}$.
2. Refine a set of parameters $\boldsymbol{x}$ that minimizes $F(\boldsymbol{x})$.
3. If $P_l(\boldsymbol{x})$, $P_\phi(\boldsymbol{x})$, and $P_\omega(\boldsymbol{x})$ in Eq. (5.2) are reduced to nil, stop the calculation since the current values of $\boldsymbol{x}$ are the solution.
4. Add 1 to J. Increase $t^{(J)}$ by multiplying it by a user-specified constant and return to step 2.

The nonlinear restraints are introduced into the program by means of function subprogram CON, whose purpose is to calculate one of the following three function from the $\boldsymbol{x}$ vector:

$$\sqrt{w(l_{12j})}\,\min\bigl[0, \Delta l_{12j}(\boldsymbol{x}) - \bigl|l_{12j}(\boldsymbol{x}) - l_{12j}(\mathrm{exp})\bigr|\bigr], \tag{5.8}$$

$$\sqrt{w(\phi_{123k})}\,\min\bigl[0, \Delta\phi_{123k}(\boldsymbol{x}) - \bigl|\phi_{123k}(\boldsymbol{x}) - \phi_{123k}(\mathrm{exp})\bigr|\bigr], \tag{5.9}$$

$$\sqrt{w(\omega_{1234l})}\,\min\bigl[0, \Delta\omega_{1234l}(\boldsymbol{x}) - \bigl|\omega_{1234l}(\boldsymbol{x}) - \omega_{1234l}(\mathrm{exp})\bigr|\bigr]. \tag{5.10}$$

Those partial derivatives of the functionals of restraints with respect to refinable parameters which are used in the set-up of a normal equation (see 4.1.1 and 4.1.2) are approximated by centered differences, not only to save preparation times in formulating analytical derivatives but also to avoid human errors.

5.3 Specification of Restraints on Bond Lengths and Angles

RIETAN-FP has a feature to output file hoge.xyz for ORFFE [136] to calculate geometrical parameters. After dealing with hoge.xyz, ORFFE outputs file hoge.dst as well as hoge.ffe where serial numbers are added to interatomic distances and bond angles. It should be noted that hoge.ffe is created only when hoge.ffe is absent in a folder where hoge.ins is located. Geometrical parameters on which restraints are imposed are specified using these serial numbers. Accordingly, at least one unconstrained Rietveld refinement should be carried out prior to constrained one to obtain hoge.ffe. If we want to update hoge.ffe because of appreciable changes in refinable fractional coordinates, we must remove it prior to the execution of ORFFE.

RIETAN-FP reads in symmetry operations and translations from hoge.ffe and apply them to fractional coordinates of atoms related to interatomic distances and/or bond angles with the serial numbers specified by users. This technique of introducing nonlinear constraints with a reference file output by ORFFE is referred to as 'Eleonora,' which is named after a mysterious short novel by E. A. Poe.

A chemical species plus a serial number, *e.g.*, `Fe1`, `Ti2`, and `O3`, with a maximum length of 25 are input as part of a label for each site in the standard input file, hoge.ins (see 17.3.14). The 'chemical species' is alphabetical characters at the top of a site name and not related to any elemental symbols. Such a manner of assigning a kind of a metadata (data that describes and gives information about other data) to each site has an advantage that we can distinguish two or more chemical species with different bond lengths by adopting site names such as

- `Car` (C within an aromatic ring; `ar`: **ar**omatic ring)
- `Cth` (tetrahedral C with an sp^3 hybrid orbital; `th`: **t**etra**h**edral)
- `Ctr` (C with triangular coordination and an sp^2 hybrid orbital; `tr`: **tr**iangular)
- `Cli` (C with linear coordination and an sp hybrid orbital; `li`: **li**near)
- `Os` (O with a single bond; `s`: **s**ingle bond)
- `Od` (O with a double bond; `d`: **d**ouble bond)
- `Oeq` (equatorial O atom bonded to Cu; `eq`: **eq**uatorial)
- `Oax` (axial O atom bonded to Cu; `ax`: **ax**ial)
- `Alt` (tetrahedrally-coordinated Al; `t`: **t**etrahedral)
- `Alo` (octahedrally-coordinated Al; `o`: **o**ctahedral).

- `Fedi` (Fe^{2+}; `di`: **di**valent).
- `Fetr` (Fe^{3+}; `tr`: **tr**ivalent)

Each restraint is specified by inputting names of chemical species, minimum and maximum geometrical parameters, expected value of the geometrical parameter, and an allowance for the geometrical parameter. Geometrical parameters whose values lie between the minimum and maximum ones are selected from hoge.ffe and restrained with expected values and allowed deviations. The minimum geometrical parameter is required to reject extraordinarily short bonds in split-atom models.

When P−O bond lengths and O−P−O bond angles are respectively restrained within (1.50 ± 0.08) Å and $(109.47 \pm 6)^\circ$, restraints are given as follows:

```
If LPAIR = 1 then
   'A'  'B'  l_min  l_max  l_exp  Allowed dev.  Weight{
   'P'  'O'  1.3    1.7    1.50   0.08          0.0
   }
end if

If LTRIP = 1 then
   'A'  'B'  'C'   phi_min  phi_max  phi_exp  Allowed dev.  Weight{
   'O'  'P'  'O'   99.47    119.47   109.47   6.0           0.0
   }
end if
```

where `LPAIR` and `LTRIP` are flags to specify whether restraints are automatically generated for bond lengths and angles, respectively, `exp` is the expected value of a geometrical parameter, and `Allowed dev.` is its allowed deviation. Once the restraints is automatically generated, data specifying restraints imposed on all the geometrical parameters are output to the standard output file, hoge.lst, in the following way:

```
I    NSCONS      EXPCTD    DEVDA       WDA     CALCTD   A         B         C
1        34      1.5000   0.0800  0.000000     1.5314   P         O3
2        36      1.5000   0.0800  0.000000     1.5604   P         O2
3        37      1.5000   0.0800  0.000000     1.5786   P         O2
4       224    109.4700   6.0000  0.000000   108.2086   O3        P         O2
5       225    109.4700   6.0000  0.000000   110.1301   O3        P         O1
6       226    109.4700   6.0000  0.000000   108.7823   O3        P         O2
7       231    109.4700   6.0000  0.000000   110.7484   O1        P         O2
```

In this list, `WDA` is the weight (in this case, the default value of zero), `CALCTD` is the geometrical parameter calculated by ORFFE, and `A`, `B`, and `C` are site names. To customize restraints, the rectangular part of `NSCONS` (serial numbers for geometrical parameters output in hoge.ffe), `EXPCTD` (Expected value), and `DEVDA` (Allowed deviation) are copied and pasted in hoge.ins, and then parts of the data are edited, if necessary.

5.4 Imposing Restraints on Dihedral Angles

For a sequence of four atoms A, B, C, and D, the dihedral angle, ω, is defined as the angle between ABC and BCD planes. Let $\alpha = \angle$(B−C−D), $\beta = \angle$(B−A−D′), and $\gamma = \angle$(A−B−C), where D′ denotes the D atom when C−D is translated in such a way that the C atom overlaps with the A atom. Then, $\cos\omega$ is formulated as [137]:

$$\cos\omega = \frac{\cos\alpha\cos\gamma - \cos\beta}{\sin\alpha\sin\gamma}. \tag{5.11}$$

The three angles, α, β, and γ, in this equation can be calculated from the fractional coordinates of atoms A, B, C, and D′ with Eq. (A.46).

Because ORFFE does not output any dihedral angles in hoge.ffe, restraints imposed about them are specified not with hoge.ffe but with VESTA [1, 25, 26, 138]. To obtain information on a specific dihedral angle in VESTA [139], a ball-and-stick model is displayed after reading in hoge.ins or hoge.lst. After the Angle mode has been selected in the Manipulation panel, four atoms, A, B, C, and D, bonded to each other are selected while pressing the Shift key. Then, a dihedral angle is output in the text area, followed by four lines giving crystallographic information on the four atoms. For examples, in the case of C1 (= A), C2 (= B), C3 (= C), and C4 (= D) atoms contained in an aromatic ring of 3-[4-(dimethylamino)phenyl]-1-(2-hydroxyphenyl)prop-2-en-1-one [140], the following five lines

```
omega(C1-C2-C3-C4) =   2.36(8) deg.
   5      C1   C  0.58190  0.79990  0.21900 ( 0, 0, 0)+ x, y, z
   7      C2   C  0.52280  0.72240  0.11990 ( 0, 0, 0)+ x, y, z
   9      C3   C  0.41240  0.66560  0.09830 ( 0, 0, 0)+ x, y, z
  10      C4   C  0.36010  0.68130  0.17850 ( 0, 0, 0)+ x, y, z
```

are output in a text area below a graphic window (**Fig. 5.1**). Lines No. 2−5 for the four atoms include site numbers, site names, chemical species, fractional coordinates (x, y, z), translation along $\boldsymbol{a}$, $\boldsymbol{b}$, and $\boldsymbol{c}$, and equivalent positions.

To input restraints on dihedral angles in hoge.ins, flag `LQUART` is at first set at `1`; `QUART` is the abbreviation of quartet. Next, the four lines (No. 2−5) giving information about the four atoms are selected, copied, and pasted in hoge.ins with some spaces at the tops of the lines if necessary. An estimated dihedral angle and its allowed deviation is input in the next line. When inputting two or more restraints on dihedral angles, quartets of lines are repeated with a vacant line inserted between two blocks. Finally, '`}`' (plus a comment) is placed to show the end of restraints on dihedral angles.

5.5 Performance of Restrained Refinement with RIETAN-FP

RIETAN-FP with the above features is suitable for Rietveld refinements of compounds containing many atoms in asymmetric units, for example, organic compounds and zeolites. In such cases, least-squares solutions are often trapped in local minima near initial fractional coordinates even if we adopt Rietveld analysis using a basically correct structural model, imposing a lot of constraints

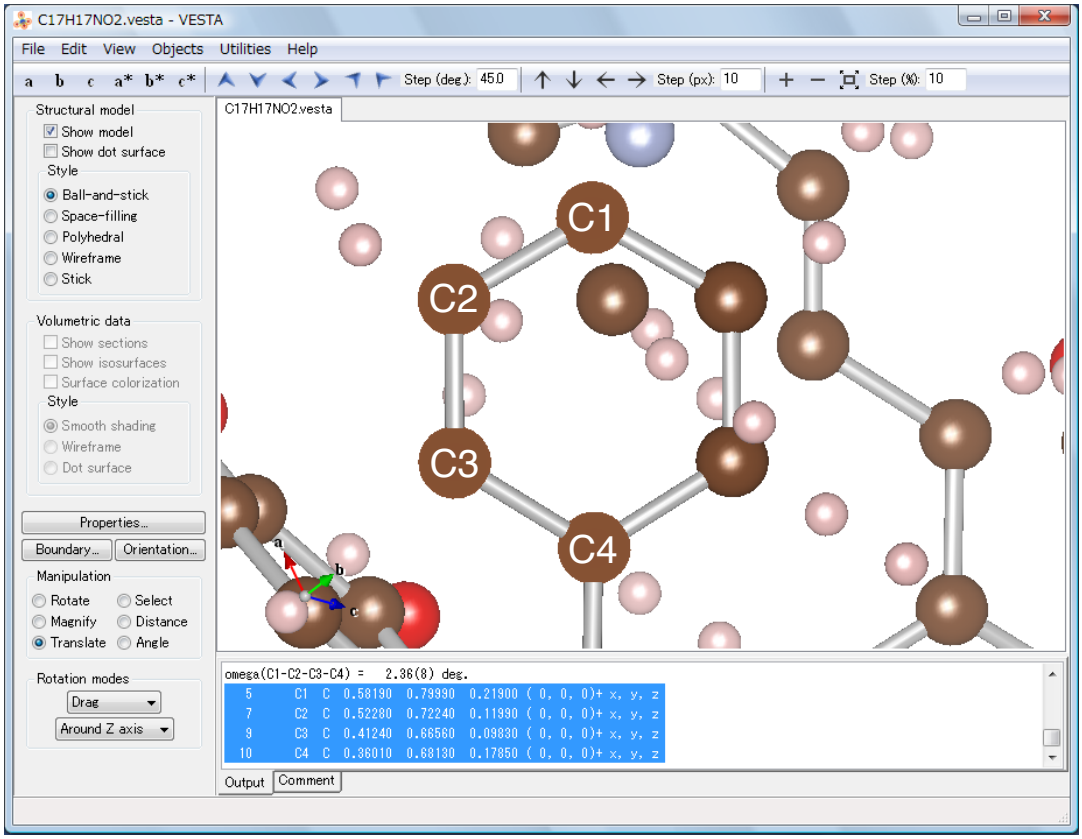

Figure 5.1: Calculation of a dihedral angle for four carbon atoms in an aromatic ring in 3-[4-(dimethylamino)phenyl]-1-(2-hydroxyphenyl)prop-2-en-1-one with VESTA

or restraints on geometrical parameters. The conjugate-direction method (see 4.1.3), which is one of the fastest direct-search methods, implemented in RIETAN-FP makes it easier to escape from local minima relatively easily in combination with Rietveld analysis under restraints.

In nearly all reanalyses from X-ray powder-diffraction data of organic compounds distributed on the Web with RIETAN-FP, reliability indices have been improved more or less. On further use of MPF, reliability indices, in particular R_{B} and R_F based on integrated intensities, decrease dramatically. **Table 5.1** lists results of reanalyses of three organic compounds from synchrotron X-ray powder diffraction data [141–143]. The MPF method was not applied to the diffraction data of $Ge(SnMe_3)_4$ because it shows too many reflections to carry out MEM analysis with PRIMA [13] on Windows XP. Reliability indices were appreciably improved by reanalyzing them by the Rietveld and MPF methods with RIETAN-FP and PRIMA.

Table 5.1: Reliability indices (%) obtained in Rietveld refinements and subsequent MPF analyses (in parentheses) from three sets of synchrotron X-ray powder-diffraction data

Compounds	R_{wp}	R_{B}	R_F	Ref.
$Ge(SnMe_3)_4$	8.44	–	10.3	[141]
$Ge(SnMe_3)_4$	7.86	3.74	3.43	This work
$[Cr(C_7H_8)_2]\,C_{60}$	10.5	26.5	17.6	[142]
$[Cr(C_7H_8)_2]\,C_{60}$	6.77 (6.61)	4.03 (1.87)	3.91 (2.33)	This work
D-Sorbitol	4.38	1.66	2.18	[143]
D-Sorbitol	2.48 (2.44)	0.88 (0.44)	1.09 (0.49)	This work

Chapter 6

REFINEMENT STRATEGIES

When applying the Rietveld method to actual samples, we usually proceed according to the following procedures (**Fig. 6.1**).

1. Index reflections in powder-diffraction patterns by using computer programs such as ITO, TREOR, and DICVOL (available for download from CCP14[1]) and/or selected-area electron diffraction, and determine possible space groups on the basis of conditions limiting possible reflections [144].

2. After determining peak positions of reflections, refine lattice parameters by the Pawley method [130], the Le Bail method [9], or a method of linear least-squares [145]. Rietveld analysis often does not converge to the global minimum unless the initial values of the lattice parameters are fairly close to the true values. Accordingly, it is safe to refine the lattice parameters prior to Rietveld analysis.

3. Roughly infer atomic configurations in the unit cell through structural data described in the literature, a search for an isomorphous compound or a compound with a similar crystal structure using a database [146] (see 9), a chemical composition, or the direct observation of crystal-structure images by HRTEM. Otherwise, *ab initio* structure analysis [147] has to be tried.

4. Simulate a powder-diffraction pattern on the basis of the structural model. If the calculated diffraction pattern is not similar to the powder pattern actually measured, return to step 3 and assemble another structure model.

5. Perform Rietveld refinement. The lattice parameters determined in step 2 are used as initial values. Use profile parameters for standard samples such as Si (*e.g.*, NIST Standard Reference Material[2] 640c) as initial ones unless broadening of diffraction lines due to strain and particle size is not very marked.

6. Modify the structural model and return to step 5 if reliability indices are not decreased to sufficiently low values. Fourier or difference Fourier synthesis, and MEM analysis from a set

[1] http://www.ccp14.ac.uk/
[2] http://www.nist.gov/srm/

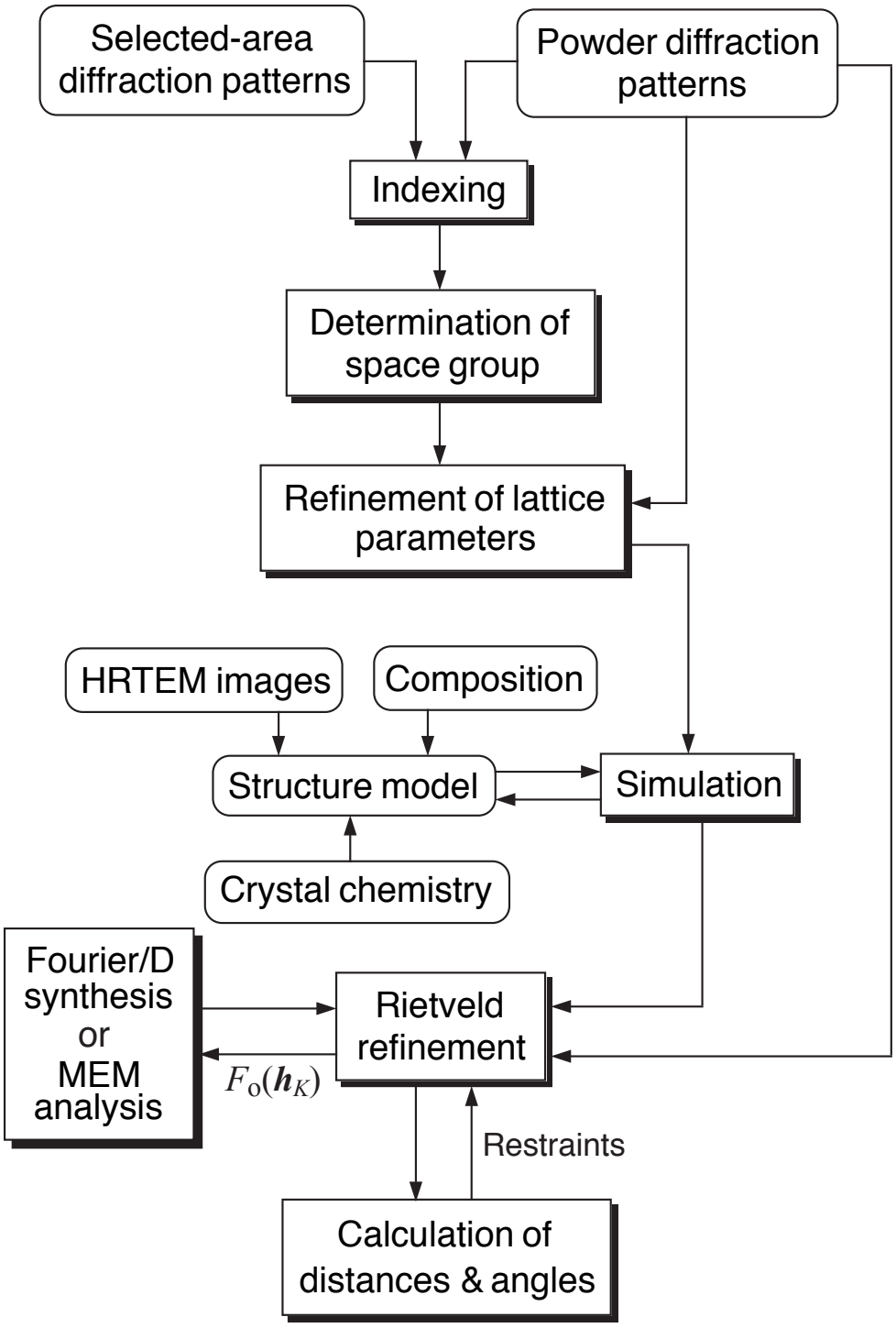

Figure 6.1: A series of procedures related to Rietveld refinement

of $I_o(\boldsymbol{h}_K)$'s estimated after Rietveld analysis (see 4.3.2) and subsequent 3D visualization of density distribution are often helpful in this process.

7. If the B_j value of a site is extraordinarily large or small, return to step 5 after checking the validity of the Wyckoff-position assignment and occupation model for the site. For example, a split-atom model may give better results.

8. Calculate interatomic distances and bond angles from structure and lattice parameters obtained by the Rietveld analysis. Some values of them may be unreasonable in view of crystal data reported in the literature, typical interatomic distances [148], information on crystal chemistry [149, 150], effective ionic radii [151], bond-valence sums [152, 153], charge distribution [154–156], *etc.* In such a case, return to step 5 after modifying the structure model or imposing appropriate restraints on the interatomic distances and/or bond angles (see 5.2).

For more details of procedures in Rietveld analysis, refer to refs. [157] and [158]. A book written by Pecharsky and Zavalij [159] also provides us with a variety of information on the execution of Rietveld analysis.

Chapter 7

QUANTITATIVE ANALYSIS OF MIXTURES

7.1 Determination of Mass Fractions

Most Rietveld-refinement programs have a feature for dealing with mixtures of two or more phases. Mass fractions, w_p, of phases p can easily be calculated from scale factors, s_p ($p = 1, 2, \cdots$), refined by using this multi-phase capability:

$$w_p = \frac{s_p Z_p M_p V_p}{\sum_j s_j Z_j M_j V_j}, \tag{7.1}$$

where Z is the number of the formula unit contained in the unit cell, M is the mass of the formula unit, and V is the unit-cell volume [37, 38]. The summation is carried out over all the phases contained in the mixture. The March–Dollase function (3.55) and the modified March–Dollase functions (3.56) have the advantage that they conserves scattering matter, allowing their use in quantitative phase determination. In RIETAN-FP, the mole fraction of each phase is also calculated from Z_j's and output to the standard output file hoge.lst.

This method does not require any working curves and affords more reliable results than the conventional method using only a limited number of reflections. Because structure and lattice parameters are refined at the same time, it is useful as a versatile data-processing method for powder diffraction.

7.2 Correction for Microabsorption

The above method of calculating mass factions does not take into account any microabsorption effects. They will be important unless the linear attenuation coefficients, μ are the same, or nearly so, for all phases being analyzed. Hence, the neglect of microabsorption effects will generally be a much more serious error in the X-ray powder diffraction case than in the neutron powder diffraction case.

A beginning effort at providing a microabsorption correction on the analysis of X-ray powder-diffraction data has been made in RIETAN-FP. It involves the use of a particle absorption factor,

τ_p, for phase p:

$$\tau_p = \frac{1}{A_p}\int_0^{A_p} \exp\bigl[-(\mu_p - \overline{\mu})\,R_p\bigr]\mathrm{d}A, \tag{7.2}$$

where A_p is the particle volume, $\overline{\mu}$ is the mean linear attenuation coefficient of the solid matrix of the powder, and R_p is the effective particle radius.

The linear attenuation coefficient, μ_p, of phase p is evaluated from the density, ρ_p, in units of $\mathrm{g\,cm^{-3}}$, the mass fractions, w_i, of constituent elements, and their mass attenuation coefficients, $(\mu_\mathrm{m})_i$ [160], in units of $\mathrm{cm^2\,g^{-1}}$:

$$\mu_p = \rho_p \sum_i w_i (\mu_\mathrm{m})_i. \tag{7.3}$$

The summation is over all the constituent elements. The mass attenuation coefficient, μ_m, is sometimes written as μ/ρ.

For this calculation, RIETAN-FP provides us with mass attenuation coefficients, μ_m, of all the elements for characteristic X rays (Ag $K\alpha$, Mo $K\alpha$, Cu $K\beta$, Cu $K\alpha$, Co $K\alpha$, Fe $K\alpha$, and Cr $K\alpha$ radiations) [160]; they are given in `DATA` statements in the source code of RIETAN-FP. On the other hand, when analyzing synchrotron X-ray powder diffraction data, μ_m values at the wavelength of X rays are automatically calculated by interpolating $\mu_\mathrm{m}/(\mathrm{cm^2\,g^{-1}})$ values (photon energy, $E = 0.001$–$20\,\mathrm{MeV}$) tabulated by Hubbell and Seltzer [161] and saved in a text file, mac.tbl (see 17.1), in the RIETAN_VENUS folder.

Beware lest virtual chemical species (see 17.3.9) are defined when analyzing X-ray diffraction data of multiphase samples containing solid solutions by correcting for microabsorption; $(\mu_\mathrm{m})_i$ cannot be calculated correctly on the use of virtual chemical species.

The mean linear attenuation coefficient, $\overline{\mu}$, [162] is obtained by

$$\begin{aligned}\overline{\mu} &= \frac{\sum_j w_j \left(\dfrac{\mu_j}{\rho_j}\right)}{\sum_j \dfrac{w_j}{\rho_j}} \\ &= \frac{\sum_j w_j \left(\mu_\mathrm{m}\right)_j}{\sum_j \dfrac{w_j}{\rho_j}}.\end{aligned} \tag{7.4}$$

The summation with respect to j is carried out over all the phases contained in the mixture. Keep in mind that $\overline{\mu}$ is the mean value for the solid material with the spaces between particles excluded.

Necessarily, such a correction also involves the sizes and shapes, and distributions thereof, of the particles. Brindley [163, 164] proposed a method of correcting for microabsorption from the relative absorption capacity and the size of spherical particles for each phase contained in a mixture. Introduction of Brindley's theory into Eq. (7.1) gives the mass fraction corrected for microabsorption [165]:

$$w_p = \frac{\dfrac{s_p Z_p M_p V_p}{\tau_p}}{\displaystyle\sum_j \frac{s_j Z_j M_j V_j}{\tau_j}}. \tag{7.5}$$

Brindley [163, 164] tabulated τ_p as a function of $\mu_p - \overline{\mu}$, where μ_p is calculated from the chemical formula and mass attenuation coefficients, μ/ρ, of each element, and $\overline{\mu}$ from μ_p and the estimated values of w_p ($p = 1, 2, \cdots$). However, values of τ_p in Brindley's table are far from perfect because of low computational accuracy. For example, $\tau_p = 0.866$ at $\mu_p - \overline{\mu} = 0.1$ and $\theta = 45°$ in Brindley's table should be 0.86282. Therefore, τ_p values for $\theta = 0°$–$90°$ (step: 15°) were recalculated over a $\mu_p - \overline{\mu}$ range from -1 to 1 (step: 0.01), using an Igor Pro macro where formulae described by Thorkildsen and Larsen [50] were implemented by T. Ida of Nagoya Institute of Technology.[1] The resulting values of τ_p were included in the source code of RIETAN-FP with a `DATA` statement.

In RIETAN-FP, R_p is either determined experimentally, *e.g.*, by scanning electron microscopy (SEM) or laser scattering or assumed empirically. If the accurate R_p value is known, the resulting mass fractions are quite precise. However, a wrong particle size will yield results that are less accurate compared to those obtained without any size correction. The w_p value of each phase is first calculated from s_p refined in Rietveld analysis with Eq. (7.1). These w_p's are mere approximate values because they were obtained without any correction for microabsorption. To improve w_p's, we adopted the following iterative method. For a start, τ_p's are at first determined by interpolation of data in our table of τ_p's described above, and w_p's are calculated from the resulting τ_p's with Eq. (7.5). Then, w_p's are optimized by repeating the calculations of $\mu_p - \overline{\mu}$ and w_p until the relative change in $\overline{\mu}$ decreases down to 0.01 %.

Bear in mind that setting R_p at 0 leads to neglecting microabsorption and calculating mass fractions with Eq. (7.1). In this case, input only '/' (slash) as follows because initial R_p values are zero:

```
# Effective radii for NPHASE@ phases. Enter '/' when neglecting microabsorption.
/
```

If $|(\mu_p - \overline{\mu})\, R_p| > 1$, τ_p cannot be interpolated, which leads to the discontinuance of correcting for microabsorption. In such a case, the following error message appears in the standard output of RIETAN-FP:

```
Too large negative value of [mu - mu(mean)]R
```

or

```
Too large value of [mu - mu(mean)]R
```

Brindley [163] computed τ_p's for spherical particles for use as a 'better than none' approximation. Of course, a naturally occurring material consisting entirely of spherical particles of identical size would be rarely found. Nevertheless, the spherical-particle model serves fairly well in quantitative analysis of crystalline phases.

In the case of a mixture of LiF (60 mass%) and $Pb(NO_3)_2$ (40 mass%) [165], quantitative analysis without any correction for microabsorption gives mass fractions of LiF (75.3 mass%) and $Pb(NO_3)_2$ (24.7 mass%) far from the true mass percentages with a $\overline{\mu}$ value of 200.6 cm^{-1}. On

[1] http://www.crl.nitech.ac.jp/~ida/software/IgorMacro/index.html

the other hand, when correcting for microabsorption on the assumption that $R_p = 5$ µm, mass fractions of LiF (60.4 mass%) and $Pb(NO_3)_2$ (39.6 mass%) comparable to the weighted ones were obtained after three cycles.

7.3 Quantitative Analysis of Amorphous Phases

Bish and Howard [38] proposed a method to determine the content of an amorphous phase contained in a sample by adding a crystalline internal standard material, *e.g.*, NIST SRM 674b (CeO_2, Cr_2O_3, TiO_2, and ZnO), weighted on ahead. In RIETAN-FP, if the phase number k of the internal standard material and its mass fraction w_k are input, w_p's corrected for the mass fractions of the amorphous phase are calculated and output in hoge.lst.

Let define parameter C for the internal standard material s as

$$C = \frac{s_s Z_s M_s V_s}{w_s}. \tag{7.6}$$

Then, the mass fraction, w_p, for a crystalline phase p is obtained by

$$w_p = \frac{s_p Z_p M_p V_p}{C}, \tag{7.7}$$

and that of the amorphous phase a by

$$\begin{aligned} w_a &= 1 - \sum_p w_p \\ &= 1 - \frac{1}{C} \sum_p s_p Z_p M_p V_p. \end{aligned} \tag{7.8}$$

Chapter 8

ANALYSIS OF SIMPLE MAGNETIC STRUCTURES

8.1 Fundamental Procedures for Analyzing Commensurate and Collinear Magnetic Structures

When a crystallographic unit cell (CUC) does not coincide with a magnetic unit cell (MUC) [166], Bragg reflections that do not appear in conformity with space-group symmetry are observed in neutron diffraction patterns. Typical examples are antiferromagnets, where adjacent spins are anti-parallel with no net magnetization in zero field. In ferrimagnetic materials, *e.g.*, ferrites, two or more magnetic atoms with magnetic moments of different magnitudes are arranged anti-parallel, which leads to net magnetization in zero field. Ferrimagnets have MUCs that may be either the same or larger than the CUCs.

Commensurate magnetic structures of antiferromagnetic and ferrimagnetic materials can be determined by regarding them as consisting of the following two virtual phases:

1. a CUC phase with $F(\boldsymbol{h}_K, \text{cryst.}) \neq 0$ and $F(\boldsymbol{h}_K, \text{magn.}) = 0$,
2. an MUC phase with $F(\boldsymbol{h}_K, \text{cryst.}) = 0$, $F(\boldsymbol{h}_K, \text{magn.}) \neq 0$, and a triclinic space group of $P1$.

The CUC phase contains all the constituent atoms whereas the triclinic MUC phase contains only magnetic ones. In other words, the virtual CUC and MUC phases show only nuclear and magnetic scattering, respectively. Coherent-scattering lengths, b_c, of all the magnetic atoms in the MUC are set at zero, for convenience. For this purpose, all the pure chemical species in the CUC phase are simply shown by elemental names (*e.g.*, 'Fe' and 'Ni') whereas those in the MUC phase are attached with '%' (*e.g.*, 'Fe%' and 'Ni%'). Elements whose names are attached with '%' have b_c values of zero and non-zero magnetic form factors, f_j(magn.). On the other hand, elements attached with '*' (*e.g.*, 'Fe*' and 'Ni*') have non-zero b_c and f_j(magn.) (see 17.3.9). Let `Me` be the elemental name of a metal, then b_c and f_j(magn.) have the following values:

In Rietveld analysis of the virtual two-phase mixture (see Chap. 7), appropriate linear constraints are imposed on scale factors, profile, lattice, and crystal-structure parameters manually or automatically after each cycle of nonlinear least-squares calculations. Equation (3.49) is used to calculate $F(\boldsymbol{h}_K, \text{magn.})$'s for the triclinic MUC phase during the Rietveld refinement.

Name	b_c	f_j(magn.)
Me	$\neq 0$	$= 0$
Me%	$= 0$	$\neq 0$
Me*	$\neq 0$	$\neq 0$

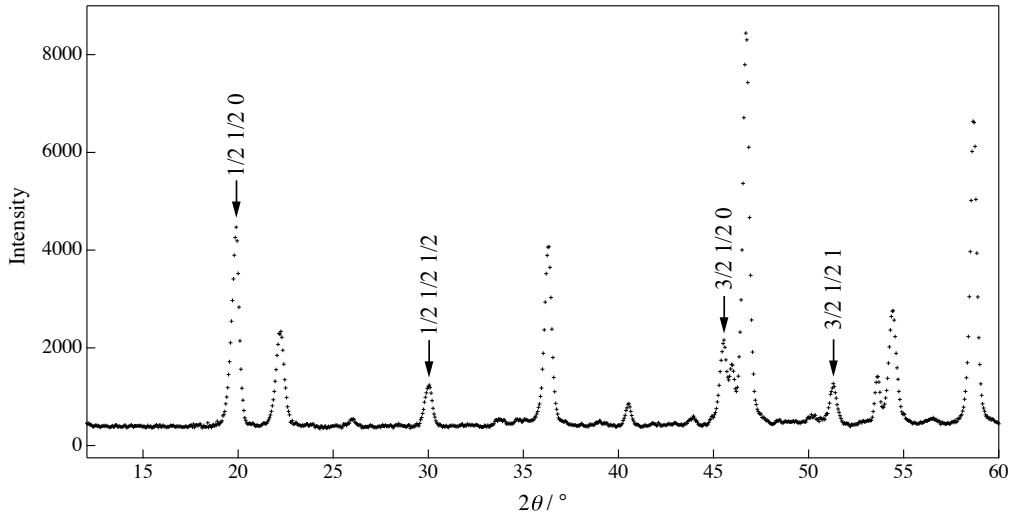

Figure 8.1: Neutron powder diffraction pattern of $BiCoO_3$ below 60°. Four reflections to which arrows and reflection indices are attached are magnetic one.

We have to build the magnetic-structure model on the basis of the propagation vector $\boldsymbol{k}$. Read Refs. [76, 167] for the method of deriving $\boldsymbol{k}$ from hkl indices of magnetic reflections and constructing possible magnetic-structure model.

In what follows, an example of analyzing the magnetic structure of $BiCoO_3$ [168] will be additionally described to make the procedures more comprehensive. $BiCoO_3$ is tetragonal with space group $P4mm$ and lattice parameters of $a = 0.3729\,\text{nm}$ and $c = 0.4724\,\text{nm}$ at 5 K. It is an insulator with a Néel temperature, T_N, of 470 K. **Figure 8.1** illustrates a neutron powder diffraction pattern of $BiCoO_3$ measured on HRPD at the JRR-3 reactor of JAEA with a wavelength of 1.8233 Å. A propagation vector of $\boldsymbol{k} = (1/2, 1/2, 0)$ was derived from indices of some magnetic reflections observed below T_N. $BiCoO_3$ proved to have a collinear antiferromagnetic structure with magnetic moments of MUC dimensions of $\boldsymbol{a}' = 2\boldsymbol{a}$ and $\boldsymbol{c}' = 2\boldsymbol{c}$ as illustrated in **Fig. 8.2**.

8.2 Standardization of Crystal Data

At first, crystal data input either from a file or by the user in the Structure dialog box are standardized by selecting [Standardization of Crystal Data] in the Utilities menu and executing STRUCTURE TIDY [169] (see Chap. 9) embeded in VESTA [25, 26]. In the case of $BiCoO_3$, the origin is shifted from (0, 0, 0) reported in Ref. [168] to (1/2, 1/2, 0.5669) to give fractional coordinated listed in **Table 8.1**. The standardization of the crystal data decreases Γ defined by Eq. (9.1) from 2.5269 to 1.9916.

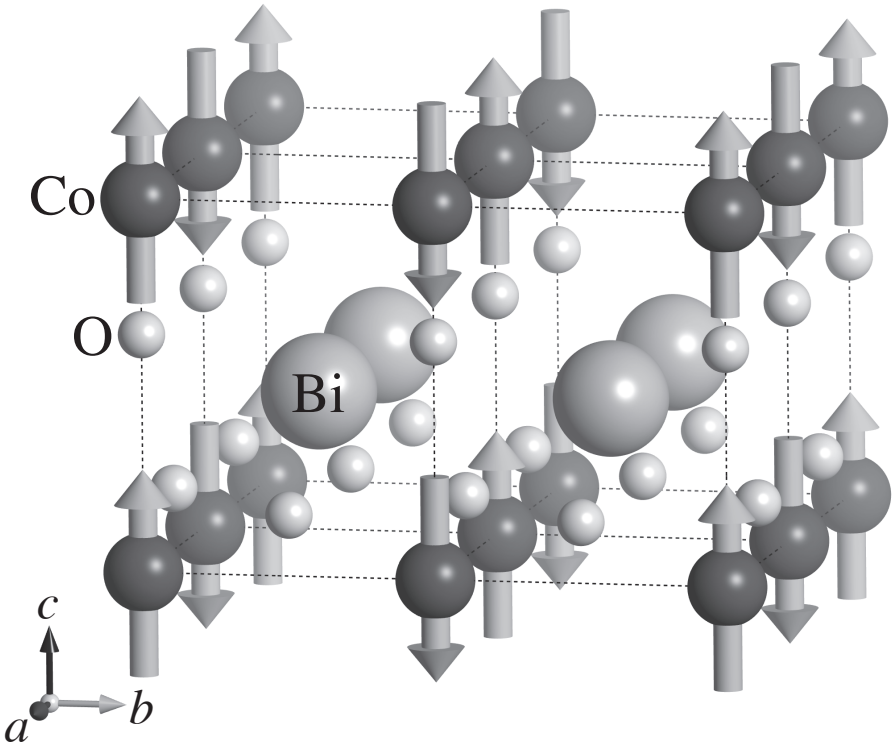

Figure 8.2: Collinear magnetic structure of $BiCoO_3$. Broken lines show CUCs, and arrows attached to Co^{3+} ions illustrate magnetic moments

Table 8.1: Positions and fractional coordinates of four sites before (upper) and after (lower) standardization of crystal data for $BiCoO_3$ by STRUCTURE TIDY

Atom	Site	x	y	z
Bi	1a	0	0	0
Co	1b	1/2	1/2	0.5669
O1	1b	1/2	1/2	0.2034
O2	2c	1/2	0	0.7300
Bi	1b	1/2	1/2	0.4331
Co	1a	0	0	0
O1	1a	0	0	0.6365
O2	2c	1/2	0	0.1631

8.3 Conversion of the CUC into the MUC

An MUC including only magnetic atoms is generated in VESTA. All the nonmagnetic atoms (Bi, O1, and O2 atoms in $BiCoO_3$) are deleted in the [Structure] dialog box, and the [Remove symmetry] button is clicked to lower space-group symmetry to $P1$. The resulting triclinic phase with the MUC is composed of only Co^{3+} ions.

In general, transformation of the coordinate system consists of two parts: a linear part $\boldsymbol{P}$ and

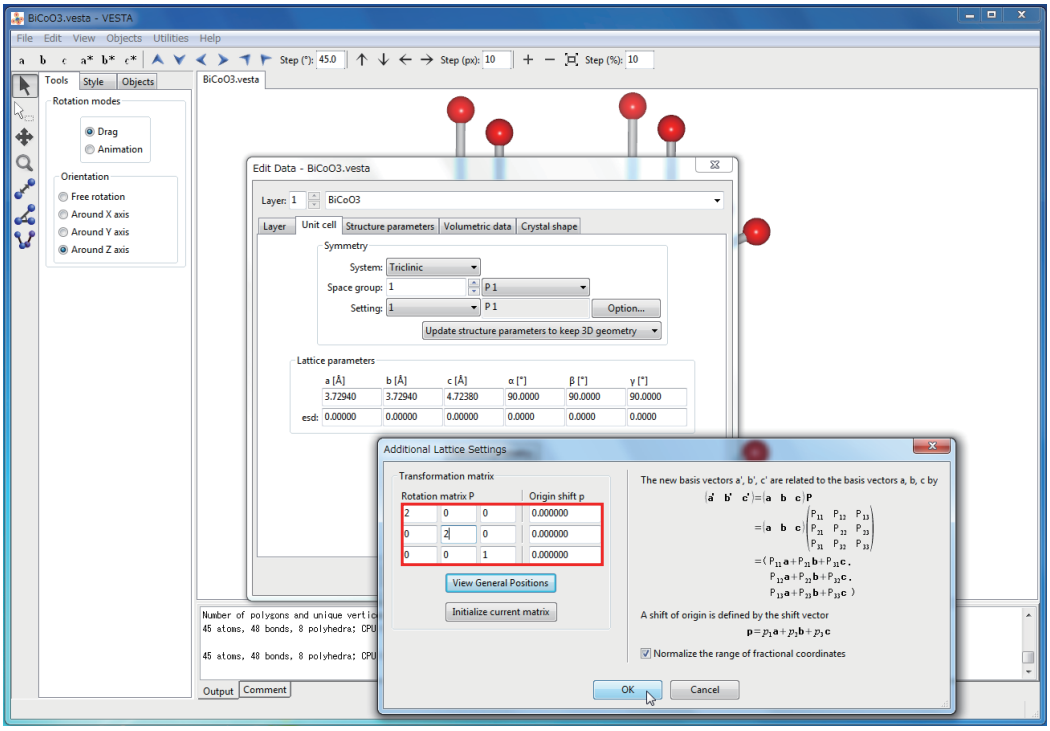

Figure 8.3: Inputting arrays $\boldsymbol{P}$ and $\boldsymbol{p}$ used to convert the CUC of $BiCoO_3$ to the MUC in VESTA

ashift of origin $\boldsymbol{p}$ [170]. After clicking the [Option...] button in `Space-group symmetry`, a (3×3) array $\boldsymbol{P}$ and a (3×1) array $\boldsymbol{p}$ to convert the CUC into the MUC are input in the Additional Lattice Settings dialog box (**Fig. 8.3**) [171].

We will hereafter attach a prime to each physical quantity relevant to the MUC, *e.g.*, $\boldsymbol{a}'$ and x'. Array $\boldsymbol{P}$ is used to change the dimensions and orientation of the CUC into those of the MUC:

$$\begin{aligned}
\left(\boldsymbol{a}', \boldsymbol{b}', \boldsymbol{c}'\right) &= (\boldsymbol{a}, \boldsymbol{b}, \boldsymbol{c}) \cdot \boldsymbol{P} \\
&= (\boldsymbol{a}, \boldsymbol{b}, \boldsymbol{c}) \begin{pmatrix} P_{11} & P_{12} & P_{13} \\ P_{21} & P_{22} & P_{23} \\ P_{31} & P_{32} & P_{33} \end{pmatrix} \\
&= (P_{11}\boldsymbol{a} + P_{21}\boldsymbol{b} + P_{31}\boldsymbol{c}, P_{12}\boldsymbol{a} + P_{22}\boldsymbol{b} + P_{32}\boldsymbol{c}, P_{13}\boldsymbol{a} + P_{23}\boldsymbol{b} + P_{33}\boldsymbol{c}) \,. \qquad (8.1)
\end{aligned}$$

The Miller indices of a plane, (hkl), in direct space are likewise transformed by use of $\boldsymbol{P}$ [170]:

$$\left(h', k', l'\right) = (h, k, l)\, \boldsymbol{P}. \qquad (8.2)$$

Array $\boldsymbol{P}$ is fundamental to all the unit-cell transformations. In the case of $BiCoO_3$, $\boldsymbol{a}' = 2\boldsymbol{a}$, $\boldsymbol{b}' = 2\boldsymbol{b}$, and $\boldsymbol{c}' = \boldsymbol{c}$, which are compared with Eq. (8.1) to afford the following elements of $\boldsymbol{P}$: $P_{11} = P_{22} = 2$, $P_{33} = 1$, and $P_{12} = P_{13} = P_{21} = P_{23} = P_{31} = P_{32} = 0$.

On the other hand, the translation vector

$$\begin{aligned} \boldsymbol{t} &= (\boldsymbol{a}, \boldsymbol{b}, \boldsymbol{c}) \cdot \boldsymbol{p} \\ &= (\boldsymbol{a}, \boldsymbol{b}, \boldsymbol{c}) \begin{pmatrix} p_1 \\ p_2 \\ p_3 \end{pmatrix} \\ &= p_1 \boldsymbol{a} + p_2 \boldsymbol{b} + p_3 \boldsymbol{c} \end{aligned} \tag{8.3}$$

corresponding to translation from the origin is calculated from $\boldsymbol{p}$. In $BiCoO_3$, the origin of the CUC coincides with that of the MUC, which gives $p_1 = p_2 = p_3 = 0$.

All the elements of arrays $\boldsymbol{P}$ and $\boldsymbol{p}$ are later input at the part of information on the virtual MUC phase in hoge.ins to calculate arrays $\boldsymbol{Q}$ and $\boldsymbol{q}$ (see 8.5).

8.4 Obtaining Information on Magnetic Atoms

Those structure parameters of all the Co sites in the MUC which are displayed at the lowest part of the [Structure] dialog box in VESTA 3[1] are those of independent sites for the MUC. In the case of $BiCoO_3$, they are (0, 0, 0), (0, 1/2, 1/2), (1/2, 1/2, 0), and (1/2, 0, 0). Comparison of the CUC and MUC (**Fig. 8.4**) show that these four atoms occupy corners at the $z = 0$ level in the CUC. By selecting the Co sites successively, the following four lines, each of which is followed by another line containing an occupancy, an atomic displacement parameter, *etc.*, are output in the text area:

```
Atom:  1    Co Co  0.00000  0.00000  0.00000  ( 0, 0, 0)+ x, y, z
Atom:  2    Co Co  0.00000  0.50000  0.00000  ( 0, 0, 0)+ x, y, z
Atom:  3    Co Co  0.50000  0.50000  0.00000  ( 0, 0, 0)+ x, y, z
Atom:  2    Co Co  0.50000  0.00000  0.00000  ( 0, 0, 0)+ y, -x, z
```

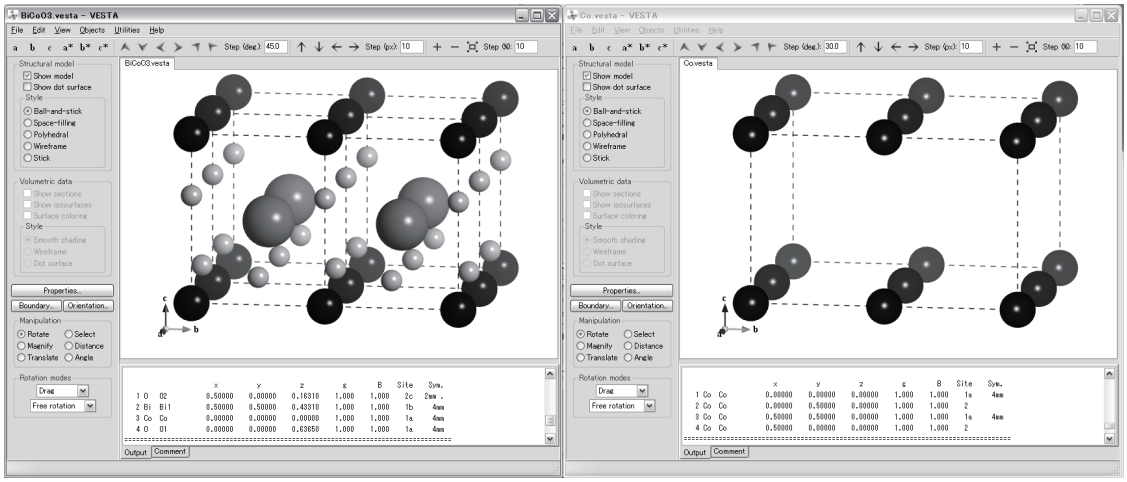

(a) (b)

Figure 8.4: Comparison of the (a) CUC phase ($BiCoO_3$) and (b) the MUC phase (Co) with VESTA

[1]Use not VESTA 2.4.X but VESTA 3 for the present purpose.

These four lines are copied into a prescribed position in hoge.ins. RIETAN-FP calculates fractional coordinates of the four Co atoms in the CUC from those of the Co atom in the asymmetric unit of the CUC using the symmetry operations and translation vectors contained in the four lines starting with '`Atoms:`'.

8.5 Conversion of the Unit Cell and Fractional Coordinates in RIETAN-FP

As described in 8.3, RIETAN-FP calculates the (3×3) array $\boldsymbol{Q}$,

$$\boldsymbol{Q} = \boldsymbol{P}^{-1}, \tag{8.4}$$

which serves to transform the basis vectors of reciprocal space and the (3×1) array $\boldsymbol{q}$

$$\boldsymbol{q} = -\boldsymbol{P}^{-1} \cdot \boldsymbol{p} \tag{8.5}$$

from $\boldsymbol{P}$ and $\boldsymbol{p}$ [170] input in hoge.ins. They are used for conversion of the unit cell and fractional coordinates.

As described in Appendix A, the metric tensors, $\boldsymbol{G}$ and $\boldsymbol{G}^*$, incorporate information on the lattice, *i.e.*, the lattice parameters, into a single matrix. With arrays $\boldsymbol{Q}$ and $\boldsymbol{P}$ described above, $\boldsymbol{G}$ and $\boldsymbol{G}^*$ can be converted into the metric tensors of the MUC, $\boldsymbol{G}'$ and $\boldsymbol{G}^{*\prime}$, respectively (see Appendix A.11).

The fractional coordinates of the magnetic atoms in the CUC are converted into those in the MUC using $\boldsymbol{Q}$ and $\boldsymbol{q}$ [170]:

$$\begin{pmatrix} x' \\ y' \\ z' \end{pmatrix} = \boldsymbol{Q} \begin{pmatrix} x \\ y \\ z \end{pmatrix} + \boldsymbol{q}. \tag{8.6}$$

The anisotropic atomic displacement tensor, $\boldsymbol{\beta}$ (see Eq. (3.21)), of the CUC can be converted into that of the MUC, $\boldsymbol{\beta}'$, by use of $\boldsymbol{Q}$ and its transposed matrix $\widetilde{\boldsymbol{Q}}$:

$$\boldsymbol{\beta}' = \boldsymbol{Q}\boldsymbol{\beta}\widetilde{\boldsymbol{Q}}. \tag{8.7}$$

8.6 Rietveld Analysis with RIETAN-FP

In the part of inputting crystal- and magnetic-structure parameters for the MUC phase, μ_j $(= \pm|\boldsymbol{\mu}_j|)$ is given as the last structure parameter of each site. Furthermore, the structure parameters and ID(I)'s of the last site are followed by angles, φ_{a*}, φ_{b*}, and φ_{c*}, between $\boldsymbol{\mu}_j$ and a^*, b^*, and c^* axes, respectively (see 3.6). You should input initial values of these magnetic-structure parameters, considering that the component of $\boldsymbol{\mu}_j$ perpendicular to the reciprocal-lattice vector, $\boldsymbol{s}_K$ $(= h\boldsymbol{a}^* + k\boldsymbol{b}^* + l\boldsymbol{c}^*)$, *i.e.*, the component parallel to the (hkl) plane contributes to $F(\boldsymbol{h}_K, \text{magn.})$.

In Rietveld analysis of mixtures, a scale factor is assigned to each phase. Let M be the mass of the formula unit (f.u.), s the scale factor, Z the number of the f.u. per unit cell, and V the volume of the CUC. The f.u.(MUC) corresponds to magnetic atoms extracted from f.u.(CUC) [37].

Because the magnetic material is regarded as a mixture of the CUC and MUC phases in a mass ratio of M:M', the relation

$$\frac{M}{M'} = \left(\frac{M}{M'}\right)\left(\frac{sZV}{s'Z'V'}\right) \tag{8.8}$$

is derived from Eq. (7.1). Division of the both sides of Eq. (8.8) by M/M' affords

$$s' = \left(\frac{Z}{Z'}\right)\left(\frac{V}{V'}\right)s. \tag{8.9}$$

In the case of $BiCoO_3$, the f.u.(CUC) is $BiCoO_3$ while the f.u.(MUC) is Co. It therefore follows that $s' = (1/4)(V/4V)s = s/16$. This linear constraint is input in hoge.ins, with the ID(I) of s' set at 2.

After each cycle of nonlinear least-square calculations, $\boldsymbol{G}^{*\prime}$ (lattice parameters of the MUC), the fractional coordinates of all the sites in the MUC, and s' are, respectively, calculated by Eqs. (A.48), (8.6), and (8.9). We, therefore, need not input any constraints relating the lattice parameters and fractional coordinates of the MUC phase to those of the CUC phase. Further, the profile parameters, occupancies, and atomic displacement parameters of the MUC phase are simply set equal to those of the CUC phase.

Make a mental note to set the refinement identifiers, ID(I), of profile and lattice parameters, occupancies, fractional coordinates, and atomic displacement parameters of the MUC phase at zero (dummy) because they are automatically updated after every cycle of least-squares calculations.

Rietveld analysis from neutron powder diffraction data measured on HRPD of JAEA at 5 K gave a μ_j values of $3.24(1)\mu_B$ for Co atoms at (0, 0, 0) and (1/2, 1/2, 0) and $-3.24(1)\mu_B$ for those at (0, 1/2, 0) and (1/2, 0, 0). **Figure 8.5** gives the top part of a reflection list output for $BiCoO_3$ after the Rietveld refinement. Phases No. 1, 2, and 3 are, respectively, $BiCoO_3$ (CUC), Co_3O_4 (impurity), and Co (MUC). Needless to say, $|F(\boldsymbol{h}_K, \text{cryst.})| \neq 0$ and $|F(\boldsymbol{h}_K, \text{magn.})| = 0$ for $BiCoO_3$ (CUC) while $|F(\boldsymbol{h}_K, \text{cryst.})| = 0$ and $|F(\boldsymbol{h}_K, \text{magn.})| \neq 0$ for Co (MUC). In Co (MUC), $1\bar{1}0$ and 110 reflections with $d = 5.26058$ Å are equivalent to each other, and $1\bar{1}\bar{1}$, $1\bar{1}1$, 111, and $11\bar{1}$ reflections with $d = 3.5128$ Å are actually equivalent ones. All of them have a multiplicity, m_K, of 2 because Co (MUC) formally belongs to $P1$ (triclinic) with the lowest space-group symmetry. The $|F(\boldsymbol{h}_K, \text{magn.})|$ values of the equivalent reflections should, therefore, be combined together. It should also be noted that most reflections practically have $|F(\boldsymbol{h}_K, \text{magn.})|$ of zero because their intensities do not contain any contributions of magnetic scattering.

As described above, the feature of analyzing commensurate collinear magnetic structures by the collaboration of RIETAN-FP and VESTA is quite understandable, straightforward, and user-friendly. No constraints need to be imposed on the profile, lattice, and crystal-structure parameters of the MUC phase. Its application to a variety of metal and inorganic materials with collinear magnetic structures is highly desired.

Phase	h	k	l	Code	2-theta	d	Iobs	Ical	|F(nucl)|	|F(magn)|	POF	FWHM	m
3	1	0	0	1	14.077	7.43958	W	0	0.0000	0.0000	1.000	0.3634	2
3	0	1	0	1	14.077	7.43958	W	0	0.0000	0.0000	1.000	0.3634	2
3	1	-1	0	1	19.959	5.26058	25336	23239	0.0000	32.5063	1.000	0.3530	2
3	1	1	0	1	19.959	5.26058	25336	23239	0.0000	32.5063	1.000	0.3530	2
3	0	0	1	1	22.277	4.71910	0	0	0.0000	0.0000	1.000	0.3766	2
1	0	0	1	1	22.277	4.71910	27774	25936	9.5742	-	1.000	0.3766	2
2	1	1	1	1	22.539	4.66489	1393	1334	29.6127	-	1.000	0.3105	8
3	1	0	1	1	26.449	3.98500	0	0	0.0000	0.0000	1.000	0.3724	2
3	0	1	1	1	26.449	3.98500	0	0	0.0000	0.0000	1.000	0.3724	2
3	0	1	-1	1	26.449	3.98500	0	0	0.0000	0.0000	1.000	0.3724	2
3	1	0	-1	1	26.449	3.98500	0	0	0.0000	0.0000	1.000	0.3724	2
1	1	0	0	1	28.373	3.71979	23	32	0.2995	-	1.000	0.3430	4
3	0	2	0	1	28.373	3.71979	0	0	0.0000	0.0000	1.000	0.3430	2
3	2	0	0	1	28.373	3.71979	0	0	0.0000	0.0000	1.000	0.3430	2
3	1	-1	-1	1	30.083	3.51280	2515	3911	0.0000	19.8418	1.000	0.3702	2
3	1	-1	1	1	30.083	3.51280	2515	3911	0.0000	19.8418	1.000	0.3702	2
3	1	1	1	1	30.083	3.51280	2515	3911	0.0000	19.8418	1.000	0.3702	2
3	1	1	-1	1	30.083	3.51280	2515	3911	0.0000	19.8418	1.000	0.3702	2

Figure 8.5: Reflection list of the sample comprising $BiCoO_3$ (CUC), Co_3O_4 (impurity), and Co (MUC) in the large-d region

Chapter 9

STANDARDIZATION OF CRYSTAL DATA

9.1 Rules and Indices Adopted in STRUCTURE TIDY

On the use of RIETAN-FP, it is highly desirable for an axis setting and fractional coordinates to be standardized in compliance with definite rules [172], particularly when refining anisotropic atomic displacement parameters, β_{ij} (see 17.3.16). Even crystal data based on $P2_1/a$ and $P2_1/n$, which are nonstandard settings of a monoclinic space group $P2_1/c$ (No. 14) often adopted in a huge number of papers reporting crystal structures of organic compounds, has to be standardized with $P2_1/c$. For this purpose, STRUCTURE TIDY, which was developed by Gelato and Parthé [169], was incorporated into RIETAN-FP. Crystal data should be standardized in the simulation mode (`NMODE = 1`). Standardization of crystal data is also possible with VESTA [25, 26] under the Utilities menu.

This feature of standardization of crystal-structure data is particularly useful when searching for compounds with similar structures using the Inorganic Crystal Structure Database (ICSD) [146]. Furthermore, STRUCTURE TIDY makes it possible to output the following data in a list of final structure parameters:

1. site multiplicities,
2. Wyckoff letters,
3. first coordinate triplets of all the sites compiled in chap. 6 of ref. [72],
4. types of linear constraints imposed on anisotropic atomic displacement parameters, β_{ij} (derived from the Wyckoff letters using file constr_beta; see Table 17.1).

In STRUCTURE TIDY and LAZY PULVERIX [66], which was also included in RIETAN-FP, the following three standard settings are preferred to other settings:

1. monoclinic system: b-axis unique setting ($\beta \neq 90^\circ$),
2. trigonal system: hexagonal lattice ($a = b \neq c$ and $\gamma = 120^\circ$),
3. centrosymmetric space groups: an inversion center at the origin.

Needless to say, location of the inversion center at the origin leads to the reduced time of calculating structure factors (see 3.5.3).

Let n be the number of atoms in the asymmetric unit, and $(x_j, y_j, z_j;\ j = 1, 2, \cdots, n)$ their fractional coordinates, then the standardization parameter, Γ, is defined as

$$\Gamma = \sum_{j=1}^{n} \left(x_j^2 + y_j^2 + z_j^2 \right)^{\frac{1}{2}}. \tag{9.1}$$

Note that this equation does not contain occupancies, g_j. STRUCTURE TIDY selects a set of x_j, y_j and z_j $(j = 1, 2, \cdots, n)$ minimizing the Γ value. For better distinction between different structure-type branches, STRUCTURE TIDY further outputs another standardization parameter, CG, depending also on lattice parameters:

$$\begin{aligned} \mathrm{CG} = \frac{1}{nV} \Bigg[& \left(a \sum_{j=1}^{n} x_j \right)^2 + \left(b \sum_{j=1}^{n} y_j \right)^2 + \left(c \sum_{j=1}^{n} z_j \right)^2 \\ & + 2ab \cos\gamma \left(\sum_{j=1}^{n} x_j y_j \right) + 2ac \cos\beta \left(\sum_{j=1}^{n} x_j z_j \right) + 2bc \cos\alpha \left(\sum_{j=1}^{n} y_j z_j \right) \Bigg]^{\frac{1}{2}}, \end{aligned} \tag{9.2}$$

where V denotes the unit-cell volume.

The absolute value of each fractional coordinate to be converted by STRUCTURE TIDY should be less than unity; otherwise, the corresponding part of the printer output becomes disordered. If lattice parameters and fractional coordinates of atoms in the asymmetric unit are changed on the transformation of the crystal lattice, corresponding data in hoge.ins must be replaced with them. Such replacement is unnecessary if a standard lattice setting has already been selected.

The following lattice settings are inhibited:

1. c-axis unique settings ($\gamma \neq 90^\circ$) in the monoclinic system,
2. rhombohedral lattices ($a = b = c$ and $\alpha = \beta = \gamma \neq 90^\circ$) in the trigonal system,
3. centrosymmetric space groups in which the center of symmetry is shifted from the origin (0, 0, 0).

Crystal axes compatible with STRUCTURE TIDY are indispensable for Rietveld analysis using RIETAN-FP; otherwise LAZY embeded fails in deriving correct diffraction indices hkl and their multiplicities m_K. For example, suppose that a standard input file, hoge.ins, for Si (space group: $Fd\bar{3}m$) is created on the basis of the first setting where Si in the asymmetric unit occupies the $8a$ site at (0, 0, 0). Subsequent standardization using STRUCTURE TIDY moves Si from (0, 0, 0) to (1/8, 1/8, 1/8) in such a way that a center of symmetry is present at the origin (second setting in "International Tables for Crystallography," Vol. A). When lattice parameters (a and α) and fractional coordinates based on a rhombohedral lattice are input in a trigonal compound, STRUCTURE TIDY converts them into lattice parameters (a and c) and fractional coordinates based on a hexagonal lattice.

Parts of monoclinic space groups (*e.g.*, $C2/m$, $P2/c$, and $P2_1/c$) in "International Tables for Crystallography," Vol. A have multiple cell choices with the center of symmetry at the origin and the unique axis of b. In such cases, standardization of crystal data by STRUCTURE TIDY is highly recommended for safety.

In orthorhombic compounds, the origin may be shifted, and a, b, and c axes may be changed by STRUCTURE TIDY, which leads to the output of multiplicities plus Wyckoff letters, and coordinate triplets different from those for the current structure refinement in the list of final structure parameters in hoge.lst. Just to be safe, standardization of crystal data is always recommended in orthorhombic compounds.

9.2 How to Standardize Crystal Data

We can standardize crystal data easily by setting `NMODE` at 1 and putting '`*`' at the tail of a Hermann–Mauguin space-group symbol recorded in Spgr.daf, for example,

```
P 1 21/c 1*
```

as a second input data for lines concerning each phase. If the last number in each line in Spgr.daf is a non-zero integer, it means the line number of a line that follows the current line; other three or four Hermann–Mauguin symbols are recorded in the line with the line number. In the integrated assistance environments for RIETAN-FP–VENUS (see 16.1.1 and 16.1.2), macros can be used to open Space_groups.xls (**Fig. 9.1**) with the Excel book format by Microsoft Excel or OpenOffice.org (scalc.exe). This file containing all the space-group symbols recorded in Spgr.daf is much easier to browse. In each space group whose last column is '2', the second setting is the standard axis setting (the center of symmetry at the origin).

Never delete spaces in the Hermann–Mauguin symbol, which should be copied and pasted from Spgr.dat or Space_groups.xls onto hoge.ins to avoid careless mistakes. If the names of space groups for two or more phases are attached with '`*`', only crystal data of the first phase are standardized.

In 1992, IUCr changed the Hermann–Mauguin symbols of five orthorhombic space groups belonging to a base-centered lattice oS as follows:

Table 9.1: Symbols of five orthorhombic space groups with glide planes e

Space-group number	39	41	64	67	68
New symbols	$Aem2$	$Aea2$	$Cmce$	$Cmme$	$Ccce$
Old symbols	$Abm2$	$Aba2$	$Cmca$	$Cmma$	$Ccca$

A new symbol is output in the standard output, hoge.lst, of RIETAN-FP as a reminder that the new one containing 'e' should formally be used.

In each of pattern-fitting (Rietveld analysis, Le Bail analysis, hybrid pattern decomposition, MEM-based pattern fitting), space-group symbols and lattice settings derived by STRUCTURE

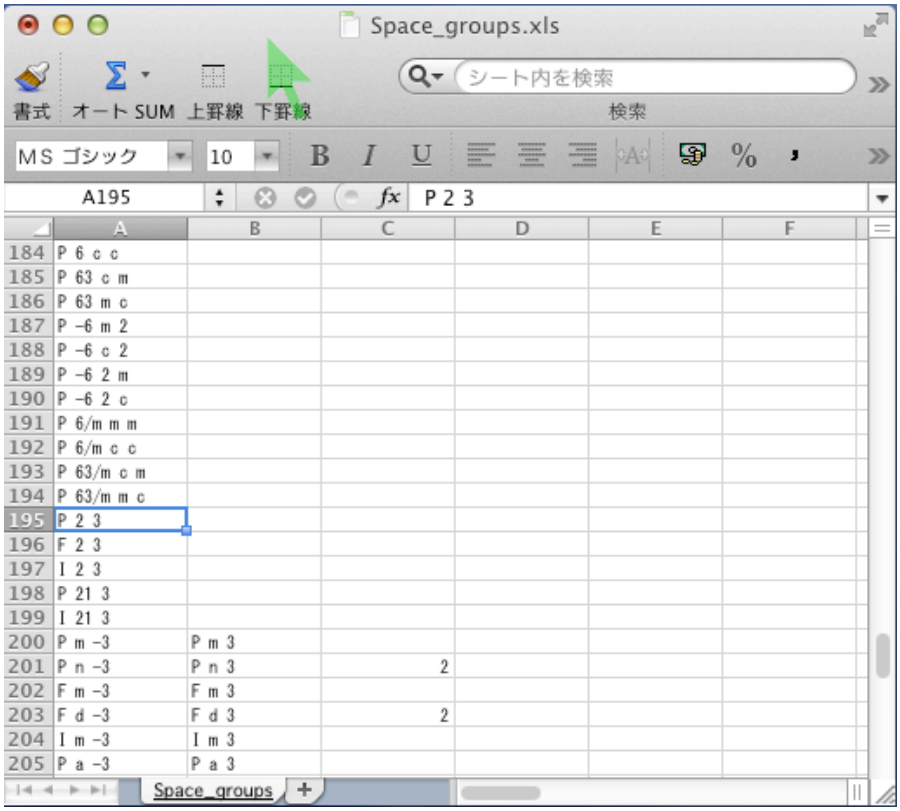

	A	B	C	D	E	F
184	P 6 c c					
185	P 63 c m					
186	P 63 m c					
187	P -6 m 2					
188	P -6 c 2					
189	P -6 2 m					
190	P -6 2 c					
191	P 6/m m m					
192	P 6/m c c					
193	P 63/m c m					
194	P 63/m m c					
195	P 2 3					
196	F 2 3					
197	I 2 3					
198	P 21 3					
199	I 21 3					
200	P m -3	P m 3				
201	P n -3	P n 3	2			
202	F m -3	F m 3				
203	F d -3	F d 3	2			
204	I m -3	I m 3				
205	P a -3	P a 3				

Figure 9.1: Browsing a part of orthorhombic space groups recorded in Space_groups.xls with Microsoft Excel

TIDY must always be input in hoge.ins. Of course, no '*' should be input after the space-group symbol.

A special rule is applied to labels given to crystallographic sites on the standardization of crystal data; its details are described in rule No. 7 in 17.3.14.

9.3 An Example of Standardizing Crystal Data

An example of standardization of crystal data is given below. The structure of a high-T_c superconductor $YBa_2Cu_4O_8$ is usually represented with the c axis perpendicular to the CuO_2 conduction sheet and space group *Ammm* (No. 65) [173]. However, the standard setting described in "International Tables for Crystallography," Vol. A [72] is *Cmmm*; Rietveld analysis with RIETAN-FP has to be carried out on the basis of *Cmmm*. To transform crystal data for *Ammm* into those for *Cmmm* and then standardize fractional coordinates, we need to input a space-group name as

```
HKLM = 'A m m m*': Crystal data based on the Hermann-Mauguin symbol ···
```

and then lattice and structure parameters as given in hoge.ins:

```
CELLQ   3.8402   3.8708   27.2309   90.0   90.0   90.0   0.0   1110000

Y/Y      1.0   0.5   0.5   0.0       0.49   00001
```

```
Ba/Ba   1.0  0.5  0.5  0.13502  0.48  00011
Cu1/Cu  1.0  0.0  0.0  0.21296  0.43  00011
Cu2/Cu  1.0  0.0  0.0  0.06138  0.30  00011
O1/O    1.0  0.0  0.0  0.14562  0.73  00011
O2/O    1.0  0.5  0.0  0.05253  0.55  00011
O3/O    1.0  0.0  0.5  0.05214  0.47  00011
O4/O    1.0  0.0  0.5  0.21822  0.77  00011
```

Running RIETAN-FP, we obtain optimum crystal data based on space group *Ammm* at the tail of hoge.lst:

```
Axes changed to : b,c,a

 Setting x,y,z              origin  0.00000 0.00000 0.00000   gamma =   2.9785

 ( 65) C m m m     - j2 i5 c                                      oS30
 ------------------------------------------------------------------------
 DATA   YBa2Cu4O8                                              2.9785  0.7284
 CELL           3.8708 27.2309  3.8402                                    *
 ATOM    O1         4(j)   0        0.05253  1/2                   O2
 ATOM    Ba         4(j)   0        0.36498  1/2                   Ba
 ATOM    Cu1        4(i)   0        0.06138  0                     Cu2
 ATOM    O2         4(i)   0        0.14562  0                     O1
 ATOM    Cu2        4(i)   0        0.21296  0                     Cu1
 ATOM    O3         4(i)   0        0.28178  0                     O4
 ATOM    O4         4(i)   0        0.44786  0                     O3
 ATOM    Y          2(c)   1/2      0        1/2                   Y
 TRANS  b,c,a
 REMARK Transformed from setting  A m m m.
```

The first line means that STRUCTURE TIDY converted a, b, and c axes in *Ammm* into b, c, and a axes in *Cmmm*, respectively. The value of `2.9785` is the standardization parameter '`gamma`', the last data, `0.7284`, in the '`DATA`' line is CG, and the last data of each site is the site name input in hoge.ins.

Then, we change the space-group symbol in hoge.ins as

```
HKLM = 'C m m m': hkl and m are generated from the Hermann-Mauguin symbol.
```

and proceed to Rietveld analysis after inputting the above standardized lattice and structure parameters. As mentioned in the above comment line, LAZY PULVERIX [66] generates reflection indices, $\boldsymbol{h}_K$, and multiplicities, m_K, from the Hermann–Mauguin symbol using a routine written by Burzlaff and Zimmermann [174].

Chapter 10

LE BAIL ANALYSIS

10.1 Principle of the Le Bail Method

Whole-pattern decomposition, where lattice parameters and $|F_o(\boldsymbol{h}_K)|^2$'s are determined from whole powder diffraction data is becoming more and more important as a main step in *ab initio* structure analysis. The Le Bail method [9] is a representative method of whole-pattern decomposition without the use of a structural model.

Parameters refined in Le Bail analysis are SPPs, peak-shift parameters, lattice parameters, and background parameters. No integrated intensities, $|F(\boldsymbol{h}_K)|^2$, are refined in contrast to another representative method of whole-pattern decomposition: the Pawley method [130]. In Le Bail analysis, we refine the above variable parameters by a method of nonlinear least squares, giving a set of initial integrated intensities, $|F(\boldsymbol{h}_K)|^2$. After each cycle (not after the whole Le Bail analysis) of successive refinement cycles, $|F_o(\boldsymbol{h}_K)|^2$ data are estimated on the basis of current parameters. Thus, the Le Bail method is characterized by two-step refinements in each cycle, as illustrated in **Fig. 10.1**.

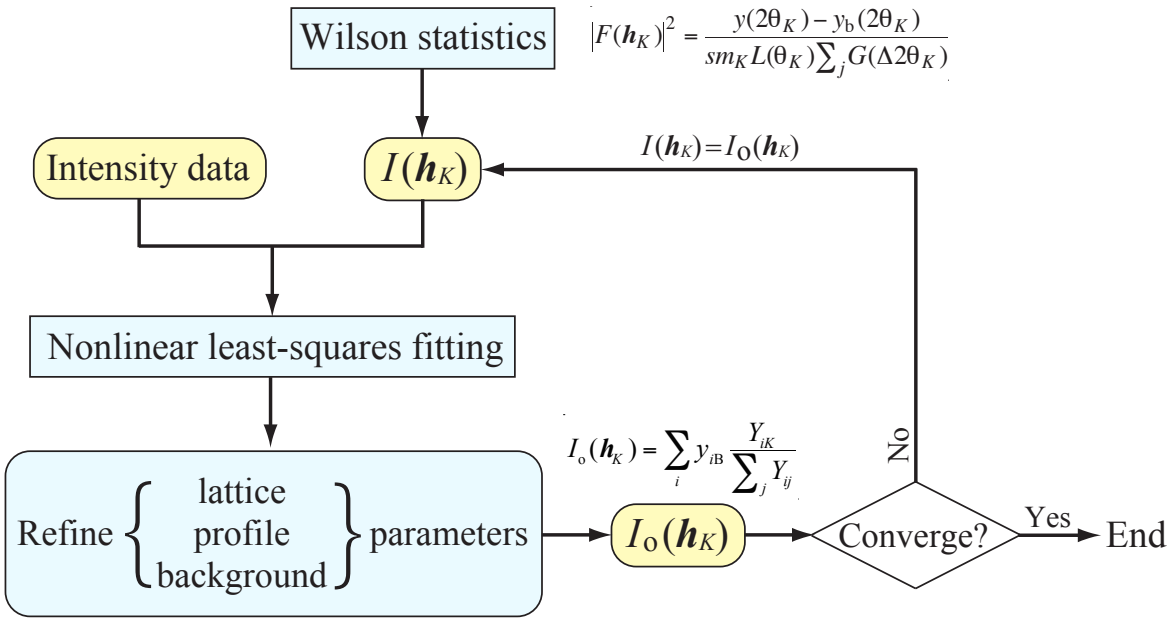

Figure 10.1: Flow chart of Le Bail analysis

RIETAN-FP enables us to carry out Le Bail analysis

1. with initial integrated intensities estimated by Wilson's statistics,
2. with the same initial integrated intensities (= 100),
3. with initial integrated intensities input from a file hoge.ffi
   (a) and varied during least-squares fitting,
   (b) and kept constant during least-squares fitting (in a manner different from Le Bail analysis),
4. into which a partial structure is introduced.

10.2 Initial Values of Integrated Intensities

Strictly speaking, we should state $|F(\boldsymbol{h}_K)|^2$ instead of "integrated intensities." Initial values of $|F(\boldsymbol{h}_K)|^2$ for Le Bail analysis are given in the following three ways.

1. $|F(\boldsymbol{h}_K)|^2$ data for all the reflections are set at a constant value (*e.g.*, 100) [9].
2. $|F(\boldsymbol{h}_K)|^2$ data are estimated by Wilson's statistics [8, 175].
3. $|F(\boldsymbol{h}_K)|^2$ calculated on the basis of a partial structure which has been revealed by *ab initio* structure analysis [175].

In the second option, $|F(\boldsymbol{h}_K)|^2$ is estimated with

$$|F(\boldsymbol{h}_K)|^2 = \frac{y(2\theta_K) - y_\mathrm{b}(2\theta_K)}{sm_K L(\theta_K) \sum_j G(\Delta 2\theta_{Kj})}, \tag{10.1}$$

where $y(2\theta_K)$ is the observed intensity at the peak position of $2\theta_K$, $G(\Delta 2\theta_{Kj})$ is the value of the profile function for reflection K at $2\theta_K$, and the summation is carried out over all the Bragg reflections contributing to $y(2\theta_K)$. Since option 3 cannot be regarded as pure Le Bail analysis, it will be described in 10.5. Then, whole-pattern fitting where $|F(\boldsymbol{h}_K)|^2$ data are fixed and updating of $|F(\boldsymbol{h}_K)|^2$ data are repeated to refine SPPs, lattice and background parameters, which lead to iterative refinements of $|F(\boldsymbol{h}_K)|^2$ for overlapped reflections. In such a case, $|F(\boldsymbol{h}_K)|^2$ necessarily remains near its initial values.

10.3 Successive Two-Step Refinements

Next, we proceed to whole-pattern fitting. As described above, $|F(\boldsymbol{h}_K)|^2$ data are not refined by fixed in least-squares fitting. After each cycle, $I_\mathrm{o}(\boldsymbol{h}_K)$ is calculated with Eq. (4.26) from a set of refined parameters $\boldsymbol{x}$ and converted into $|F_\mathrm{o}(\boldsymbol{h}_K)|^2$ with

$$|F_\mathrm{o}(\boldsymbol{h}_K)|^2 = \frac{I_\mathrm{o}(\boldsymbol{h}_K)}{sm_K L(\theta_K)} \tag{10.2}$$

which is derived by substituting 1 for P_K in Eq. (4.24). The resulting $|F_o(\boldsymbol{h}_K)|^2$ data are used as $|F(\boldsymbol{h}_K)|^2$ in the next cycle.

In the case of an isolated reflection, accurate $|F_o(\boldsymbol{h}_K)|^2$ is, of course, obtainable if $y_b(2\theta_i)$'s in the profile range of reflection K are accurate enough. On the other hand, overlapped reflections where peak positions are fairly separated from each other, $|F_o(\boldsymbol{h}_K)|^2$ data approach from initial values to true ones gradually. As in the Pawley method [130], the accuracy of $|F_o(\boldsymbol{h}_K)|^2$ is lowered with increasing degree of overlapping of reflections.

Since $|F(\boldsymbol{h}_K)|^2$ data are not refined in the Le Bail method, the size of arrays contained in the normal equation is generally small. Equation (4.26) is included in every modern Rietveld analysis program because it is a numerical-integration equation proposed by Rietveld for calculating two reliability indices, R_B and R_F, after Rietveld analysis. Hence, it is very easy to implement Le Bail analysis in a Rietveld analysis program; the Le Bail method has gone mainstream as a method of whole-pattern decomposition.

$|F(\boldsymbol{h}_K)|^2$ depends on s because Eqs. (10.1) and (10.2) contain s, Though refining s seems to be meaningless in the absence of a structural model, s may be refined or fixed, with a result that $|F(\boldsymbol{h}_K)|^2$ data obtained by Le Bail analysis practically contains s. On the construction of a possible structural model by direct or Patterson (heavy-atom) methods after Le Bail analysis, the absolute measure of $|F(\boldsymbol{h}_K)|^2$ must be at first determined by Wilson's statistics [176], which is also the case with the determination of $I(\boldsymbol{h}_K)$ and $|F(\boldsymbol{h}_K)|^2$ by the Pawley method.

10.4 Characteristics of the Le Bail Method

The Le Bail method by which $|F(\boldsymbol{h}_K)|^2$'s are not refined by a least-squares method has the following advantages over the Pawley method [130]:

1. Its algorithm is relatively simple.
2. Because sizes of matrices in the normal equation, Eq. (4.1), are much smaller than those in Pawley's one [177] owing to the absence of refinable observed integrated intensities, least-squares calculations are fairly rapid.
3. No negative values of $I(\boldsymbol{h}_K)$ result from Le Bail analysis.

However, initial lattice parameters for Le Bail's method should be known with a greater precision than in Pawley's method. Another disadvantage of the Le Bail method is that $|F(\boldsymbol{h}_K)|^2$ for overlapped reflections tend to converge near their initial values in the same way as with the Pawley method. In other words, $|F(\boldsymbol{h}_K)|^2$ data of overlapped reflections strongly depend on initial $|F(\boldsymbol{h}_K)|^2$'s. It is these initial values that hold the key to getting accurate $|F(\boldsymbol{h}_K)|^2$ data by the Le Bail method.

10.5 Le Bail Analysis Introducing a Partial Structure

In Le Bail analysis where $I(\boldsymbol{h}_K)$'s are not refined by a method of least squares, we need not impose constraints of equi-partition on a group of heavily overlapped reflections. A high degree

of superposition necessarily leads to equi-partition (or close enough to it) of observed Bragg intensities.

We can improve initial $|F(\boldsymbol{h}_K)|^2$'s by introducing a partial structure into Le Bail analysis. If parts of atom positions can be obtained by direct or heavy-atom methods, $|F(\boldsymbol{h}_K)|^2$'s calculated from them are improved in comparison with those determined in the three different ways described in 10.2. Then, the accuracy of $|F(\boldsymbol{h}_K)|^2$'s resulting from Le Bail analysis will be raised, which may increase the possibility to reach the real structure. For example, when analyzing X-ray powder-diffraction data of a compound containing both heavy and light elements, the initial values of $|F(\boldsymbol{h}_K)|^2$ approach the true ones considerably after the positions of the heavy atoms have been known at any rate. Consequently, the accuracy of $|F(\boldsymbol{h}_K)|^2$'s obtained by the Le Bail method is effectively improved.

Note that the scale factor s, which may be considerably changed by introducing a partial structure, has to be appropriately adjusted to achieve the convergence of Le Bail analysis, if necessary.

10.6 How to Use the Le Bail Method with RIETAN-FP

On the execution of conventional Le Bail analysis (`NMODE = 4`), conventional Le Bail refinement is applicable only to the first phase whereas conventional Rietveld refinement is applied to the other phases, if any. This means that no structure parameters should be input for the first phase when `NMODE = 4`.

In Le Bail refinement into which a partial structure is introduced (`NMODE = 5`), structure parameters should be given for all the phases because initial integrated intensities are calculated from these structure parameters. Refinement identifiers, ID(I), for the first phase should be fixed at zero.

A file named hoge.ffo is always created after Le Bail refinement. Only reflections for which normal values of $|F(\boldsymbol{h}_K)|^2$, *i.e.*, `Iobs` described in 17.8.10, have been obtained are output to hoge.ffo. If hoge.ffo is renamed hoge.ffi, integrated intensities are input from that file when `NSFF = 1`. Both hoge.ffo and hoge.ffi are compatible with hoge.hkl for SIRPOW [178] for resolving the phase problem by the direct method.

It is highly recommend that in the first Le Bail refinement, initial integrated intensities are estimated by means of Wilson's statistics (`NSFF = 0`). In subsequent Le Bail analyses, integrated intensities are usually input from hoge.ffo by setting `NSFF` at `1`.

Be sure that 2θ ranges in which profile functions are calculated should be narrow enough during an initial stage to estimate background intensities appropriately. For this purpose, a coefficient named CHGPC is input in hoge.ins.

The top part of hoge.ffo output after Le Bail analysis of $BaSO_4$ from X-ray powder-diffraction data taken with Cu $K\alpha_1$ radiation is given below (some spaces between data were removed, for convenience):

h	k	l	FWHM	|F|^2	d	2-theta	I	I/I1	Io
1	0	1	0.0723	5.32920	5.5694	15.900	0.244691	2.5	0.239582
2	0	0	0.0738	110.467	4.4378	19.992	1.58814	15.9	1.58012

```
0   1   1        0.0740    94.5744          4.3362          20.465          2.59164          25.8    2.57909
1   1   1        0.0750    101.516          3.8961          22.806          4.44986          43.6    4.41452
2   0   1        0.0753    54.2373          3.7710          23.574          1.10999          10.8    1.11123
0   0   2        0.0759    347.148          3.5765          24.876          3.17701          30.7    3.16799
2   1   0        0.0764    588.136          3.4418          25.865          9.92449          95.0    9.97043
1   0   2        0.0768    510.676          3.3173          26.854          7.96783          75.7    7.97827
2   1   1        0.0778    395.207          3.1014          28.762          10.6791          100.0   10.5879
1   1   2        0.0792    257.478          2.8340          31.544          5.72508          52.4    5.66617
.....
```

In hoge.ffo, hkl, H_K, $|F_o(\boldsymbol{h}_K)|^2$, d, $2\theta_K$, $I(\boldsymbol{h}_K)$, the relative peak intensity (`I/I1`; `I1`: the peak intensity of the strongest reflection), and $I_o(\boldsymbol{h}_K)$ are recorded in a form which can be input by RIETAN-FP and EXPO [22]. EXPO inputs only hkl, H_K, and $|F_o(\boldsymbol{h}_K)|^2$; the remaining data are dummy ones, in this case.

Fits in parts of 2θ regions often remain worse because of negligibly small shifts in integrated intensities of partial reflections at the final stage of Le Bail analysis. In such cases, the use of hybrid patter decomposition (see Chap. 11), where only integrated intensities are refined after Le Bail analysis, is highly recommended.

10.7 Feedback of Results Obtained by the Maximum-Entropy Patterson Method

ALBA [20, 21] (see 14.7.1) outputs a text file, hoge.ffi, storing $|F(\boldsymbol{h}_K)|^2$ determined by the maximum-entropy Patterson method [21], where Patterson functions are dealt with by the maximum-entropy method to improve $|F(\boldsymbol{h}_K)|^2$ data of overlapped reflections in comparison with those obtained by conventional pattern-decomposition techniques such as the Le Bail method [9] and the Pawley method [130]. Then, we can get much better $|F(\boldsymbol{h}_K)|^2$ data, starting from those in hoge.ffi output by ALBA. The MEP method will be further described in 11.7.

Figure 10.2 shows a flow chart of *ab initio* structure analysis by the combined use of EXPO–RIETAN-FP–VENUS. Though automatic Le Bail analysis with EXPO [175] is very convenient and practical, the fit between observed and calculated patterns is not the greatest. Therefore, reanalysis with RIETAN-FP using $|F_o(\boldsymbol{h}_K)|^2$ estimated by EXPO as initial values is highly recommended. On the use of ALBA, we must always reanalyze because $\sigma\left(|F_o(\boldsymbol{h}_K)|\right)$' are indispensable for the maximum-entropy Patterson method; As shown in p. 89, the output file, hoge.ffo, of RIETAN-FP contains $I_o(\boldsymbol{h}_K)$ from which ALBA can calculate $\sigma\left(|F_o(\boldsymbol{h}_K)|\right)$ with Eq. (14.18).

Improvements of $|F(\boldsymbol{h}_K)|^2$ by ALBA will significantly help us to derive an approximate structural model by EXPO. Le Bail analysis introducing a partial structure may further improve $|F_o(\boldsymbol{h}_K)|^2$'s; a utility program called res2ins (see 17.3.18) is convenient when introducing the structural model into hoge.ins. Once a structural model has been obtained, the subsequent Rietveld analysis, MEM/Rietveld analyses, and 3D visualization of electron densities will proceed smoothly by combination of RIETAN-FP, Dysnomia [17, 23], and VESTA [25, 26]. As described in 14.6, the MEM/Rietveld method is very effective for modification of a structural model.

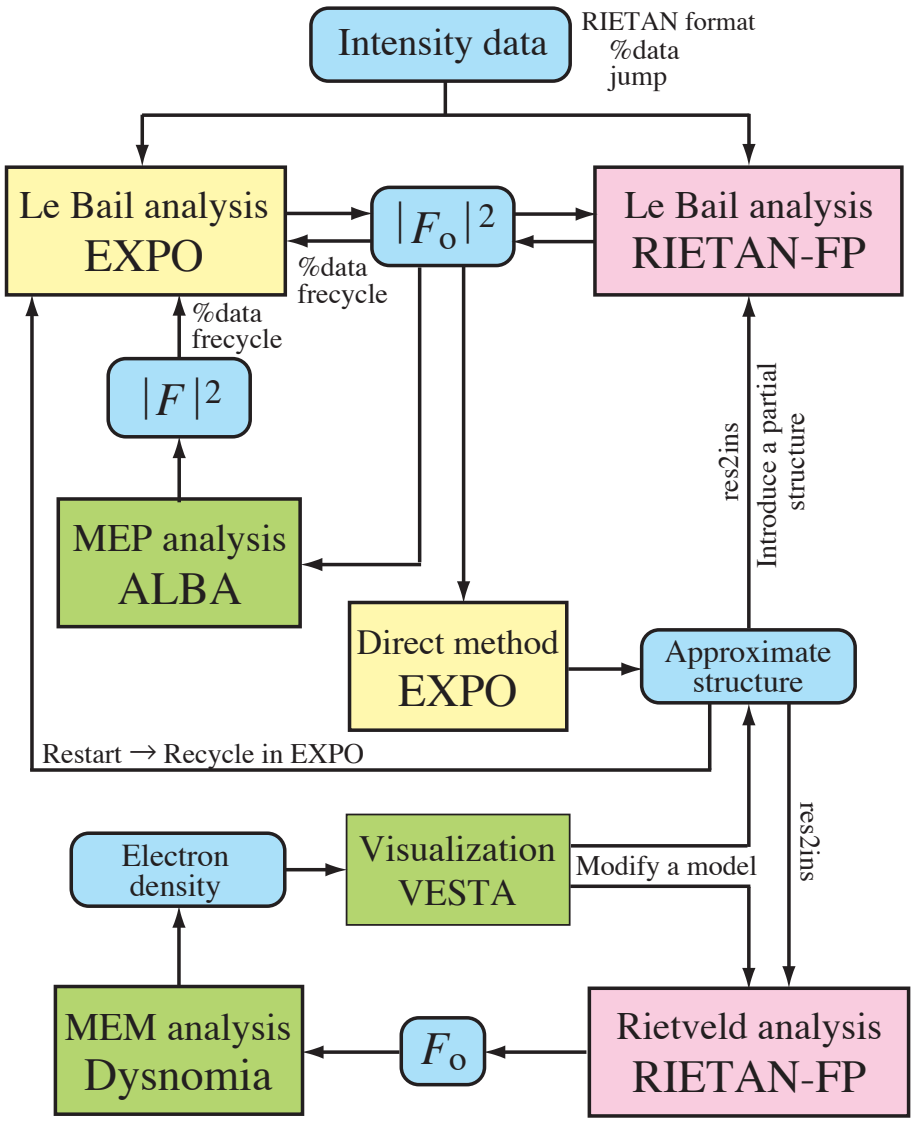

Figure 10.2: Flow chart of *ab initio* structure analysis by combination of EXPO–RIETAN-FP–ALBA–Dysnomia–VESTA

Chapter 11

HYBRID PATTERN DECOMPOSITION

11.1 Four-Step Estimation of Integrated Intensities

Unfortunately, the routine implemented in RIETAN-FP for Le Bail analysis (see Chap. 10) has not been widely utilized as yet because of issues with convergence performance and convenience. In Le Bail analysis using RIETAN-FP, 2θ ranges of calculating diffraction profiles have to be expanded step by step to minimize the influence of neighboring reflections on the resulting integrated intensities. Furthermore, once observed structure factors fall in inappropriate values, they tend to remain there, which leads to worse local fits between observed and calculated patterns.

Then, a new feature called hybrid pattern decomposition was added to RIETAN-FP in an effort to achieve performance higher than that in existing programs. This original technique can be applied to powder diffraction data measured with monochromatic beams (synchrotron X rays, $K\alpha_1$ and Cu $K\beta$ characteristic X rays, constant-wavelength neutrons) and Cu $K\alpha$ characteristic X rays ($K\alpha_1$ + $K\alpha_1$).

Procedures for hybrid pattern decomposition consist of the following four steps:

1. creation of a background file, hoge.bkg,
2. Le Bail analysis,
3. individual profile fitting where only integrated intensities, $|F(\boldsymbol{h}_K)|^2$, are refined by the conjugate direction method [118],
4. Le Bail analysis where parameters with `ID(I) = 1` are simultaneously refined by the modified Marquardt method [113].

Step 3 will hereafter be referred to as "refinement of integrated intensities," for simplicity. In hybrid pattern decomposition, the first Le Bail analysis (Step 2) and the refinement of integrated intensities (Step 3) play complementary roles with each other, giving the best fit finally. The second Le Bail analysis (Step 4) gives standard uncertainties of refinable parameters, decreasing R_{wp} a little. Only one cycle of the least-squares refinement is executed because experience shows that $S(\boldsymbol{x})$ usually increases in the second cycle.

In what follows, techniques to converge pattern decomposition stably and steadily will be described with an illustration of dealing with a set of files, hoge.* (hoge.ins, hoge.int, hoge.bkg, *etc.*). Finally, section 11.7 deals with an additional method of analyzing integrated intensities resulting from hybrid pattern decomposition by the maximum-entropy Patterson method with ALBA to overcome the tendency of the Le Bail method toward equi-partition for overlapped reflections.

11.2 Preparation of a Background File hoge.bkg

Initial background intensities need to be accurate enough to converge Le Bail analysis stably. If the initial background level is fairly different from the true one, errors in integrated intensities in an early stage of Le Bail analysis necessarily increase, which hinders stable convergence. In hybrid pattern decomposition, background intensities are, at first, roughly estimated by a simple method proposed by Sonneveld and Visser [106].

In their method, about 5 % of the data (every twentieth point) need to be picked up for the background determination. The resulting n sample points can be considered to be a first approximation of the background. This approximation is far from perfect because some samples are taken from places where Bragg reflections are observed. The approximation is, therefore, improved according to the following iterative procedure:

1. Pick up sample points, p_i (i = 1, 2, 3, ... $n-1$).
2. Calculate $m_i = (p_{i+1} + p_{i-1})/2$.
3. If $p_i > m_i + c$, P_i is replaced by m_i.
4. Return to step 1.

The parameter c depends on the curvature of the background. In the case of powder diffraction data from photographs with an intensity scale from 0 to 255, c was found to be approximately equal to 0.02 [106]. In this way, every point of the background curve is replaced by the mean of its neighbors if the latter has a lower value. Repeating the whole procedure about 30 times affords shifts small enough for the procedure to be stopped.

Background intensities are either fixed at the values resulting from the above procedure or represented with the composite background function, Eq. (3.107), which improves goodness-of-fit most surely.

NRANGE (see 3.12) is set at 2 (fixed at values recorded in hoge.bkg) or 3 (the product of values given in hoge.bkg and the Legendre polynomial). RIETAN-FP inputs hoge.bkg if it exists; for example, hoge.bkg may be created using PowderX [104,105]. On the other hand, RIETAN-FP creates hoge.bkg with the Igor text format (see 17.5.2) only in the absence of hoge.bkg. To create hoge.bkg, confirm the absence of hoge.bkg and then input the following three parameters in hoge.ins:

1. `NPICKUP`: Intensity data are taken out in every NPICKUP-th points for background estimation.

2. `NREPEAT`: A repeating number for background determination.

3. `CURVATURE`: A constant to take into account the curvature of the background.

The parameter c related to the curvature of the background is set at (the largest diffraction intensity)$\times$`CURVATURE`. In the case of powder diffraction data measured with photographs, c was approximately equal to 0.02 on the intensity scale from 0 to 255 [106], which corresponds to a `CURVATURE` value of `7.843E-5`. An appropriate value of `CURVATURE` can be determined through a trial and error process. On the use of the Bragg–Brentano geometry where the background are relatively flat, `CURVATURE` may be set at zero.

Igor Pro[1] can input the resulting file, hoge.bkg, by selecting

`Load Waves ▸ Load Igor Text...`

under the `Data` > menu. Then, observed and background intensities are automatically plotted against 2θ to check whether the background curve is appropriate.

11.3 Input Data Related to Le Bail Analysis

Background parameters should be input in the following way:

```
BKGD  1  0  0  0  0  0  0  0  0  0  0  0  111111111111
```

which makes initial background intensities practically the same as those in hoge.bkg to enhance the accuracy of initial integrated intensities estimated by means of Wilson's statistics [8, 175]. The number of refinable background parameters may be appropriately decreased, depending on the complexity of the background.

The scale factor may be refined or fixed while no preferred orientation is corrected:

```
PREF  1.0  1.0  0.0  0.0  0.0  0.0  000000
```

Structure parameters and linear constraints imposed on them with `ID(I) = 2` are commented out or deleted.

Further, various flags are set as follows:

```
 NMODE = 4: Conventional Le Bail analysis.
  NINT = 1: General (X-Y) format.
NRANGE = 3: Background = (background in hoge.bkg) * (Legendre polynomials).
  NSFF = 0: Estimated according to the Wilson statistics.
 NLESQ = 0: Marquardt method (recommended in most cases).
 NAUTO = 2: Refine incrementally (automatic; recommended in most cases).
    NC = 0: No nonlinear restraints are imposed on geometric parameters.
  LSER = 0: Input site names for restrained bond lengths/angles.
LQUART = 0: Input no quartets of atoms related to restrained torsion angles.
```

`NRANGE = 3` corresponds to the specification of the composite background function, *i.e.*, Eq. (3.107).

[1] http://www.wavemetrics.com/

11.4 Input Date Related to the Refinement of Integrated Intensities

In the local refinement of integrated intensities, profile, lattice, and background parameters are fixed at those refined in the preceding Le Bail analysis, integrated intensities determined by the Le Bail analysis are used as initial ones, and integrated intensities that minimize the weighted error sum of squares in limited ranges of intensity data are successively obtained by the conjugate direction method [118] (see 4.1.3). In the case of integrated intensities estimated by the Le Bail method, fits in 2θ regions where serial correlations are considerably improved. The weighted error sum of squares is minimized by the conjugate-direction method because programming is relatively easy and the solution is hardly trapped in local minima.

The whole powder diffraction pattern is automatically divided into many parts on the basis of 2θ ranges to calculate diffraction profiles (profile cutoff) and numbers of reflections that appear in each 2θ region. Because individual profile fitting by the conjugate-direction method generally becomes slower with increasing number of reflections in each 2θ region, each region contains up to a dozen or a little more reflections. Repetition of local pattern fitting is required because of the following two reasons:

- Contributions of integrated intensities of reflections to the weighted error sum of squares should be large enough.
- In the conjugate-direction method, convergence is slowed down with increasing number of variable parameters (integrated intensities in the present case).

Data associated with the refinement of integrated intensities are input in the following part of hoge.ins:

```
NOPT = 0! No |F|^2's are refined after Le Bail analysis.
NOPT = 1: |F|^2's are refined after Le Bail analysis.

If NOPT = 1 then
   MREG = 10: Maximum number of reflections in each group of overlapped reflections.
   RWID = 0.350: |F|^2's of reflections with Delta.2-theta < RWID*FWHM are set equal.
   XMAX = 135.0: |F|^2's are refined up to XMAX/degrees.
   WNEG = 1.0E11: Weight to suppress negative |F|^2's.
end if
```

If `NOPT = 1`, conventional Le Bail analysis is followed by the refinement of integrated intensities.

`MREG` is an integer to limit the number of reflections in each group of overlapped reflections. The actual number of reflections is greater than or equal to `MREG` because it is recalculated from profile cutoffs after dividing the whole 2θ pattern into many parts. If the difference, $\Delta 2\theta$, in the peak positions of two reflections is less than `RWID`×FWHM, their integrated intensities can hardly be refined independently owing to extremely high correlations among them. Their integrated intensities are, therefore, regarded as being equal to each other, which is referred to as "equipartition."

`XMAX` is $2\theta_{\max}$ in the 2θ region where integrated intensities are refined in hybrid pattern decomposition. Small-d reflections are not very useful in *ab initio* structure analysis by a real-space method because of the heavy overlap of reflections and decreases in diffraction intensities in the high-Q region. A relatively low $2\theta_{\max}$ is, therefore, sufficient in the real-space method. On the other hand, the direct method [22] and the charge-flipping method [179] require a resolution of at least $d = 1.1$ Å.

Parts of integrated intensities refined by the conjugate-direction method often converge at physically meaningless negative values. In RIETAN-FP, the appearance of negative integrated intensities is avoided by a penalty-function method. Let $\boldsymbol{x}$ (x_1, x_2, ... x_j, ...) be a set of integrated intensities of grouped reflections, w_{neg} (= `WNEG`) the weight for the penalty imposed on negative integrated intensities, then the weighted error sum of squares, $S(\boldsymbol{x})$, in each 2θ region is formulated as

$$S(\boldsymbol{x}) = \sum_i w_i \left[y_i - f_i(\boldsymbol{x})\right]^2 + w_{\text{neg}} \sum_j \left[\min\left(0, x_j\right)\right]^2. \tag{11.1}$$

It is $|F|^2$'s of reflections included in the present 2θ region that are refined by the conjugate-direction method. If a sufficiently large value of `WNEG` is input to increase the second term in the right-hand side of Eq. (11.1), *i.e.*, the penalty function, reflections with $x_j < 0$ disappear in this region.

Setting `NRINT` at `1` helps to determine an appropriate value of `WNEG`. In the following example of a group containing reflections No. 66–76, refined integrated intensities, `|F1|**2`, for reflections No. 74–76 were made positive by setting `WNEG` at `1.0E30`. Equal signs, '`=`', before `|F1|**2` mean that the integrated intensities are constrained to be equal to those which are not preceded by '`=`'.

```
  No.   h   k   l   2-theta        d      FWHM    |F0|**2          |F1|**2
.....
-------------------------------------------------------------------------
   66   8   8   0    22.248    2.2028   0.0622    4372.58          4404.86
   67   3  11   1    22.511    2.1775   0.0626    186.187          187.661
   68  11   3   1    22.511    2.1775   0.0626    186.187        =  187.661
   69   9   5   5    22.511    2.1775   0.0626    186.187        =  187.661
   70   7   9   1    22.511    2.1775   0.0626    186.187        =  187.661
   71   9   7   1    22.511    2.1775   0.0626    186.187        =  187.661
   72   8   8   2    22.598    2.1692   0.0627    286.435          285.951
   73  10   4   4    22.598    2.1692   0.0627    286.435        =  285.951
   74   8   6   6    22.942    2.1371   0.0633    0.00000          3.157724E-10
   75   6  10   0    22.942    2.1371   0.0633    0.00000        = 3.157724E-10
   76  10   6   0    22.942    2.1371   0.0633    0.00000        = 3.157724E-10
-------------------------------------------------------------------------
```

11.5 Execution of Hybrid Pattern Decomposition

Editing hoge.ins as described above is followed by hybrid pattern decomposition. Partial profile relaxation (see 4.4) may be applied to (nearly) isolated reflection, if necessary. Reliability indices are output after both of the two Le Bail analyses.

The preliminary hybrid pattern decomposition is usually followed by analyses where PC or CHGPC are changed a little to check changes in the reliability indices. After minimization of $R_{\rm wp}$, change NUPDT in the following way to update variable parameters:

```
NUPDT = 1: Variable parameters (ID = 1, 2) are updated in the packing mode.
```

Then, CHGPC should be restored to 1.0.

Reliability indices may be somewhat improved by setting NSFF at 1, changing hoge.ffo into hoge.ffi, and repeating Le Bail analysis and refinement of integrated intensities once more. However, reliability indices sometimes increase apparently because the refinement of profile parameters *etc.* and repartition of integrated intensities are simultaneously executed during the course of Le Bail analysis.

An elaborate technique to improve fits comprises the following steps. At first, profile, peak-shift, lattice, and (if possible) background parameters are refined with flag settings of NSFF = 1, NCONST = 1, NOPT = 0, and NLESQ = 2 with any value of MITER. Then, only integrated intensities are refined with flag settings of NCONST = 0, NOPT = 1, NLESQ = 0, and NCYCL = 1. The previous file, hoge.ffi, is deleted, and hoge.ffo is renamed hoge.ffi, and the above procedure is repeated, which makes it possible to improve fits to the limit. If convergence has been attained to some extent, pattern decomposition where profile parameters and integrated intensities are optimized may increase reliability indices. In general, executing

1. the refinement of various parameters while fixing integrated intensities
2. the refinement of integrated intensities

after the first hybrid pattern decomposition will lead to stable convergence.

Because the shape of the background is relatively simple in the case of flat-plate samples, the refinement of background parameters with no use of hoge.bkg (NRANGE = 0) may give better results than the use of hoge.bkg (NRANGE = 0 or 3). Fixing integrated intensities with NCONST = 1 may be useful in such a process.

In general, hybrid pattern decomposition, which affords better reliability indices than conventional Le Bail analysis, is quite helpful in constructing structural models by the direct method with EXPO [22] and charge flipping [180–182] with superflip[2] [179].

File hoge.ffo output after hybrid pattern decomposition is compatible with instruction REF2 (DATA routine) in EXPO [22] and can be dealt with EXPO directly. If NEXP is set at 1, RIETAN-FP creates an input file for EXPO, hoge.exp, where the name of hoge.ffo is recorded after REF2 in the %data block, *e.g.*,

```
%data
  pattern Fapatite.int
  > Change the following line if necessary:
  filetype xy
  cell   9.36906   9.36906   6.88389  90.00000  90.00000 120.00000
```

[2] http://superflip.fzu.cz/

```
content Ca 10 P 6 O 24 F 2
spacegroup P 63/m
wavelength 1.540593
> Change the extension of the following file if necessary:
>ref2 Fapatite.ffo
```

If necessary, hoge.exp is appropriately modified by a text editor such as Hidemaru Editor and Jedit X to be input by EXPO, which will derive possible candidates of structural models from data recorded in hove.exp. On use of $|F|^2$ data obtained with RIETAN-FP, '`>ref2 BaSO4.ffo`' must be uncommented out by deleting '`>`' , and other lines related to Le Bail analysis should be commented by attaching '`>`' as the first character. Further, beware lest an intensity data file, hoge.int, has a format incompatible with EXPO.

With RIETAN-FP, a template file, hoge.inflip, for charge flipping with superflip [179] can also be created by setting `NCF` at 1 in hoge.ins. File hoge.inflip virtually includes the whole content of hoge.ffo, *i.e.*, diffraction indices hkl, FWHMs, and integrated intensities, $|F|^2$, in a block sandwiched between `fbegin` and `endf`, *e.g.*, in the case of hybrid pattern decomposition from X-ray powder diffraction data of $BaSO_4$ as follows:

```
#----------------
# Reflection list
#----------------

dataformat fwhm intensity
#fwhmseparation 0.2
lambda  1.54059

fbegin
#  h   k   l           FWHM         |Fc|^2
   1   0   1      0.0706548      4.0496001
   2   0   0      0.0728465    108.4026184
   0   1   1      0.0731047     98.2846603
   1   1   1      0.0743952    101.5643692
   2   0   1      0.0748233     59.0495415
   0   0   2      0.0755561    365.9663391

   .....

  10   2   0      0.2207206      7.5805116
endf
```

Note that the scale factor in hoge.ins must be adjusted in such a way that $|F|^2$ values recorded in hoge.inflip have sufficient numbers of significant figures.

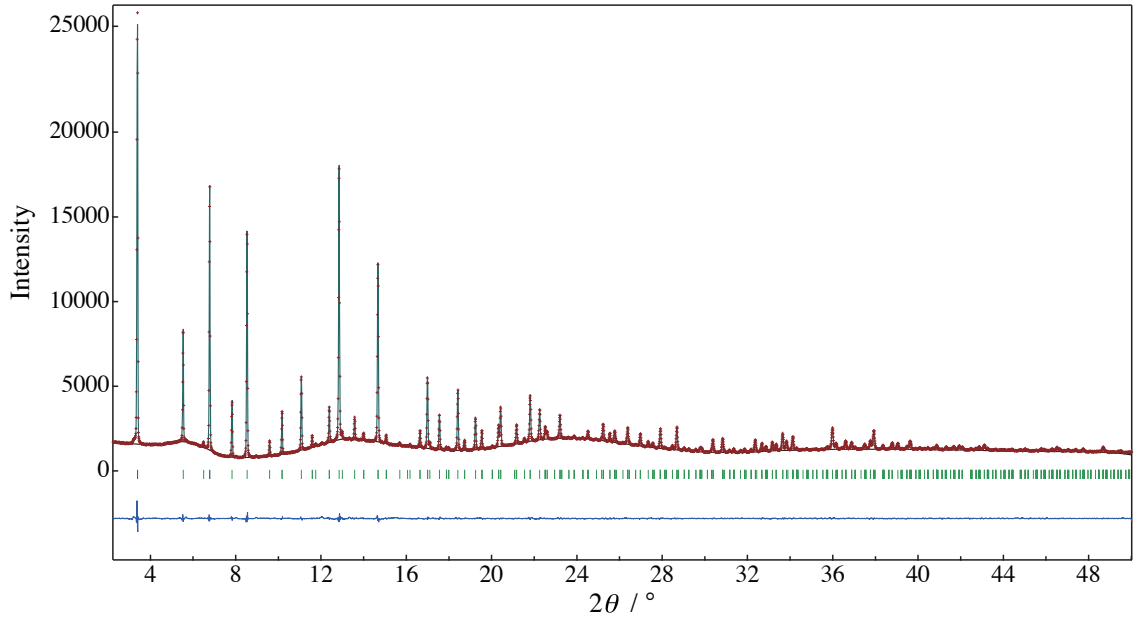

Figure 11.1: Observed, calculated, and difference patterns obtained by hybrid pattern decomposition from synchrotron X-ray powder diffraction data ($\lambda = 0.85$ Å) of zeolite Na-FAU containing CuI

11.6 Examples of Hybrid Pattern Decomposition

In the case of X-ray diffraction data of barium sulfate (in folder BaSO4_LB included in the distribution file), reliability indices resulting from Le Bail analysis with `NSFF = 0` were $R_{wp} = 10.56\,\%$ ($R_e = 10.28\,\%$), $R_p = 7.29\,\%$, and $R_B = 0.51\,\%$. The subsequent refinement of integrated intensities significantly lowered R_{wp} to 8.12 % and R_p to 5.40 % at the expense of R_B, which was slightly increased to 0.70 %.

Figure 11.1 shows the result of hybrid pattern decomposition for zeolite Na-FAU doped with CuI from synchrotron X-ray powder diffraction data measured with the Debye–Scherrer geometry on a powder diffractometer at BL15XU of SPring-8.[3] Parameters related to a background determination according to the procedure of Sonneveld and Visser [106] were `NPICKUP = 20`, `NREPEAT = 30`, and `CURVATURE = 1.0E-05`, and those for refining integrated intensities after Le Bail analysis were `MREG = 6`, `RWID = 0.05`, `XMAX = 99.0`, and `WNEG = 1.0E+30`. The rolling background arising from diffuse scattering caused by the dopant and a glass tube of capillary to contain the sample was successfully represented by the composite background function (`NRANGE = 3`). As Fig. 11.1 shows, an excellent fit could be achieved by hybrid pattern decomposition to give sufficiently small reliability indices: $R_{wp} = 1.53\,\%$ ($R_e = 2.52\,\%$), $R_p = 1.14\,\%$, and $R_B = 1.72\,\%$.

[3]Presented by Dr. Takuji Ikeda (AIST), who cooperated to the greatest extent possible in the development of the routine for hybrid pattern decomposition.

11.7 The Maximum-Entropy Patterson Method

By setting flag `MEP` at 1 in hoge.ins, $|F(\boldsymbol{h}_K)|^2$ data obtained by hybrid pattern decomposition can be further analyzed by the maximum-entropy Patterson (MEP) method [19] with ALBA [20] in the VENUS system. The MEP method aims at determining those voxel data of Patterson functions, $P(x, y, z)$, in the unit cell with a volume of V which gives the maximum information entropy S:

$$P(x,y,z) = \frac{1}{V} \sum_{h=\frac{-N_x}{2}}^{\frac{N_x}{2}} \sum_{k=\frac{-N_y}{2}}^{\frac{N_y}{2}} \sum_{l=\frac{-N_z}{2}}^{\frac{N_z}{2}} |F_{\rm o}(\boldsymbol{h})|^2 \exp[-2\pi {\rm i}(hx+ky+lz)], \tag{11.2}$$

where N_x, N_y, and N_z are voxel numbers along the a, b, and c axes, respectively. Because $|F_{\rm o}(\boldsymbol{h})|^2$ is always non-negative real, MEP analysis requires no phase angle, *i.e.*, ψ in Eq. (14.19). The MEP method is, therefore, suitable for the derivation of possible models for unknown structures.

The sophisticated methodology of MEP analysis enables us to improve integrated intensities of heavily-overlapped reflections, which may give better results when analyzing $|F(\boldsymbol{h}_K)|^2$ by the direct-space and charge-flipping (dual-space) methods. The verification of the performance of MEP analysis in *ab initio* structure analysis is highly desired.

An elaborate script, *i.e.*, a batch file RIETAN.bat (Windows) or a shell script named RIETAN.command (macOS), to run RIETAN-FP pretends as if MEP analysis were continuously executed after hybrid pattern decomposition only by RIETAN-FP. UNIX-compatible utilities such as grep, sed, tail, cut, and bc[4] are utilized for this purpose; for example, in the case of rietan.command:

```
#!/bin/bash
# Execute RIETAN-FP for macOS

function elapsed_time {
   # Compare two times before and after execution of a program in seconds
   if [ $(echo "$after > $before" | bc) -eq 1 ]; then
      # The calculation has finished on the same day.
      # Insert "0" before "." if it is absent.
      echo "           Elapsed time = $(echo "scale=8; $after - $before" | bc) s" | \
      sed "s/  Elapsed time = \./  Elapsed time = 0./" >> temp.txt
   else
      # The calculation has finished on the next day.
      echo "           Elapsed time: $(echo "scale=8; 86400.000 - $before + $after" | bc) s" | \
      sed "s/  Elapsed time = \./  Elapsed time = 0./">> temp.txt
   fi
}
.....
before=$("${ALBA}seconds")
$RIETAN/rietan $sample.ins $sample.int $sample.bkg $sample.itx $sample.hkl $sample.xyz $sample.fos \
$sample.ffe $sample.fba $sample.ffi $sample.ffo $sample.vesta $sample.plt $sample.gpd $sample.alb \
$sample.prf $sample.inflip $sample.exp | tee $sample.lst

if grep -q "^ *MEP = 1$" $sample.lst ; then
   # Analyze |Fo|^2 data in $sample.ffo by the maximum-entropy Patterson method to create $sample.mep
```

[4] G*nu*W*in* utilities are used for Windows: http://gnuwin32.sourceforge.net/

```
   ${ALBA}alba $sample.alb
   after=$("${ALBA}seconds")
   # temp.txt: a scratch file to store parts of $sample.lst, $sample.out, and $sample.mep
   sed -e '/^ *\*\*\* End of job *\*\*\*/,$d' $sample.lst > temp.txt
   sed -n -e '23,/^ Number of cycles/p' $sample.out >> temp.txt
   # Option -e makes \n (line feed) effective
   echo -e "\n\n ************** Results of maximum-entropy Patterson analysis **************\n\n" >> \
   temp.txt
   PART1="   h   k   l           FWHM         |Fc|^2            d"
   PART2="      2-theta              I       I/I1            Io"
   echo $PART1$PART2 >> temp.txt
   sed -n -e '2,$p' $sample.mep >> temp.txt
   # append three line feeds, '       *** End of job ***', and two line feeds to temp.txt
   tail -n 9 $sample.lst | sed -n -e '1,6p' >> temp.txt
   elapsed_time
   # The version number of RIETAN-FP is output
   tail -n 2 $sample.lst >> temp.txt
   # -f: overwrite $sample.lst
   mv -f temp.txt $sample.lst
   # After excution of the above command, temp.txt no longer exists in the current folder.
   if grep -q "^ *NCF = 1$" $sample.lst ; then
      # Replace |Fo|^2 in $sample.inflip with |Fc|^2 resulting from maximum-entropy Patterson analysis
      sed -n -e '1,/^fbegin/p' $sample.inflip > temp.txt
      echo "#  h   k   l           FWHM         |Fc|^2" >> temp.txt
      # Append columns No. 1-42 in $sample.mep to temp.txt
      sed -n -e '2,$p' $sample.mep | cut -b 1-42 >> temp.txt
      echo "endf" >> temp.txt
      # -f: overwrite $sample.inflip
      mv -f temp.txt $sample.inflip
   fi
fi
.....
```

When `MEP` is set at 1 in hoge.ins, RIETAN-FP outputs '`MEP = 1`' in hoge.lst, creating an input file, hoge.alb, for ALBA. If a line containing '`MEP = 1`' is found in hoge.lst, ALBA is executed to input hoge.alb where the file name of hoge.ffo is given, *e.g.*,

```
# Name of the file, hoge.ffo, storing |Fo|^2.
BaSO4.ffo
```

MEP analysis with ALBA creates a file, hoge.mep, compatible with instruction `REF2` (`DATA` routine) in EXPO [22]. Then, other two output files, hoge.lst (RIETAN-FP) and hoge.out (ALBA), are dealt with the UNIX-compatible commands to overwrite hoge.lst in such a way that main parts of data in hoge.out are appended to hoge.lst. The elapsed time output at the tail end of hoge.lst is evaluated in function `elapsed_time` from two variables, `$before` and `$after`, output by a Fortran program called seconds.

If flag `NEXP` is set at 1 in hoge.ins, RIETAN-FP creates a template input file for EXPO, hoge.exp, where the name of hoge.mep is placed after `REF2`. As described in 11.5, hoge.exp may be appropriately modified with a text editor.

With RIETAN-FP, a template file, hoge.inflip, for charge flipping with superflip [179] can also be created by setting flag `NCF` at 1 in hoge.ins. The resulting file, hoge.inflip, practically

includes the whole content of hoge.mep at its tail end: hkl, FWHM, and $|F(\boldsymbol{h}_K)|^2$ values of observed reflections (see 11.5).

Chapter 12

INDIVIDUAL PROFILE FITTING

12.1 Local Pattern Decomposition

From Eqs. (4.24) and (2.5), we obtain

$$f_i(\boldsymbol{x}) = \sum_K I(\boldsymbol{h}_K) G(\Delta 2\theta_{iK}) + y_{\mathrm{b}}(2\theta_i). \tag{12.1}$$

As described in 3.9 and 3.10, $G(\Delta 2\theta_{iK})$ contains PPPs including the FWHM of the profile, H_K, parameters associated with the degree of decay from the peak to the edge of a reflection (*e.g.*, η in the pseudo-Voigt function and m in the Pearson VII function), parameters related to profile asymmetry as part of independent variables, $\boldsymbol{x}$.

In individual profile fitting [18], PPPs, $2\theta_K$, and $I(\boldsymbol{h}_K)$ assigned to each reflection are refined together with background parameters by a method of nonlinear least squares from powder-diffraction data in a limited 2θ region. Because it is local profile fitting, a linear background function,

$$y_{\mathrm{b}}(2\theta_i) = b_0 + b_1(2\theta_i), \tag{12.2}$$

containing only two background parameters is usually enough to approximate the background intensity. Of course, the number of refinable background parameters has to be increased if the shape of the background in the relevant 2θ region is somewhat complex because of the inclusion of an amorphous material or the presence of a capillary tube.

As the degree of overlapping for adjacent reflections is increased, it becomes more difficult to refine all the above parameters. Increases in correlations between refinable parameters may cause convergence to meaningless parameters and/or divergence of the solution. Because individual profile fitting deals with intensity data in a narrow 2θ range, no large errors result from neglecting the dependence of PPPs on 2θ. Therefore, convergence is usually attained by imposing equality constraints where PPPs of the same kind for overlapping reflections are constrained to be equal to each other.

12.2 Individual Profile Fitting in RIETAN-FP

In principle, it is difficult to obtain accurate and precise 2θ's and $I(\boldsymbol{h}_K)$'s of heavily overlapped reflections by individual profile fitting, in particular, when the resolution of the diffraction pattern

is not very high. In RIETAN-FP, this feature is regarded as a means to supplement Rietveld and Le Bail refinements.

With RIETAN-FP, individual profile fitting is carried out by setting `NMODE` at `6`. Only the split pseudo-Voigt function (3.84) or the split Pearson VII function (3.85) in p. 37 may be used as a profile function. *SPPs and lattice parameters are input as dummy data to be fixed while no structure parameters are necessary.* Reflection indices must be included in labels with a form of '`PPPn_h.k.l,`' (see 17.3.15), and (a) PPPs (see Sect. B in "Parameters contained in the model function in RIETAN-FP"), (b) a parameter proportional to $|F(\boldsymbol{h}_K)|$, and (c) $2\theta_K$ are refined by a least-squares method. That is, reflections whose parameters are refined are regarded as relaxed ones. Refer to Tables S-2, S-3, and S-4 for PPPs and other parameters to be input in individual profile fitting.

Figure 12.1 shows individual profile fitting of an X-ray powder-diffraction pattern for α-quartz (Cu $K\alpha$). FWHM(Lorentz), FWHM(Gauss), A, η_{L}, η_{H}, const$\times|F_{\mathrm{c}}|$, and $2\theta_K$ of each reflection were refined by setting `NPRFN` at 2 (a modified split pseudo-Voigt function for relaxed reflections). In this pattern in a 2θ range of $66^\circ - 70^\circ$, 122, 023, and 301 reflections for $K\alpha_1$ and $K\alpha_2$ radiations are observed; decomposed reflections are shown by broken lines. Diffraction indices are attached to only $K\alpha_1$ reflections. In this analysis, PPPs, $|F(\boldsymbol{h}_K)|$'s, and $2\theta_K$'s of the 122, 023, and 301 reflections were refined as listed below:

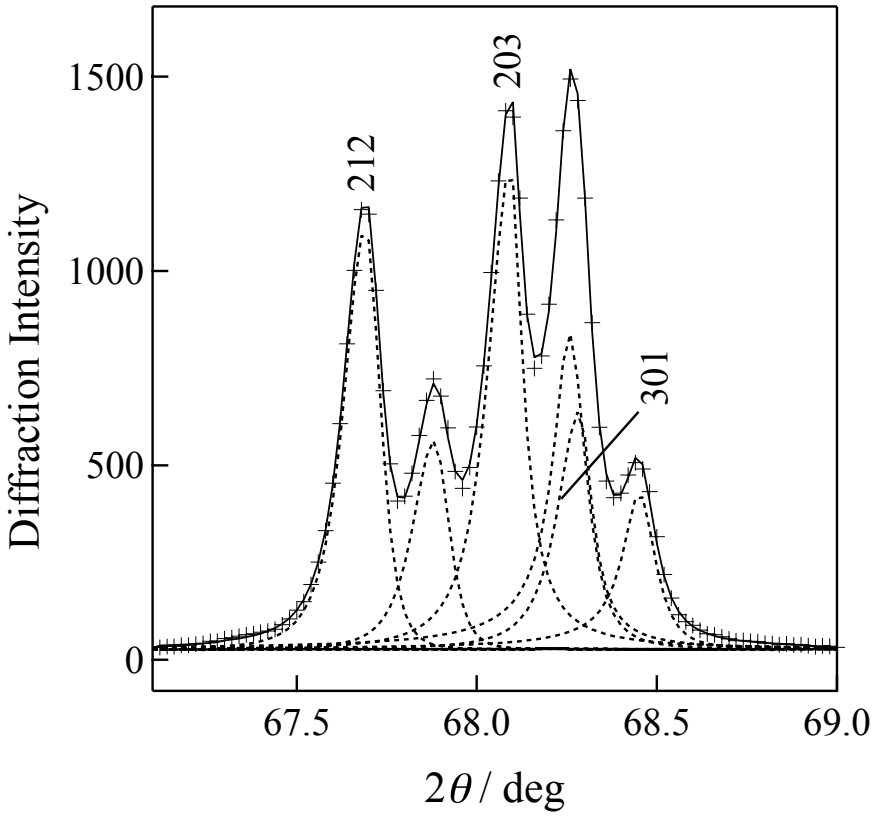

Figure 12.1: Decomposition of an X-ray powder-diffraction pattern of quartz by individual profile fitting

```
              No.      A            ID
.....
PPP1_1.2.2:   21   0.103913          1      FWHM(Lorentz) for phase 1: 1 2 2
              22   0.132359          1      FWHM(Gauss)
              23    1.55846          1      A
              24   0.556588          1      eta_L
              25   0.498263          1      eta_H
              26    535.051          1      const*|Fc|
              27    67.6924          1      2-theta(peak)
.....

PPP1_0.2.3:   49   0.119797          1      FWHM(Lorentz) for phase 1: 0 2 3
              50   0.115534          1      FWHM(Gauss)
              51    1.23611          1      A
              52   0.911778          1      eta_L
              53   0.472013          1      eta_H
              54    604.212          1      const*|Fc|
              55    68.0863          1      2-theta(peak)
.....
PPP1_3.0.1:   63   0.223776          1      FWHM(Lorentz) for phase 1: 3 0 1
              64   0.111171          1      FWHM(Gauss)
              65   0.959217          1      A
              66   0.535918          1      eta_L
              67   0.428859          1      eta_H
              68    502.977          1      const*|Fc|
              69    68.2500          1      2-theta(peak)
.....
```

Chapter 13

DETERMINATION OF CRYSTALLITE SIZES AND MICROSTRAINS

Microstructural evaluation is important to understand physical and chemical properties of polycrystalline materials, particularly in the field of nanotechnology. This chapter deals with microstructural characterization using RIETAN-FP, helping its users to learn details in procedures to determine crystallite sizes and microstrains after whole-pattern fitting of powder diffraction data measured over a wide range of 2θ by the Rietveld or Le Bail method. These features provide us with powerful and convenient means to investigate microstructures from isotropic profile broadening by X-ray and neutron powder diffraction.

Crystallite-size broadening can be used to determine the crystallite size of less than 1 μm in materials. On the other hand, microstrains are caused by a distribution of both tensile and compressive forces, which causes broadening of diffraction profiles about the original position. Crystallite-size broadening follows a $1/\cos\theta$ function whereas strain-induced profile broadening has a $\tan\theta$ dependence [183], which allows us to separate these two effects in diffraction data over a wide 2θ range. In what follows, three different methods of microstructural analysis from powder diffraction data will be described.[1] For convenience, subscript K representing the reflection number is omitted, with some equations in Chap. 3, repeated in this chapter.

13.1 Determination of Crystallite Sizes and Microstrains from Profile Parameters

With RIETAN-FP, crystallite sizes and microstrains can be estimated in the same manner as GSAS [185]. That is, profile parameters in the pseudo-Voigt function of Thompson, Cox, and Hastings [96] are refined by the Rietveld or Le Bail method from powder diffraction data of an instrumental standard and an analysis sample to determine crystallite sizes and microstrains in the latter.

In the pseudo-Voigt function of Thompson *et al.* [96] (see 3.9.3), the full-width at half

[1] This chapter is a minor revision in [184].

maximum (FWHM), H_{G}, for the Gaussian component is represented by

$$H_{\mathrm{G}} = \left[8 \ln 2 \left(U \tan^2 \theta + V \tan \theta + W\right)\right]^{\frac{1}{2}}. \tag{13.1}$$

On the other hand, the FWHM of the Lorentzian one, H_{L}, is computed by

$$H_{\mathrm{L}} = \frac{X}{\cos \theta} + Y \tan \theta, \tag{13.2}$$

where θ is the Bragg angle, and U, V, W, X, and Y are profile parameters to be refined by a method of nonlinear least squares. Equations (13.1) and (13.2) are abbreviated forms of Eq. (3.70) and Eq. (3.71), respectively. In both GSAS and RIETAN-FP, the unit of U, V, and W in Eq. (13.1) is (degrees)^2 whereas that of X and Y in Eq. (13.2) is degrees.

Let K be the shape factor (dimensionless), λ the wavelength of the X-ray or neutron beam, r a constant ($= \pi/180 = 0.0174533$) to convert degrees into radians. Then, the crystallite size, D, is determined from

$$D = \frac{K\lambda}{rX} \tag{13.3}$$

with the unit of D being equal to that of λ. K depends on assumptions made during the derivations. Microstrains corresponding to the Gaussian and Lorentzian components are, respectively, computed by

$$\epsilon_{\mathrm{G}} = r\left[8 \ln 2 \left(U - U_{\mathrm{i}}\right)\right]^{\frac{1}{2}}, \tag{13.4}$$

$$\epsilon_{\mathrm{L}} = r\left(Y - Y_{\mathrm{i}}\right), \tag{13.5}$$

where U_{i} and Y_{i} are contributions of the instrument to U and Y, respectively. U_{i} and Y_{i} can be estimated by Rietveld analysis from diffraction data of a sample whose crystallinity is high enough to show negligible profile broadening due to the sample.

There is a direct relationship between the parameters and a physical model in the Larson–Von Dreele formulation, which is therefore appealing in terms of its soundness based on physics motivation. The pseudo-Voigt function of Thompson *et al.* is, accordingly, preferred to the Pearson VII function (3.63) to obtain information on D and ϵ. This simple method, however, suffers from possible errors due to strong correlations among profile parameters, U, V, W, X, and Y. The presence of the two kinds of the microstrains, ϵ_{G} and ϵ_{L}, complicates the understanding of the nature of isotropic microstrain. In addition, no dependence of profile broadening on a function containing θ is graphically illustrated, which is unfavorable for finding variations in the data and anisotropic broadening of diffraction profiles.

To overcome such drawbacks of the methodology adopted in GSAS [185], the Williamson–Hall [186] and Halder–Wagner [187, 188] methods were added to RIETAN-FP. With these two methods, D and ϵ can easily be determined from integral breadths, β, defined as (peak area)/(peak intensity) after Rietveld or Le Bail analysis. Powder diffraction data measured with characteristic X-rays such as Cu $K\alpha$ radiation are good enough to get reliable D and ϵ values. Because the graphing of the two kinds of plots with free software, gnuplot[2] [63] (see 17.7.1), is supported in RIETAN-FP, additional information is obtainable on the characterization of polycrystalline materials by use of profile broadening, for example, anisotropic one depending on directions of scattering vectors.

[2] http://gnuplot.sourceforge.net/

13.2 Williamson–Hall method

Crystallites whose size, D, is less than *ca.* 1 μm exhibit profile broadening. The integral breadth (in radians), β, due to the effect of small crystallites is related to D *via* the so-called Scherrer equation [189],

$$\beta_D = \frac{K\lambda}{D\cos\theta}, \tag{13.6}$$

corresponding to Eq. (13.3).

The effect of isotropic microstrain, ϵ, on profile broadening can be derived by differentiating Bragg's law,

$$\lambda = 2d\sin\theta, \tag{13.7}$$

with respect to θ:

$$\Delta\theta = -\frac{\Delta d}{d}\tan\theta = -\epsilon\tan\theta. \tag{13.8}$$

That is, profile broadening due to microstrain, $\epsilon = \Delta d/d$, is proportional to $\tan\theta$. Stokes and Wilson [190] pointed out that the integral breadth, β_ϵ, arising from isotropic microstrain is related to the integral breadth of the strain distribution, ξ, by

$$\beta_\epsilon = 2\xi\tan\theta. \tag{13.9}$$

Comparison between Eq. (13.6) and Eq. (13.9) shows that the dependence of β_D on θ is quite different from that of β_ϵ. Williamson and Hall [186] introduced a simple approximation that the integral breadth, β, due to both of small crystallite sizes and microstrains is simply the sum of Lorentzian component, β_D, and the Gaussian one, β_ϵ:

$$\beta = \beta_D + \beta_\epsilon. \tag{13.10}$$

Thus, Eq. (13.6) and Eq. (13.9) are combined together to yield

$$\beta = C\epsilon\tan\theta + \frac{K\lambda}{D\cos\theta} \tag{13.11}$$

with

$$\epsilon = C\xi. \tag{13.12}$$

The proportional constant, C, which depends on the assumptions made concerning the nature of the inhomogeneous strain, lies between 4 and 5, with $C = 4$ corresponding to the maximum (upper limit) of strain [191, 192]. In part of previous work, C was carelessly set at 2, which probably arose out of confusing ξ with ϵ. Multiplying both sides of Eq. (13.11) by $\cos\theta$, we obtain

$$\beta\cos\theta = C\epsilon\sin\theta + \frac{K\lambda}{D}. \tag{13.13}$$

Equation (13.13) is regarded as a straight line, $y = Px + Q$. The slope of the straight line is $P = C\epsilon$ while its y intercept is $Q = K\lambda/D$. A plot of $y = \beta\cos\theta$ against $x = \sin\theta$ is referred to as the Williamson–Hall (WH) plot since Williamson and Hall [186] proposed this methodology in 1953. However, this designation is somewhat unfair in view of the fact Hall was the first to report this methodology in 1949 [193]. Equation (13.13) holds true for isotropic line broadening.

If both of crystallite-size and microstrain profiles are Gaussian, then the plot is convex downward, having the same terminal slope at a high angle as the Lorentzian case and intercepting the y axis at $K\lambda/D$ [194].

The WH plot is a very useful diagnostic tool for learning the kind(s) of profile broadening and determining approximate values of D and ϵ.

Regrettably, various K values such as 0.89, 0.9, 0.94, and 1.0 have been arbitrarily used in the literature without any regard to the definition of the crystallite size or the selection of FWHM or β as a measure of line broadening. Ida *et al.* [195] derived the K value of 4/3 for the mean volume-weighted average size, $\langle D\rangle_V$, defined as the ratio of the mean forth power of D divided by the mean cube of D,

$$\langle D\rangle_V = \frac{\langle D\rangle^4}{\langle D\rangle^3}, \tag{13.14}$$

in the case of spherical crystallites. Note that the K value of 4/3 is valid on the representation of profile broadening not by the FWHM but by the integral breadth, β, in the same way as Eq. (13.13).

13.3 Halder–Wagner method

For the determination of D and ϵ, Halder and Wagner [187,188] proposed an alternative equation containing the integral breadth, β^*, of the reciprocal lattice point and the lattice-plane spacing, d^*, for the reciprocal cell:

$$\left(\frac{\beta^*}{d^*}\right)^2 = \frac{K}{D}\cdot\frac{\beta^*}{(d^*)^2} + (2\epsilon)^2 \tag{13.15}$$

with

$$\beta^* = \frac{\beta\cos\theta}{\lambda}, \tag{13.16}$$

$$d^* = \frac{2\sin\theta}{\lambda} \tag{13.17}$$

on the assumptions that the Lorentzian and Gaussian components of β^* are solely due to the size and strain effects, respectively. Equation (13.15) can be rewritten as

$$\left(\frac{\beta}{\tan\theta}\right)^2 = \frac{K\lambda}{D}\cdot\frac{\beta}{\tan\theta\sin\theta} + 16\epsilon^2 \tag{13.18}$$

on the basis of direct space. Inside RIETAN-FP, another equation,

$$\left(\frac{\beta\cos\theta}{\sin\theta}\right)^2 = \frac{K\lambda}{D}\cdot\frac{\beta\cos\theta}{\sin^2\theta} + 16\epsilon^2, \tag{13.19}$$

equivalent to Eq. (13.18) is adopted because both of Eq. (13.13) and Eq. (13.19) contain $\sin\theta$ and $\beta\cos\theta$.

Equation (13.18) has a form of a straight line, $y = Px + Q$, in a similar manner as Eq. (13.13). In the Halder–Wagner (HW) plot, $y = (\beta/\tan\theta)^2$ is plotted against $x = \beta/(\tan\theta\sin\theta)$. Then, the slope and y intercept of the resulting straight line afford $P = K\lambda/D$ and $Q = 16\epsilon^2$, respectively. As described in the previous section, the value of $K = 4/3$ [195] is believed to be

valid on the definition of the crystallite size as the volume-weighted average one for spherical crystallites.

Despite the approximations and assumptions made on the derivation of Eq. (13.18), the HW formulation has a great advantage that data for reflections at low and intermediates angles are given more weight than those at higher diffraction angles, which are often less reliable. Further, Eq. (13.18) does not contain the constant C unlike Eq. (13.13), which is another advantage of the HW formulation over the WH one.

13.4 Calculation of Crystallite Sizes and Microstrains

13.4.1 An instrumental standard

After Rietveld or Le Bail analysis with a pair of files, hoge.ins and hoge.int, has been finished, $\sin\theta$ and $\beta(\mathrm{instr})\cos\theta$, where $\beta(\mathrm{instr})$ denotes the integral breadth due to the instrument, are estimated for all the reflections observed in the whole diffraction pattern and output to the gnuplot data file, hoge.gpd. Profile broadening arising from the instrument includes spectral distribution of X-ray and neutron beams, deviations from the ideal geometry, axial divergence, sample transparency, *etc.* In all the profile functions, $G(\Delta 2\theta)$, used in RIETAN-FP, the peak area of each reflection is normalized in such a way that

$$\int_{-\infty}^{+\infty} G(\Delta 2\theta)\mathrm{d}(2\theta) = 1 \tag{13.20}$$

Therefore, β is simply equal to the reciprocal of the peak intensity.

Equations (13.13) and (13.18) are calculated from $\sin\theta$ and $\beta(\mathrm{instr})\cos\theta$, which is followed by linear regression analysis to obtain D and ϵ from the slope and y intercept. The D and ϵ values output to hoge.lst are expected to give an approximately straight line, which can easily be checked by drawing a graph by gnuplot [63] with a pair of files, hoge.gpd and hoge.plt, created by RIETAN-FP (see 13.4.3).

An instrumental standard having the same crystal structure and chemical composition is preferred, of course. Unless such a sample of high crystallinity is available, a standard reference material such as NIST SRM 640 (Si) and SRM 660 (LaB6) with a similar linear attenuation coefficient, μ, may be used as a substitute. Such a caution is demanded particularly when a sample of a small μ value is mounted on a flat-plate holder in an X-ray powder diffractometer with the Bragg–Brentano geometry where the effect of sample transparency is appreciable.

13.4.2 A sample showing broadened diffraction profiles

The hoge.gpd file for the instrument standard sample is renamed instrument.gpd and copied into a folder where a series of files, *e.g.*, hoge.ins and hoge.int, for an analysis sample are contained. If needed, one or more lines storing hkl, $\sin\theta$, $\beta\cos\theta$, *etc.* for another instrument standard may be inserted into instrument.gpd to complement reflection data in a low-angle region. Then, Rietveld or Le Bail analysis is carried out to obtain $\sin\theta$ and $\beta(\mathrm{obs})\cos\theta$. The $\sin\theta$ and $\beta(\mathrm{instr})\cos\theta$ values are input from instrument.gpd and interpolated by spline interpolation to

give $\beta(\text{instr})\cos\theta$ corresponding to the present sample. Such a procedure is very convenient, requiring only instrument.gpd.

Strictly speaking, the observed profile is the convolution of profiles due to the instrument and the sample. To evaluate the approximate contribution of the broadening, β(sample), originating in the sample, the following approximation formula is used:

$$[\beta(\text{sample})]^n = [\beta(\text{obs})]^n - [\beta(\text{instr})]^n \,. \tag{13.21}$$

The power, n, is input by the user in hoge.ins. In happy and special situations, n is 1 for Lorentzian instrumental and sample broadening and 2 for Gaussian instrumental and sample broadening [194]. In the case of the intermediate character (Voigtian instrumental and sample broadening), n is expected to lie between 1 and 2. Equations (13.13) and (13.18) are then calculated from a set of $\sin\theta$ and $\beta(\text{sample})\cos\theta$ pairs, which is followed by linear regression analysis to yield D and ϵ. Of course, graphing of the plot with gnuplot (see 13.4.3) is also possible in this case because both $\sin\theta$ and $\beta(\text{sample})\cos\theta$ for all the reflections in the whole 2θ range are output to hoge.gpd together with the corresponding script file, hoge.plt, for gnuplot. Deviations from the linear relationships, *i.e.*, Eq. (13.13) and Eq. (13.18), because of anisotropic profile broadening can easily be recognized by the resulting graph.

13.4.3 Graphical representation of a Williamson–Hall or Halder–Wagner plot

Commands to draw a WH or HW plot are output as comment lines following

```
## Determination of crystallite size and microstrain
```

in the gnuplot script file, hoge.plt, where both $\beta\cos\theta$ (WH method) and $(\beta/\tan\theta)^2$ (HW method) are multiplied by 1000 to shorten numerical values on the y axis. These commands are extracted and executed by gnuplot to obtain a PDF file, hoge-mscs.pdf, of a graph with an MSCS macro included in the integrated assistance environments for RIETAN–VENUS. The resulting PDF file is usually browsed with Sumatra PDF[3] for Windows or Preview for macOS.

Of course, part of the comment lines (*e.g.*, document sizes, line widths, font and circle sizes) to draw the WH or HW plot may be freely modified by the user to improve the appearance of the graph. A script file, hoge-mscs.plt, which was converted from hoge.plt by a stream editor named sed, is left in the current folder for reference. This file may be input to be edited by a GUI front-end application to change various settings.

For details in MSCS, see Readme_macros.pdf and Readme_scpt.pdf.

13.4.4 Determination of a crystallite size with diffraction data of cerium dioxide

The features of the WH and HW methods in RIETAN- FP were tested with two sets of X-ray powder diffraction data for CeO_2: a broadened sample and an instrumental standard used in the first size/strain round robin [192]. These two intensity data (a "common" instrumental setup with Cu $K\alpha$ radiation) were downloaded from a Web page of the round robin.[4]

[3] http://blog.kowalczyk.info/software/sumatrapdf/free-pdf-reader.html
[4] http://www.ccp14.ac.uk/ccp/web-mirrors/balzar/div853/balzar/s-s_rr.htm

Nanocrystalline CeO_2 exhibiting profile broadening due to the crystallite-size effect was produced by the thermal treatment of hydrated ceria at 923 K for 45 h [196]. Substantial microstrain is expected to be absent in this sample. The instrumental standard was prepared by annealing commercially available CeO_2 at 1573 K for 3 h in air.

With RIETAN-FP, the two intensity data were analyzed by the Rietveld method to determine the crystallite size and microstrain of the annealed sample of CeO_2 according to the procedures described in 13.4.2. The n value in Eq. (13.21) was set at 2.

Figure 13.1 illustrates the HW plot drawn from the two sets of the Rietveld refinement. A distinct linear relationship is found between $(\beta/\tan\theta)^2$ and $\beta/(\tan\theta\sin\theta)$. The y intercept is as small as 9.443×10^{-6}, corresponding to a very small microstrain of 0.07682 % in this sample annealed at the high temperature. The WH plot also showed that $\beta\cos\theta$ bears a linear relationship to $\sin\theta$. The upper limit of ϵ was estimated at 0.4957 % from the slope of the resultant straight line with $C = 4$. This strain value is comparable to the average one, 0.4(9) %, in the round robin [192]. The crystallite sizes determined by the WH and HW methods were $22.47K$ nm and $21.69K$ nm, respectively. K depends on the definition of the crystallite size. If the K value of 4/3 for the mean volume-weighted size of spherical crystallites [195] is adopted, $\langle D\rangle_V$ is calculated at 29.96 nm in the WH method and 28.92 nm in the HW one. These two values slightly less than 30 nm fall within ranges of $\langle D\rangle_V$, (32 ± 11) nm, reported by Balzar *et al.* [192] and are comparable to $\langle D\rangle_V$ determined by a fundamental-parameter approach [197] (see Fig. 4 in Ref. [192]).

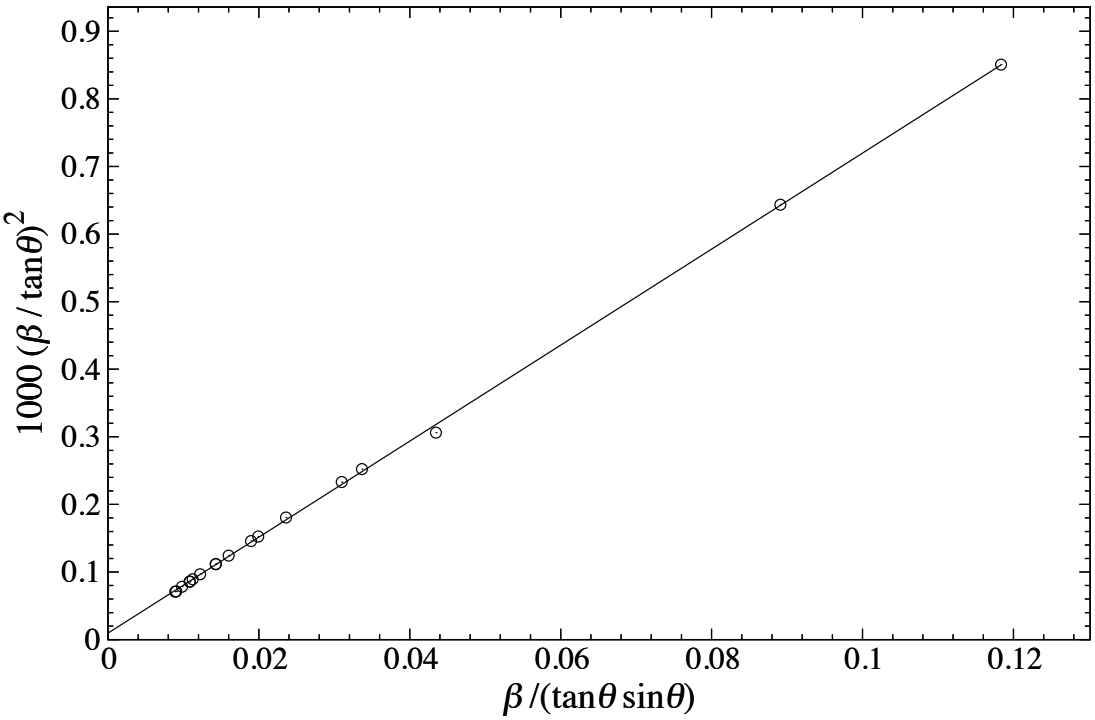

Figure 13.1: A Halder–Wagner plot for the round-robin sample of nanocrystalline CeO_2. The straight line was obtained by linear regression analysis.

13.4.5 Summary

The WH and HW plots are the most rapid diagnostic tools for determining the kinds(s) of profile broadening present in samples analyzed by the Rietveld or Le Bail method [194]. Both of them present the following valuable information about microstructures of various polycrystalline materials:

(a) Clear discrimination between crystallite-size and microstrain effects,

(b) An estimate of the crystallite size, D,

(c) An estimate of the microstrain, ϵ,

(d) Clear distinction between isotropic (monotonic curve) and anisotropic (scatter) broadening by graphical representation with gnuplot.

For example, (b) and (c) are useful to characterize nano-crystalline materials showing marked surface effects while (c) helps us to estimate the degree of inhomogeneous distribution of solute atoms in solid solutions. With only numerical data, anisotropic broadening cannot be well perceived contrary to (d). We are confident that the WH and HW methods of microstructural characterization in RIETAN-FP deliver added value to its users in both academic institutions and industries.

Chapter 14

WHOLE-PATTERN FITTING BASED ON THE MAXIMUM-ENTROPY METHOD

14.1 Introduction

The maximum-entropy method (MEM) is a versatile approach to estimation of a model from a limited amount of information by maximizing information entropy under constraints consistent with observed physical quantities. Sakata *et al.* [198, 199] have been applying MEM to determination of electron and nuclear (strictly speaking, coherent-scattering length b_c) densities from powder-diffraction data. Diffraction intensities scattered in the reciprocal space are converted into electron/nuclear densities filling the real space; that is, the densities are visualized in three dimensions. MEM can estimate structure factors of reflections in the high-Q region excluded in the analysis of the powder-diffraction data, which is favorable for improving the S/N ratio in the 3D densities.

When dealing with compounds exhibiting heavily overlapping reflections, integrated intensities are often estimated on the basis of the result of Rietveld analysis. In this procedure, the observed intensity at each point is apportioned in the ratio of profiles calculated from final parameters and summed up for each reflection. The resultant 'observed' structure factors are then analyzed by MEM to give 3D electron/nuclear densities in the unit cell. Unfortunately, 'observed' structure factors evaluated in this way are doubly biased towards the structural model because both phases and calculated integrated intensities used for the intensity partitioning are taken from the model.

We have been claiming that the above undesirable effect, which is overlooked or disregarded by Sakata *et al.*, should be overcome if only partially. Even if the structural model in the Rietveld analysis from X-ray powder-diffraction data is essentially correct, chemical bonding is hardly represented with structure parameters such as fractional coordinates and atomic displacement parameters. This is the main reason for the necessity of difference Fourier synthesis in studies of electron densities by single-crystal X-ray diffraction. Refinement of isotropic atomic displacement parameters, U, in Rietveld analysis (anisotropic atomic displacement parameters, U_{ij}, cannot practically be refined from X-ray powder-diffraction data) and that of a scale factor on the basis of the inadequate structural model will lower the accuracy of the 'observed' structure factors.

In this chapter, we will describe our original technology named MEM-based pattern fitting (MPF) [11–17].[1] We have integrated a multipurpose pattern-fitting program RIETAN-FP, a MEM analysis program Dysnomia [17, 23], and a 3D visualization program VESTA [1, 25, 26, 138] to construct a system to refine crystal structures by MPF from powder-diffraction data. With this MPF system, the bias imposed on final electron/nuclear densities can efficiently be reduced by running RIETAN-FP and Dysnomia alternately.

14.2 Background

In single-crystal X-ray analysis, we often carry out difference Fourier synthesis, *i.e.*, the inverse Fourier transform of differences, between observed structure factors, $F_{\rm o}(\boldsymbol{h}_K)$, and structure factors, $F(\boldsymbol{h}_K)$, calculated from structure parameters:

$$\Delta F(\boldsymbol{h}_K) = F_{\rm o}(\boldsymbol{h}_K) - F(\boldsymbol{h}_K). \tag{14.1}$$

Difference Fourier synthesis is suitable for detecting subtle differences between real and modeled structures.

Two serious problems hinder the satisfactory application of difference Fourier synthesis to powder-diffraction data. One is the appearance of 'ripples' due to the termination effect even in difference Fourier synthesis where Fourier coefficients with higher orders are regarded as negligible. This effect makes it difficult to extract physically meaningful residual distribution from D-synthesis maps. The other is difficulty in obtaining accurate observed structure factors, $|F_{\rm o}(\boldsymbol{h}_K)|$, owing to the collapse of the 3D reciprocal space onto the one-dimensional diffraction pattern.

In MEM analysis, no model function is fit to the observed pattern unlike Rietveld analysis using least-squares methods; that is, we estimate density distribution whose information entropy is maximized within errors in observed diffraction data. Structural information contained in diffraction data is accordingly extracted by MEM and reflected on the 3D densities provided that the diffraction data have been measured in an appropriate way. Electron densities are calculated from $F_{\rm o}(\boldsymbol{h}_K)$'s in Fourier synthesis. On the other hand, in MEM, we solve a kind of an inverse problem where electron densities are determined prior to calculation of structure factors, F(MEM). The termination effect is, consequently, far less marked in MEM analysis than in Fourier synthesis. Further, the MEM can estimate structure factors of reflections in the high-Q region excluded in the analysis of intensity data, as described earlier. MEM analysis, therefore, gives less noisy 3D densities than Fourier synthesis from a limited number of observed reflections.

The distribution of $b_{\rm c}$ is also determinable by MEM analysis from neutron diffraction data. The term "nuclear density" may be substituted for "electron density" in subsequent general descriptions common to X-ray and neutron diffraction.

[1] The review article [12] is obtainable at http://www.fkf.mpg.de/4112052/cpd26.pdf

14.3 Maximum-Entropy Equation

The general principle of MEM analysis is to find the maximum of the information entropy, S, under several constraints. There are a few variations of the MEM formalism. In what follows, we will follow Collins's formalism [200] based on Jaynes's expression of the information entropy [201].

In MEM analysis of X-ray/neutron diffraction data, electron/nuclear densities are represented with those in voxels (parallelepipeds) whose numbers along a, b, and c axes are N_a, N_b, and N_c, respectively. Let N_p ($= N_a N_b N_c$) be the total number of voxels in the unit cell, ρ_j the normalized density at the position $\boldsymbol{r}_j$ in the 3D gridded space, ρ_j^* the density at $\boldsymbol{r}_j$, and τ_j the normalized density at $\boldsymbol{r}_j$ derived from prior information, then S is formulated as

$$S = -\sum_{j=1}^{N_\mathrm{p}} \rho_j \ln\left(\frac{\rho_j}{\tau_j}\right) \tag{14.2}$$

with

$$\rho_j = \frac{\rho_j^*}{\sum_{j=1}^{N} \rho_j^*}. \tag{14.3}$$

S is maximized under the following three constraints:

$$\rho_j > 0, \tag{14.4}$$

$$\frac{1}{M_F} \sum_{K=1}^{M_F} \left[\frac{|F(\boldsymbol{h}_K) - F_\mathrm{o}(\boldsymbol{h}_K)|}{\sigma\left(|F_\mathrm{o}(\boldsymbol{h}_K)|\right)}\right]^2 = 1, \tag{14.5}$$

$$\sum_{j=1}^{N_\mathrm{p}} \rho_j = 1, \tag{14.6}$$

where M_F is the total number of reflections with known phases, $F(\boldsymbol{h}_K)$ is the calculated structure factor for reflection $\boldsymbol{h}_K$, $F_\mathrm{o}(\boldsymbol{h}_K)$ is the observed structure factor, and $\sigma\left(|F_\mathrm{o}(\boldsymbol{h}_K)|\right)$ is the standard uncertainty (s.d.) of $|F_\mathrm{o}(\boldsymbol{h}_K)|$. Densities, ρ_j ($j = 1, 2, 3, \cdots, N$), that maximize S are refined iteratively by the use of Lagrange undetermined multipliers.

The inequality constraint (14.4) prevents electron densities in part of voxels from falling into negative values. For random errors, the experimental values, F_o's and σ_K's, impose the F-constraint (14.5) of a χ^2 statistics type on S. That is, MEM derives densities giving $F(\boldsymbol{h}_K)$'s that agree with $F_\mathrm{o}(\boldsymbol{h}_K)$'s within their errors. The normalization constraint (14.6) holds the total number of electrons in the unit cell, $F(000)$ (X-ray diffraction), or the sum of b_c's (neutron diffraction) constant. Thus, the physical quantities, $F_\mathrm{o}(\boldsymbol{h}_K)$'s, in reciprocal space are converted into densities in real space.

14.4 Calculation of Structure Factors from Densities

14.4.1 X-Ray diffraction

When dealing with X-ray diffraction data of a compound where n_e is the total number of electrons in the unit cell, $F(\boldsymbol{h}_K)$ is calculated by the Fourier transform of electron densities in the unit

cell:

$$F(\boldsymbol{h}_K) = n_\mathrm{e} \sum_{j=1}^{N_\mathrm{p}} \rho_j \exp\left(2\pi \mathrm{i} \boldsymbol{h}_K \cdot \boldsymbol{r}_j\right). \tag{14.7}$$

Note that we can obtain not $|F(\boldsymbol{h}_K)|$ but $F(\boldsymbol{h}_K)$. Calculation of $F(\boldsymbol{h}_K)$ with this equation corresponds to the determination electron-density distribution in conformity with space-group symmetry while keeping n_e constant. For users' convenience, n_e is output near the last part of hoge.lst.

14.4.2 How to deal with elements of negative coherent-scattering lengths

MEM is simply applicable to the analysis of F_o data for compounds containing elements with negative b_c values, *e.g.*, H, Li, Ti, and Mn [24]. In such cases, S is represented as the sum of those for positive and negative densities [202]:

$$S = S^+ + S^-. \tag{14.8}$$

This is a good approximation to S because of the negligible overlap of nuclear densities for two atoms. Thus, Eq. (14.7) is rewritten as

$$F(\boldsymbol{h}_K) = \sum_{j=1}^{N_\mathrm{p}} \left(\rho_j^+ + \rho_j^-\right) \exp\left(2\pi \mathrm{i} \boldsymbol{h}_K \cdot \boldsymbol{r}_j\right) \tag{14.9}$$

with

$$\rho_j^+ = T^+ \rho_j, \tag{14.10}$$

$$\rho_j^- = T^- \rho_j. \tag{14.11}$$

In Eqs. (14.10) and (14.11), ρ_j is the nuclear density normalized with Eq. (14.6); T^+ and T^- are the total numbers of positive and negative b_c's, respectively. After the number of atoms in the unit cell has been multiplied by b_c for each element contained in a compound, the resulting positive and negative values are separately summed up to yield T^+ and T^-, respectively. T^+ and T^- are output near the last part of hoge.lst for users' convenience.

In the case a site occupied by two or more elements, it should be regarded as being occupied by a virtual chemical species with an average coherent-scattering length calculated from the occupancies of the elements. The resulting value of b_c should be multiplied by the number of the virtual species in the unit cell to be added to T^+ or T^-.

14.4.3 Reliability indices

In MEM analysis, two reliability indices are calculated to judge agreements between observed and calculated structure factors:

$$R = \frac{\sum_K \left|F_\mathrm{o}(\boldsymbol{h}_K) - F(\boldsymbol{h}_K)\right|}{\sum_K \left|F_\mathrm{o}(\boldsymbol{h}_K)\right|}, \tag{14.12}$$

$$R_{\mathrm{w}} = \left\{ \frac{\displaystyle\sum_K \left[\frac{|F_{\mathrm{o}}(\boldsymbol{h}_K) - F(\boldsymbol{h}_K)|}{\sigma\big(|F_{\mathrm{o}}(\boldsymbol{h}_K)|\big)} \right]^2}{\displaystyle\sum_K \left[\frac{|F_{\mathrm{o}}(\boldsymbol{h}_K)|}{\sigma\big(|F_{\mathrm{o}}(\boldsymbol{h}_K)|\big)} \right]^2} \right\}^{\frac{1}{2}} . \tag{14.13}$$

R corresponds to R_F in Rietveld analysis whereas R_{w} uses the weighted sum of squares for a measure of agreement.

14.5 Standard Uncertainties of Observed Structure Factors

Strictly speaking, we should state "standard uncertainties of the absolute values of observed structure factors", $|F_{\mathrm{o}}(\boldsymbol{h}_K)|$, instead of "standard uncertainties of observed structure factor." From Eq. (4.24), we can derive

$$|F_{\mathrm{o}}(\boldsymbol{h}_K)| = \left[\frac{I_{\mathrm{o}}(\boldsymbol{h}_K)}{s m_K P_K L(\theta_K)} \right]^{\frac{1}{2}} \tag{14.14}$$

and its standard uncertainty,

$$\sigma\big(|F_{\mathrm{o}}(\boldsymbol{h}_K)|\big) = \frac{|F_{\mathrm{o}}(\boldsymbol{h}_K)|}{2} \left\{ \left[\frac{\sigma\big(I_{\mathrm{o}}(\boldsymbol{h}_K)\big)}{I_{\mathrm{o}}(\boldsymbol{h}_K)} \right]^2 + \left[\frac{\sigma(s)}{s} \right]^2 \right\}^{\frac{1}{2}} , \tag{14.15}$$

where $\sigma\big(I_{\mathrm{o}}(\boldsymbol{h}_K)\big)$ and $\sigma(s)$ are the standard uncertainties of $I_{\mathrm{o}}(\boldsymbol{h}_K)$ and s, respectively. For simplicity, let us suppose an isolated reflection, whose observed integrated intensity can be obtained by numerical integration with Eq. (4.29). On the basis of the law of propagation of errors [203] in combination with counting statistics, we obtain

$$\begin{aligned} \left[\sigma\big(I_{\mathrm{o}}(\boldsymbol{h}_K)\big) \right]^2 &= (\Delta 2\theta)^2 \sum_i \sigma^2(y_{i\mathrm{B}}) \\ &= (\Delta 2\theta)^2 \sum_i y_{i\mathrm{B}} \\ &= \Delta 2\theta I_{\mathrm{o}}(\boldsymbol{h}_K). \end{aligned} \tag{14.16}$$

Thus, Eq. (14.15) is rewritten as

$$\sigma\big(|F_{\mathrm{o}}(\boldsymbol{h}_K)|\big) = \frac{|F_{\mathrm{o}}(\boldsymbol{h}_K)|}{2} \left\{ \frac{\Delta 2\theta}{I_{\mathrm{o}}(\boldsymbol{h}_K)} + \left[\frac{\sigma(s)}{s} \right]^2 \right\}^{\frac{1}{2}} . \tag{14.17}$$

In actual MEM analysis from powder-diffraction data, Eq. (14.17) is modified as

$$\sigma\big(|F_{\mathrm{o}}(\boldsymbol{h}_K)|\big) = \frac{|F_{\mathrm{o}}(\boldsymbol{h}_K)|}{2} \left\{ \frac{1}{E I_{\mathrm{o}}(\boldsymbol{h}_K)} + \left[\frac{\sigma(s)}{s} \right]^2 \right\}^{\frac{1}{2}} , \tag{14.18}$$

regardless of the degree of overlapping of reflections. E is a factor to adjust $\sigma\big(|F_{\mathrm{o}}(\boldsymbol{h}_K)|\big)$'s properly.

E is inversely proportional to $\Delta 2\theta$, depending on $\Delta 2\theta$ primarily. An estimated value of E, `E(SCIO)`, which is roughly equal to the reciprocal of average $\Delta 2\theta$, is given for each phase in

the standard output, hoge.lst (see 17.8.6). In general, E should be decreased on the analysis of diffraction data of poor statistics. E is usually determined so as to give reasonable $\sigma\big(|F_{\rm o}(\boldsymbol{h}_K)|\big)$ values and a relatively small number of cycles in a series of MEM analyses where 0th-order single-pixel approximation is used with a fixed and small λ_0. Smaller $R_{\rm wp}$ values resulting from MPF are also desirable because they reflect the improvement of $F(\boldsymbol{h}_K)$'s by MEM.

In addition, E must be adjusted in such a way that the resulting density distribution is physically and chemically reasonable. In our experience, optimum values of E lie between $3000\,{\rm rad}^{-1}$ and $4000\,{\rm rad}^{-1}$ for Cu $K\alpha$ radiation and between $8000\,{\rm rad}^{-1}$ and $10000\,{\rm rad}^{-1}$ for synchrotron X rays. Sometimes, comparison of electron-density distributions determined by MPF and electronic-state calculations with Gaussian,[2] GAMESS,[3] WIEN2k,[4] VASP,[5] ABINIT,[6] DVSCAT,[7] *etc.* is useful for this purpose.

Nuclear densities are concentrated in a relatively few number of voxels near atomic nuclei except for compounds containing highly disordered atomic species. Therefore, the convergence of MEM analysis from neutron diffraction data requires fairly large $\sigma\big(|F_{\rm o}(\boldsymbol{h}_K)|\big)$ data, which can be obtained by setting E between $200\,{\rm rad}^{-1}$ and $500\,{\rm rad}^{-1}$.

Such an arbitrary property of $\sigma\big(|F_{\rm o}(\boldsymbol{h}_K)|\big)$ may cause deviation of final electron- or nuclear-density distribution from true one. This problem is believed to be partially overcome by MPF where fitting of the calculated pattern to the observed one is repeated during REMEDY cycles (see 14.7.2).

14.6 MEM/Rietveld Method

In recent years, Takata *et al.* [204] have applied it actively to the determination of 3D electron/nuclear densities from X-ray/neutron powder-diffraction data. MEM infers the 3D densities in such a way that they give the maximum variance of structure factors, $F(\boldsymbol{h}_K) \equiv F({\rm MEM})$, within errors in observed structure factors, $F_{\rm o}(\boldsymbol{h}_K)$. Structural information can effectively be extracted from the diffraction data and reflected on the resulting 3D densities by MEM if the data have been appropriately measured. Because MEM can estimate nonzero structure factors for high-Q reflections excluded in the analysis of the powder diffraction data, the termination effect is less marked in MEM analysis than in Fourier synthesis. Thanks to these advantages, MEM provides us with less noisy 3D densities than Fourier synthesis.

Takata *et al.* have estimated 'observed' structure factors, $F_{\rm o}(\boldsymbol{h}_K) \equiv F_{\rm o}({\rm Rietveld})$, on the basis of the result of Rietveld analysis when dealing with overlapping reflections. That is, the observed net intensity at each point is apportioned in the ratio of profiles calculated from final structure and profile parameters and summed up for each reflection according to the procedure proposed by Rietveld [10].This expedient technique is also utilized to evaluate $R_{\rm B}$ and R_F in Rietveld analysis (see 4.3.2), integrated intensities in the Le Bail method, and 3D densities by

[2] http://www.gaussian.com/
[3] http://www.msg.ameslab.gov/GAMESS/GAMESS.html
[4] http://www.wien2k.at/
[5] http://cms.mpi.univie.ac.at/vasp/
[6] http://www.abinit.org/
[7] http://www.dvxa.org/

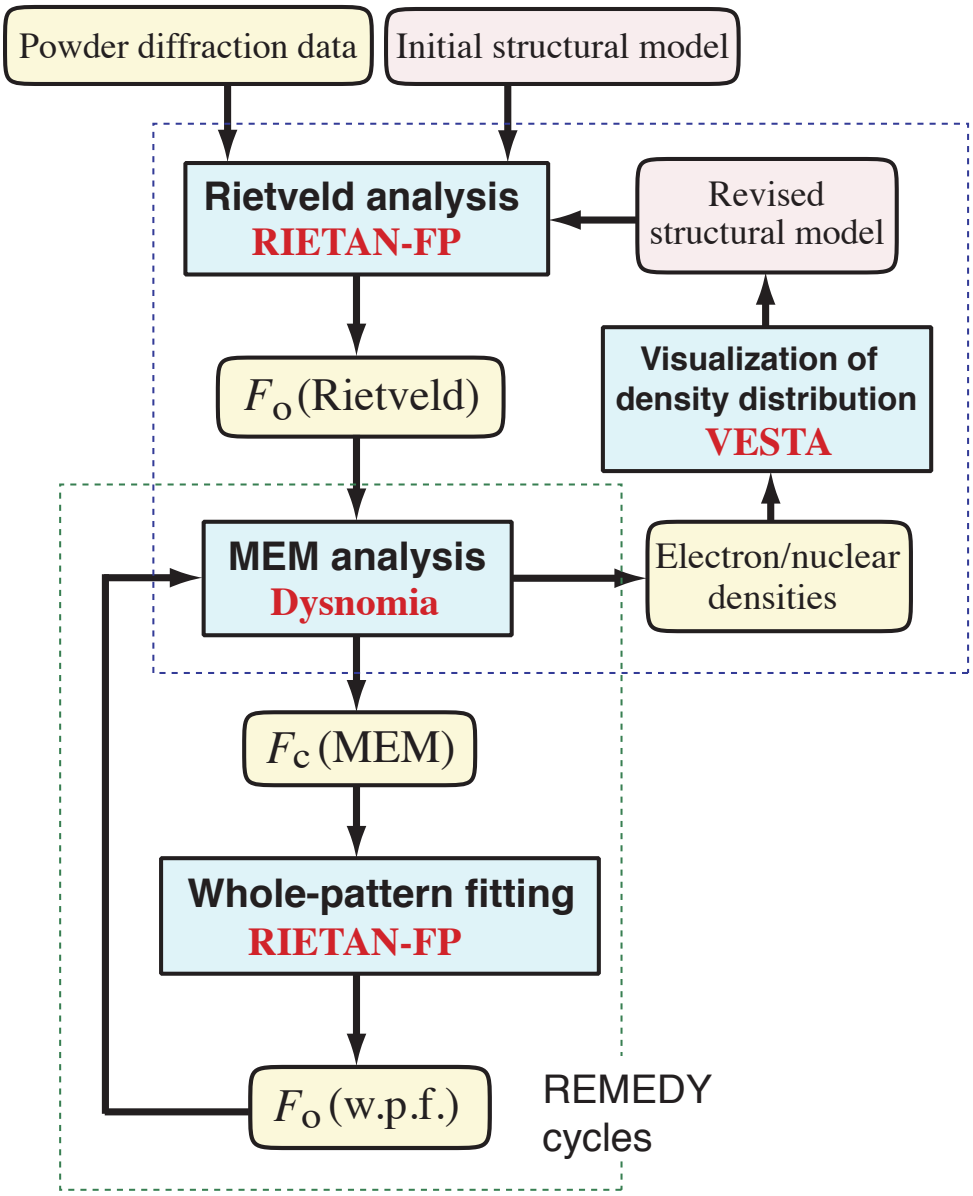

Figure 14.1: Structure refinement by MEM/Rietveld analyses followed by iterative MEM-based pattern fitting; 'Rietveld', 'MEM', and 'w.p.f.', each in a pair of parentheses, denote analyses by which structure factors are derived

Fourier synthesis. After close checking of the resulting 3D densities, the structural model in Rietveld analysis is modified, if necessary. Rietveld and MEM analyses are alternately repeated until a reasonable structural model is reached, as shown in the upper box in **Fig. 14.1**. Such an iterative technique is referred to as the MEM/Rietveld method [204].

However, the F_o(Rietveld) data estimated from the refinable parameters are where $F(\boldsymbol{h}_K)$ is the structure factor calculated from structure parameters refined by the Rietveld method. doubly biased toward a structural model in the Rietveld analysis because both phase angles, ψ, and calculated profiles used for the intensity partitioning are derived from the model. That is, $F_o(\boldsymbol{h}_K)$ is approximated as

$$F_o(\boldsymbol{h}_K) = |F_o(\boldsymbol{h}_K)| \exp(i\psi) \tag{14.19}$$

with

$$\begin{aligned} \exp(\mathrm{i}\psi) &= \cos\psi + \mathrm{i}\sin\psi \\ &= \frac{F(\boldsymbol{h}_K)}{|F(\boldsymbol{h}_K)|}, \end{aligned} \tag{14.20}$$

The bias for ψ is relatively small in centrosymmetric space groups because ψ is 0 or π. This approximate nature of the procedure for extracting integrated intensities lowers the accuracy of 3D densities determined by MEM analysis of F_o(Rietveld)'s. The undesirable bias in favor of the structural model enlarges with increasing degree of overlap of reflections and lowering resolution in a powder pattern.

Nevertheless, the MEM analysis ogf F_o(Rietveld)'s is certainly effective in modifying imperfect structural models for Rietveld analysis, as verified by location of (a) a pair of H atoms in the paraelectric phase of KH_2PO_4 at room temperature [205], (b) residual water in β cages of a dehydrated zeolite Na-LTA [206], (c) $(CH_3)_4N^+$ and Na^+ ions, in a helix layered silicate [207], and (d) Na^+ and H_3O^+ ions, and H_2O molecules between two CoO_2 layers in a superconducting sodium cobalt dioxide hydrate [208].

Figure 14.2 illustrates that electron-density distribution on the (110) plane in Na-LTA which was determined by (a) Fourier synthesis and (b) MEM analysis [206]. In this figure, the range of electron densities is 0.1–5/Å^3, the step is 0.1/Å^3, and the vertical axis is parallel to the [001] direction. Both results were obtained by Rietveld analysis followed by Fourier and MEM analyses with the same number of F_o(Rietveld) data. The termination effect makes it nearly impossible to distinguish between residual water molecules and ripples in (a). By contrast, residual water can be clearly seen in (b) at four positions indicated by arrows inside the β cage despite an occupancy as low as 0.028. Though this simple method is far from perfect for determining accurate 3D densities, MEM allows us to extract a maximum amount of structural details from the F_o(Rietveld) data containing contributions neglected in the structural model. In addition, F_o(Rietveld) data can be evaluated with a fair degree of accuracy for (nearly) isolated reflections. Structural information contained in these reflections serves to improve the accuracy of F(MEM)'s estimated by MEM for the overlapping reflections.

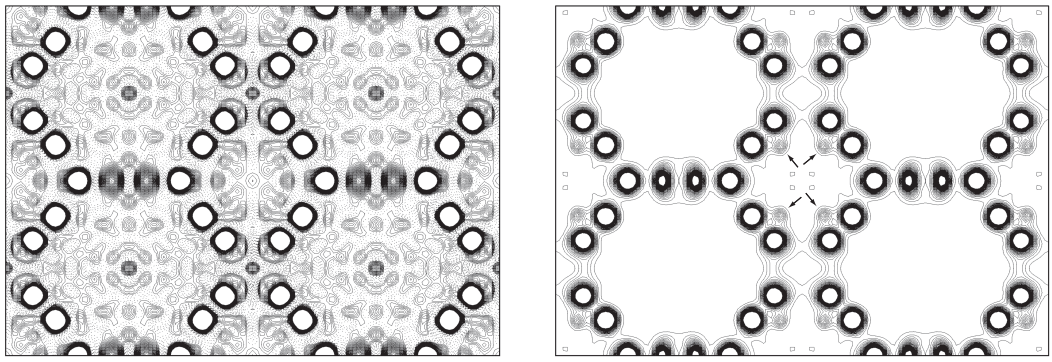

Figure 14.2: Electron-density distribution on the (110) section determined for Na-LTA by (a) Fourier synthesis and (b) MEM analysis

14.7 MEM-Based Pattern Fitting

To overcome the serious flaws in the oversimple procedure of Takata *et al.*, we devised a state-of-the-art technique of structure refinement called MPF.

14.7.1 Software for MPF

Prior to a detailed description of MPF, the three dimensional visualization system VENUS[8] will be introduced shortly [209, 210].[9].

VENUS, which has been developed by Dilanian, Izumi, Momma, and Kawamura since 2001, currently comprises the following five programs:

1. VESTA (**V**isualization for **E**lectronic and **ST**ructural **A**nalysis) for 3D visualization of crystal structures and volumetric data [1, 25, 26, 138],
2. Dysnomia [17, 23], which is the successor to PRIMA [13], for MEM analysis from X-ray and neutron diffraction data,
3. ALBA [20, 21] (**A**fter **L**e **B**ail **A**nalysis) for the maximum-entropy Patterson method proposed by David [19, 20],
4. Alchemy [211]: a file converter to make it possible to analyze observed structure factors, which result from Rietveld analysis using GSAS [87] and FullProf [110], by MEM with Dysnomia.

VESTA

To overcome some faults in VICS and VEND [209, 210, 212], we at first upgraded VICS to VICS-II employing a modern C++ GUI framework wxWidgets[10] [213] to build a new state-of-art GUI and further integrated VICS-II and VEND into the next-generation 3D visualization system VESTA, adding new capabilities.

VESTA is a 3D graphic application written in the C++ language on the basis of OpenGL technology. It runs fast on personal computers equipped with video cards accelerating OpenGL. Windows, macOS, and Linux versions are available. For each platform, both 32- and 64-bit applications will be distributed on the Web.

Thanks to wxWidgets, we can open multiple files using tabbed graphic windows; pull-down menus and tabbed dialog boxes are also supported. Needless to say, the annoying bug related to the close button described above has now been fixed. VESTA allows us to deal with a practically unlimited number of objects as far as memory size goes. It requires much less system resources than VICS and VEND.

VESTA represents crystal structures as ball-and-stick, space-filling, polyhedral, wireframe, stick, and displacement-ellipsoid models. Ball-and-stick, wireframe, and stick models can be overlapped with dotted surfaces corresponding to van der Waals radii. Polyhedra may be made

[8] http://fujioizumi.verse.jp/visualization/VENUS.html
[9] The review article [210] is obtainable at http://www.fkf.mpg.de/4111956/cpd32.pdf
[10] http://www.wxwidgets.org/

translucent so as to make inside atoms and bonds visible. We can insert a movable lattice plane with variable opacities into a structural model. Drawing boundaries can be defined by ranges along x, y, and z axes as well as lattice planes.

Electron/nuclear densities, wave functions, and electrostatic potentials are visualized as isosurfaces, bird's-eye views, and two-dimensional (2D) maps. VESTA has a feature of surface colorization to show another kind of a physical quantity at each point on isosurfaces. Translucent isosurfaces can be overlapped with a structural model.

The latest version of VESTA can read in files with 47 kinds of formats such as CIF,[11] ICSD[12] [146], and PDB.[13] VESTA outputs files with 19 kinds of formats such as CIF and PDB. Users of RIETAN-FP must be pleased to learn that standard input files, hoge.ins, can be both input and output by VESTA. Three-dimensional electron densities in files hoge.xplor output by superflip [179] in the X-PLOR/CNS format can easily be visualized to locate atoms in unit cells with negative densities removed for clarity.

The entire crystal data and graphic settings can be saved in a small text file, hoge.vesta, without duplicating huge 3D voxel data. File hoge.vesta with the VESTA format contains relative paths to 3D data files and optionally a crystal-data file that are read in automatically when hoge.vesta is reopened. VESTA also makes it possible to export graphic files with 14 image formats including 4 vector-graphic ones.

VESTA 3

We further developed a next-generation 3D visualization system, VESTA 3 [26], whose main new features are summarized below:

1. drawing the external morphology (faces) of crystals,
2. superimposing displays of multiple structural models and isosurfaces with different levels,
3. extended bond-search algorithm to allow more sophisticated search for complex molecules, cage-like structures, etc.,
4. Significant performance improvements in rendering of isosurfaces and calculation of slices,
5. calculations of electron and nuclear densities, and Patterson functions from structure parameters,
6. integration of electron densities or densities of coherent-scattering lengths by Voronoi tessellation,[14]
7. improved support for various file formats,
8. undo and redo in GUI operations.

[11] http://www.iucr.org/resources/cif
[12] http://www.fiz-karlsruhe.de/icsd_home.html
[13] http://www.wwpdb.org/
[14] A C++ program for Voronoi tessellation was kindly presented by professor Takashi Ida of Nagoya Institute of Technology.

Dysnomia

As described above, Dysnomia [17, 23] is the successor to PRIMA [13]. Two types of MEM algorithms, *i.e.*, 0th-order single-pixel approximation [214], a variant of the Cambridge algorithm [215], and the Limited-memory Broyden–Fletcher–Goldfarb–Shanno (L-BFGS) algorithm [216], were implemented in Dysnomia in combination with a linear combination of generalized F constraints and arbitrary weighting factors for them. The fast L-BFGS algorithm makes it possible to reach the exact solution giving the maximum information entropy without any commercial program library such as MemSys [215].

Dysnomia outperforms its predecessor, PRIMA, in computation speed, memory efficiency, scalability, and reliability. Dysnomia automatically switches between discrete Fourier transform (DFT) and fast Fourier transform (FFT) algorithms depending on the number of observed reflections, the number of voxels in the unit cell, and space-group symmetry. In both DFT and FFT routines, symmetry operations are fully utilized wherever possible to reduce computation time. In addition, recent advances in multi-core CPUs prompted us to introduce multi-threaded parallel processing into MEM calculations.

Reliability indices in MPF analyses proved to be improved by use of multiple F constraints and weighting factors based on d in comparison with those obtained with Dysnomia. For further details in Dysnomia, refer to Refs. [17, 23].

ALBA

ALBA [20, 21] is a Fortran 90 program for the maximum-entropy Patterson (MEP) analysis of observed integrated intensities [19] (a) estimated by the Le Bail method from powder-diffraction data and (b) determined from single-crystal diffraction data. The name of the program originates from the most significant feature of the program; that is, MEP analysis is carried out **A**fter **L**e **B**ail **A**nalysis. Only a program for MEP analysis from integrated intensities obtained by the Pawley method [130] has hitherto been developed by David of RAL. No MEP analysis program has yet been distributed on the Web. Accordingly, we built a powerful MEM engine into ALBA, making alterations to that of PRIMA [13]. Thus, ultra-fast MEP analysis is possible with ALBA.

Integrated intensities of overlapped reflections in powder-diffraction data are, more or less, improved by the sophisticated MEP method, which is favorable for *ab initio* structure analysis from powder-diffraction data.

ALBA is used in combination with RIETAN-FP or EXPO [22] for *ab initio* structure analysis from powder-diffraction data by direct methods. ALBA outputs a binary file, hoge.pgrid, storing 3D Patterson functions, which are, in turn, visualized with VEND, as described in Section 5. The resulting 3D images in the unit cell serve for construction of an initial structural model by the heavy-atom method.

Most Rietveld-analysis programs incorporate the feature of Le Bail analysis because of the ease with which it can be implemented in this type of software. ALBA allows us to improve observed integrated intensities obtained with them for overlapped reflections, adding value to them.

Alchemy

Alchemy is a text converter to get file, hoge.mem, storing $|F_{\rm o}(\boldsymbol{h}_K)|$ and $\sigma\left(|F_{\rm o}(\boldsymbol{h}_K)|\right)$ for Dysnomia from results of Rietveld analysis with RIETAN-FP, GSAS, and FullProf. Only a feature of analyzing observed integrated intensities obtained from TOF neutron diffraction data by GSAS [87] was reported with regard to Alchemy [211]. Only a minor feature to convert a MEM data set binary file, hoge.fos, output by RIETAN-FP into a MEM data set text file, hoge.mem, is currently opened to the public by giving two examples, fap and garnet, in Examples.tbz. The resulting file, hoge.mem, can be analyzed by Dysnomia to give a feedback data file, hoge.fba, and a 3D densities file, hoge.pgrid or hoge.den. Details of Alchemy will be reported elsewhere.

14.7.2 Optimization of density distribution by MPF

MPF comprises the following iterative procedures.

1. Intensity data in hoge.int are analyzed by the Rietveld method with RIETAN-FP on the basis of a structural model. Optimum numbers of voxels along a, b, and c axes can be determined by (1) inputting *.lst by VESTA, (2) selecting "Model Electron densities" under the Utilities menu of VESTA, and (3) inputting resolution (< 0.1 Å). The resulting three numerical values after "Dimensions" in the Text window are voxel numbers along the three axes must be input as NBOXA, NBOXB, and NBOXC in *.ins.

2. RIETAN-FP estimates $I_{\rm o}(\boldsymbol{h}_K) = I_{\rm o}$(Rietveld) with Eq. (4.26) and calculates $F_{\rm o}(\boldsymbol{h}_K) = F_{\rm o}$(Rietveld) from $I_{\rm o}$(Rietveld) with Eqs. (4.28), (14.19), and (14.20). The real and Imaginary parts of $F_{\rm o}$(Rietveld), where contributions of X-ray dispersion, $\Delta F(\boldsymbol{h}_K)$, have been subtracted in the case of X-ray diffraction (see Friedel pairs in 3.5.1), are output to file hoge.fos in addition to $I_{\rm o}$(Rietveld).

3. Dysnomia reads in hoge.fos, calculates $\sigma\left(|F_{\rm o}(\boldsymbol{h}_K)|\right) = \sigma\left(|F_{\rm o}(\text{Rietveld})|\right)$ from $I_{\rm o}$(Rietveld) and E with Eq. (14.18), and analyzes $F_{\rm o}$(Rietveld) and $\sigma\left(|F_{\rm o}(\text{Rietveld})|\right)$ by MEM to yield 3D densities, $\rho(x, y, z)$, which are stored in file hoge.den (text file) or hoge.pgrid (binary file). Dysnomia also computes $F(\boldsymbol{h}_K) = F$(MEM) by the Fourier transform of $\rho(x, y, z)$'s in the unit cell having a volume of V:

$$F(\text{MEM}) = V \iiint \rho(x, y, z) \exp\bigl[2\pi\mathrm{i}(hx + ky + lz)\bigr]\mathrm{d}x\,\mathrm{d}y\,\mathrm{d}z. \tag{14.21}$$

   The resulting F(MEM)'s are output to file hoge.fba.

4. The $\rho(x, y, z)$ data stored in hoge.den or hoge.pgrid are visualized as isosurfaces in three dimensions with VESTA.

5. After close examination of the density images, return to step 1 to modify the structural model if necessary.

6. With RIETAN-FP, the model function is fit to the whole observed diffraction pattern by refining parameters irrelevant to the crystal structure: peak-shift parameters, scale factor,

profile parameters, lattice parameters, and background parameters (w.p.f.: **w**hole **p**attern **f**itting). Each structure factor in the model function is not calculated from any structure parameters but fixed at F(MEM) (plus $\Delta F(\boldsymbol{h}_K)$ in X-ray diffraction).

7. RIETAN-FP estimates $I_{\rm o}(\boldsymbol{h}_K)$ in a similar manner as in Eq. (4.26), that is,

$$\begin{aligned} I_{\rm o}(\boldsymbol{h}_K) &\equiv I_{\rm o}(\text{w.p.f.}) \\ &= \Delta 2\theta \sum_i y_{i\rm B} \frac{Y'_{iK}}{\sum_j Y'_{ij}}, \end{aligned} \tag{14.22}$$

and calculates $F_{\rm o}(\boldsymbol{h}_K) = F_{\rm o}$(w.p.f.) from $I_{\rm o}$(w.p.f.) with Eqs. (4.28), (14.19), and (14.20). The real and Imaginary parts of $F_{\rm o}$(w.p.f.), where contributions of X-ray dispersion, $\Delta F(\boldsymbol{h}_K)$, have been subtracted in X-ray diffraction, are output to file hoge.fos in addition to $I_{\rm o}$(w.p.f).

8. Terminate unless decreases in reliability indices, usually $R_{\rm wp}$, in step 6 are significant compared with those in the previous whole-pattern fitting.

9. Dysnomia reads in hoge.fos, calculates $\sigma\left(|F_{\rm o}(\text{w.p.f.})|\right)$ from $I_{\rm o}$(w.p.f.) and E with Eq. (14.18), and analyzes $F_{\rm o}$(w.p.f.) and $\sigma\left(|F_{\rm o}(\text{w.p.f.})|\right)$ by MEM to afford 3D densities, $\rho(x, y, z)$, from which F(MEM)'s are calculated by the Fourier transform using Eq. (14.21).

10. Return to step 6.

Let the total contributions of the nondispersive elements to F(MEM) be $A_{\rm n} + {\rm i}B_{\rm n}$ [67], which is a structure factor in the absence of X-ray dispersion (see 3.5). $A_{\rm n}$ and $B_{\rm n}$ are output in hoge.fba, as exemplified below:

```
$FB-MEM-DATA
 1374
    2    0    0     0.1802409E+02     0.1409778E-04
    2    1    0     0.6445232E+01    -0.5900732E-05
    0    2    0    -0.1726383E+01     0.6218339E-05
    1    2    0     0.2330152E+02    -0.8580548E-04
    2    2    0     0.3911456E+02     0.2979780E-04
    3    1    0     0.8400697E+02    -0.4658433E-04
    1    3    0    -0.5303686E+01    -0.4255980E-04
    3    2    0     0.4795771E+02    -0.1949889E-04
 ....
```

The first and second lines are a comment and the total number of reflections, respectively. Each line after the second line consists of h, k, l, $A_{\rm n}$, and $B_{\rm n}$.

MPF (lower box drawn with broken lines) follows the MEM/Rietveld analyses [204] (upper box drawn with broken lines). Structural details are changed in step 3 while the agreement between observed and calculated patterns is improved by fixing structure factors at F(MEM) in step 6. It is the F(MEM) data that minimize the bias toward the structural model. Steps 6−10

repeated till the convergence is attained is referred to as REMEDY cycles, serving to minimize the bias imposed on density distribution by the structural model in Rietveld analysis. The influence of the structural model in the Rietveld analysis on $\rho(x, y, z)$'s diminishes by repeating REMEDY cycles. In other words, intensity partitioning for overlapping reflections becomes more accurate with increasing number of iterations owing to derivation of additional structural information by MEM.

Such an iterative method is somewhat similar to the Le Bail method but differs from it in the point that structure factors in whole-pattern fitting are fixed at values of F(MEM) resulting from the previous MEM analysis. The REMEDY cycles weaken the influence of the structural model on $F_{\rm o}$(w.p.f.)'s. In other words, intensity repartitioning for overlapping reflections becomes more appropriate with increasing number of cycles owing to extraction of additional structural information from observed intensities of Bragg reflections.

It should be emphasized that step 6 is not Rietveld analysis but MEM-based whole-pattern fitting to get $|F_{\rm o}$(w.p.f.)|'s on which structural information contained in the intensity data is reflected more closely. Takata *et al.* [204] utilized not the whole procedures shown in Fig. 14.1 but only the part of iterative MEM/Rietveld analyses (upper box) for modifying structural models, proving its validity and capability.

The goodness-of-fit must reach a high level for successful MPF. For this purpose, we have been utilizing the powerful technique of partial profile relaxation (see 4.4) in both Rietveld analysis and whole-pattern fitting with RIETAN-FP.

As described above, the phases, ψ, resulting from the final Rietveld analysis remain unchanged throughout the REMEDY cycles though real ψ values change more or less before and after these cycles. Therefore, the final structural model needs to be reasonable to minimize the changes in ψ during MPF.

The above sophisticated methodology achieves a significant breakthrough in better representation of static and dynamic disorder, chemical bonding, nonlocalized electrons, and anharmonic thermal motion. Crystal structures are expressed not by structure parameters but in practice by 3D densities in voxels in the unit cell. MPF is, therefore, flexible enough to attain the above purposes better than a traditional approach to structure refinement, *i.e.*, Rietveld analysis. MPF is generally effective in X-ray diffraction than in neutron diffraction because structure factors are calculated from spherical atomic scattering factors by ignoring bonding electrons in Rietveld analysis. Structures of organic compounds where chemical bonds are highly covalent are particularly better represented by MPF than by Rietveld analysis.

The establishment of the MPF method leads to the availability of ultra-high-resolution 'X-ray/neutron microscopes' that allow us to visualize powder-diffraction data as 3D density images. X-Ray and neutron diffraction can be complementarily utilized for (a) more adequate expression of chemical bonding and (b) analysis of static and dynamic disorder, and anharmonic thermal vibration, respectively.

Table S-7 at the end of this document lists features of four methods of whole-pattern fitting: Pawley method [130], Le Bail method [9] (see Chap. 10), Rietveld method [10] (see Chap. 2), and whole pattern fitting in MPF (this chapter). Of course, the main purpose of MPF in

which MEM analysis and whole-pattern fitting are repeated is the determination of electron- or nuclear-density distribution. MPF can also be regarded as a kind of structure refinement, where crystal structures are represented not by structure parameters but virtually by density distribution in the unit cell.

14.7.3 Three reflection types

The algorithm for MEM analysis of $F_{\rm o}(\boldsymbol{h}_K)$'s is fundamentally the same, regardless of diffraction procedures. Some special techniques are, however, required to analyze $F_{\rm o}(\boldsymbol{h}_K)$'s derived from powder data. In principle, the MEM deals with isolated reflections whose phases have been estimated by some means. For convenience, they are referred to as type 1 reflections. $F_{\rm o}(\boldsymbol{h}_K)$'s gotten with the result of Rietveld analysis fall into type 1.

Assigning the sum of $F_{\rm o}(\boldsymbol{h}_K)$'s for a group of overlapped reflections may enhance the ability of estimation by MEM. The sums of $F_{\rm o}(\boldsymbol{h}_K)$'s are therefore allowed to be given for overlapped reflections belonging to type 2.

In the case of type 3 reflections, their peak positions are so near to $2\theta_{\rm max}$ that their full profiles are not included in the 2θ region analyzed in step 6. Such high-angle reflections are marked with 'H' (see 17.8.10) in 'Summary of possible reflections' output at the tail of hoge.ins. Nevertheless, we should also calculate the F(MEM)'s of type 3 reflections because excluding them necessarily leads to a bad profile fit near $2\theta_{\rm max}$. The F(MEM)'s of type 3 reflections are thus estimated from electron/nuclear densities determined with only $F_{\rm o}(\boldsymbol{h}_K)$'s for reflections of types 1 and 2.

On the execution of MPF, be sure to specify '1: Yes (output structure factors including those for grouped reflections and estimated for unobserved reflections) for a question 'Will you save a feedback data file?' Otherwise, a fit between observed and calculated patterns near $2\theta_{\rm max}$ become worse, which leads to an appreciable increase in $R_{\rm wp}$.

Type 2 reflections are decomposed to yield their individual $F_{\rm o}(\boldsymbol{h}_K)$'s. $F_{\rm o}(\boldsymbol{h}_K)$'s, sums of $F_{\rm o}(\boldsymbol{h}_K)$'s, and only hkl indices are provided for reflections with types 1, 2, and 3, respectively.

For overlapped reflections of type 2, the evaluation of $F_{\rm o}$(Rietveld)'s by Rietveld's procedure [10] may depend strongly on the structural model adopted in Rietveld analysis. Therefore, we implemented an option in which the sums of $F_{\rm o}(\boldsymbol{h}_K)$'s, $G_{\rm o}$, may be supplied for part of overlapped reflections to Dysnomia:

$$G_{\rm o} = \left[\frac{\sum_K I_{\rm o}(\boldsymbol{h}_K)}{s \sum_K m_K P_K L(\theta_K)} \right]^{\frac{1}{2}} \tag{14.23}$$

with the summation $\sum_K$ carried out over all the overlapped reflections. The standard uncertainty of G_0 is estimated by

$$\sigma(G_{\rm o}) = \frac{G_{\rm o}}{2} \left\{ \left[\frac{\sigma\left(\sum_K I_{\rm o}(\boldsymbol{h}_K)\right)}{\sum_K I_{\rm o}(\boldsymbol{h}_K)} \right]^2 + \left[\frac{\sigma(s)}{s} \right]^2 \right\}^{\frac{1}{2}} \tag{14.24}$$

similar to Eq. (14.15). G_o's derived in this manner are input by Dysnomia as type 2 data.

Because overlapped reflections are decomposed during the first MEM analysis without use of any structural model, they are regarded as type 1 reflections in subsequent processes in REMEDY cycles.

14.7.4 Strategy for stable convergence

We should pay attention to electron-density maps obtained from F(MEM) data in addition to the convergence test in each iteration. There is particularly a fair chance for structural estimation to be misdirected at the first iteration. Accordingly, we need to repeat steps 6−10 while comparing density maps resulting from MEM analysis with those obtained from F(Rietveld). This comparison is needed to judge whether the electron-density distribution is affected by the structural model or estimated properly by MEM.

For reflections with unsatisfactory fits between observed and calculated intensities, standard uncertainties, $\sigma(|F_o(\boldsymbol{h}_K)|)$, (see 14.5) should appropriately be increased to enhance the degree of freedom in estimation by MEM; such large residuals usually arise from imperfect representation of the real structure on condition that the intensity data are collected appropriately. If this part were partitioned among overlapped reflections in proportion to their values of Y_{iK}, MEM would estimate the structure in a way biased in favor of the structural model.

The efficiency of REMEDY cycles depends on the validity of the starting structural model. If the structure refined in step 1 differs considerably from the real one, MEM analysis may fail in structure refinement owing to the inaccurate partition of observed Bragg intensities among overlapped reflections.

Reliability indices in the whole-pattern fitting are used as the measure of the convergence in REMEDY cycles. Reliability indices in model-free MEM analysis are comparable regardless of the progress of the REMEDY cycles because the convergence criterion is a constraint function being equal to unity. Accordingly, the two reliability indices, Eqs. (14.12) and (14.13), output by Dysnomia should not be used to judge the convergence of the iterations.

14.8 Features Relevant to MEM in RIETAN-FP

14.8.1 Rietveld analysis with NMEM = 1

If `NMODE = 0` (Rietveld analysis) and `NMEM = 1`, F_o(Rietveld) data estimated on the basis of the result of Rietveld analysis are output to a MEM data set binary file, hoge.fos. This file is read in by Dysnomia, which carries out MEM analysis to record a 3D densities file, hoge.den or hoge.pgrid, and a feedback data file, hoge.fba, storing structure factors, F(MEM). VEND or VESTA is used to input hoge.pgrid or hoge.den to visualize 3D electron/nuclear-density distribution. The structural model in the Rietveld analysis is rebuilt after close checking of the density image, if necessary. These processes correspond to the so-called MEM/Rietveld method (see 14.6).

14.8.2 Subsequent MPF analysis

Further, MPF must be used to determine more accurate electron/nuclear densities. When `NMODE` is `2` (MPF) and `NMEM` is `1` (first phase) in hoge.ins, F(MEM)'s are input from hoge.fba by RIETAN-FP, and whole-pattern fitting, where parameters other than structure parameters are refined, is carried out by a nonlinear least-squares method. The resulting $|F_{\rm o}$(w.p.f.)$|$ are output to hoge.fos, which is analyzed by MEM to get hoge.fba again. In this way, MEM analysis with Dysnomia and whole-pattern fitting with RIETAN-FP are alternately repeated until reliability indices in the latter no longer decrease.

In MPF (`NMODE = 2, 3`), all the structure parameters that have been refined in the final Rietveld analysis must be input together with their ID(I)'s (dummies). They are used to calculate dispersion corrections in X-ray diffraction whereas they are dummy data in neutron diffraction. Even if part of ID(I)'s for structure parameters are set at 1, they are regarded as 0 in the interest of saving time. Accordingly, we need not change ID's at all when proceeding from Rietveld analysis to MPF. ID(I)'s set at 2 and corresponding linear constraints other than those for structure parameters may be left in hoge.ins without any changes. In other words, linear constraints for structure parameters must be commented out, if any, in MPF.

14.8.3 Option for exceptional treatment of relaxed reflections

$|F(\boldsymbol{h}_K)|$'s of reflections whose profiles are relaxed can be refined directly in MEM-based whole-pattern fitting; $|F(\boldsymbol{h}_K)|$ is input after label '`PPPn_h.k.l`' (see 17.3.15). This feature, which can be used if `NMODE = 3` and (`NPRFN = 1`, `2`, or `3`), may accelerate the convergence of MEM-based structure refinement, provided that calculated profiles are in good agreement with observed ones for the relaxed reflections. We recommend to apply this feature to only (a) X-ray diffraction data of centrosymmetric compounds and (b) neutron diffraction data in order to avoid the complexity of Friedel pairs.

14.8.4 Automatic MPF analyses

If E in Eq. (14.18) is set at too large a value, each of $F_{\rm c}$(MEM) is confined within a very narrow range near $F_{\rm o}(\boldsymbol{h}_K)$ to cause increases in noise in real space. E is usually determined so as to give reasonable $\sigma(\boldsymbol{h}_K)$'s and achieve fast convergence with fewer MEM cycles. In addition, E must be adjusted in such a way that the resulting density distribution is physically and chemically reasonable. These conditions unnecessarily require us to test a series of different E values to optimize it; meanwhile, MEM analyses must be repeated during REMEDY cycles, as described above. Executing a series of MPF analyses while changing E values is, of course, very laborious and susceptible to making mistakes because file handling and editing must be repeated several times.

To enhance laborsaving, convenient shell scripts, MPF_multi.command, written in bash for automatic execution of MPF analyses were developed [17]. They are included in the distribution files of RIETAN-FP–VENUS systems.

Figure 14.3 illustrates a flowchart of a series of MPF. Because hoge.prf is never overwritten,

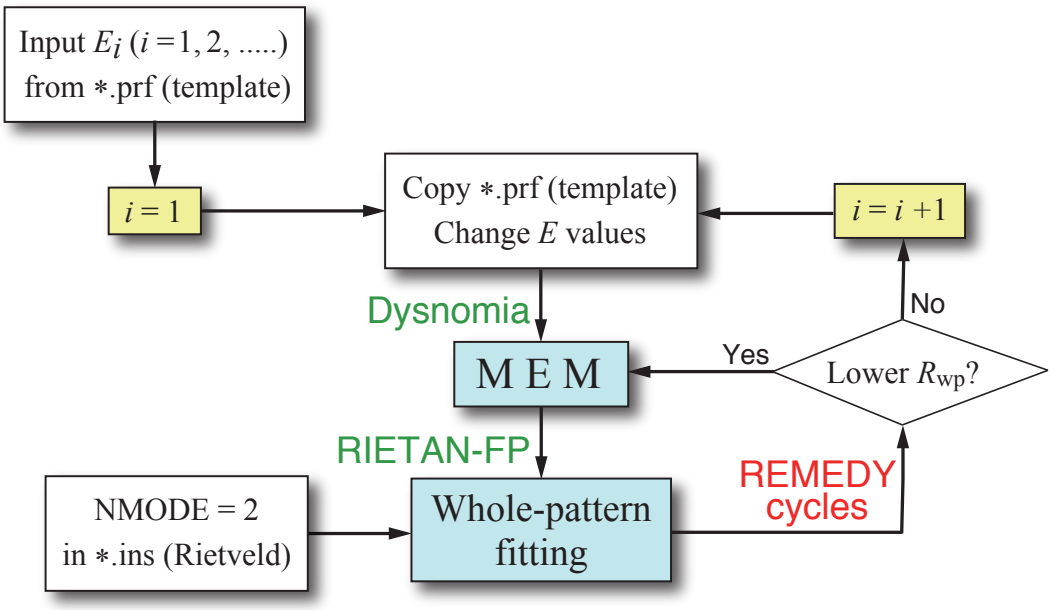

Figure 14.3: A flow chart of automatic MPF analyses for a set of E_i values.

it must be deleted prior to the execution of RIETAN-FP to update it. analyses where E is changed as specified in an input file, hoge.prf, for MEM analysis. With RIETAN.bat (a batch file for Windows) and RIETAN.command (a shell script for macOS) to run RIETAN-FP, both hoge.prf and MPF_multi.command are automatically created in the current directory if `NMEM` is set at 1 in hoge.ins. Input files for Dysnomia and RIETAN-FP are automatically set up by MPF_multi.command, while reliability indices, elapsed time, and other information about the Rietveld, MEM, and w.p.f. analyses are recorded in a log file, hoge.log. The optimum value of E is determined by (a) checking hoge.log closely and (b) visualizing 3D voxel data recorded in hoge.den or hoge.pgrid.

The two scripts have been working well for MPF analyses of a variety of compounds with combinations of RIETAN-FP and Dysnomia, helping us to make the analyses more efficient and pleasant. The content of an output file, hoge.rin, in an MPF analysis of fluorapatite from X-ray diffraction data with $E = 2894\,\mathrm{rad}^{-1}$ is listed below:

```
Rietveld analysis
  Rwp =  8.214    Rp =  6.390    RR =  9.879    Re =  5.588    S = 1.4699.....
   RB =  3.782    RF =  1.924    RF^2 =  1.933    E(SCIO) =   2832.06

MEM-based pattern fitting with E = 2894

MEM analysis No. 1
  Elapsed time: 35.223 s
  Number of cycles = 2814
  CONSTR =  9.9999742E-01   RF = 0.010790
 CONSTRw =  9.9999742E-01  wRF = 0.011087
```

```
w.p.f. No. 1
  Elapsed time: 1.694 s
  Rwp =  7.549    Rp =  5.721    RR =  8.828    Re =  5.598    S = 1.3485.....
   RB =  1.402    RF =  0.902    RF^2 =  0.924    E(SCIO) =   2830.47

MEM analysis No. 2
  Elapsed time: 38.043 s
  Number of cycles = 3009
  CONSTR =  9.9999823E-01   RF = 0.010909
 CONSTRw =  9.9999823E-01  wRF = 0.010690

w.p.f. No. 2
  Elapsed time: 1.730 s
  Rwp =  7.599    Rp =  5.691    RR =  8.784    Re =  5.598    S = 1.3575.....
   RB =  1.312    RF =  0.857    RF^2 =  0.904    E(SCIO) =   2832.48
```

This MPF analysis converged in w.p.f. No. 1 because R_{wp} increased from 7.549 % in w.p.f. No. 1 to 7.599 % in w.p.f. No. 2. R_{wp} decreased considerably from 8.214 % in the Rietveld analysis to 7.549 % in w.p.f. No. 2, which is mainly ascribed to the high covalent character of P–O bonds in phosphate ions.

Chapter 15

STRUCTURE REFINEMENT BASED ON MAXIMUM-LIKELIHOOD ESTIMATION

Structure refinement from powder diffraction data is based on the premise that the sample contains an infinite number of crystallites which satisfy Bragg's condition of diffraction. However, unless the sample powder is fine enough, this prerequisite no longer holds approximately, which exerts a dominant influence of statistical variations (particle statistics) on observed diffraction intensities [48, 217]. Particle statistics are improved by measuring diffraction data while rotating a sample holder in a sample plane, which has a disadvantage that the quantity of the sample is considerably increased.

Ida and Izumi [218, 219] proposed an original method of structure refinement where statistical uncertainties are estimated from X-ray powder diffraction data measured with the Bragg–Brentano geometry without rotating the sample. In this method, a proper model is constructed for the statistical uncertainty at each observed point, and structure and profile parameters are refined by maximum-likelihood estimation (MLE) [220] on the basis of the statistical-uncertainty model. In their approach, the objective function to be minimized by nonlinear least-squares fitting is modified from Eq. (2.1) to

$$S(\boldsymbol{x}) = \sum_{i=1}^{N} \left\{ \ln \sigma_i + \frac{[y_i - f_i(\boldsymbol{x})]^2}{\sigma_i} \right\} \tag{15.1}$$

with

$$\sigma_i^2 = [\sigma_i(\text{count})]^2 + [\sigma_i(\text{particle})]^2, \tag{15.2}$$

where σ_i is the standard uncertainty of the observed intensity, y_i, at step i, $\sigma_i(\text{count})$ is that due to counting statistics ($w_i = 1/[\sigma_i(\text{count})]^2$ in Eq. (2.1)), and $\sigma_i(\text{particle})$ is that due to particle statistics. In conventional X-ray diffraction experiments,

$$[\sigma_i(\text{count})]^2 = y_i, \tag{15.3}$$

$$[\sigma_i(\text{particle})]^2 = \frac{C(\text{particle})[y_i - y_\text{b}(2\theta_i)]^2 \sin\theta_i}{m_K}, \tag{15.4}$$

where C(particle) is the unknown proportional constant, $y_{\mathrm{b}}(2\theta_i)$ is the background function at step i, and m_K is the multiplicity. The value of C(particle) can be uniquely determined by minimizing $S(\boldsymbol{x})$.

Ida and Izumi applied this elaborate technique to X-ray powder diffraction data of fluorapatite, lead(II) sulfate, and barium sulfate and successfully obtained structure parameters that are close to those resulting from single-crystal X-ray analyses, which is a strong piece of evidence for the validity of their new methodology.

This sophisticated methodology is particularly effective for samples that are not fine enough and those containing heavy elements. A software package, which consists of macros for Igor Pro, for the new technique is distributed free of charge at a Web page of Ida.[1] RIETAN-FP is used as a pattern-fitting engine in the new method of structure refinement.

On the use of this technique, integer flags `NINT`, `NPAT`, and `INDREF` in hoge.ins must be set as follows:

```
NINT = 11: General-3 format.
NPAT = 2: Output an Igor text file, hoge.itx, to plot Rietveld-refinement patterns.
INDREF = 1: The profile of each reflection is output to waves XREF and YREF.
```

Refer to 17.4.12 and 17.7.2 for further information about the above flags.

[1] Available for download at http://www.crl.nitech.ac.jp/~ida/research/introduction/ida_izumi/index-j.html

Chapter 16

PORTING AND APPLICATION INTERACTION

16.1 Supported Platforms

The following two operating systems are currently supported: macOS and Microsoft Windows (hereafter abbreviated to Windows).

The distribution files for macOS and Windows were compressed into archive files with the dmg and zip formats, respectively. The disk image file, ∗.dmg, can easily be mounted by double-clicking on its icon. The zip file, ∗.zip, can easily be decompressed with any archivers for Windows or a decompression feature included in Windows.

Regardless of the platforms, names of folders (entire file hierarchy) used to install the RIETAN-FP–VENUS system and execution of programs contained in it must consist only of alphanumeric characters, hyphen '-', underscore '_', and space. No safe performance is ensured if other characters such as parentheses, '(' and ')', are contained in them. On the other hand, Names of files used to execute programs in the RIETAN-FP–VENUS system must consist only of alphanumeric characters, '-', '_', and dot '.' (only one for the extension). Beware lest spaces may be included. The extension may contain only alphanumeric characters

16.1.1 macOS version

RIETAN-FP for macOS was built with Intel Fortran Composer XE 2011 (update 13) for the Intel 64 architecture. It is not a universal binary. Macs equipped with 64-bit processors are, therefore, required to run it whereas it cannot be run on PowerPC Macs. This macOS version has been built with a bash script for OS X 10.6.X (Snow Leopard) or later. It is a Terminal (console) application dedicated for 64-bit operating systems.

On macOS, RIETAN-FP and related programs are run using shell scripts hoge.commands created by make_commands, whose source code (make_commands.scpt) was written in AppleScript. Their standard outputs can be browsed with editors such as less, emacs, nano, vim,[1] Jedit X (commercial program),[2] and mi.[3]

[1] macOS includes less, emacs, nano, and vim.
[2] http://www.artman21.com/en/jedit_x/
[3] http://www.mimikaki.net/en/index.html

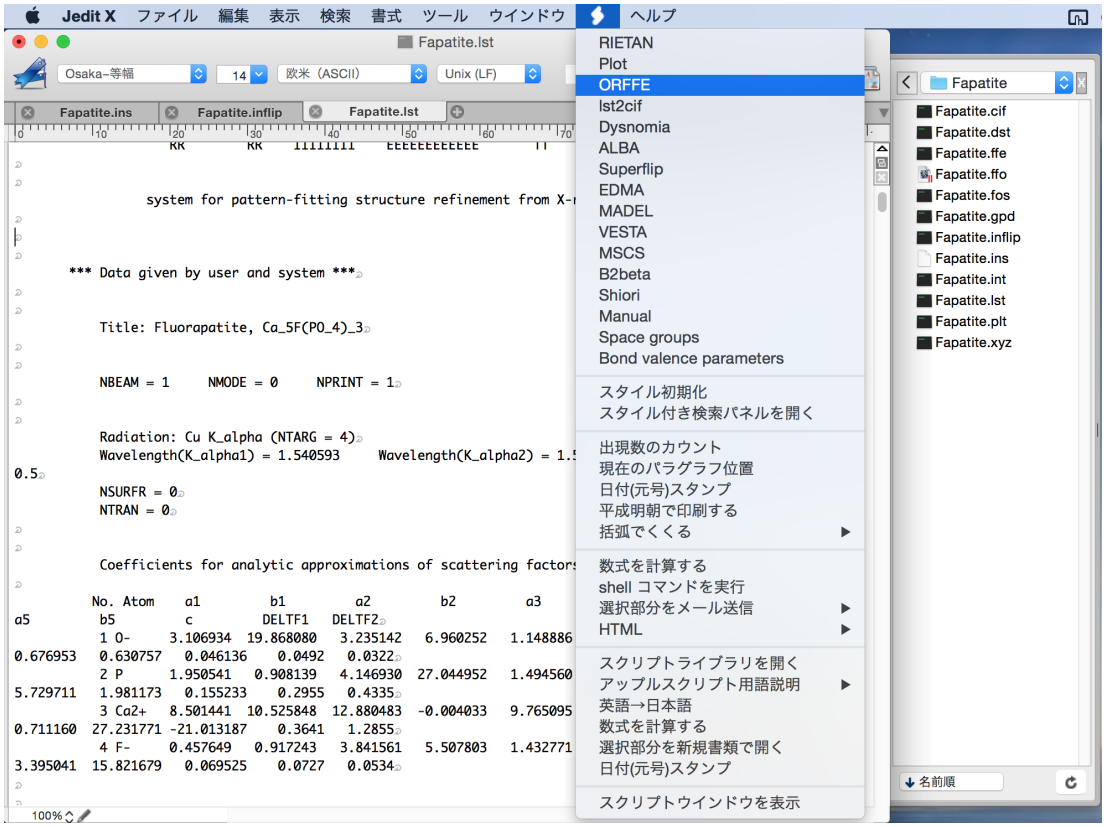

Figure 16.1: Selecting ORFFE in the pull-down menu of macros after the Rietveld refinement of fluorapatite. A file drawer appears at the right-hand side

In addition, the use of Jedit X makes it possible to use the RIETAN-FP–VENUS assistance environment utilizing macros written in AppleScript. In this user-friendly environment, RIETAN-FP and related programs can be driven with a pull-down menu of macros (**Fig. 16.1**), a context menu (control + click), or keyboard shortcuts assigned by the user. Outputs from the programs are automatically opened by Jedit X, whose multiple-tab window is very useful when dealing with two or more files. Details in the RIETAN-FP–VENUS assistance environment are described in Readme_scpt.pdf included in an archive file documents.zip.

16.1.2 Windows version

Though RIETAN-FP may run just fine on Windows XP/Vista, Windows 7/8/10 are preferred to Windows XP/Vista because RIETAN-FP for Windows has now been used almost exclusively on Windows 7/8/10.

RIETAN-FP for Windows was built with Intel Visual Fortran Composer XE 2013 SP1 for IA-32 and Intel 64 architectures in combination with an application development environment called Microsoft Visual Studio 2010 Shell bundled with Visual Fortran Composer XE 2013. Only the 32-bit version is installed on 32-bit Windows with an installer, Install_RIETAN_VENUS.bat, included in a distribution file.

An integrated assistance environment for RIETAN-FP–VENUS has been built to edit input and output files, launch various applications including not only the RIETAN-FP and VENUS

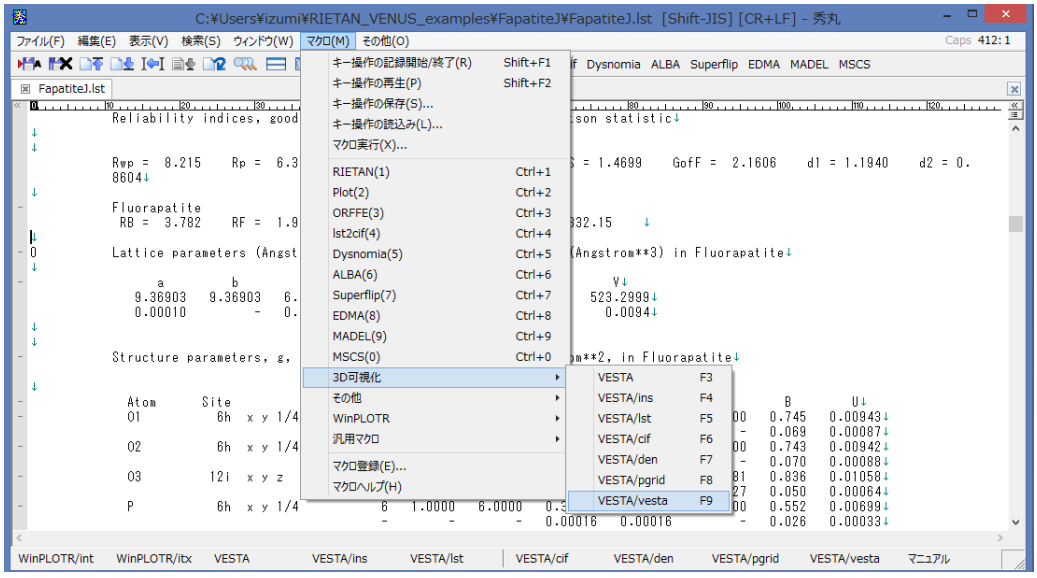

Figure 16.2: Selection of an item, VESTA/vesta, in the pull-down menu of Macro in the integrated assistance environment based on Hidemaru Editor. Buttons, function keys, and tabs of files are seen in this window.

systems but also EXPO [22], superflip [179], EDMA [221], PowderX [104], MADEL (a Fortran program to calculate electrostatic site potentials and a Madelung energy by the Fourier method), WinPLOTR [107], and DICVOL14 [222] (with the aid of WinPLOTR), and manipulate files within a popular text editor, Hidemaru Editor,[4] for Windows. With the environment consisting of original Hidemaru macros and a dynamic link library (DLL) called Dengaku DLL,[5] we can enjoy GUI operations through pull-down menus, buttons, function keys, and a popup menu using mice and shortcut keys (**Fig. 16.2**).

Hidemaru macros are similar in grammar to the C language. It is, therefore, relatively easy to delete, add, and reconstruct the structure of Hidemaru macros.

This assistance environment must be a great boon to those who hate character user interfaces using the command prompt. For details in this environment, read Readme_macros.pdf contained in the archive file documents.zip.

16.1.3 End-of-line characters in text files

Beware lest the end-of-line character in each text file is incompatible with the current operating system. The end-of-line characters should be

1. Windows: CR+LF
2. macOS: LF or CR+LF

Be sure that the end-of-line character of all the text files used by RIETAN-FP on macOS is not CR.

For further details in RIETAN-FP for the two platforms, see Readme files included in the distribution files for macOS and Windows.

[4] http://hide.maruo.co.jp/software/hidemaru.html
[5] http://www.ceres.dti.ne.jp/~sugiura/

16.2 Collaboration with VESTA

VESTA [1, 25, 26] is cross-platform free software to visualize crystal structures and 3D voxel data in three dimensions. It is included in the 3D visualization system VENUS. A C++ GUI framework called wxWidgets [213] is adopted in VESTA to build the graphical user interface of VESTA, providing us with function wxExecute and class wxProcess to call external programs easily from existing processes. Therefore, we can virtually extend VESTA by running other applications as a child process, yet keeping its core code simple and small.

VESTA utilizes wxWidgets to simulate X-ray and neutron powder-diffraction patterns with RIETAN-FP. On selection of the "Powder Diffraction Pattern···" item under the Utilities menu, a series of procedures, *i.e.*, generation of an input file, hoge.ins, for RIETAN-FP (see 17.3), execution of RIETAN-FP, and graphic representation of the resulting data in file hoge.itx with a graphing program such as Igor Pro and gnuplot (see 17.7), are executed by VESTA as if they were implemented in VESTA.

As described in 8, the feature of converting crystal lattices in VESTA helps us to relate the MUC (magnetic unit cell) phase of a magnetic material to the CUC (crystallographic unit cell) phase, facilitating Rietveld refinements of collinear magnetic structures. VESTA is also very useful in representing magnetic structures by attaching arrows to magnetic atoms, as can be appreciated from Fig. 8.2.

VESTA can also be used to visualize bonds and bond angles recorded in hoge.ffe output by ORFFE [136] as well as atoms within the drawing boundaries (see 17.6).

The user of RIETAN-FP must be very pleased to hear that VESTA can both input and output hoge.ins, which helps beginners to get a starting hoge.ins file. An output file, hoge.ins (**Fig. 16.3**), is obtained from a template hoge.ins file specified in the "Preferences" dialog box under the File menu in VESTA.

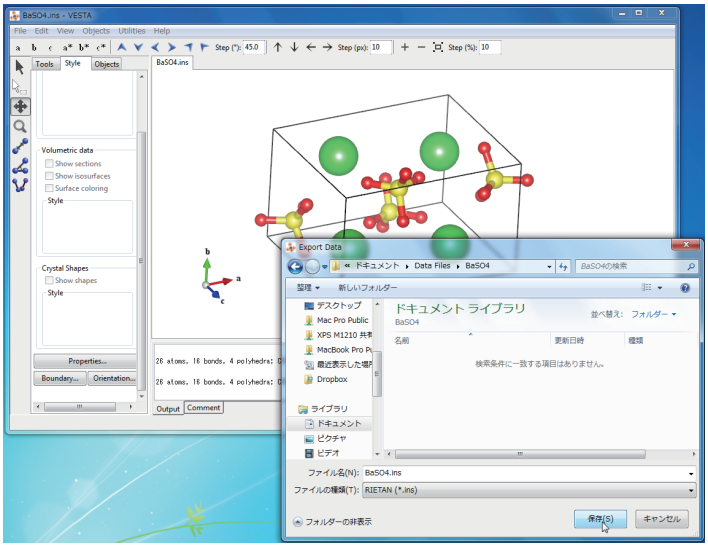

Figure 16.3: Outputting a hoge.ins file for $BaSO_4$ in VESTA

VESTA can input a standard output, hoge.lst, of RIETAN-FP to display a crystal structure. It should be noted that (site multiplicities) plus (Wyckoff letters) recorded in hoge.lst are saved in hoge.vesta with the VESTA format (see 17.1).

VESTA is capable of outputting a series of *_hoge.vesta containing lattice and structure parameters obtained in spcified cycles of nonlinear least-squares fitting. Let i ($i = 1, 2, 3, ...$) be cycle numbers in structure refinement, j the starting cycle number, and k the increment of cycle numbers. If hoge.vesta shares the same folder with hoge.ins and hoge.int, including either of the following two comment lines,

`#Cycle` j k (modified Marquardt method or Gauss–Newton method),
`#Iter` j k (conjugate-direction method),

RIETAN-FP creates a new subfolder named VESTA_folder if it is absent in the current folder whereas all $*$.vesta files remaining in VESTA_folder are deleted in the presence of VESTA_folder. Next, RIETAN-FP outputs a series of VESTA files, *_hoge.vesta, in subfolder VESTA_folder:

- Cycle$i$_hoge.vesta (i: cycle numbers in the modified Marquardt method or Gauss–Newton method)
- Iter$i$_hoge.vesta (i: cycle numbers in the conjugate-direction method)

where lattice and structure parameters are dynimically updated to those refined in cycle number $j + k(i - 1)$. During the execution of RIETAN-FP, crystal structures displyaed in VESTA are dynamically updated by inputting *i_hoge.vesta by VESTA.

A utility program named lst2cif (see Appendix E) included in the distribution files of RIETAN-FP enables us to convert hoge.lst and hoge.dst (see Appendix D) into a CIF (Crystallographic Information File) [223], which can also be input by VESTA.

Chapter 17

INPUT AND OUTPUT FILES

17.1 Files Used by RIETAN-FP

RIETAN-FP inputs and outputs text files as many as 36 to carry out several different kinds of jobs. These files fall into four categories: (a) data base files sharing the same folder with the executable binary file of RIETAN-FP, (b) files input by RIETAN-FP, (c) files output by RIETAN-FP, and (d) scratch files with no names.

Table 17.1 summarizes main input and output files of RIETAN-FP; part of them were described in ref. [105]. Files belonging to categories (b) and (c) have to be named according to a definite fashion. The names of the files in this section were given for a basename of 'hoge'; needless to say, 'hoge' in Table 17.1 should be replaced by any other name. Beware lest the basename of each input file contains a space, '(', or ')'.

Extensions of files in categories (b) and (c) may be changed appropriately by modifying batch files (Windows) or shell scripts (macOS and Linux). For example, changing '`itx`' into '`pat`' is of no matter at all. Nevertheless, the extensions in Table 17.1 will be described throughout this document for convenience.

Unit numbers assigned to the input and output files in the source code must be useful when error messages are received during inputting or outputting them because such messages usually include unit numbers.

Note that those refinable parameters in hoge.ins which are contained in the model function are updated after Rietveld analysis if `NUPDT = 1`, which is the reason why hoge.ins can be both input and output by RIETAN-FP, as written in Table 17.1. This is the reason why hoge.ins may be output by RIETAN-FP.

The format of two files, hoge.ffi and hoge.ins, is compatible with that of hoge.hkl output by EXPO [22] to record results of Le Bail analysis. Accordingly, EXPO can be used after Le Bail analysis using RIETAN-FP, and *vice versa*.

Table 17.1 includes the names of the following five related programs:

1. STRUCTURE TIDY [169]: a program (incorporated into RIETAN-FP) to standardize crystal data,

2. ORFFE [136]: a program to calculate geometrical parameters from lattice and crystal-structure parameters (included in the distribution files of RIETAN-FP),

3. Dysnomia [17, 23]: a program for MEM from X-ray and neutron diffraction data,

4. ALBA [20, 21]: a program for the maximum-entropy Patterson method,

5. VESTA [1, 25, 26]: a 3D visualization system for crystal and electronic structures

A pair of file, xdc.plt and xdc.gpd, are, respectively, converted into xdc-∗.plt and xdc-∗.gpd (*: atomic symbol) by a Hidemaru or AppleScript macro xdc to give a PDF file, xdc-∗.pdf, of a graph where f' and f'' are plotted against λ (E) by gnuplot (see Fig. 3.2). The xdc macro is applicable to both characteristic and synchrotron X rays.

PyAbstantia was written by Dr. S. Nishimura of the University of Tokyo to create a file, BVS3d.pgrid, storing differences, $|\Delta V|$, between calculated and ideal BVSs. Only a macOS version is presented at present. BVS3d.pgrid is relatively compact since it is a binary file containing voxel data only in the asymmetric unit. PyAbstantia consists of three Python scripts (pyabst.py, calbvm.py, and write_bvf.py) and a Fortran program, bvs_omp.so. Two Python libraries must be installed to use PyAbstantia: NumPy[1] and Pymatgen.[2]

Three-dimensional visualization of $|\Delta V|$ values with VESTA is useful in shedding light on conduction pathways of mobile ions in ion conductors such as lithium, sodium, and oxide ion ones. Continuous spaces with $|\Delta V| = 0.1$–0.4 are desirable in ion conductors. The BVS mapping is based on a most simplified model, neglecting some significant effects. We, therefore, need to be conscious of its limitation. If the /Applications/PyAbstantia folder exists on Macs, PyAbstantia can be launched by inputting `NMODE = 1` and `NBVS3D = 1` in hoge.ins after executing RIETAN-FP on the RIETAN-FP–VENUS assistance environment. That is, the simulation mode of RIETAN-FP enables us to plot X-ray and neutron powder diffraction patterns and, further, visualize conduction pathways in ion conductors.

Arguments of the executable file for RIETAN-FP are

```
hoge.ins hoge.int hoge.bkg hoge.itx hoge.hkl hoge.xyz hoge.fos hoge.ffe
hoge.fba hoge.ffi hoge.ffo hoge.vesta hoge.plt hoge.gpd hoge.alb hoge.prf
hoge.inflip hoge.exp
```

while the standard output should be redirected to `hoge.lst`. Dysnomia, ALBA, and VESTA are contained in the three-dimensional visualization system VENUS. If needed, parts of hoge.plt, hoge.alb, hoge.prf, hoge.inflip, and hoge.exp may be modified before executing an external program.

[1] http://www.numpy.org/
[2] http://pymatgen.org/

Table 17.1: Input and output files of RIETAN-FP; No.: unit number, In: input, Out: output

File	No.	In	Out	Content
asfdc	2	○		A file storing numerical values such as atomic weights, eleven coefficients for analytical approximation of atomic scattering factors [55], dispersion corrections for characteristic X rays [60], bound coherent-scattering lengths, bound incoherent-scattering cross section, and absorption cross sections [24]
xdc.bin	90	○		A binary file storing f_1, f_2, $f_{\rm rel}$, $f_{\rm NT}$, and Z for 92 elements (see 3.5.1)
mac.tbl	93	○		A text file where mass attenuation coefficients, $\mu_{\rm m}/(\mathrm{cm}^2\ \mathrm{g}^{-1})$, of 92 elements are recorded as a function of the photon energy E/MeV [161] (see 7.2)
spgra	11	○		A file storing information on 230 space groups, *e.g.*, coordinates of equivalent positions compiled in Ref. [72] and Hall's symbols of space groups [224]
Spgr.daf	121	○		A file storing Hermann–Mauguin space-group symbols read in by STRUCTURE TIDY (see Chap. 9)
Sets.daf	120	○		A file read in by STRUCTURE TIDY
constr_beta	12	○		A file storing types of constraints imposed on anisotropic atomic displacement parameters, β_{ij}, for all the general and special positions of 230 space groups [70, 71]; these types are output after a list of final atomic displacement parameters
j0_j2.dat	130	○		A file storing coefficients to approximate $\langle j_0 \rangle$ and $\langle j_2 \rangle$ magnetic form factors [81]
hoge.ins	5	○	○	A standard input file created by a user (see 17.3)
N/A	4	○	○	A scratch text file converted by a preprocessor called Tink (see 17.3) from hoge.ins
N/A	13	○	○	A scratch file (`FORM = 'UNFORMATTED'`) output and input when NRANGE = 1 (see 3.12.2)
N/A	14	○	○	A scratch text file output and input when imposing restraints on geometrical parameters (see 5.2)
hoge.int	3	○		A file storing X-ray/neutron intensity data (see 17.4)
hoge.bgr	16	○		A file created by WinPLOTR [107] or pcr2bgr to store discrete background intensities (see 3.12.3 and 3.12.4)
hoge.bkg	8	○		A file storing background intensities (see 3.12 and 11.2)
hoge.ffe	10	○		A file output by ORFFE [136] to store geometrical parameters and their series numbers (see 5.2) for imposing nonlinear constraints on geometrical parameters (hoge.ffe = hoge.dst + serial numbers; see Chap. 5); created only when hoge.ffe is absent and `NDA > 0`

(continued on the following page)

(continued from the previous page)

File	No.	In	Out	Content
hoge.fba	32	○		A file created by Dysnomia for whole-pattern fitting based on MEM with RIETAN-FP (see 14.7.2)
hoge.itx	20		○	A file storing data to plot a Rietveld-refinement pattern (observed, calculated, and difference patterns) or a simulated pattern with a graphing program Igor Pro and RietPlot
hoge.hkl	21		○	An input file for Fourier or difference Fourier synthesis with VESTA (see 14.7.1)
hoge.xyz	9		○	An input file for ORFFE [136] to calculate interatomic distances and bond angles
hoge.fos	30		○	A file storing data to be analyzed by MEM with Dysnomia
hoge.ffi	22		○	A file storing initial estimated $I_{\rm o}(\boldsymbol{h}_K)$'s for Le Bail analysis; output by RIETAN-FP, EXPO [22], and ALBA [20, 21]
hoge.ffo	23		○	A file storing $I_{\rm o}(\boldsymbol{h}_K)$'s resulting from Le Bail analysis
hoge.vesta	98		○	An input file to draw a crystal structure with VESTA
hoge.plt	19		○	A gnuplot script file for plotting results of Rietveld analysis or simulation of a X-ray or neutron powder pattern (see 17.7.1)
hoge.gpd	18		○	A gnuplot data file for plotting results of Rietveld analysis or simulation of a X-ray or neutron powder pattern (see 17.7.1)
Rwp.gpd	15		○	A file storing reliability indices, $R_{\rm wp}$, in all cycles.
hoge.alb	33		○	An input file for the maximum-entropy Patterson method program, ALBA [20, 21]
hoge.prf	34		○	An input file for the maximum-entropy method program, Dysnomia [23]
hoge.inflip	31		○	An input file for charge flipping with superflip [179] for the dual-space method
hoge.exp	24		○	An input file for *ab initio* structure analysis with EXPO [22]
hoge.lst	6		○	A standard output file corresponding to printer output
xdc.plt	91		○	A gnuplot script file, xdc.plt, to plot f' and f'' against λ (E)
xdc.gpd	92		○	A text file where f' and f'' for constituent elements are recorded as a function of λ (E)
BVS.inp	140		○	An input file for PyAbstantia to visualize bond-valence-sum (BVS) maps [225, 226]
BVEL.inp	140		○	An input file for PyAbstantia to visualize Bond-Valence Energy Landscape (BVEL) maps [227]

17.2 Limitation of Data Sizes

Table 17.2 lists integer constants to set maximum dimensions of many arrays are defined in PARAMETER statements in the source code of RIETAN-FP. These values are so large that we seldom need to increase them to adapt RIETAN-FP for specific refinements.

Table 17.2: Maximum numbers of data dealt with RIETAN-FP

Name	Value	Remark
NB	20000	Reflections
NP	80000	Intensity data points
NA	15	Chemical species including virtual ones
NT	2000	Parameters to calculate model functions
NR	1500	Refinable parameters
NSF	1200	Refinable crystal and magnetic structure parameters
NAP	400	Atoms in the asymmetric unit
NCS	400	Linear constraints
MAXNL	1000	Nonlinear restraints
NPH	16	Phases
MAXLAB	800	Labels
MAX_MAGN_ATOM	50	Magnetic atoms per phase

17.3 Standard Input File

Some Rietveld-refinement programs require fixed-column, formatted input data and codewords for parameters contained in the model function. Such an input manner is too old-fashioned and inconvenient for most users. Interactive menu operations using graphical user interfaces are much more user-friendly but rather troublesome for routine use, making the overlooking of the whole input data nearly impossible because of hierarchic menu structures. In addition, users cannot modify the content of a menu system at all or write some comments on input data. RIETAN-FP presents a novel and creative method of entering data using a preprocessor, Tink, for hoge.ins. The resulting character user interface is suitable not only for experts of Rietveld analysis and/or computers but for beginners.

Input files described in conformation to rules of Tink with a text editor are converted into scratch files by a preprocessor called Tink, which was named after a pretty fairy, Tinker Bell, in "Peter and Wendy." Tink removes comments, skips unnecessary lines, decodes remaining lines, and writes a scratch file. The resultant scratch file contains only integer-, real-, and character-type variables input and dealt with actually by RIETAN-FP. Tink is simple but user-friendly, enabling us to enter data without referring to the manual in nearly all the cases. Main advantages of Tink over graphical user interfaces are its portability, straightforwardness, speedy operation, and

flatness (*i.e.*, not hierarchic).

Usually, we modify one of template files for hoge.ins, which are sufficiently self-explanatory, included in distribution files of RIETAN-FP to adapt it to our analysis. Beware lest the order of data in the template file is changed; this will cause a serious trouble during preprocessing by Tink.

Another convenient manner of getting hoge.ins is conversion of a template file with a fixed name, template.ins, into hoge.ins from a crystallographic information file (CIF), hoge.cif, by a utility program, cif2ins, which can be used on the RIETAN-FP–VENUS assistance environment (see 16.1). The starting files, template.ins and hoge.cif, must share the same folder, where hoge.ins is output by cif2ins. A close check of hoge.cif is highly desirable. For the official specification of the CIF, refer to the Web page of CIF.[3] The progress of data processing by cif2ins can be monitored in a command prompt window (Windows) or a Terminal window (macOS), where an error message or warnings may appear. For example, execution of cif2ins by inputting a CIF of brookite-type titanium(IV) oxide gives the following standard output:

```
Checking lengths of lines .....
Lines in this CIF are no longer than 80 characters
Reading a phase name .....
_chemical_name_mineral: Brookite
Phase name: Brookite
_chemical_formula_sum: Ti O2
Getting element names and amounts of substances from _chemical_formula_sum .....
Ti: 1
 O: 2
Reading a Hermann-Mauguin symbol or a space-group number .....
_symmetry_space_group_name_H-M: P b c a
Space-group number obtained from spgr.daf:  61
Reading lattice parameters .....
Lattice parameters:  9.17400  5.44900  5.13800  90.0000  90.0000  90.0000
Determining kinds of columns from lines containing '_atom_site_' .....
_atom_site_label
_atom_site_fract_x
_atom_site_fract_y
_atom_site_fract_z
Strictly speaking, '_atom_site_U_iso_or_equiv' must be supplied in a CIF
Reading label/atom and structure parameters for all the sites ...
Ti   0.12890   0.09720   0.86280
O1   0.00950   0.14910   0.18350
O2   0.23140   0.11100   0.53660
Number of sites in the asymmetric unit:  3
Determining kinds of columns from lines containing '_atom_site_aniso_U_' if any .....
_atom_site_aniso_label
_atom_site_aniso_U_11
_atom_site_aniso_U_22
_atom_site_aniso_U_33
_atom_site_aniso_U_12
_atom_site_aniso_U_13
_atom_site_aniso_U_23
```

[3] http://www.iucr.org/resources/cif

```
Reading label/atom and anisotropic itomic displacement parameters, U_ij .....
Ti 0.00554 0.00572 0.00294 0.00000 0.00024 -0.00028
O1 0.00725 0.00677 0.00348 -0.00101 0.00167 -0.00113
O2 0.00298 0.01143 0.00588 0.00152 0.00119 0.00184
Writing the top part before the title .....
Writing the title .....
Writing the element names and their amounts of substances .....
Writing the element names .....
Writing f' and f'' (= 0.0) .....
Writing the phase name .....
Writing the space-group number .....
Writing the Hermann-Mauguin symbol .....
Writing the lattice parameters .....
Calculating coefficients to convert U_ij into beta_ij .....
Writing structure parameters .....
Writing the remaining part .....
```

Inserting a line containing only '`#std`' in hoge.cif makes it possible to output hoge.ins for standardization of crystal data in conformity with Structure Tidy (see Chap. 9) in the simulation mode (`NMODE = 1`). The standardization can be carried out by running RIETAN-FP subsequently to input hoge.ins and obtain standardized lattice and structure parameters in hoge.lst. Then, the resulting standardized crystal data must be introduced into hoge.ins by oneself.

17.3.1 General rules for inputting data consistently

The following eight rules should be obeyed throughout the input file.

1. One line should be less or equal to 80 columns.
2. Comments (see 17.3.2) may be input up to 150 columns. Comments in columns larger than 150 are wasted when updating hoge.ins by setting `NUPDT` at 1.
3. When two or more data are input in one line, one or more space(s) should be placed between two data.
4. Never input tabs to separate two data or to indent lines.
5. If the number of data input in one line is variable and has not been determined as yet, the end of input for the line must be indicated by '`/`' at its tail.
6. When entering a series of lines whose number has not been determined as yet, the end of these lines must be indicated by '`}`' at the tail of the last line or at the top of the next line.
7. In (a) lines to contain two or more CHARACTER data or (b) lines where CHARACTER data are mixed with numerical values (real and integer), CHARACTER data containing at least one space, ' ', have to be enclosed by a pair of single quotation marks to indicate their ranges. Of course, CHARACTER data may be enclosed by a pair of single quotation marks even if they contains no spaces.
8. Rule 7 is not applicable if the whole line is read in as a single CHARACTER variable.

If rule 1 is violated, for example in line No. 871, an error message,

```
Line #871 may contain input data in columns exceeding 80
```

is output, and RIETAN-FP stops immediately. Rules 5 and 6 are required so as not to input various numbers of data by users themselves. We can learn lines (positions) where '/' and '}' should be located, referring to template files included in the distribution files of RIETAN-FP. For example, in the following lines to give mole fractions of two virtual chemical species, M1 and M2 [228],

```
M1  Ba  0.633  Nd  0.367 /
M2  Nd  0.675  Ce  0.325 /
}
```

'/' in the second and third lines shows the end of input data for current virtual chemical species while '}' in the final line indicates the end of virtual chemical species. The above three lines state that `M1` is composed of 63.3 % of Ba and 36.7 % of Nd while `M2` is composed of 67.5 % of Nd and 32.5 % of Ce.

Beware lest two-byte characters, in particular a space, control characters, or tabs are input as data, which causes inexplicable errors.

17.3.2 Comments

With several kinds of template files, we can easily learn which data should be input in each line because many comment lines are included whose first columns are '`#`'. '`#`' can be also located after input data; the part from '`#`' to the end of the line is regarded as a comment. Two-bytes characters, *e.g.*, chinese (kanji), hiragana, katakana, and hangul characters, can be used in comments. These lines can be freely deleted or modified, and new lines as well as memoranda may be added by users. Data located separately in two or more lines can be combined together if they are input by list-directed READ statements. It is a disadvantage of menu operations that no such memoranda can be added at all in the screen output.

Lines where the first character except space is '`!`' are another kind of comment lines, in analogy with Fortran 90/95. They can be used as bookmarks (Shiori in Japanese) in the RIETAN-FP–VENUS integrated assistance environments using Hidemaru Editor and Jedit X (see 16.1). Clicking a bookmark in an outline analysis frame (Windows) or an information drawer (macOS) makes it possible to jump to the corresponding string in the text window of hoge.ins. This feature greatly enhances the convenience of the assistance environments. For details in Shiori, refer to Readme_macros.pdf for Windows and Readme_scpt.pdf for macOS.

Lines whose last characters are '`{`' are regarded as comment lines if their lengths are less than 81. Comments may be also placed after '`}`' without being preceded by '`#`'. This feature is very convenient when '`{`' is followed by '`}`' showing the end of a series of lines. That is, a block surrounded by a pair, '`{`' (begin) and '`}`' (end) is made clear as in the C language. For example, the input data for the virtual chemical species [228] (see 17.3.1) may include comments as follows:

```
Virtual chemical species {
M1  Ba  0.633  Nd  0.367 / # Metal on the rock-salt layer
M2  Nd  0.675  Ce  0.325 / # Eight-coordinated atom in the fluorite block
} End of virtual chemical species.
```

Another example of comments, which are attached to linear constraints imposed on structure and profile parameters, are given below:

```
Linear constraints for parameters with ID(I) = 2 {
A(O2,B)=A(O1,B); A(O3,B)=A(O1,B); A(O4,B)=A(O1,B)
A(O5,B)=A(O1,B); A(O6,B)=A(O1,B); A(O7,B)=A(O1,B)
A(O8,B)=A(O1,B); A(O9,B)=A(O1,B); A(O10,B)=A(O1,B)
A(O11,B)=A(O1,B); A(O12,B)=A(O1,B)
A(GAUSSO12,1)=A(GAUSSO1,1)
A(GAUSSO12,2)=A(GAUSSO1,2)
A(GAUSSO12,3)=A(GAUSSO1,3)
A(LORENTZO12,1)=A(LORENTZO1,1); A(LORENTZO12,3)=A(LORENTZO1,3)
A(ASYMO12,1)=A(ASYMO1,1)
A(GAUSSO13,1)=A(GAUSSO1,1)
A(GAUSSO13,2)=A(GAUSSO1,2)
A(GAUSSO13,3)=A(GAUSSO1,3)
A(LORENTZO13,1)=A(LORENTZO1,1); A(LORENTZO13,3)=A(LORENTZO1,3)
A(ASYMO13,1)=A(ASYMO1,1)
} End of linear constraints.
```

Another type of comments is used which follow values of variables and start with colons (:); this will be described in the next section.

17.3.3 Reading both names and values of variables

When the first word in a line is a variable name (INTEGER, REAL, or CHARACTER), '=' plus the value of the variable should follow it.

For example, the kind of the angle-dispersive diffraction method is input as

```
NBEAM = 1: Conventional X-ray powder diffraction with characteristic X rays.
```

'NBEAM' is the variable name, and its value is equal to 1. A colon placed after the value and characters following it ('`: Conventional X-ray` $\cdots$') are both optional and regarded as a comment. Tink decodes this line to obtain the value of an integer (*e.g.*, `2`), a real (*e.g.*, `3.14159`), or a string (*e.g.*, '`Ba`'). The name of an integer variable is also stored and referred to in logical expressions in If blocks and Select case statements described below.

The variable name consists of alphabetical capital letters, numbers (`0`–`9`), and '`@`' with the first character being an alphabet. Its maximum length is 10 characters. In a manner similar to that in Fortran, the first character of the name for an integer variable should be `I`, `J`, `K`, `L`, `M`, or `N` whereas that of a real variable other than `I`, `J`, `K`, `L`, `M`, and `N`. Integer variables whose name end with '`@`' are local ones that are also referred to in logical expressions. However, they are not

real data but dummy ones used only in preprocessing by Tink, disappearing after conversion of hoge.ins. Duplications among labels should be eliminated at any rate.

In the following example, the value of NBEAM is set at 1 by giving '#' at the tops of the other two lines:

```
# NBEAM = 0: Neutron powder diffraction.
  NBEAM = 1: Conventional X-ray powder diffraction with characteristic X rays.
# NBEAM = 2: Synchrotron X-ray powder diffraction.
```

If the value of NBEAM is changed, we have to remove one '#' and add another '#' in two lines, which is somewhat troublesome. We may alternatively set the value of the variable after three comment lines:

```
# NBEAM = 0: Neutron powder diffraction.
# NBEAM = 1: Conventional X-ray powder diffraction with characteristic X rays.
# NBEAM = 2: Synchrotron X-ray powder diffraction.
  NBEAM = 1
```

Then, we need to only replace the value (in this case, 1) of the variable. Such a manner of entering a variable value is convenient when it is frequently altered because only one number need to be changed.

We have a convenient way of converting a whole line with the above form into a comment line: putting '!' instead of ':' after the value of a variable. For example, the value of NBEAM is set at 1 in the following way:

```
NBEAM = 0! Neutron powder diffraction.
NBEAM = 1: Conventional X-ray powder diffraction with characteristic X rays.
NBEAM = 2! Synchrotron X-ray powder diffraction.
```

The first and third lines are regarded as comment lines. The number of '#' in the input file can be reduced greatly according to this manner.

17.3.4 Comments written in multi-byte characters

As described in 17.3.2, the two types of comments may contain multi-byte characters. In such a case, standard input files, hoge.ins, have to be saved with the encoding of EUC (Extended UNIX Code) such as EUC-JP, EUC-CN, and EUC-KR. Otherwise, incomprehensible errors may occur during conversion of hoge.ins by New Tink because parts of characters with other types of encoding may be regarded as control characters by New Tink (*e.g.*, in Shift_JIS) or lengths of comment lines may be practically larger than 80 (*e.g.*, in three-byte characters such as UTF-8). Note that two bytes, *i.e.*, two columns in hoge.ins, are used per Kanji or Kana character in EUC-JP.

17.3.5 If block

Lines containing Fortran-like statements '`If` ··· `then`', '`else if` ··· `then`', '`else`', and '`end if`' serve to make Tink not hierarchic but completely flat. One or more lines may be inserted between

'`If ··· then`', '`else if ··· then`', '`else`', and '`end if`' to form an If block in the following manner:

```
If NBEAM >= 1 then
   LPAIR1 = 0: No Friedel pairs (hkl & -h-k-l) are generated.
   LPAIR1 = 1! Friedel pairs (hkl & -h-k-l) are generated.
end if

If NBEAM = 1 and NTRAN = 1 then
   DSANG = 0.5: Angle/degree of the divergence slit at the minimum 2-theta.
   RGON = 185.0: Goniometer radius/mm.
   SWIDTH = 20.0: Irradiation width/mm for the sample.
else if NBEAM = 1 and NTRAN = 2 then
   PCOR1 = 0.5: Fraction of the perfect crystal contribution.
   SABS = 1.0: (Linear attenuation coefficient)*(effective thickness).
else if NBEAM = 1 and NTRAN = 3 then
   XMUR1 = 0.0: (Linear attenuation coefficient)*(radius).
end if

If NPRFN = 0 then
   SHIFT0  0.14849  -1.14695E-1  1.28877E-2  0.0  1110
else
   SHIFTN  7.11671E-2  2.42176E-2  3.77026E-3  0.0  1000
end if
```

The function of the If block is similar to that in Fortran. Six rules listed below have to be obeyed on the use of the If block feature.

1. Up to two logical expressions may be placed either (a) between '`If`' and '`then`' or (b) between '`else if`' and '`then`'.

2. Each logical expression contains (a) the name of an integer variable, (b) a logical operator, '`=`', '`>`', '`>=`', '`<`', '`<=`', or '`<>`' ($\neq$), and (c) an integer.

3. Two logical expressions are related to each other with a relational operator, '`and`' (logical multiplication) or '`or`' (logical sum), *e.g.*,
   `If NPRFN = 0 and NASYM = 1 then`
   and
   `If NBEAM = 2 or NTARG = 3 then`

4. When the condition described either (a) between '`If`' and '`then`' or (b) between '`else if`' and '`then`' is false (not satisfied), a block of data lines following this line is skipped automatically.

5. If the condition is true (satisfied), the block of the data lines is read in by the program.

6. A block of data lines after a line '`else`' is input if no conditions above this line have been satisfied.

The If block feature is most convenient because we can leave lines that would otherwise be attached with '`#`' or deleted. Someone may be afraid that this feature is not easy to understand for most users. However, I believe that those who cannot comprehend this concept will never be able to carry out Rietveld refinements, too.

Be sure that '`If`', '`then`', '`else if`', '`else`', and '`end if`' must be input just as they are; capital and small letters are differentiated during decoding lines containing them by Tink.

17.3.6 Select block

Select blocks similar to those in Fortran 90 can be used in RIETAN-FP. Only integer variables may be place after '`Select case`', for example, in the following lines

```
Select case NSAMPLE
case 1
   (Data input if NSAMPLE = 1 are placed here)
case 2,3
   (Data input if NSAMPLE = 2 or 3 are placed here)
case 4-6
   (Data input if NSAMPLE = 4-6 are placed here)
case default
   (Data that do not fall into the above cases are placed here)
end select
```

lines input by RIETAN-FP change, depending on the value of NSAMPLE. The statement '`case default`' means 'otherwise.' '`Select case`' is followed by the name of an integer variable, and '`case`' by up to two integers with '`,`' or '`-`' (different from '`:`' in Fortran 90) between two integers if any. Variable names and integers after '`case`' are not enclosed by a pair of parentheses unlike Fortran 90. Be careful to input '`Select`', '`case`', '`case default`', and '`end select`' just as they are; capital and small letters are differentiated during decoding lines containing them by Tink.

Tink converts Select blocks into equivalent If blocks, which is responsible for the limitation of up to two integers after '`case`'. Complex selection such as '`case 2,4,6`' and '`1-3,5`' is not allowed because integer values are assigned so as to require only simple selection.

17.3.7 Nest of If and Select blocks

A nest of up to two If and Select blocks is allowed provided, however, that inner blocks must be indented at least 1 column, with two or three columns preferred to 1 column. As described above, never use tabs for indention. This feature will be self-evident if template files included in distribution files of RIETAN-FP are browsed. In the following example, an If block includes a Select block:

```
If NMODE = 4 then
   # Initial values of multiplicity X |Fc|**2 for the 1st phase are
   NSFF = 0: estimated according to the Wilson statistics.
   NSFF = 1! read in from hoge.ffi.
   NSFF = 2! all set at 100.0.

   Select case NSFF
   case 1
      NCONST = 0: |Fc|'s are varied during least-squares fitting.
      NCONST = 1! |Fc|'s remain constant during least-squares fitting.
   case default
      INCMULT = 0: The integrated intensity is regarded as |F|**2.
      INCMULT = 1! The integrated intensity is regarded as m*|F|**2.

      CHGPC = 1.0: Cut-off is at first set at CHGPC*PC.
   end select
end if
```

Of course, all the data in the current Select block are input only when `NMODE = 4`.

Nests between If blocks and between Select blocks, and inclusion of an If block inside a Select block are also permitted. The following lines exemplifies a case where an If block is included within a Select block:

```
Select case LSER
case 0
   LPAIR = 0! Input no pairs of site names, 'A' and 'B', for restrained A-B distances.
   LPAIR = 1: Input pairs of site names, 'A' and 'B', for restrained A-B distances.

   LTRIP = 0! Input no triplets of site names for restrained A-B-C bond angles.
   LTRIP = 1: Input triplets of site names for restrained A-B-C bond angles.

   If LPAIR = 1 then
      # Bond lengths between l_min and l_max are restrained.
      'A'  'B'  l_min  l_max  Exp. value  Allowed dev. {
      'P'  'O'  1.3    1.7    1.50        0.08
      } End of nonlinear restraints for bond lengths.
   end if
   If LTRIP = 1 then
      # Bond angles between phi_min and phi_max are restrained
      'A'  'B'  'C'   phi_min  phi_max  Exp. value  Allowed dev. {
      'O'  'P'  'O'   99.47    119.47   109.47      6.0
      } End of nonlinear restraints for bond angles.
   end if
case 1
   Ser. No.  Exp. value  Allowed dev. {
   122       1.47        0.01
   123       1.54        0.01
```

```
   178       108.0       3.0
   } End of nonlinear restraints.
end select
```

17.3.8 Go to statement

If a line with a form of '`Go to *destination`' (`destination`: a string given appropriately by the user) is present in hoge.ins, Tink unconditionally jumps from this line to a line whose top is `*label`. It is usually combined with an If or Select block. Note that '`Go`' and '`to`' must be input just as they are; capital and small letter are differentiated during decoding lines containing them by Tink.

An example of a `Go to` statement is included in template files, where a jump to a label named `*ORFFE` is included if `NMODE` is `1`:

```
If NMODE = 1 then
   NDA = 0! No file storing ORFFE data is output.
   NDA = n! Filename.xyz for ORFFE is output for the n-th phase (n > 0)
   NDA = 0

   Go to *ORFFE
end if
.....
*ORFFE
If NDA > 0 then
.....
```

17.3.9 Real and virtual chemical species

Real chemical species denote neutral atoms, cations, and anions whose various physical quantities are stored in the database file asfdc. **Table 17.3** lists their names with annotations given for species attached with daggers.

Table 17.3: Names of real chemical species recorded in file asfdc

No.						Annotation
1	H.S†	H	H-	D		Stewart *et al.* [229]
2	He					
3	Li	Li7†	Li+			^{7}Li (neutron diffraction)
4	Be	Be2+				
5	B	B11†				^{11}B (neutron diffraction)
6	C	C.v†				Mann [230]
7	N					
8	O	O-	O2-			
9	F	F-				
10	Ne					
11	Na	Na+				
12	Mg	Mg2+				
13	Al	Al3+				
14	Si	Si.v†	Si4+			Mann [230]
15	P					
16	S					
17	Cl	Cl-				
18	Ar					
19	K	K+				
20	Ca	Ca2+				
21	Sc	Sc3+				
22	Ti	Ti2+	Ti3+	Ti4+		
23	V	Vm†	V2+	V3+	V5+	$\sigma_{\mathrm{i}} = 5.187$ barns
24	Cr	Cr2+	Cr3+			
25	Mn	Mn2+	Mn3+	Mn4+		
26	Fe	Fe2+	Fe3+			
27	Co	Co2+	Co3+			
28	Ni	Ni2+	Ni3+			
29	Cu	Cu+	Cu2+			
30	Zn	Zn2+				
31	Ga	Ga3+				
32	Ge	Ge4+				
33	As					
34	Se					
35	Br					

No.				Annotation
35	Br-			
36	Kr			
37	Rb	Rb+		
38	Sr	Sr2+		
39	Y	Y3+		
40	Zr	Zr4+		
41	Nb	Nb3+	Nb5+	
42	Mo	Mo3+	Mo5+	Mo6+
43	Tc			
44	Ru	Ru3+	Ru4+	
45	Rh	Rh3+	Rh4+	
46	Pd	Pd2+	Pd4+	
47	Ag	Ag+	Ag2+	
48	Cd	Cd2+		
49	In	In3+		
50	Sn	Sn2+	Sn4+	
51	Sb	Sb3+	Sb5+	
52	Te			
53	I	I-		
54	Xe			
55	Cs	Cs+		
56	Ba	Ba2+		
57	La	La3+		
58	Ce	Ce3+	Ce4+	
59	Pr	Pr3+	Pr4+	
60	Nd	Nd3+		
61	Pm	Pm3+		
62	Sm	Sm3+		
63	Eu	Eu2+	Eu3+	
64	Gd	Gd3+		
65	Tb	Tb3+		
66	Dy	Dy3+		
67	Ho	Ho3+		
68	Er	Er3+		
69	Tm	Tm3+		
70	Yb	Yb2+	Yb3+	
71	Lu	Lu3+		

No.				Annotation
72	Hf	Hf4+		
73	Ta	Ta5+		
74	W	W6+		
75	Re			
76	Os	Os4+		
77	Ir	Ir3+	Ir4+	
78	Pt	Pt2+	Pt4+	
79	Au	Au+	Au3+	
80	Hg	Hg+	Hg2+	
81	Tl	Tl+	Tl3+	
82	Pb	Pb2+	Pb4+	
83	Bi	Bi3+	Bi5+	
84	Po			
85	At			
86	Rn			
87	Fr			
88	Ra	Ra2+		
89	Ac	Ac3+		
90	Th	Th4+		
91	Pa			
92	U	U3+	U4+	U6+
93	Np	Np3+	Np4+	Np6+
94	Pu	Pu3+	Pu4+	Pu6+
95	Am			
96	Cm			
97	Bk			
98	Cf			

Capital and small letters are differentiated from each other in asfdc. Atomic scattering factors of H.S were calculated by an isotropic approximation to the scattering factor for bonded hydrogen on the basis of an analysis of the hydrogen molecule by Stewart *et al.* [229] while those of C.v and Si.v are valence-state scattering factors computed from Hartree–Fock ground-state wave functions [230]. For example, not '`FE`' but '`Fe`' must be input as a name of the element, iron. Output lists are likewise represented using capital and small letters, which improves their readability considerably.

On the other hand, virtual chemical species are those composed of two or more real species. The use of such an imaginary species is very convenient when dealing with compounds where more than two kinds of atoms occupy the same site, decreasing the number of structure parameters and linear constraints imposed on them. Names and amount-of-substance fractions of the constituents

real species must be given by the user. For example, for a virtual species named '`LaCa`' consisting of 90 % of La and 10 % of Ca, we input

```
LaCa  La  0.9  Ca  0.1 /
```

Names of both real and virtual species may be input after label + '`/`' in structure-parameter lines.

In neutron diffraction, the chemical symbol of each magnetic atom is attached with '`*`' if crystallographic and magnetic unit cells coincide with each other. On the other hand, the chemical symbol of each magnetic atom in the MUC phase (see 8.1) is attached with '`%`'. In this case, the chemical species (including oxidation numbers) and Landé splitting factors, g, [82] of the magnetic atoms are input in order, for example,

```
# The following line is input for Fe% (g = 0).
Fe2+  0.0
```

17.3.10 Dispersion corrections of real chemical species

If `NBEAM = 1` and `NTARG <> 3`, the dispersion corrections, f' and f'', of all the elements for characteristic X rays (Ag $K\alpha$, Mo $K\alpha$, Cu $K\alpha$, Co $K\alpha$, Fe $K\alpha$, and Cr $K\alpha$ radiations) [60] are input from asfdc by RIETAN-FP (see 3.5.1).

On the other hand, dispersion corrections for Cu $K\beta$ radiation (`NBEAM = 1` and `NTARG = 3`) and synchrotron X rays (`NBEAM = 2`) can be given by the user. If $f' = f'' = 0.0$ are input for each element (real chemical species) in hoge.ins, both of them are evaluated from the wavelength, λ, with the binary file, xdc.bin. As described in 3.5.1, $f_0(\sin\theta/\lambda) + f_1 + f_{\rm rel} - Z + f_{\rm NT}$ is used as the real part of f when calculating f' and f'' with RIETAN-FP. If $f_1 + f_{\rm rel} - Z$ is preferred to $f_1 + f_{\rm rel} - Z + f_{\rm NT}$, input the former in hoge.ins by yourself (see 3.5.1 and 17.8.1).

17.3.11 Generation of diffraction indices and multiplicities for reflections

Diffraction indices and multiplicities for possible Bragg reflections are generated by LAZY PULVERIX implemented in RIETAN-FP. The KDRREF program built into RIETAN-2000 [5,7,8] is no longer used because of serious bugs that cannot be fixed. LAZY PULVERIX, which is used in the retrieval program in Inorganic Crystal Structure Database (ICSD) and PowderX [104], is reliable.

For the volume name of "*International Tables for Crystallography*"–(space-group number)–(setting number), *e.g.*, '`A-129-2`', data corresponding to standardized crystal-structure data (see 9) have to be entered. This data is needed to maintain compatibility with RIETAN-2000 and input coordinates of equivalent positions from spgra. The volume name should always be '`A`' [72], in contrast to RIETAN-2000 where another volume name of '`I`' was allowed.

17.3.12 Refinement identifiers

Let A(I) be the I-th parameter in a group of parameters, $\boldsymbol{x}$, contained in the model function Eq. (2.5), and ID(I) its refinement identifier. ID(I) specifies the behavior of A(I) during refinement as explained in **Table 17.4**.

Table 17.4: Control of A(I) with ID(I)

ID(I)	Behavior of A(I)
0	Fixed.
1	Refined by a least-squares method.
2	A(I) and its partial derivative (only in the Gauss–Newton and modified Marquardt methods) are calculated from other refinable parameters using a linear equality constraint (see 17.3.16).
3	Applied only to PPPs for relaxed reflections (NPRFN = 1−3). A(I) is calculated from SPPs in each cycle, which leads to variation of A(I) during the refinement.

17.3.13 Profile functions

The profile function is selected from the following four options according to the value of NPRFN (0−3).

NPRFN = 0

The pseudo-Voigt function of Thompson, Cox, and Hastings [96]. It was modified in such a way that anisotropic profile asymmetry can be corrected for by a procedure of either Finger, Cox, and Jephcoat (NASYM = 0) or (b) Howard (NASYM = 1).

NPRFN = 1

The split pseudo-Voigt function of Toraya [103]. Partial profile relaxation is also carried out with the same function.

NPRFN = 2

The split pseudo-Voigt function of Toraya is applied to reflection not to be relaxed, in the same manner as in NPRFN = 1. On the other hand, the modified split pseudo-Voigt function is applied to relaxed reflections. ID(I) is the same as in the case of NPRFN = 1. The initial FWHM's of Lorentzian and Gaussian components are set equal to each other when ID(I) is 3.

NPRFN = 3

The split Pearson VII function of Toraya is used as a profile function, regardless of the use of partial profile relaxation. ID(I) is the same as in NPRFN = 1.

NCUT = 1

If NCUT is 1, the user can specify the 2θ region where the profile of each relaxed reflection is calculated. Set NCUT at 1 if NPRFN is 2; otherwise, RIETAN-FP will stop, issuing an error message.

17.3.14 How to input labels, parameters, and refinement identifiers

Labels, parameters contained in the model function (background, profile, structure parameters, *etc.*; see Supplement), and their refinement identifiers (unnecessary in the simulation of powder diffraction patterns) are input according to the following rules.

1. A label is located at the top of a line without any preceding space, followed by a group of parameters and corresponding refinement identifiers.

2. A label consists of alphabetical letters (`a`–`z` and `A`–`Z`), numbers (`0`–`9`), and '`@`' with the first character being a capital letter, except for labels for primary profile parameters of relaxed reflections (see 4.4 and 17.3.15). Its maximum length is 25 characters (less than 8 characters are desirable for the sake of printing).

3. The label need not be enclosed by a pair of single quotation marks.

4. A label can be arbitrarily assigned to a group of parameters except that one label must be always assigned to one crystallographic site by grouping all the structure parameters for the site. The parameters are hereafter managed under the name of the label.

5. A label for an atomic site is attached with '`/`' plus the name of a chemical species without inserting any space. The term 'chemical species' denotes a real species included in the database file, asfdc, or a virtual species derived from two or more real species for a mixed-atom site. In neutron diffraction, use only neutral species (neither cations nor anions). For magnetic atoms, '`*`' must be attached to chemical species' names.

6. Two or more lines may be used for parameters grouped under a label.

7. On the standardization of crystal data (see 9), it is preferable to give a site label consisting of a chemical-species name (up to two alphabetical characters) plus an identification string starting with a number, *e.g.*, 'Al3', 'O15a', and 'H123'. The maximum length of site labels is six.

8. If a dummy '`+`' sign is attached to an isotropic atomic displacement parameter, B, in such a way as '`+1.6`', the program automatically converts it into six anisotropic atomic displacement parameters, β_{ij}. if `A(I)`'s in hoge.ins are updated after Rietveld analysis (`NUPDT = 1`), final β_{ij} parameters are output in hoge.ins. On the other hand, the refinement identifiers and linear constraints imposed on the anisotropic atomic displacement parameters [70, 71] must be input by the user.[4] The number of structure parameters and refinement identifiers per site is 10 in this case.

9. If a B value other than zero is input, and five zero values follow it as dummy parameters, six β_{ij} values are calculated from B in a similar way as in rule 8.

[4] A file converter called B2beta, which is included in the the RIETAN-FP–VENUS assistance environment, is convenient for this purpose. For details in B2beta, read Readme_macros.pdf (Windows) or Readme_scpt.pdf (macOS).

10. Refinement identifiers for fixed, varied, and constrained parameters are 0, 1, and 2, respectively, as described in Table 17.4. "Constrained" means that a parameter whose refinement identifier is equal to 2 is evaluated from other refinable parameter(s) with a linear equality constraint.

11. In parts of noncentrosymmetric space groups, no origin can be assigned to a definite position. For example, y coordinates of all the sites in space group $P2_1$ (general equivalent positions: x, y, z; $-x$, $1/2+y$, $-z$) are arbitrary; the refinement of all the y coordinates in such a space group gives solutions where all the structure parameters are shifted by the same vector (floating orign), leading to nonconvergence. In such cases, RIETAN-FP will be aborted, giving the following message: `The coefficient matrix is not positive definite`. At least one y coordinate should be not refined but fixed in structure refinement including Rietveld analysis [231, 232].

12. Lattice parameters whose `ID(I)`'s are set at 1 depend on crystal systems:

    (a) Triclinic: a, b, c, α, β, and γ

    (b) Monoclinic: a, b, c, and β

    (c) Orthorhombic: a, b, and c

    (d) Tetragonal: a and c

    (e) Trigonal (hexagonal lattice) and hexagonal: a and c

    (f) Cubic: a

    Because constraints among a, b, and c are automatically satisfied, the `ID(I)`'s of the other lattice parameters should be 0.

13. A group of refinement identifiers is input after structure parameters without inserting any space among them.

14. Even if comments are attached just after refinement identifiers, they are deleted when parameters in the input file are updated to refined ones. On the other hand, comment lines inserted between these parameter lines remain unchanged when updating refined parameters.

For instance

```
Fe/Fe3+ 1.0 0.3459 0.3459 0.5 0.6 01201
```

is a line input for a metal site. '`Fe`' is the label for this site, '`Fe3+`' is the name of a chemical species, '`1.0`' is the occupancy (g), '`0.3459  0.3459  0.5`' are fractional coordinates (x, y, and z), '`0.6`' is the isotropic atomic displacement parameter (B), and '`01201`' is the refinement identifiers for the five structure parameters. The y coordinate is constrained to be equal to the x coordinate.

Labels can be conveniently used when referring to (a) parameters in linear equality constraints and (b) serial numbers for parameters varied in early refinement cycles. Each parameter number

may be represented as 'L,I' or 'L,S', where 'L' is a label to which the parameter belongs, 'I' is the parameter number within the group of parameters under label 'L', and 'S' is the symbol of a structure parameter. Each parameter is then represented as 'A(L,I)' or 'A(L,S)' with the array name 'A' and a parameter number in the parenthesis. 'A(L,I)' may be represented as 'A(L)' if I is 1.

For structure parameters, we can use symbols, 'g' (occupancy, g), 'x', 'y', 'z' (fractional coordinates, x, y, and z), 'B' (isotropic atomic displacement parameter, B), 'beta11', 'beta22', 'beta33', 'beta12', 'beta13', and 'beta23' (anisotropic atomic displacement parameters, β_{ij}), instead of their numbers. We may replace 'beta' with 'B' for simplicity: 'B11', 'B22', 'B33', 'B12', 'B13', and 'B23'. In the case of the line

```
Mg/Mg2+  1.0  0.345  0.0  0.5  0.8  01001,
```

'A(Mg,x)' and 'A(Mg,B)' are respectively the x coordinate and isotropic atomic displacement parameter for the Mg site. 'A(Mg,x)' and 'A(Mg,B)' may be alternatively expressed as 'A(Mg,2)' and 'A(Mg,5)', respectively.

Suppose that a fractional coordinate of a small number of digits are input for a special position, for example, 0.167 in place of 0.166667 (1/6), 0.333 in place of 0.333333 (1/3), and 0.666 in place of 0.666667 (2/3). Such scamped work may cause serious troubles because of the resulting failure in selection of equivalent positions by checking overlapping of atoms generated with rotation matrices and translation vectors.

In MEM-based pattern fitting (NMODE = 2, 3), even if part of ID(I)'s for structure parameters are set at 1, they are regarded as 0 (see 14.8.2). Accordingly, we need not change those ID's at all when proceeding from Rietveld analysis to MPF.

17.3.15 Labels for relaxed reflections

When the technique of partial profile relaxation is applied to part of reflections, PPPs, which are of course optional, are placed after the background parameters. A label with a special format must be given to each group of PPPs for a reflection whose PPPs are relaxed. It has a form 'PPPn_h.k.l', where 'n' is the phase number, and 'h', 'k', and 'l' are indices of a relaxed reflection. For example, if the 310 reflection for the first phase is anisotropically broadened, label 'PPP1_3.1.0' is input together with five PPPs:

```
PPP1_3.1.0  2.64612E-2  3.07702E-2  1.23737  0.617272  0.794  11111
```

These five PPPs are refined quite independently of SPPs for the relevant phase. Needless to say, parts of the PPPs may be refined if necessary. Integrated intensities and peak positions for the user-specified relaxed reflections are calculated in the same manner as those for the other reflections.

When dealing with X-ray diffraction data of a noncentrosymmetric compound, RIETAN-FP usually generates Friedel pairs, hkl and $\bar{h}\bar{k}\bar{l}$, because X-ray dispersion makes their structure factors slightly different from each other (see 3.5). In such cases, PPPs of reflection $\bar{h}\bar{k}\bar{l}$ must be constrained (ID(I) = 2) to be equal to corresponding PPPs of reflection hkl. For example, on

use of the modified split pseudo-Voigt function, Eq. (4.33), the following linear constraints are imposed on five PPPs of a Friedel pair (111 and $\overline{111}$ reflections) for the first phase:

```
A(PPP1_-1.-1.-1,1)=A(PPP1_1.1.1,1); A(PPP1_-1.-1.-1,2)=A(PPP1_1.1.1,2);
A(PPP1_-1.-1.-1,3)=A(PPP1_1.1.1,3); A(PPP1_-1.-1.-1,4)=A(PPP1_1.1.1,4);
A(PPP1_-1.-1.-1,5)=A(PPP1_1.1.1,5)
```

An ID(I) value of 2 can also be assigned to any PPP. If an A(I) value of 0.0 is input as a dummy for a PPP of a relaxed reflection, its initial value is calculated from SPPs relevant to the PPP. If you want to set a PPP at zero practically, use a trick of inputting A(I) which is very near to zero, *e.g.*, 10^{-15}.

17.3.16 Linear equality constraints

Linear equality constrains can be imposed on profile and structure parameters. They are described in a similar manner as assignment statements in FORTRAN except that each parameter is represented as `A(L,I)` or `A(L,S)` as described above and that '`/`' should not be included in the right side. Five examples of linear constraints imposed on two SPPs, a fractional coordinate, an occupancy, and an anisotropic atomic displacement parameter are given below:

```
A(Gauss2,1)=A(Gauss1,1)
A(Asym2,1)=A(Asym1,1)
A(Fe,y)=2.0*A(Fe,x)
A(Co1,g)=1.0-0.5*A(Cu2,g)
A(O2,B12)=0.5*A(O2,B22)
```

The parameter in the left side has always a refinement identifier of 2 and constrained in such a way that the above equation is strictly satisfied. The right side includes at least one refinable parameter but no fixed parameters. In the above constraint on g, only g(Cu2) is refined, and g(Co1) is calculated from g(Cu2) with the above constraint. Of course, the above linear relation is taken into account in the calculation of the partial derivative of the model function with respect to g(Cu2).

We can describe two or more linear constrains in one line, marking off by semicolons (;) as follows:

```
A(Fe,y)=2.0*A(Fe,x); A(N2,g)=1.0-0.5*A(O2,g); A(O2,B)=A(O1,B)
```

The number of linear constraints is equal to that of parameters whose refinement identifier is equal to 2. Linear constrains on profile parameters are used in such a way that profile parameters of impurity phases are set equal to those of the main phase. Imposing such constrains considerably reduces the total number of profile parameters, in particular, in samples containing three or more phases.

As described in 17.3.14, linear constraints on anisotropic atomic displacement parameters, β_{ij}, have to be input by the user or generated with a utility called B2beta. In the latter case, the first coordinate triplet described in the "International Tables for Crystallography," Vol. A [72] must be input for each site because linear constraints recorded in file constr_beta are valid only for the

first triplet [70]. For example, in space group $P4_2/mcm$ (No. 132), not (1/2, 1/2, 3/4) but (1/2, 1/2, 1/4) should be input for site 2*d* to impose constraints $\beta_{22} = \beta_{11}$ and $\beta_{12} = \beta_{13} = \beta_{23} = 0$. For site 4*i*, not ($\bar{x}$, x, 1/2) but (x, x, 0) has to be given on the use of constraints $\beta_{22} = \beta_{11}$ and $\beta_{13} = \beta_{23} = 0$.

Keep in mind that standardization of crystal data by STRUCTURE TIDY (see Chap. 9) with RIETAN-FP or VESTA always gives the first coordinate triplet for each site.

17.3.17 Parameters refined in each cycle

When `NAUTO` is `1` (incremental refinement), parameters refined in initial cycles are customized by users. Parameter numbers are input by using `L,I` and/or `L,S` and separating two numbers with one or more space(s). '`/`' at the tail of a line indicates the end of refinable parameters in a refinement cycle. If a line does not end with '`/`', parameters in the next lines follow those in the present line. '`#`' is placed at the end of a series of lines. For example, if we input

```
BKGD,1 BKGD,2 BKGD,3 BKGD,4 BKGD,5 BKGD,6 BKGD,7 BKGD,8 SCALE,1 /
CELL,1 CELL,2 CELL,3 /
PRFL,1 PRFL,2 PRFL,3 PRFL,5 PRFL,7 PRFL,9 /
Ti,x Ti,B O1,y O1,z O1,B O2,g O2,B /
}
```

eight background parameters and a scale factor are refined in the first cycle, three lattice parameters, *a*, *b*, and *c*, in the second cycle, six profile parameters in the third cycle, and seven structure parameters in the fourth cycle. In subsequent cycles, all the parameters with ID(I) = 1 are refined simultaneously. If `NAUTO` is 2, RIETAN-FP automatically specifies appropriate combinations of refinable parameters for several cycles.

17.3.18 Introduction of a structural model derived by EXPO

Program res2ins deals with hoge.res with the SHELX format to introduce lattice and structure parameters in it into an input file, hoge.ins, of RIETAN-FP. EXPO [22] outputs hoge.res by selecting File → Export → Shelx (hoge.res). Double-click the batch file for res2ins to launch it. Answer each question displayed after a line in hoge.ins. In the questions, "`0/<Enter>`" denotes inputting "`0`" or pressing the Enter key. A backup file, hoge.ins.bak remains in the same folder after updating hoge.ins.

Beware that occupancies are always set at unity, for convenience; those of partially occupied sites should be changed if necessary.

17.4 Intensity Data File

RIETAN-FP can input intensity data files with the following 13 kinds of formats:

`NINT = 0`: RIETAN format,
`NINT = 1`: general (X-Y) format,
`NINT = 2`: Igor text file,

`NINT = 3`: FVFM (Fully Variable ForMat),
`NINT = 4`: standard DBWS format,
`NINT = 5`: DBWS format for multiple detectors,
`NINT = 6`: free format,
`NINT = 7`: GSAS format with two types,
`NINT = 8`: HRPD (JRR-3M reactor, JAEA) formats with two types,
`NINT = 9`: Rigaku RINT 2000 ASCII format,
`NINT = 10`: MAC Science format.
`NINT = 11`: general-3 format.
`NINT = 12`: PANalytical XML format.

17.4.1 RIETAN format

Optional comment lines starting with '`*`', is followed by a line where the total number of data points, the minimum 2θ, and the step width (free format). Then, a series of diffraction intensities are given with one or more spaces between two data; any number of data may be included in each line. For example, in the case of Cu3Fe4P6.int included in distribution files, its top part is as follows:

```
* Cu3Fe4(PO4)6, Cu K_alpha1 radiation
10000    10.000     0.010
   9104   9375   9335   9396   9149   9450   9180   9274   9158   9382   9192
   9115   9347   9273   9167   9238   9151   9237   9293   9313   9189   9407
   9290   9113   9303   9267   9282   9025   9099   9211   9242   9323   9159
   9163   9306   9173   9276   9127   9322   9217   9290   9220   9141   9180
   9165   9153   9179   9116   9281   9147   9358   9189   9235   9219   9199
   9080   9214   9216   9343   9164   9301   9161   9148   8993   9094   9124
   9092   9073   9203   9294   9326   9161   9164   8989   8864   9078   9014
   9267   9192   8997   8964   9232   9075   9168   8968   9164   9039   9155
   .....
```

Let `sample.int` be the name of an intensity data file recorded with observed intensities in a format of (10F8.0) or (10I8) without any comment lines. This file can be input by the *ab initio* structure-analysis system EXPO [22] if the following lines are included in an input file, hoge.exp, for EXPO:

```
   .....
%DATA
   .....
   PATTERN sample.int
   JUMP
   RANGE thmin thmax thstep
   .....
```

where `JUMP` is a directive to skip the first line containing the total number of data points, the minimum 2θ, and the step width in sample.int, `thmin` is the minimum 2θ, `thmax` is the maximum 2θ, and `thstep` is the step width.

17.4.2 General format

A string '`GENERAL`' (capital letters) is given in the first line, the total number of data points in the second line, which is followed by pairs of 2θ and diffraction intensities with one pair per line. For example, in the case of Fapatite.int included in the distribution files, its top part is as follows:

```
GENERAL
 5751
 15.00     609
 15.02     612
 15.04     673
 15.06     619
 15.08     627
 15.10     609
 15.12     549
 15.14     635
 .....
```

The second line may further contain second (`FADJUST`) real value, which has to contain '.' (period).

If `FADJUST` is input, each diffraction intensity is multiplied by `FADJUST`, which is convenient when adjusting the goodness-of-fit indicator, S (see 4.3.1); S is proportional to $c^{1/2}$ whereas $R_{\rm wp}$ remains constant regardless of the value of `FADJUST`.

This format is useful when the step width is not constant. In such a case, the first line should be not '`GENERAL`' but '`GENERAL$`'. The last character, '`$`', is required to calculate observed integrated intensities in order when step widths with respect to 2θ vary two or more times for one reflection. This tip is generally effective when an error message "Too large NREGION" appears during calculation of reliability indices.

Files with the general format can be directly input by PowderX [104] on specification of `X-Y (hoge.xrd)` in the Import Data submenu under the File Menu.

The method of converting file hoge.raw obtained on HERMES [233] into a file with the general format is described in a Web page of HERMES.[5]

17.4.3 Igor text format

Files of this format can be input by Igor Pro of WaveMetrics, Inc. A string '`IGOR`' is given in the first line, and '`WAVES/D two-theta int`' in the second line, '`BEGIN`' in the third line, which is followed by pairs of 2θ and diffraction intensities with one pair per line. The final line should be '`END`' to show the end of data.

```
IGOR
WAVES/D two-theta int
BEGIN
 0.5658  2848
```

[5] http://nc-imr.imr.tohoku.ac.jp/HERMES/Analysis/RIETAN/int_HERMES.html

```
 0.5708   2886
 0.5758   3375
 0.5808   3932
 0.5858   4373
 0.5908   5016
 0.5958   5347
.....
32.6758   3429
32.6808   3515
END
```

17.4.4 Fully variable format

RIETAN-FP can read in intensity files, hoge.int, for angle-dispersive X-ray powder-diffraction data taken with variable times per step to improve counting statistics in high-angle regions. An example of such files are shown below:

```
FVFM
  5.010   84.0   1.0
  5.020   90.0   1.0
  5.030   88.0   1.0
.....
109.990   52.0   2.0
110.000   52.0   2.0
```

where a label 'FVFM' (**F**ully **V**ariable **F**or**M**at) is located at the first line, which is followed by a series of 2θ's, counts, and multiplicities for measurement times per step. All the counts must be divided by the multiplicities to achieve smooth connection of the intensities. Statistical weights, w_i, in Eq. (2.1) are automatically calculated from the intensities and multiplicities.

17.4.5 Standard DBWS format

In a Rietveld-analysis program DBWS-9807a[6] [41, 234], an intensity file with this format is input if (`JOBTYP = 0` or `JOBTYP = 1`), `INSTRUM = 0`, and `IDATA = 0`. The first line contains the variables `START`, `STEP`, `STOP`, and `DATAID` in `FORMAT(3F8.3, A48)`:

`START`: beginning angle in degrees 2θ,
`STEP`: step size in degrees 2θ,
`STOP`: last angle in degrees 2θ,
`DATAID`: an alphanumeric string identifying the data.

The rest of the file consists of the intensity data themselves in `FORMAT(8(F7.0,1X))`. There may be, but need not be, a ninth column listing the 2θ angle for the last datum in each row as listed below:

[6] http://www.ccp14.ac.uk/ccp/web-mirrors/dbws/downloads/young/download_dbws.html

```
 20.120    .020  60.100 PS999RF 24AP90  QUARTZ, 6-7-86  T=10     20.120
     30      34      44      37      35      25      29      46  20.260
     42      34      40      35      21      39      43      30  20.420
     48      44      52      44      50      46      47      56  20.580
     64      62      86      79     103     124     197     257  20.740
    484     831    1558    2478    3169    3185    2534    1828  20.900
   1217     661     263     173     128      79      88      68  21.060
 .....
```

17.4.6 DBWS format for multiple detectors

In DBWS-9807a [41], an intensity file with this format is input if `JOBTYP = 1`, `INSTRM = 1`, and `IDATA = 0`. This format is suitable when analyzing intensity data measured on a diffractometer equipped with multiple diffracted-beam detectors (but not all detectors contribute to the count at every step). The first line contains the variables `START`, `STEP`, `STOP`, and `DATAID` in `FORMAT(3F8, A56)`:

`START`: beginning angle in degrees 2θ,
`STEP`: step size in degrees 2θ,
`STOP`: last angle in degrees 2θ,
`DATAID`: an alphanumeric string identifying the data.

The rest of the file comprises the number of counters and the intensity data in a format of `FORMAT(10(F2.0,F6.0))`:

`NCOUNT`: number of counters,
`Y(I)`: average intensity.

RIETAN-FP uses these data to reconstruct the originally observed total count at each step and, from that, to assign the statistically correct weight to each observed step intensity.

17.4.7 Free format

This is the third format supported by DBWS-9807a [41]. The first line contains the variables `START`, `STEP`, `STOP`, and `DATAID` in (3F8.2, A48) format, just as in the standard DBWS format. The rest of the file consists of only intensity data in free format. Any number of columns of any width are allowed. The delimiters are commas or spaces. Diffraction angles should not be input. Files with this format can be input by DBWS-9807a if (`JOBTYP = 0` or `JOBTYP = 1`), `INSTRUM = 0`, and `IDATA = 1`. FullProf [110] is also capable of inputting files with this format if `Ins = 0`.

17.4.8 GSAS format

When reading in a file with the GSAS format [87], RIETAN-FP searches through the header line starting with 'BANK' to find the start angle, step width, and stop angle. The rest of the file contains intensity data in `FORMAT(10(F2.0,F6.0))` for `TYPE = 'STD'` or `FORMAT(5(2F8.0))` for `TYPE = 'ESD'`. RIETAN-FP automatically determines whether the current intensity data

file has the `STD` or `ESD` type. No commas or angle data are allowed. The `ESD` type is useful on count loss correction. Note that in the GSAS format for the data all rows must be filled out to 80 characters. Use spaces to fill out the row(s) if necessary. FullProf [110] can also input files with this format (`TYPE = 'STD'`) if `Ins = 12`.

An example of an intensity data file with the `STD` format is given below:

```
Y3FE2(ALO4)3 RT 1.909
BANK 1 2679 268 STD 2400 5 0 0
 1   162 1   178 1   155 1   166 1   180 1   181 1   170 1   170 1   165 1   183
 1   192 1   187 1   197 1   202 1   192 1   187 1   176 1   174 1   194 1   196
 1   182 1   188 1   199 1   211 1   222 1   233 1   218 1   237 1   228 1   220
 1   241 1   217 1   211 1   224 1   199 1   201 1   207 1   192 1   197 1   185
 1   183 1   200 1   186 1   181 1   144 1   153 1   181 1   189 1   183 1   195
 1   182 1   179 1   176 1   169 1   178 1   168 1   159 1   168 1   167 1   175
 1   165 1   166 1   171 1   158 1   166 1   178 1   169 1   164 1   160 1   166
 1   169 1   168 1   159 1   158 1   171 1   183 1   158 1   165 1   181 1   173
 .....
```

The following lines exemplifies an intensity data file with the `ESD` format:

```
Tl2(Ba0.5Sr0.4)2Ca2Cu3Oy
BANK  1     3300     660 CONST     300.00      5.00 0 0 ESD
    572.     39.    574.     39.    580.     39.    593.     39.    572.     39.
    564.     38.    515.     37.    515.     37.    539.     38.    469.     35.
    553.     38.    585.     39.    523.     37.    537.     38.    466.     35.
    512.     37.    583.     39.    502.     36.    558.     38.    550.     38.
    604.     40.    585.     39.    502.     36.    547.     38.    502.     36.
    607.     40.    542.     38.    515.     37.    585.     39.    601.     40.
    550.     38.    650.     41.    564.     38.    682.     42.    626.     41.
    647.     41.    723.     44.    753.     45.    839.     47.    680.     42.
    .....
```

17.4.9 HRPD format

Intensities measured on the neutron powder diffractometer HRPD at the JRR-3M reactor of the Japan Atomic Energy Agency (JAEA) are recorded in two different types. Step widths are not constant in both of them. Since RIETAN-FP automatically determines the type of the current intensity data file, we need not specify it. Top lines in one of the two formats are as follows::

```
EXPNO =    460 RUNNO =    2
COMMAND = KS
DATE = 93/10/25 TIME = 17:13:18
COMMENT = NBS Si powder
WL =    0.0000
MONOCHRO NAME =          MONOCHRO ANGLE =   89.000
COLLIMATOR     =    0/   0/   0/   0
D1 =    6.1524 D2 =    6.1524 GAMMA* =   90.000 PSI0 =  166.100
DSET FILE = DUA1:[USER.SHIMOJYO.HRPD]460D1.DST
S              C =  117.280
```

```
   6.800    9.303   11.798   14.342   16.828   19.359   21.816   24.34
  26.841   29.364   31.785   34.321   36.768   39.344   41.858   44.28
  46.823   49.306   51.800   54.170   56.842   59.336   61.804   64.30
  66.798   69.297   71.814   74.325   76.820   79.346   81.823   84.31
  86.820   89.322   91.804   94.329   96.839   99.277  101.837  104.31
 106.802  109.350  111.823  114.347  116.842  119.295  121.856  124.29
 126.795  129.301  131.819  134.339  136.799  139.329  141.836  144.31
 146.826  149.301  151.817  154.318  156.828  159.314  161.835  164.31
AXIS  = S
SI    =    5.000 DS    =    0.050
NSTP =   50 PRSC = 16 PRST =  48000
DETN = ALL
```

17.4.10 Rigaku RINT 2000 ASCII format

Binary files of X-ray powder-diffraction data measured on diffractometers produced by Rigaku Corporation can be converted into text files of this format. Inquire Rigaku for obtaining information about a utility program for the file conversion.

17.4.11 MAC Science format

Binary files of X-ray powder-diffraction data measured on diffractometers produced by MAC Science, whose business was acquired by Bruker AXS in 2002, can be converted into text files of this format. The routine of reading files of this format was written by an employee of MAC Science.

17.4.12 General-3 format

This is an extended version of the general format, containing standard uncertainties of observed diffraction intensities as third data in the following way:

```
GENERAL
 5751
 15.00    609    24
 15.02    612    25
 15.04    673    26
 15.06    619    25
 15.08    627    25
 15.10    609    25
 15.12    549    23
 15.14    635    25
   ....
```

This format was added in response to a request from Takashi Ida (Nagoya Institute of Technology), who is my collaborator of research in structure refinement where the effect of particle statistics on observed intensities is taken into account [218] (see Chap. 15).

17.4.13 PANalytical XML format

This is a document written in the Extensible Markup Language (XML) to store X-ray powder diffraction data measured on diffractometers of PANalytical B.V. (Spectris Co., Ltd.). After data placed on parts of '.....' in the following lines

```
<positions axis="2Theta" unit="deg">
   <startPosition> ..... </startPosition>
   <endPosition> ..... </endPosition>
</positions>
<positions axis="Omega" unit="deg">
   <startPosition> ..... </startPosition>
   <endPosition> ..... </endPosition>
</positions>
<positions axis="Phi" unit="deg">
   <commonPosition> ..... </commonPosition>
</positions>
<commonCountingTime unit="seconds">48.195</commonCountingTime>
<intensities unit="counts"> ..... </intensities>
```

have been input by RIETAN-FP, the number of steps, the step width, and 2θ values are calculated. X-Ray diffraction intensities are recorded in between `<intensities unit="counts">` and `</intensities>` with counts separated by spaces. In hoge.int containing two or more such blocks, intensities at the same 2θ's are summed up. If intensities recorded in two or more files need to be summed up, simply combine the files into a single file, hoge.int.

17.4.14 Substitution of smoothed intensities for zero intensities

Inclusion of zero intensities in hoge.int causes 'division by zero' errors when calculating w_i in Eq. (2.1), which leads to abnormal termination of RIETAN-FP. If a zero intensity is found in hoge.int, RIETAN-FP substitutes y_i(smoothed) smoothed by a box-car approach [235] for it:

$$y_i(\text{smoothed}) = \frac{w_2 y_{i-2} + w_1 y_{i-1} + w_0 y_i + w_1 y_{i+1} + w_2 y_{i+2}}{2w_2 + 2w_1 + w_0}. \tag{17.1}$$

Because $y_i = 0$, $w_0 = 1$, $w_1 = 0.5$, and $w_2 = 0.25$, Eq. (17.1) reduces to

$$y_i(\text{smoothed}) = 0.1(y_{i-2} + y_{i+2}) + 0.2(y_{i-1} + y_{i+1}). \tag{17.2}$$

17.5 File to Store Background Intensities

A file to input background intensities are required when `NRANGE = 1−3`.

17.5.1 NRANGE = 1

In this case, list-directed READ statement in RIETAN-FP is as follows:

```
READ(UNIT=8,*) (X(J),Y(J), J=1,100)
```

where `X(J)` is the Jth 2θ value in degrees, and `Y(J)` is the background intensity, $y'_{\rm b}(2\theta_i)$, at `X(J)` degrees. As is evident from the above READ statement, we can input up to 100 diffraction points in free format. To indicate the end of data points, place '`/`' after the last background intensity.

17.5.2 NRANGE = 2 and 3

hoge.bkg containing only a pair of data per line

When `NRANGE = 2` or `3`, the list-directed READ statement in RIETAN-FP is as follows:

```
DO J = 1, NP
  READ(8, *, END = 3) DEG(J), BG(J)
END DO
```

where `DEG(J)` is the Jth 2θ value in degrees, and `BG(J)` is the background intensity, $y'_{\rm b}(2\theta_i)$, at `X(J)` degrees, and `NP` is the maximum number of data points allowed in RIETAN-FP. The 2θ and background pairs whose total number should be equal to that of observed diffraction intensities in hoge.int.

No background parameters (b_j; $j = 0{-}11$) should be refined when `NRANGE = 2` because background intensities are simply fixed at those recorded in hoge.bkg. Procedures for preparing hoge.bkg used to calculate the composite background function (3.107) are described in detail in ref. [105].

hoge.bkg created by RIETAN-FP

As described in 11.2, RIETAN-FP is capable of creating hoge.bkg storing background intensities calculated according to the procedure of Sonneveld and Visser [106]. The resulting hoge.bkg file has an Igor text format where $2\theta_i$, y_i, and $y'_{\rm b}(2\theta_i)$ are recorded as waves `twotheta`, `intensity`, `background` in the following way:

```
IGOR
WAVES/O twotheta, intensity, background
BEGIN
  4.0000      735.000      735.000
  4.0100      746.000      736.295
  4.0200      737.000      737.544
  4.0300      755.000      738.749
  4.0400      754.000      739.912
  .....
END
```

Instructions to plot observed and background intensities against 2θ are included after `END` in hoge.bkg output by RIETAN-FP. Thus, hoge.bkg can be used to see diffraction patterns together with estimated background intensities.

17.6 File to Impose Restraints on Geometrical Parameters

17.6.1 Visualization of bonds and bond angles

VESTA [1, 25, 26] is very convenient to visualize bonds and bond angles recorded in hoge.ffe to impose restraints on bond lengths and angles. When reading in hoge.lst and/or hoge.ins, VESTA also input hoge.ffe automatically provided that hoge.ffe shares the same folder with hoge.lst and/or hoge.ins. Otherwise, hoge.ffe can be input by pressing the "Read hoge.ffe" button in the "Geometrical Parameters" dialog box, which lists interatomic distances and bond angles recorded in hoge.ffe.

VESTA allows us to locate the bonds and bond angles displayed in the "Geometrical Parameters" dialog box on a graphic window [236]; this dialog box appears when the Geometrical Parameters item is selected under the Utilities menu. On selection of a bond (2 atoms) or a bond angle (3 atoms) in this dialog box, the corresponding object in a ball-and-stick model is selected (highlighted), and *vice versa*. Thus, atom pairs and triplets associated with geometrical parameters on which restraints are imposed in Rietveld analysis with RIETAN-FP are easily recognized in the ball and stick model. P−O3 bond selected in the dialog box is highlighted. **Figure 17.1** exemplifies visualization of a bond in a ball and stick model of fluorapatite; in the structural model in the graphic window.

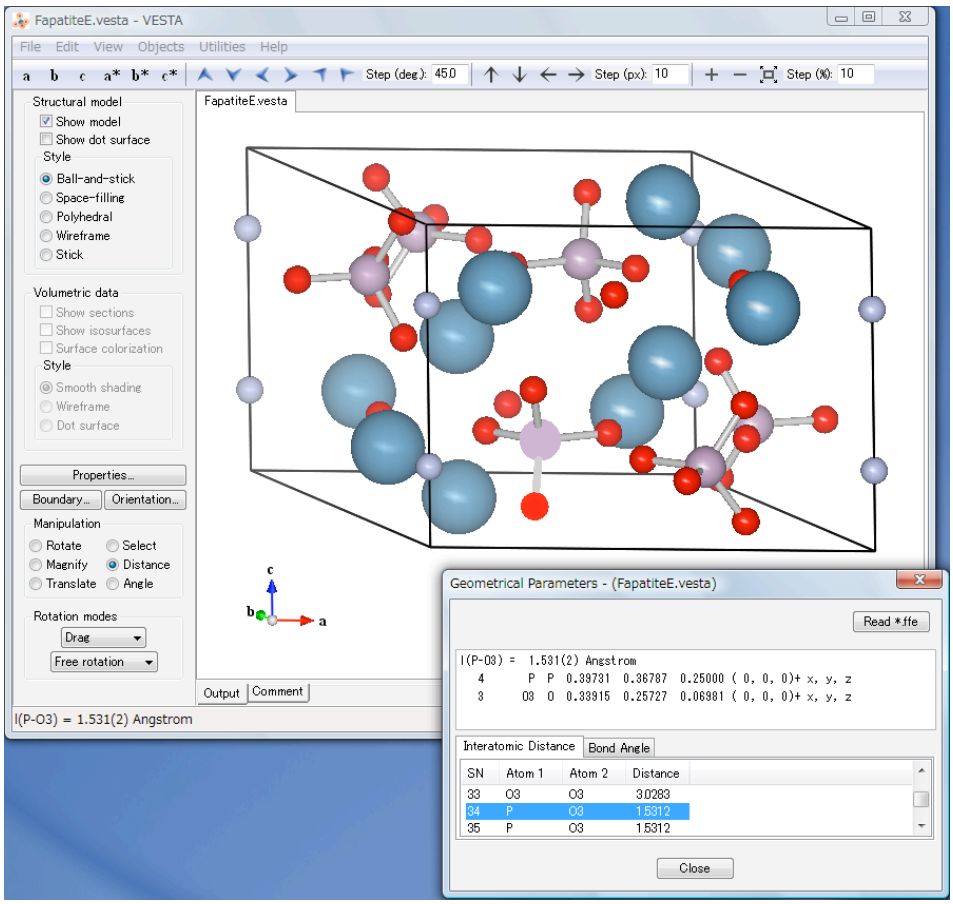

Figure 17.1: The "Geometrical Parameters" dialog box showing a list of bonds recorded for fluorapatite in Fapatite.ffe

Because ORFFE [136] calculates standard uncertainties (s.u.'s) of geometrical parameters with both diagonal and off-diagonal terms in the variance-covariance matrix, the resulting values of e.s.d.'s are more accurate than those evaluated by VESTA using only the diagonal terms.

17.6.2 Visualization of atoms

There is another additional feature to locate each atom in a ball and stick model. VESTA lists the fractional coordinates of all the atoms displayed in the graphic window in the "Vectors" dialog box that appears when selecting the Vectors item under the Edit menu. Selecting an atom in this dialog box, we can also select (highlight) the corresponding object in the Graphic window, and *vice versa*.

17.7 Files to Plot Results of Pattern Fitting and Simulation

RIETAN-FP has an option to output text files to plot results of pattern fitting and simulation in three formats: gnuplot [63], Igor Pro, and RietPlot 2000. Graphing results of Rietveld analysis is particularly effective in understanding of the reason why the current Rietveld analysis does not proceed smoothly. With RIETAN-FP, simulation of a powder diffraction pattern is possible only for a single-phase sample.

17.7.1 Gnuplot

Creation of PDF files in a batch mode

Gnuplot (`NPAT = 1`) is strongly recommended as a graphing tool if cross-platform free software is preferred to commercial one such as Igor Pro (see 17.7.2). Gnuplot is a command-driven interactive plotting utility for all the major operating systems [63] and available for download with its source code *via* its Web site.[7] Detailed Japanese information about gnuplot is presented, for example, at the Web sites of Kawano,[8] Yonezawa[9], and Sugita.[10] To avoid the trouble of having to install gnuplot further, the distribution file of the RIETAN-FP–VENUS systems for Windows includes gnuplot under the RIETAN_VENUS folder. On the other hand, gnuplot for macOS has to be installed by the user with an installer built by Allin Cottrell.[11]

Gnuplot is excellent in multiple functions, the support of many output formats,[12] full documentation, and continual upgrades. However, interactive operation where commands are input in the command line is rather troublesome and far from user-friendly for its beginners; we tend to forget how to use a variety of commands as time goes on. The batch mode in gnuplot is, therefore, used in RIETAN-FP in combination with the RIETAN-FP–VENUS assistance environment (see Sect. 11.3 of Ref. [63]). In other words, gnuplot is used as a graphing engine launched by a gnuplot command in a batch file (Windows) or a bash script (macOS).

[7] http://www.gnuplot.info/
[8] http://folk.uio.no/hpl/scripting/doc/gnuplot/Kawano/
[9] http://www.ss.scphys.kyoto-u.ac.jp/person/yonezawa/contents/program/gnuplot/
[10] http://www.gnuplot-cmd.com/
[11] http://ricardo.ecn.wfu.edu/pub/gnuplot/
[12] Referred to as "terminals" in gnuplot.

When NPAT is set at 1 in hoge.ins, RIETAN-FP creates a pair of text files, hoge.plt and hoge.gpd, after pattern fitting (Rietveld analysis, pattern decomposition, MEM-based pattern fitting, *etc.*) or simulation of a powder diffraction pattern. Commands to plot graphs from numerical data in hoge.gpd are described in the gnuplot script file, hoge.plt, outputting graphic data automatically after running gnuplot in a batch mode. In other words, the two files enable us to display the graph on the screen without entering any commands in the command line of gnuplot.

From the large number of graphic formats supported by gnuplot, the Portable Document Format (PDF) defined by Adobe was selected to display professional-quality images on the screen and export them to other applications such as Adobe Illustrator, Microsoft Office, and LaTeX. A PDF file is a self-contained cross-platform document containing vector data. With PDF files attached with an extension of pdf, documents can be represented in a manner independent of application software, hardware, and operating system without any degradation of vector graphics. In addition, many PDF viewers are distributed free of charge over the internet.

Gnuplot script file, hoge.plt

An example of a gnuplot script file, Fapatite.plt, to create a graph from results of Rietveld analysis from X-ray powder diffraction data of fluorapatite (included in the distribution files of the RIETAN-FP–VENUS packages) with gnuplot will be listed below to instruct how to modify it:

```
# LPS = 0: Plot no axis for lattice-plane spacings
# LPS = 1: Plot an axis for lattice-plane spacings
LPS = 1

 WIDTH = 24.5 # Width/cm of the graph
HEIGHT = 13.0 # Height/cm of the graph

XMIN =  10.0 # Minimum value for the x axis
XMAX = 110.0 # Maximum value for the x axis

YMIN = -4000 # Minimum value for the y axis
YMAX = 45000 # Maximum value for the y axis
YINC = 10000 # Increment for ticks on the y axis

IVSIZE = 15  # Size of numerical values for the x and y axes
ILSIZE = 17  # Size of labels for the x and y axes
SYLBL = -1.5 # Shift of the y label (Intensity) along the x axis in the unit of a character

PSIZE = 0.35 # Size of '+' marks representing observed intensities
TSIZE = 0.90 # Length (in percent of the y-axis length) of tick marks to show peak positions

OFFSETD =  -900 # Offset for the residual curve

OFFSET1 =  4200 # Offset for tick marks (peak positions) for phase No. 1
OFFSET2 =  3100 # Offset for tick marks (peak positions) for phase No. 2
OFFSET3 =  2000 # Offset for tick marks (peak positions) for phase No. 3
```

```
DLW = 1.1 # Default linewidth
BLW = 1.1 # linewidth of graph borders

set border linewidth BLW
set tics scale 1.7, 0.9

LEN_BAR = 0.01*TSIZE*(YMAX-YMIN)
set bars 0

set terminal pdfcairo linewidth DLW size WIDTH/2.54, HEIGHT/2.54 fontscale 0.75

ITSIZE = ILSIZE + 2
set title "A mixture of Cu_3Fe_4(PO_4)_6, Cu_3(PO_4)_2, and Cu_2P_2O_7" font ",".ITSIZE

set label 1 at graph 0.8500, 0.92 "{/:Italic R}_{wp} = 1.50 %" font ", 17"
set label 2 at graph 0.8622, 0.84 "{/:Italic R}_p = 1.19 %" font ", 17"
set label 3 at graph 0.8608, 0.76 "{/:Italice R}_B = 4.28 %" font ", 17"
set label 4 at graph 0.8577, 0.68 "{/:Italic R_F}&{/=30 |}= 3.86 %" font ", 17"

set ytics mirror offset 0.4, 0.22 font ",".IVSIZE 0, YINC
set mytics 2 # The number of sub-intervals between major tics
set ylabel "Intensity" offset SYLBL, 0 font ",".ILSIZE

set mxtics 5 # The number of sub-intervals between major tics
set xlabel "2{/:Italic \316\270}&{/=15 |}/&{/=15 |}\302\260" offset 0, -0.1 font ",".ILSIZE

if ( LPS == 0 ) {
  set xtics mirror offset -0.22, 0.3 10 font ",".IVSIZE # increment = 10
} else {
  set xtics nomirror offset -0.22, 0.3 10 font ",".IVSIZE # increment = 10

  lambda = 1.540593
  set angles degrees
  set x2tics offset -0.31, 0.1 autofreq font ",".IVSIZE
  set link x2 via 0.5*lambda/sin(0.5*x) inverse 2.0*asin(0.5*lambda/x)
  set mx2tics 10 # The number of sub-intervals between major tics
  set x2label "{/:Italic d}&{/=14 |}/&{/=10 |}\342\204\253" offset 0, -0.4 font ",".ILSIZE
}

# Margins measured in character widths or heights (a negative value: automatic)
set margins -1, -1, 4, -1 # <left>, <right>, <bottom>, <top>

plot [XMIN:XMAX] [YMIN:YMAX] "Cu3Fe4P6.gpd" \
   every :::0::0 using 1:($3) notitle with lines linetype 11 linecolor rgbcolor "cyan", \
'' every :::0::0 using 1:2 notitle with points pointtype 1 pointsize PSIZE \
   linecolor rgbcolor "red", \
'' every :::1::1 using 4:(OFFSET1):(LEN_BAR) notitle with yerrorbars linetype 4 pointtype 0 \
   linecolor rgbcolor "forest-green", \
'' every :::2::2 using 4:(OFFSET2):(LEN_BAR) notitle with yerrorbars linetype 4 pointtype 0 \
   linecolor rgbcolor "forest-green", \
'' every :::3::3 using 4:(OFFSET3):(LEN_BAR) notitle with yerrorbars linetype 4 pointtype 0 \
   linecolor rgbcolor "forest-green", \
'' every :::0::0 using 1:($4+OFFSETD) notitle with lines linetype 3 linecolor rgbcolor "blue"
```

In hoge.plt, strings following '#' are regarded as comments in just the same manner as in hoge.ins. If '#' at the top of a line is deleted, the command is executed when replotting the graph. For example, removing '#' in

```
#set mytics 5 # The number of sub-intervals between major tics
```

puts four minor tics between two major ones in the y axis.

Changing '`LPS = 0`' in the third line into '`LPS = 1`' adds tics of lattice-plane spacings, d, on the x2 axis (see Fig. 17.3), which is understandable by reading the part of a `if ..... else` block.

In the plot command divided into 8 lines, '`every :::n::n`' (`n` = 0 or 1) means that data in block `n` are plotted. A backslash, '\', placed at the tail of a line denotes continuation of the line. *Be careful not to input any spaces after '\' (backslash).*

Setting `INDREF` at 1 in hoge.ins gives the following two lines

```
'' every :::0::0 using 1:($4+OFFSETD) notitle with lines linetype 3 linecolor rgbcolor "blue", \
'' every :::2::2 using 1:($2) notitle with lines linetype 11 linecolor rgbcolor "steelblue"
```

in place of

```
'' every :::0::0 using 1:($4+OFFSETD) notitle with lines linetype 3 linecolor rgbcolor "blue"
```

to plot individual profile intensities of all the reflections, which disappears by commenting out the last line and removing '`, \`' preceding it:

```
'' every :::0::0 using 1:($4+OFFSETD) notitle with lines linetype 3 linecolor rgbcolor "blue"
#'' every :::2::2 using 1:($2) notitle with lines linetype 11 linecolor rgbcolor "steelblue"
```

However, the same graph is plotted even if '`, \`' remains.

The latter half of hoge.plt consists of commands, which are commented out, to draw a Williamson–Hall (WH) or Halder–Wagner (HW) plot (see Chap. 13). With an `MSCS` macro of the RIETAN-FP–VENUS assistance environment, only the part of these commands is extracted and uncommented to give hoge-mscs.plot, which is then input by gnuplot to display the WH or HW plot. To modify settings for the plot, not hoge-mscs.plot but the above comment lines in hoge.plt must be edited prior to execution of `MSCS`.

Procedures to plot and view graphs on the assistance environment

The RIETAN-FP–VENUS assistance environment (see Chap. 16) is used to create a PDF file, display a graph, and modify it according to the following procedures (**Fig. 17.2**):

1. After clicking a [Plot] button (Windows) or selecting a [Plot] item (macOS), gnuplot directly generates a PDF file, hoge.pdf, from hoge.plt and hoge.gpd in the batch mode.

2. A PDF viewer associated with the extension, pdf, automatically inputs hoge.pdf to display a graph on the screen.

3. The script file, hoge.plt, is opened by Hidemaru Editor for Windows or Jedit X for macOS to make it possible to edit it for replotting.

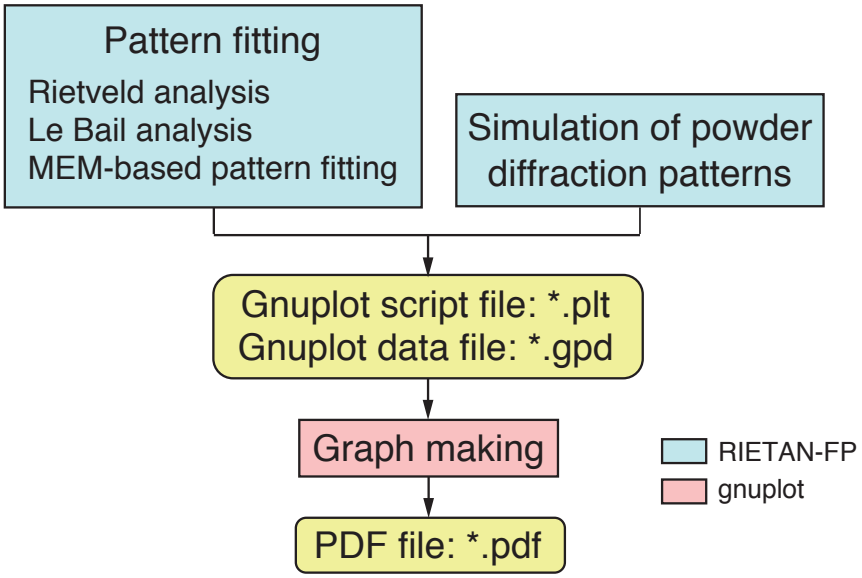

Figure 17.2: Procedures for creating a PDF file storing a graph resulting from pattern fitting or simulation of a powder diffraction pattern

4. Browsing and magnifying this graph, we can easily determine appropriate setting values in hoge.plt. Modification of hoge.plt with the editor and replotting graphs with gnuplot are alternately repeated until a satisfactory graph is obtained. New commands and keywords may be freely added in hoge.plt if desired.

As described above, plotting graphs with gnuplot presupposes the use of the RIETAN-FP–VENUS assistance environment based on Hidemaru Editor (Windows) or Jedit X (macOS). Commands need not be entered in the gnuplot window; only pressing the button or the shortcut leads to the immediate appearance of a graph reflecting the content of hoge.plt. Selection of [Plot] in pulldown and popup menus is also possible with a mouse. Thus, those who are not very familiar with the operation of gnuplot can easily look desired graphs for demonstration and publishing.

Free PDF viewers called Sumatra PDF for Windows and Preview, which is an macOS's application, are more suitable than Adobe Reader. Both of them are more lightweight than Adobe Reader and never lock any PDF file, allowing to input a new PDF file with the same name and display its content in the same window or another one. In the case of Sumatra PDF, a setting

```
ReuseInstance = false
```

in SumatraPDF-setting.txt,[13] must be changed as

```
ReuseInstance = true
```

to let a single application of Sumatra PDF to display PDF files successively.

[13] http://blog.kowalczyk.info/software/sumatrapdf/settings.html

Various commands used in hoge.plt

The destination, '`pdfcairo`', of the graphic data generated by gnuplot is specified in the `set terminal` command:

```
set terminal pdfcairo linewidth DLW size WIDTH/2.54, HEIGHT/2.54 fontscale 0.75
```

The graphing backend of terminal pdfcairo specified in hoge.plt takes full advantage of contemporary features of a single set of libraries for graphics and text rendering to produce high-quality graphs through the use of over-sampling, anti-aliasing, and so on (p. 14 in Ref. [63]). Terminal pdfcairo has the benefit of outputting PDF files where empty spaces aroung the graph are automatically cropped, which is very convenient when including the resulting PDF files in documents of LaTeX, Microsoft Word, Pages, Adobe Illustrator, Microsoft PowerPoint, Keynote, *etc.* Because no font option is given here, the default font, sans, is used, which enhances the visual clarity of a graph (see p. 312 in Ref. [63]). Using option `fontscale`, we can adjust the font size separately relative to the current one with a default value of 0.5 (See pp. 220–221 in Ref. [63]).

In the above script file, values of user-defined variables in lines from

```
 WIDTH = 24.5 # Width/cm of the graph"
```

to

```
OFFSET1 =  -700 # Offset for tick marks (peak positions) for phase No. 1"
```

are taken from corresponding data specified in Fapatite.ins except for `SYLBL`. In general, it is only necessary to check observed and calculated intensities to give proper settings. Contents of the variables are self-evident because of comments after numerical numbers.

In two lines,

```
DLW = 1.1 # Default linewidth
BLW = 1.1 # Linewidth of graph borders
```

following the above ones, the two kinds of line widths are continuously specified. The values of `WIDTH`, `HEIGHT`, `XMIN`, `XMAX`, `YMIN`, `YMAX`, `YINC`, `IVSIZE`, `ILSIZE`, `PSIZE`, `TSIZE`, `OFFSETD`, `OFFSETn` (`n`: phase number), `DLW`, and `BLW` after '`=`' may be changed to modify the appearance of the graph as needed. it should be remembered that graph borders are determined from not only `BLW` but also `DLW`.

The margin, which is the distance between the plot border and the outer edge of the canvas, is chosen automatically, but can be overridden by the set margins commands, *e.g.*,

```
set margins -1, -1, 4, -1 # <left>, <right>, <bottom>, <top>
```

where a negative value of `-1` causes gnuplot to revert to the computed value. If parts of labels and titles are lacking, please change each `-1` into an appropriate value in a character unit.

The first line of the plot command includes the name of the numerical data file, Fapatite.gpd:

```
plot [XMIN:XMAX] [YMIN:YMAX] "Fapatite.gpd" \
```

Of course, the lines of the `plot` command may be modified as required. For example, colors of lines, points, and bars can be changed easily. The following color names as many as 111 are predefined together with their hexadecimal numbers in gnuplot:

```
white              #ffffff = 255 255 255
black              #000000 =   0   0   0
dark-grey          #a0a0a0 = 160 160 160
red                #ff0000 = 255   0   0
web-green          #00c000 =   0 192   0
web-blue           #0080ff =   0 128 255
dark-magenta       #c000ff = 192   0 255
dark-cyan          #00eeee =   0 238 238
dark-orange        #c04000 = 192  64   0
dark-yellow        #c8c800 = 200 200   0
royalblue          #4169e1 =  65 105 225
goldenrod          #ffc020 = 255 192  32
dark-spring-green  #008040 =   0 128  64
purple             #c080ff = 192 128 255
steelblue          #306080 =  48  96 128
dark-red           #8b0000 = 139   0   0
dark-chartreuse    #408000 =  64 128   0
orchid             #ff80ff = 255 128 255
aquamarine         #7fffd4 = 127 255 212
brown              #a52a2a = 165  42  42
yellow             #ffff00 = 255 255   0
turquoise          #40e0d0 =  64 224 208
grey0              #000000 =   0   0   0
grey10             #1a1a1a =  26  26  26
grey20             #333333 =  51  51  51
grey30             #4d4d4d =  77  77  77
grey40             #666666 = 102 102 102
grey50             #7f7f7f = 127 127 127
grey60             #999999 = 153 153 153
grey70             #b3b3b3 = 179 179 179
grey               #c0c0c0 = 192 192 192
grey80             #cccccc = 204 204 204
grey90             #e5e5e5 = 229 229 229
grey100            #ffffff = 255 255 255
light-red          #f03232 = 240  50  50
light-green        #90ee90 = 144 238 144
light-blue         #add8e6 = 173 216 230
light-magenta      #f055f0 = 240  85 240
light-cyan         #e0ffff = 224 255 255
light-goldenrod    #eedd82 = 238 221 130
```

```
light-pink          #ffb6c1 = 255 182 193
light-turquoise     #afeeee = 175 238 238
gold                #ffd700 = 255 215   0
green               #00ff00 =   0 255   0
dark-green          #006400 =   0 100   0
spring-green        #00ff7f =   0 255 127
forest-green        #228b22 =  34 139  34
sea-green           #2e8b57 =  46 139  87
blue                #0000ff =   0   0 255
dark-blue           #00008b =   0   0 139
midnight-blue       #191970 =  25  25 112
navy                #000080 =   0   0 128
medium-blue         #0000cd =   0   0 205
skyblue             #87ceeb = 135 206 235
cyan                #00ffff =   0 255 255
magenta             #ff00ff = 255   0 255
dark-turquoise      #00ced1 =   0 206 209
dark-pink           #ff1493 = 255  20 147
coral               #ff7f50 = 255 127  80
light-coral         #f08080 = 240 128 128
orange-red          #ff4500 = 255  69   0
salmon              #fa8072 = 250 128 114
dark-salmon         #e9967a = 233 150 122
khaki               #f0e68c = 240 230 140
dark-khaki          #bdb76b = 189 183 107
dark-goldenrod      #b8860b = 184 134  11
beige               #f5f5dc = 245 245 220
olive               #a08020 = 160 128  32
orange              #ffa500 = 255 165   0
violet              #ee82ee = 238 130 238
dark-violet         #9400d3 = 148   0 211
plum                #dda0dd = 221 160 221
dark-plum           #905040 = 144  80  64
dark-olivegreen     #556b2f =  85 107  47
orangered4          #801400 = 128  20   0
brown4              #801414 = 128  20  20
sienna4             #804014 = 128  64  20
orchid4             #804080 = 128  64 128
mediumpurple3       #8060c0 = 128  96 192
slateblue1          #8060ff = 128  96 255
yellow4             #808000 = 128 128   0
sienna1             #ff8040 = 255 128  64
tan1                #ffa040 = 255 160  64
```

```
sandybrown          #ffa060 = 255 160  96
light-salmon        #ffa070 = 255 160 112
pink                #ffc0c0 = 255 192 192
khaki1              #ffff80 = 255 255 128
lemonchiffon        #ffffc0 = 255 255 192
bisque              #cdb79e = 205 183 158
honeydew            #f0fff0 = 240 255 240
slategrey           #a0b6cd = 160 182 205
seagreen            #c1ffc1 = 193 255 193
antiquewhite        #cdc0b0 = 205 192 176
chartreuse          #7cff40 = 124 255  64
greenyellow         #a0ff20 = 160 255  32
gray                #bebebe = 190 190 190
light-gray          #d3d3d3 = 211 211 211
light-grey          #d3d3d3 = 211 211 211
ark-gray            #a0a0a0 = 160 160 160
slategray           #a0b6cd = 160 182 205
gray0               #000000 =   0   0   0
gray10              #1a1a1a =  26  26  26
gray20              #333333 =  51  51  51
gray30              #4d4d4d =  77  77  77
gray40              #666666 = 102 102 102
gray50              #7f7f7f = 127 127 127
gray60              #999999 = 153 153 153
gray70              #b3b3b3 = 179 179 179
gray80              #cccccc = 204 204 204
gray90              #e5e5e5 = 229 229 229
gray100             #ffffff = 255 255 255
```

The above data can be displayed by inputting

```
gnuplot> set terminal pdfcairo
gnuplot> show colors
```

in command lines of gnuplot. The above colors are displayed in a Web page of Yonezawa.[14]

Replotting the graph after uncommenting the `set title` command

```
#set title "Rietveld analysis of fluorapatite, Ca_5F(PO_4)_3" font ",".ITSIZE
```

by deleting the top character, '`#`', puts a title above the graph:

Rietveld analysis of fluorapatite, $Ca_5F(PO_4)_3$

The title was imput as the first data in hoge.ins. Further, if the four comment lines

[14] http://www.ss.scphys.kyoto-u.ac.jp/person/yonezawa/contents/program/gnuplot/colorname_list.html

```
#set label 1 at graph 0.8500, 0.92 "{/:Italic R}_{wp} = 8.21 %" font ", 17"
#set label 2 at graph 0.8622, 0.84 "{/:Italic R}_p = 1.19 %" font ", 17"
#set label 3 at graph 0.8608, 0.76 "{/:Italice R}_B = 4.28 %" font ", 17"
#set label 4 at graph 0.8577, 0.68 "{/:Italic R_F}&{/=30 |}= 3.86 %" font ", 17"
```

are uncommented, four reliability indices

$$R_{\rm wp} = 8.21\,\%$$
$$R_{\rm p} = 6.39\,\%$$
$$R_{\rm B} = 3.78\,\%$$
$$R_F = 1.92\,\%$$

appear at a right upper part of Rietveld-refinement patterns. These four were obtained after convergence was reached in the Rietveld analysis. Note that $R_{\rm B}$ and R_F are output for only the first phase.

In the `set title set label` commands, which are commented out in the above list, `_` denotes subscripts. On the other hand, superscripts are represented by '`^`'. If the number of subscripts or superscripts is larger than unity, they should be enclosed by a pair of '`{`' and '`}`', *e.g.*, '`C_{117}H_{200}N_{32}O_{59}P_4`', '`Ca^{2+}`' and '`^{90}Sr`'. Parts of characters in titles and labels are made italic with `{/:Italic .....}` as exemplified in the above `set label` commands. A Greece character can be output using its octal code, *e.g.*, θ: `"{/:Italic \316\270}"` (normal) and θ: `{\316\270}`.[15] Narrow spaces can be conveniently inserted with '`&{/=ps |}|` (ps: font size), *e.g.*, `abc&{\10 |}def`, where `|` is used as a typical character whose width is very small.

To learn details in commands used in hoge.plt as well as other ones, the manual of gnuplot 5.X[16] should be consulted. GUI front-end applications may also input and edit hoge.plt to change various settings of graphs.

An example of plotting Rietveld-refinement patterns for a multi-phase sample

The number of lines for the `plot` command, where a new line is started by putting '`\`' at end-of-line, increases with increasing number of phases because y coordinates of short vertical bars representing peak positions, $2\theta_K$, are different from phase to phase. For example, in the case of Rietveld analysis from X-ray powder diffraction data of a mixture of $Cu_3Fe_4(PO_4)_6$, $Cu_3(PO_4)_2$, and $Cu_2P_2O_7$,[17] the plot command is as listed below:

```
plot [XMIN:XMAX] [YMIN:YMAX] "Cu3Fe4P6.gpd" \
   every :::0::0 using 1:($3) notitle with lines linetype 11 linecolor rgbcolor "cyan", \
'' every :::0::0 using 1:2 notitle with points pointtype 1 pointsize PSIZE \
   linecolor rgbcolor "red", \
'' every :::1::1 using 4:(OFFSET1):(LEN_BAR) notitle with yerrorbars linetype 4 pointtype 0 \
   linecolor rgbcolor "forest-green", \
'' every :::2::2 using 4:(OFFSET2):(LEN_BAR) notitle with yerrorbars linetype 4 pointtype 0 \
```

[15] http://blog.fujioizumi.verse.jp/?eid=311

[16] A manual translated into Japanese is distributed at the Web site of the Takeno laboratory of Niigata Institute of Technology: http://takeno.iee.niit.ac.jp/~foo/gp-jman/gp-jman.html

[17] Cu3Fe4P6 included in the distribution files of RIETAN-FP–VENUS package.

```
   linecolor rgbcolor "forest-green", \
'' every :::3::3 using 4:(OFFSET3):(LEN_BAR) notitle with yerrorbars linetype 4 pointtype 0 \
   linecolor rgbcolor "forest-green", \
'' every :::0::0 using 1:($4+OFFSETD) notitle with lines linetype 3 linecolor rgbcolor "blue"
```

In the `plot` command, '`every :::n::n`' (`n` = 1–3) specifies block numbers of peak positions, $2\theta_K$, for the three phases in Cu3Fe4P6.gpd, which is specified in the first line. Values of offsets, `OFFSET1`, `OFFSET2`, and `OFFSET3`, for tick marks ($2\theta_K$) along the y axis, whose initial values were input in hoge.ins, were optimized by trial and error.

Figure 17.3 illustrates Rietveld-refinement patterns resulting from X-ray powder diffraction data of the above three-phase sample. This figure has a title containing subscripts above the graph and an inset of four reliability indices, which were output by `set title` and `set label` commands in hoge.plt, respectively. Sub-intervals between major tics were set at 5 for the x axis and 2 for the y axis:

```
set mxtics 5 # The number of sub-intervals between major tics
.....
set mytics 2 # The number of sub-intervals between major tics
```

The starting major tick was set at 10000:

```
set ytics mirror offset  0.6, 0 font ",".IVSIZE 10000, YINC
```

Note that the font size of characters for the title is defined as

```
ITSIZE = ILSIZE + 2
```

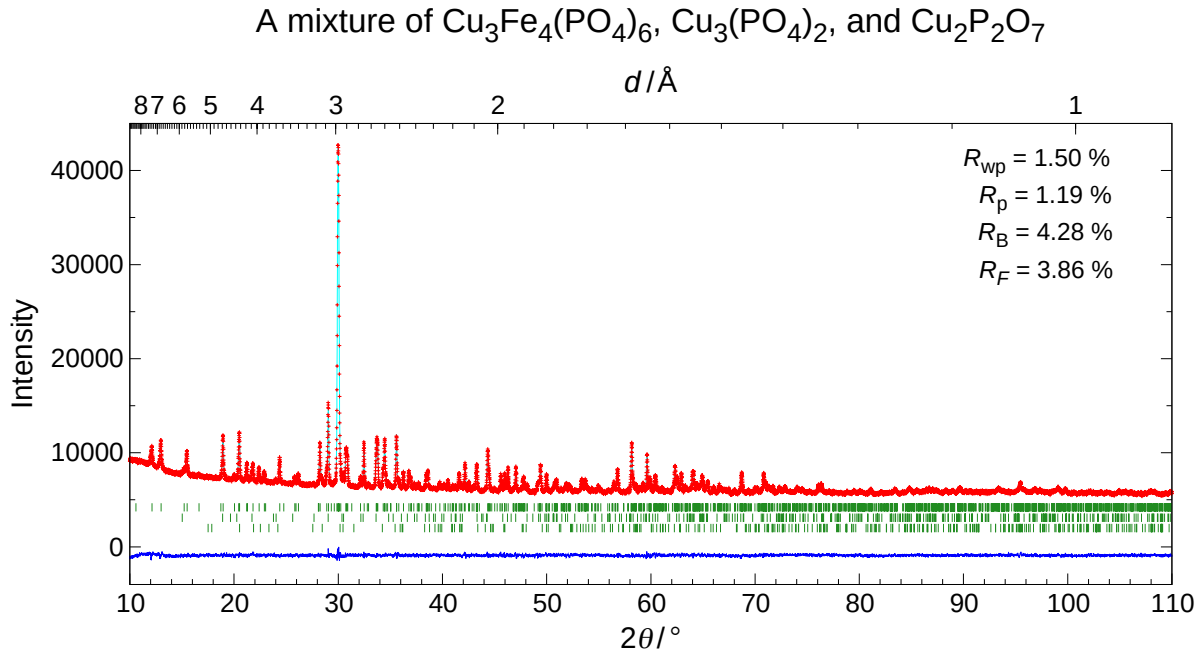

Figure 17.3: Observed, calculated, and difference patterns obtained in the Rietveld analysis from X-ray powder diffraction data of the mixture of $Cu_3Fe_4(PO_4)_6$, $Cu_3(PO_4)_2$, and $Cu_2P_2O_7$. Pay attention to the addition of an upper horizontal axis.

Of course, the increment, '`+ 2`', in this line may be changed as you like.

Gnuplot data file, hoge.gpd

In hoge.gpd resulting from pattern fitting, data are divided into two or more blocks, separated by a blank line plus a comment line. For example, Fapatite.gpd consists of two blocks:

```
# 2-theta, observed intensity, calculated intensity, residual, background
1.50000E+1  6.09000E+2  6.15140E+2 -6.13977E+0  6.15140E+2
1.50200E+1  6.12000E+2  6.14135E+2 -2.13519E+0  6.14135E+2
.....
1.29980E+2  8.40000E+1  8.37117E+1  2.88254E-1  7.13560E+1
1.30000E+2  8.40000E+1  8.29299E+1  1.07008E+0  7.14041E+1

# h, k, l, 2-theta (shifted), 2-theta (not shifted), d, sin(theta),
# FWHM*cos(theta), and beta*cos(theta) for phase No. 1
  1   0   1  16.826  16.877  5.2492  0.146746  0.00128500  0.00171137
  1   0   1  16.868  16.919  5.2492       NaN         NaN         NaN
  1   1   0  18.878  18.929  4.6845  0.164435  0.00128176  0.00170951
  1   1   0  18.925  18.976  4.6845       NaN         NaN         NaN
.....
```

For convenience, a comment line for the second block were divied into two parts here. Thanks to the comment lines, the content of this file will be self-explanatory. The meaning of '`residual`' is explicitly explained in the following lines in hoge.ins:

```
LRES = 0: Plot Delta_y = (observed intensity - calculated intensity).
LRES = 1! Plot Delta_y/(standard deviation).
LRES = 2! Plot [Delta_y/(observed intensity)]/(standard deviation).*
# * Refer to Eq. (1.13) in R. A. Young, "The Rietveld Method," p. 24.
```

In the second block, $\sin\theta$ and $\beta\cos\theta$ are used to draw Williamson–Hall and Halder–Wagner plots (see 13.4.3). '`NaN`'s are given to $\sin\theta$ and $\beta\cos\theta$ of Cu $K\alpha_2$ reflections because none of them need to be plotted in the graph.

In multi-phase samples, hkl, 2θ (shifted), 2θ (not shifted), and d of phase No. 2, 3, ... follow those of phase No. 1 with a blank line plus a comment line between data lines for two phases. The total number of blocks is equal to (the number of phases)+1. The first block is block 0, which is followed by blocks 1, 2, 3, ... while the first point in each block is point 0, which is followed by points 1, 2, 3, ... In `each` keywords in the `plot` command, start and end blocks, which are equal to each other, are specified to input data in the block.

If `INDREF` is set at 1 in hoge.ins, lines to plot individual profile intensities are appended. For example, in the case of Fapatite.gpd,

```
# xrefl, yrefl, ynet, phase, h, k, l, code, and m
 16.120  5.63006E+02  1.89397E+00  1   1   0   1 1  12
 16.140  5.62194E+02  2.00542E+00  1   1   0   1 1  12
```

```
 16.160   5.61394E+02   2.12701E+00   1    1    0    1 1   12
 16.180   5.60606E+02   2.25997E+00   1    1    0    1 1   12
 .....
```

where `xrefl`, `yrefl`, and `ynet` are, respectively, 2θ, the individual profile intensity, and the net intensity of the 101 reflection (code = 1: Cu $K\alpha_1$ radiation) with a multiplicity, m, of 12 for fluorapatite (phase 1).

On simulation of a powder diffraction pattern (`NMODE = 1`), hoge.gpd is output in a similar format with two blocks.

17.7.2 Igor Pro

A powerful commercial program, Igor Pro, is also suitable for plotting Rietveld-analysis and simulated patterns. Both Windows and macOS versions are available.

Advantages of Igor Pro over self-made plotting utilities are its high capabilities including

1. a programming language,
2. exporting files with several different formats,
3. page layouts.

Unfortunately, Igor Pro lacks one of the most important features of programs for scientists and engineers: free of charge. Part of users may complaint of not possessing an enough budget to buy it. However, WaveMetrics extends academic pricing to students and teachers. In the case of on-line ordering, WaveMetrics further permits students with limited financial resources to purchase Igor Pro at an unbelievably cheap price of $85.

Igor Pro for Linux is not sold. However, virtualization software such as VMware makes it possible to run Igor Pro for Windows on Linux machines.

File hoge.itx with the Igor text format is obtainable when `NPAT` is set at `2` in hoge.ins. It can be input by Igor Pro directly when its icon is double-clicked. Then, Igor Pro plots data automatically thanks to a series of commands recorded by RIETAN-FP at the end of hoge.itx, as exemplified below:

```
WAVES/O xppp_1, x0ppp_1, yppp_1
BEGIN
END
X Display ycal,delta vs twoth
X AppendToGraph yobs vs twoth
X SetAxis bottom  15.00, 130.00
X SetAxis left   -2500,   20000
X AppendToGraph yphase_1 vs xphase_1
X AppendToGraph yppp_1 vs xppp_1
.....
```

Various parameters included in these commands are input by the user in hoge.ins. Figure 2.1 was plotted with Igor Pro from file hoge.itx output by RIETAN-FP.

If hoge.plt created by gnuplot shares the same folder with hoge.itx, hoge.plt is preferentially opened by clicking the [Plot] button (Windows) or pressing the shortcut for [Graph] (macOS) in the RIETAN-FP–VENUS assistance environment (see 17.7.1). Accordingly, hoge.plt has to be absent when wanting to plot data in hoge.itx in the same folder.

If `INDREF` is set at `1` in hoge.ins, the net intensity of each reflection is output to wave `ynet` as follows:

```
WAVES/O xrefl, yrefl, ynet, phase, h, k, l, code, m
BEGIN
 15.000  6.15390E+2  2.87933E-1  1   1   0   1 1 12
 15.020  6.14392E+2  2.94340E-1  1   1   0   1 1 12
 15.040  6.13397E+2  3.00963E-1  1   1   0   1 1 12
 15.060  6.12403E+2  3.07812E-1  1   1   0   1 1 12
 15.080  6.11411E+2  3.14897E-1  1   1   0   1 1 12
 .....
```

Waves `xrefl`, `yrefl`, `phase`, `h`, `k`, `l`, `code`, and `m` are 2θ, the intensity of each reflection (= net intensity + background), phase number, h, k, l, code number (= 1 for monochromatic beams or $K\alpha_1$ radiation; = 2 for $K\alpha_2$ radiation), and multiplicity, respectively. For convenience, the same values are redundantly output for `phase`, `h`, `k`, `l`, `code`, and `m`, as listed above. They are used in the original structure-refinement method, which was developed in collaboration with Takashi Ida of Nagoya Institute of Technology, taking into account particle statistics in X-ray powder diffraction [218] (see Chap. 15). Diffraction profiles of each reflection are separated by a line showing the end of a series of data:

```
NaN NaN NaN NaN NaN NaN NaN NaN NaN
```

In the simulation mode (`NMODE = 1`), powder diffraction patterns of multi-phase samples can be plotted with Igor Pro. However, short vertical bars, which show positions of Bragg reflections, of all the phases are mixed together in this case.

17.7.3 WinPLOTR

WinPLOTR [107] has a feature to input hoge.int (NINT = 1, 2, 5–7, 11, and 12) in addition to hoge.itx. Unfortunately, neither background intensities nor the profile of each reflection can be plotted with WinPLOTR. After inputting hoge.int, WinPLOTR is able to estimate discrete background intensities to create hoge.bgr, which is, in turn, converted into hoge.bkg by RIETAN-FP (see 3.12.3). WinPLOTR is also useful in precessing diffraction data for peak search, removal of $K\alpha_2$ profiles, and indexing.

17.7.4 RietPlot 2000

This is a Windows application written in Visual Basic by Naoki Ohashi of National Institute for Materials Science. It is distributed free of charge for noncommercial use.[18]

[18] Information on RietPlot 2000 is obtainable at http://www.nims.go.jp/rietplot/

17.7.5 RIETVIEW

RIETVIEW is a program written by Dr. Hell for Windows and briefly introduced in ref. [105]. It is recommended for routine use because of its high-speed capability. RIETVIEW is available for download at the Web site of Dr. Hell.[19]

17.7.6 Patmill

PatMill written by Zentaro Akase of Tohoku University for Windows requires ActivePerl and Drop on Script in addition to gnuplot included in the RIETAN-FP package. It also runs just fine under Linux. PatMill is available for download at Akase's Web page.[20]

17.7.7 Other programs

Some programs other than the above three are currently distributed on the Web: MYPLOT, PlotRietRefPat (using program pro Fit of QuantumSoft), PowderPlot, and RietPlot (different from RietPlot 2000 described above).

17.8 Standard Output File

17.8.1 Dispersion corrections calculated by RIETAN-FP

When `NPRINT` is set at `2` in hoge.ins, detailed information on the calculation of f' and f'' is output to hoge.lst. For example, in the case of Cimetidine.ins included in the distribution files, Cimetidine.lst contains the following lines near its top part:

```
 Dispersion corrections calculated for synchrotron X rays at lambda = 1.52904 Angstroms (E =  8.10863 keV)
 f' + f(NT) = f1 + f(rel) - Z + f(NT) will be used as f' for elements listed below.
 If f1 + f(rel) - Z is preferred to f1 + f(rel) - Z + f(NT), input the former in hoge.ins by yourself.

No. Atom    f1          f(rel)      Z      f(NT)          f'         f'+f(NT)        f''
 1   C    6.01891    -1.800000E-3   6  -1.644200E-3  1.710939E-2  1.546519E-2  9.441026E-3
 2   N    7.03208    -3.000000E-3   7  -1.919100E-3  2.908278E-2  2.716368E-2  1.806140E-2
 3   S    16.3328    -2.100000E-2  16  -4.380400E-3  0.311846     0.307465     0.542838
```

As suggested in the third line, f' may be input in hoge.ins instead of $f' + f_{\mathrm{NT}}$.

The output of such a detailed table to hoge.lst enables us to utilize RIETAN-FP as a tool for obtaining f_1, f_{rel}, f_{NT}, f', $f' + f_{\mathrm{NT}}$, and f'' at an arbitrary wavelength.

17.8.2 Variables output during least-squares fitting

The following variables are output during least-squares fitting.

`OF`: Weighted sum of squares, $S(\boldsymbol{x})$, calculated with Eq. (2.1).

`AOF`: Augmented objective function, $F(\boldsymbol{x})$, calculated with Eq. (5.2); output only when imposing restraints.

`PF`: Sum of two penalty terms in Eq. (5.2).

`NPTS`: Number of data points to be analyzed.

[19] http://drhell.web.fc2.com/labo/index.html
[20] http://www.tagen.tohoku.ac.jp/labo/shindo/staff/akase/patmill.htm

`NFNEV`: Number of calculating the weighted sum of squares (Gauss–Newton and modified Marquardt methods).

`ITER`: Iteration number (conjugate-direction method).

`NFUNCT`: Number of calculating the weighted sum of squares (conjugate-direction method).

`DAMP`: Damping factor, d, in the Gauss–Newton method (see 4.5).

`LAMBDA`: Marquardt parameter, λ, in the modified Marquardt method (see 4.1.2).

`T`: Penalty parameter, $t^{(J)}$, in Eq. (5.2).

Note that the message

```
Too large Marquardt parameter
```

means either divergence or convergence of the solution. After the convergence has been attained, λ increases necessarily because $S(\boldsymbol{x})$ ($F(\boldsymbol{x})$ in Rietveld analysis under restraints) can no longer be reduced in the current least-squares calculation.

17.8.3 Ensuring convergence

IF `NPRINT` is 1 or 2, `DELTA.A/SIGMA`, $|\Delta x_j|/\sigma_j$, is output in the final list of fixed and refined parameters. The standard uncertainty, σ_j, of the jth parameter, x_j is calculated with Eq. (4.13). Whereas IUCr imposes a requirement of $|\Delta x_j|/\sigma_j \leqslant 0.05$ for all the variable parameters to ensure the completeness of structure refinements from single-crystal diffraction data, $|\Delta x_j|/\sigma_j < 0.1$ is quite satisfactory in those from powder diffraction data [237].

17.8.4 Information about the restraints imposed on geometrical parameters after refinement

After the above title, the following data obtained from final lattice and structure parameters are output for all the restraints imposed on geometrical parameters:

`I`: Serial number of this restraint.

`KIND`: BL = bond length, BA = bond angle, and TA = dihedral angle.

`GEOM_PAR`: Geometrical parameter.

`EXPCTD`: Expected geometrical parameter, *i.e.*, $l_{12j}(\mathrm{exp})$ in Eq. (5.8), $\phi_{123k}(\mathrm{exp})$ in Eq. (5.9), or $\omega_{1234l}(\mathrm{exp})$ in Eq. (5.10).

`DEV`: Allowed deviation from the expected geometrical parameter, *i.e.*, $\Delta l_{12j}(\boldsymbol{x})$ in Eq. (5.8), $\Delta\phi_{123k}(\boldsymbol{x})$ in Eq. (5.9), or $\Delta\omega_{1234l}(\boldsymbol{x})$ in Eq. (5.10).

`WEIGHT`: $1/l_{12j}(\boldsymbol{x})$ in Eq. (5.8), $1/\phi_{123k}(\boldsymbol{x})$ in Eq. (5.9), or $w(\omega_{1234l})$ in Eq. (5.10).

`VR`: Violated restraint, *i.e.*, function min in Eq. (5.8), (5.9), or (5.10).

`PERCENT`: Percentage of this penalty in the total of penalty terms, *i.e.*, $P_l(\boldsymbol{x}) + P_\phi(\boldsymbol{x}) + P_\omega(\boldsymbol{x})$ in Eq. (5.2).

`A`: Atom A relevant to the geometrical parameter.

`B`: Atom B relevant to the geometrical parameter.

`C`: Atom C relevant to the bond angle or dihedral angle.

`D`: Atom D relevant to the dihedral angle.

17.8.5 Reliability indices, a goodness-of-fit indicator, and Durbin–Watson statistics

After a title line

```
Reliability factors, a goodness-of-fit indicator, and Durbin-Watson statistic
```

their seven values are output:

`Rwp`: R-weighted pattern, R_{wp}, calculated with Eq. (4.15).
`Rp`: R-pattern, R_{p}, calculated with Eq. (4.16).
`RR`: R-Rietveld, R_{R}, calculated with Eq. (4.17).
`Re`: R-expected, R_{e}, calculated with Eq. (4.18).
`S`: Goodness-of-fit indicator, S, calculated with Eq. (4.19).
`d1`: The weighted form of the Durbin–Watson statistic, d_{DW}, calculated with Eq. (4.30).
`d2`: The unweighted form of the Durbin–Watson statistic, d_{DW}, calculated with Eq. (4.31).

From the two forms of the Durbin–Watson statistics, select whichever we like.

17.8.6 Estimated factor to adjust errors of observed structure factors

For each phase, the following reliability indices based on integrated intensities plus a regulating factor are output:

`RB`: R-Bragg factor, R_{B}, calculated with Eq. (4.21).
`RF`: R-structure factor, R_F, calculated with Eq. (4.22).
`RF^2`: R_{F^2}, calculated with Eq. (4.23).
`E(SCIO)`: estimated factor, E/rad, to adjust $\sigma(|F_{\mathrm{o}}(\boldsymbol{h}_K)|)$ (see 14.5).

After hoge.fos output by RIETAN-FP has been read in by Dysnomia, $\sigma\left(|F_{\mathrm{o}}(\boldsymbol{h}_K)|\right)$ is calculated with Eq. (14.18). `E(SCIO)` will serve as an initial estimate of E on the use of Dysnomia for MEM analysis; Dysnomia allows us to specify E to adjust $\sigma\left(|F_{\mathrm{o}}(\boldsymbol{h}_K)|\right)$.

17.8.7 Information on final structure parameters in the asymmetric unit

Only parameter values are output without any standard uncertainties (s.u.'s) for structure parameters on which linear constrains are imposed, *i.e.*, ID(I) = 2. For example, in a certain compound with space group $R\bar{3}m$, no s.u.'s are given for y coordinates in the 18h site where $y = -x$:

```
O2          18h  x -x z          18   1.0000   18.0000   0.17091  -0.17091   0.10566...
                                  -        -         -   0.00019          -   0.00009...
O3          18h  x -x z          18   0.3333    5.9999   0.68870  -0.68870  -0.00226...
                                  -        -         -   0.00221          -   0.00023...
```

If necessary, add s.u.'s in parentheses just after parameter values with appropriate numbers of significant figures in lists of structure parameters.

Note that the first coordinate triplet is output in hoge.lst for (multiplicity + Wyckoff letter) of each site, *e.g.*, in the case of fluorapatite,

```
Atom      Site                 neq  *   g    =   n        x         y         z      .....
O1          6h  x y 1/4          6   1.0000   6.0000   0.32417   0.48535   0.25000   .....
                                 -       -        -    0.00033   0.00034         -   .....
O2          6h  x y 1/4          6   1.0000   6.0000   0.59177   0.46981   0.25000   .....
                                 -       -        -    0.00035   0.00037         -   .....
O3         12i  x y z           12   1.0000  12.0000   0.33915   0.25727   0.06981   .....
                                 -       -        -    0.00027   0.00027   0.00027   .....
P           6h  x y 1/4          6   1.0000   6.0000   0.39731   0.36787   0.25000   .....
                                 -       -        -    0.00016   0.00016         -   .....
Ca1         4f  1/3 2/3 z        4   1.0000   4.0000   0.33333   0.66667   0.00133   .....
                                 -       -        -          -         -   0.00023   .....
Ca2         6h  x y 1/4          6   1.0000   6.0000   0.24180  -0.00795   0.25000   .....
                                 -       -        -    0.00012   0.00015         -   .....
F           2a  0 0 1/4          2   1.0000   2.0000   0.00000   0.00000   0.25000   .....
                                         -        -          -         -         -   .....
```

Each (multiplicity + Wyckoff letter) output in hoge.lst is obtained by STRUCTURE TIDY [169] embedded in RIETAN-FP, and the Wyckoff letter is further used to output a linear-constraint number, `NCON`, for anisotropic atomic displacement parameters, β_{ij}, of the site; `NCONS` is included in '`.....`' in the above list. Therefore, the standardization of crystal data (see Chap. 9) with RIETAN-FP or VESTA is highly recommended both to get the right (multiplicity + Wyckoff letter) and to refine β_{ij}'s, in particular when the standardization by STRUCTURE TIDY accompanies changes in a, b, c axes or the origin. At any rate, checking fractional coordinates of sites, where β_{ij}'s are assigned by referring to the above part in hoge.lst, is strongly recommended on the refinement of β_{ij}'s.

Of course, each multiplicity in (multiplicity + Wyckoff letter) must be equal to `neq`, which is evaluated from fractional coordinates by checking the overlap of equivalent positions generated from coordinate triplets recorded in spgra (see Table 17.1). If they differ from each other, check the values of x, y, and z (*e.g.*, numbers of digits) input for the site.

Numerical values in the list of atomic displacement parameters are equal to $10^6\beta_{ij}$ (dimensionless), $10^6U_{ij}/\text{Å}^2$, $B_{\text{eq}}/\text{Å}^2$, and $U_{\text{eq}}/\text{Å}^2$. Note that β_{ij} and $U_{ij}/\text{Å}^2$ are multiplied by 10^6 to represent them and their s.u.'s by integers.

It is very easy to learn whether the three conditions, Eqs. (3.26), (3.27), and (3.28), are satisfied for each site. On the other hand, the other conditions, Eqs. (3.29) and (3.30), need to be checked by calculating their left-hand sides. After `NCON`, `betacon` is output for each site where anisotropic atomic displacement parameters (β_{11j}, β_{22j}, β_{33j}, β_{12j}, β_{13j}, and β_{23j}) have been input by the user. Two signs are output for the fourth and fifth conditions, Eqs. (3.29) and (3.30), that have to be satisfied among six anisotropic atomic displacement parameters after Rietveld refinement:

- $+$, $+$: $\beta_{11j}\beta_{22j} + \beta_{22j}\beta_{33j} + \beta_{33j}\beta_{11j} - \beta_{12j}^2 - \beta_{13j}^2 - \beta_{23j}^2 > 0$ and $\det\boldsymbol{\beta} > 0$
- $+$, $-$: $\beta_{11j}\beta_{22j} + \beta_{22j}\beta_{33j} + \beta_{33j}\beta_{11j} - \beta_{12j}^2 - \beta_{13j}^2 - \beta_{23j}^2 > 0$ and $\det\boldsymbol{\beta} < 0$
- $-$, $+$: $\beta_{11j}\beta_{22j} + \beta_{22j}\beta_{33j} + \beta_{33j}\beta_{11j} - \beta_{12j}^2 - \beta_{13j}^2 - \beta_{23j}^2 < 0$ and $\det\boldsymbol{\beta} > 0$
- $-$, $-$: $\beta_{11j}\beta_{22j} + \beta_{22j}\beta_{33j} + \beta_{33j}\beta_{11j} - \beta_{12j}^2 - \beta_{13j}^2 - \beta_{23j}^2 < 0$ and $\det\boldsymbol{\beta} < 0$

Unless `'+, +'` is given, a set of β_{ij}s for a crystallographic site is physically meaningless, which is, most probably, caused by imperfect modeling of absorption, backgrounds, neglected thermal diffuse scattering, *etc.* Not β_{ji}s but an isotropic atomic displacement parameter, B_j, should be refined for such a site.

Below the list of anisotropic atomic displacement parameters, a list of linear constraints imposed on β_{ij}'s [70] is output:

NCON	beta11	beta22	beta33	beta12	beta13	beta23
1				0		0
* 2					0	0
3				0	0	
4				0	0	0
5	A	A			0	0
6	A	A			B	B
7	A	A			B	-B
8	A	A		0	0	0
9		A	A	0	0	
10		A	A	B	B	
11		A	A	-B	B	
12		A	A	0	0	0
13		A		A/2		0
14		A		A/2	0	0
15		A		A/2	B	2B
* 16	A	A		A/2	0	0
17	A	A	A	0	0	0
18	A	A	A	B	B	B

where asterisks before `NCON` values are attached to sites included in the asymmetric unit of fluorapatite.

17.8.8 Mass fractions in a mixture

A part of Cu3Fe4P6.lst giving results of quantitative analysis is listed below, with some spaces (between `Phase` and `R`) deleted:

Phase	R	mu/rho	mu	[mu-mu(mean)]R	tau	w	X	w(cor)	X(cor)
Cu3Fe4(PO4)6	5.000	97.540	390.558	0.00418	0.994	0.9487	0.8700	0.9557	0.8864
Cu3(PO4)2	5.000	42.104	189.115	-0.09655	1.155	0.0370	0.0873	0.0321	0.0766
Cu2P2O7	5.000	41.684	173.468	-0.10437	1.169	0.0143	0.0427	0.0123	0.0370

In the above output, `R` is R_p, `mu/rho` is the mass attenuation coefficient (μ_p/ρ_p), `mu` is μ_p, `[mu-mu(mean)]R` is $(\mu_p - \overline{\mu})\,R_p$, `tau` is τ_p, `w` is w_p, and `X` is the mole fraction; 'cor' denotes correction for microabsorption (see 7.2).

17.8.9 Columns in the summary of possible reflections

`Phase`: Phase number.
`h`: Reflection index, h.
`k`: Reflection index, k.
`l`: Reflection index, l.
`Code`: Three-character code to represent characteristics of the hkl reflection.
`2-theta`: Diffraction angle, $2\theta_K$.
`d`: Lattice-plane spacing, d_K.
`Iobs`: Observed integrated intensity, $I_{\rm o}(\boldsymbol{h}_K)$.
`Ical`: Calculated integrated intensity, $I(\boldsymbol{h}_K)$.
`|F(crys)|`: Crystal-structure factor, $|F(\boldsymbol{h}_K, \text{cryst.})|$.
`|F(magn)|`: Magnetic-structure factor, $|F(\boldsymbol{h}_K, \text{magn.})|$ (output only in neutron diffraction).
`POF`: Preferred-orientation function, P_K.
`FWHM`: Full-width at the half-maximum intensity, H_K.
`m`: Multiplicity, m_K.
`Dd/d`: Resolution, $\Delta d_K/d_K = H_K/\tan\theta_K$.

Defaults of the first and second characters of `Code` are both ' ' (space). When using the split pseudo-Voigt or Pearson VII profile functions, partial profile relaxation (see 4.4) was applied to this reflection if the first character is '`*`'. Signs '`+`' and '`-`' given as the second character in the case of X-ray diffraction are, respectively, hkl and $\bar{h}\bar{k}\bar{l}$ reflections for a Friedel pair (see 3.5.1). Numbers 2 and 1 in the third column are assigned to $K\alpha_2$ radiation in characteristic X rays and other radiation (neutron and synchrotron X rays), respectively.

In the simulation mode (`NMODE = 1`), `Ical` is adjusted in such a way that the strongest reflection has an integrated intensity of 10^5.

17.8.10 Marks given to observed integrated intensities

In 'Summary of possible reflections' output at the tail of hoge.lst, column `Iobs` gives the following data and marks:

`Iobs`: Full observed (positive) and calculated profiles have been obtained.
`'-'`: Part of the observed profile is lacking as a result of excluding a 2θ region.
`'W'`: Full observed (negative) and calculated profiles have been obtained.
`'H'`: Part of the profile exceeds $2\theta_{\rm max}$.
`'G'+Iobs`: Group of reflections with nearly equal lattice-plane spacings, d.

`Iobs` denotes $I_{\rm o}(\boldsymbol{h}_K)$ rounded off to an integer. Marks '`-`', '`W`', '`H`', and '`G`' provide us with important information about 'imperfect' reflections when MEM analysis is performed from powder-diffraction data. Reflections with these marks are excluded from calculations of $R_{\rm B}$ and R_F with Eqs. (4.21) and (4.22), respectively. If 2θ ranges of calculating reflection profiles are very wide, '`-`' may be output for low-angle reflections when deleting intensity data in the low-angle region in pattern fitting.

No observed structure factors, $F_{\rm o}(\boldsymbol{h}_K)$, of high-angle reflections marked with '`H`' are output in hoge.fos, where only their indices, hkl, are given (see 14.7.3). After MEM analysis from $F_{\rm o}(\boldsymbol{h}_K)$ and $\sigma\big(|F_{\rm o}(\boldsymbol{h}_K)|\big)$, Dysnomia outputs the estimated $F(\boldsymbol{h}_K)$'s of the '`H`' reflections in hoge.fba for subsequent whole-pattern fitting.

Chapter 18

LICENSE AGREEMENT

RIETAN-FP is currently copyrighted but distributed free of charge with its source code not open to the public because I wish to control its development and future by myself.

Whenever original results acquired with RIETAN-FP are published in journals, proceedings, facility reports, *etc.* or reported in scientific meetings with abstracts, the program name "RIETAN-FP" should explicitly be stated. Furthermore, cite the following paper [1]:

> F. Izumi and K. Momma, "Three-dimensional visualization in Powder Diffraction," *Solid. State Phenom.*, **130**, 15–20 (2007).

Only giving credit to RIETAN-FP for Rietveld or MPF analysis is fine in the cases of abstracts, short reports, and so forth with limited spaces, *e.g.*, as follows:

> The structure parameters of $CaTiO_3$ were refined by the Rietveld method from the X-ray diffraction data with RIETAN-FP.

You should not redistribute any copy of the distributed files unless you have a written permission from us.

Although RIETAN-FP has exhaustively been tested with intensity data of many compounds, it may still contain a fair number of bugs. RIETAN-FP is distributed in the hope that it will be useful and reliable. It is, however, provided "as it is" without any warranty since I have a number of commitments on my time. There is no charge for the program, *per se*, whereas technical service concerning it is not free.

Appendix A

PHYSICAL QUANTITIES CALCULATED FROM METRIC TENSORS

A.1 Metric Tensors of Direct and Reciprocal Lattices

The metric tensor (matrix) of the direct lattice is defined as

$$\begin{aligned} \boldsymbol{G} &= \begin{pmatrix} \boldsymbol{a}\cdot\boldsymbol{a} & \boldsymbol{a}\cdot\boldsymbol{b} & \boldsymbol{a}\cdot\boldsymbol{c} \\ \boldsymbol{b}\cdot\boldsymbol{a} & \boldsymbol{b}\cdot\boldsymbol{b} & \boldsymbol{b}\cdot\boldsymbol{c} \\ \boldsymbol{c}\cdot\boldsymbol{a} & \boldsymbol{c}\cdot\boldsymbol{b} & \boldsymbol{c}\cdot\boldsymbol{c} \end{pmatrix} \\ &= \begin{pmatrix} a^2 & ab\cos\gamma & ac\cos\beta \\ ba\cos\gamma & b^2 & bc\cos\alpha \\ ca\cos\beta & cb\cos\alpha & c^2 \end{pmatrix}, \end{aligned} \tag{A.1}$$

where $\boldsymbol{a}$, $\boldsymbol{b}$, and $\boldsymbol{c}$ are the primitive lattice vectors of the direct lattice. The elements of $\boldsymbol{G}$ define both the moduli of $\boldsymbol{a}$, $\boldsymbol{b}$, and $\boldsymbol{c}$, and the angles between them [238]. As well as for the direct lattice, a metric tensor may be defined for the reciprocal lattice:

$$\begin{aligned} \boldsymbol{G}^* &= \begin{pmatrix} \boldsymbol{a}^*\cdot\boldsymbol{a}^* & \boldsymbol{a}^*\cdot\boldsymbol{b}^* & \boldsymbol{a}^*\cdot\boldsymbol{c}^* \\ \boldsymbol{b}^*\cdot\boldsymbol{a}^* & \boldsymbol{b}^*\cdot\boldsymbol{b}^* & \boldsymbol{b}^*\cdot\boldsymbol{c}^* \\ \boldsymbol{c}^*\cdot\boldsymbol{a}^* & \boldsymbol{c}^*\cdot\boldsymbol{b}^* & \boldsymbol{c}^*\cdot\boldsymbol{c}^* \end{pmatrix} \\ &= \begin{pmatrix} a^{*2} & a^*b^*\cos\gamma^* & a^*c^*\cos\beta^* \\ b^*a^*\cos\gamma^* & b^{*2} & b^*c^*\cos\alpha^* \\ c^*a^*\cos\beta^* & c^*b^*\cos\alpha^* & c^{*2} \end{pmatrix}. \end{aligned} \tag{A.2}$$

In Eq. (A.2), $\boldsymbol{a}^*$, $\boldsymbol{b}^*$, and $\boldsymbol{c}^*$ are the primitive lattice vectors of the reciprocal lattice [238]:

$$\begin{aligned} \boldsymbol{a}^* &= \frac{\boldsymbol{b}\times\boldsymbol{c}}{\boldsymbol{a}\cdot(\boldsymbol{b}\times\boldsymbol{c})} \\ &= \frac{\boldsymbol{b}\times\boldsymbol{c}}{V}, \end{aligned} \tag{A.3}$$

$$\begin{aligned} \boldsymbol{b}^* &= \frac{\boldsymbol{c}\times\boldsymbol{a}}{\boldsymbol{b}\cdot(\boldsymbol{c}\times\boldsymbol{a})} \\ &= \frac{\boldsymbol{c}\times\boldsymbol{a}}{V}, \end{aligned} \tag{A.4}$$

$$\begin{aligned} \boldsymbol{c}^* &= \frac{\boldsymbol{a} \times \boldsymbol{b}}{\boldsymbol{c} \cdot (\boldsymbol{a} \times \boldsymbol{b})} \\ &= \frac{\boldsymbol{a} \times \boldsymbol{b}}{V}, \end{aligned} \tag{A.5}$$

where V is the unit-cell volume that can easily be calculated from $\boldsymbol{G}$ (see A.8).

$\boldsymbol{G} \rightleftharpoons \boldsymbol{G}^*$ conversions are very easy; $\boldsymbol{G}^*$ is equal to the inverse matrix of $\boldsymbol{G}$,

$$\boldsymbol{G}^* = \boldsymbol{G}^{-1}, \tag{A.6}$$

and *vice versa*:

$$\boldsymbol{G} = (\boldsymbol{G}^*)^{-1}. \tag{A.7}$$

General equations to calculate cosines of α^*, β^*, γ^*, and a^*, b^*, and c^* from direct-lattice ones are as follows:

$$a^* = \frac{bc \sin \alpha}{V}, \tag{A.8}$$

$$b^* = \frac{ac \sin \beta}{V}, \tag{A.9}$$

$$c^* = \frac{ab \sin \gamma}{V}, \tag{A.10}$$

$$\sin \alpha^* = \frac{V}{abc \sin \beta \sin \gamma}. \tag{A.11}$$

$$\cos \alpha^* = \frac{\cos \beta \cos \gamma - \cos \alpha}{\sin \beta \sin \gamma}, \tag{A.12}$$

$$\sin \beta^* = \frac{V}{\sin \alpha \sin \gamma}, \tag{A.13}$$

$$\cos \beta^* = \frac{\cos \gamma \cos \alpha - \cos \beta}{\sin \gamma \sin \alpha}, \tag{A.14}$$

$$\sin \gamma^* = \frac{V}{\sin \alpha \sin \beta}, \tag{A.15}$$

$$\cos \gamma^* = \frac{\cos \alpha \cos \beta - \cos \gamma}{\sin \alpha \sin \beta}. \tag{A.16}$$

The metric tensor incorporates the information for the lattice, *i.e.*, the lattice parameters, into a single matrix. In general, geometrical parameters related to lattice dimensions can easily be calculated from $\boldsymbol{G}$ and $\boldsymbol{G}^*$, as described in what follows.

A.2 Reciprocal-Lattice Vector

The reciprocal-lattice vector, $\boldsymbol{s}_K$, is defined as

$$\boldsymbol{s}_K = h\boldsymbol{a}^* + k\boldsymbol{b}^* + l\boldsymbol{c}^*. \tag{A.17}$$

It is related to $\boldsymbol{h}$ by

$$\boldsymbol{s}_K \cdot \boldsymbol{a} = h, \tag{A.18}$$

$$\boldsymbol{s}_K \cdot \boldsymbol{b} = k, \tag{A.19}$$

$$\boldsymbol{s}_K \cdot \boldsymbol{c} = l. \tag{A.20}$$

The magnitude of $\boldsymbol{s}_K$ can be evaluated from the diffraction indices hkl and $\boldsymbol{G}^*$:

$$\begin{aligned} s_K^2 &= |\boldsymbol{s}_K|^2 \\ &= |h\boldsymbol{a}^* + k\boldsymbol{b}^* + l\boldsymbol{c}^*|^2 \\ &= \widetilde{\boldsymbol{h}} \cdot \boldsymbol{G}^* \cdot \boldsymbol{h} \\ &= \begin{pmatrix} h & k & l \end{pmatrix} \begin{pmatrix} a^{*2} & a^*b^* \cos\gamma^* & a^*c^* \cos\beta^* \\ b^*a^* \cos\gamma^* & b^{*2} & b^*c^* \cos\alpha^* \\ c^*a^* \cos\beta^* & c^*b^* \cos\alpha^* & c^{*2} \end{pmatrix} \begin{pmatrix} h \\ k \\ l \end{pmatrix} \\ &= h^2a^{*2} + k^2b^{*2} + l^2c^{*2} + 2klb^*c^* \cos\alpha^* + 2lhc^*a^* \cos\beta^* + 2hka^*b^* \cos\gamma^*. \end{aligned} \tag{A.21}$$

A.3 Scattering Vector

Because the scattering vector, $\boldsymbol{Q}_K$, is given by

$$\boldsymbol{Q}_K = 2\pi\boldsymbol{s}_K, \tag{A.22}$$

its magnitude can be calculated from the elements of $\boldsymbol{G}^*$ (a^{*2}, b^{*2}, c^{*2}, $b^*c^* \cos\alpha^*$, $c^*a^* \cos\beta^*$, and $a^*b^* \cos\gamma^*$):

$$\begin{aligned} Q_K &= |\boldsymbol{Q}_K| \\ &= 2\pi s_K. \end{aligned} \tag{A.23}$$

A.4 Lattice-Plane Spacing

The lattice-plane spacing, d_K, is equal to the reciprocal of s_K:

$$\begin{aligned} d_K &= \frac{1}{d_K^*} \\ &= \frac{1}{s_K}. \end{aligned} \tag{A.24}$$

A.5 Bragg Angle

Because d_K and the Bragg angle, θ_K, are related by the Bragg equation,

$$\lambda = 2d_K \sin\theta_K, \tag{A.25}$$

we can calculate $\sin\theta_K$ using

$$\begin{aligned} \sin\theta_K &= \frac{\lambda}{2d_K} \\ &= \frac{\lambda s_K}{2}. \end{aligned} \tag{A.26}$$

Then, it follows that

$$\theta_K = \arcsin\left(\frac{\lambda s_K}{2}\right). \tag{A.27}$$

The profile function, $G(\Delta 2\theta_{iK})$, in the model function, (2.5), contains θ_K, which is calculated from lattice parameters as described above. In other words, the lattice parameters are contained in $G(\Delta 2\theta_{iK})$.

Partial derivatives of the Bragg angle, θ_K, with respect to the six elements of $\boldsymbol{G}^*$ are described in Appendix A.7.

A.6 Partial Derivatives of Lattice Parameters with Respect to the Elements of the Metric Tensor for the Reciprocal Lattice

In Rietveld analysis with RIETAN-FP, lattice parameters are at first converted into $\boldsymbol{G}$ with Eq. (A.1) and then into $\boldsymbol{G}^*$ with Eq. (A.6). The values of d_K and θ_K are calculated from the elements of $\boldsymbol{G}^*$ with Eqs. (A.27) and (A.24), respectively. Thus, it is not (direct) lattice parameters (a, b, c, α, β, and γ) but the elements of $\boldsymbol{G}^*$ that are actually refined in Rietveld analysis. After refining $\boldsymbol{x}$ by the Rietveld method, $\boldsymbol{G}^*$ is reconverted into $\boldsymbol{G}$ with Eq. (A.7) to obtain the lattice parameters.

Let $x_1 = a^{*2}$, $x_2 = b^{*2}$, $x_3 = c^{*2}$, $x_4 = b^*c^* \cos\alpha^*$, $x_5 = c^*a^* \cos\beta^*$, and $x_6 = a^*b^* \cos\gamma^*$ for simplicity. Then, Eq. (A.21) can be rewritten as

$$s_K^2 = h^2x_1 + k^2x_2 + l^2x_3 + 2klx_4 + 2lhx_5 + 2hkx_6. \tag{A.28}$$

Kelsey [239] derived equations to calculate standard uncertainties of lattice parameters from those of the elements of $\boldsymbol{G}^*$, *i.e.*, x_1, x_2, x_3, x_4, x_5, and x_6 in Eq. (A.28). Partial derivatives of lattice parameters, F, for the triclinic system [239] are listed in **Table A.1**, where A, B, and C are defined as

$$A = 2\cos\beta\cos\gamma - \cos\alpha\left(\cos^2\beta + \cos^2\gamma\right), \tag{A.29}$$

$$B = 2\cos\alpha\cos\gamma - \cos\beta\left(\cos^2\alpha + \cos^2\gamma\right), \tag{A.30}$$

$$C = 2\cos\alpha\cos\beta - \cos\gamma\left(\cos^2\alpha + \cos^2\beta\right). \tag{A.31}$$

Table A.1: Partial derivatives of lattice parameters for the triclinic system

F	$\partial F/\partial x_1$	$\partial F/\partial x_2$	$\partial F/\partial x_3$	$\partial F/\partial x_4$	$\partial F/\partial x_5$	$\partial F/\partial x_6$
a	$-\frac{1}{2}a^3$	$-\frac{1}{2}ab^2\cos^2\gamma$	$-\frac{1}{2}ac^2\cos^2\beta$	$-abc\cos\beta\cos\gamma$	$-a^2c\cos\beta$	$-a^2b\cos\gamma$
b	$-\frac{1}{2}a^2b\cos^2\gamma$	$-\frac{1}{2}b^3$	$-\frac{1}{2}bc^2\cos^2\alpha$	$-b^2c\cos\alpha$	$-abc\cos\alpha\cos\gamma$	$-ab^2\cos\gamma$
c	$-\frac{1}{2}a^2c\cos^2\beta$	$-\frac{1}{2}b^2c\cos^2\alpha$	$-\frac{1}{2}c^3$	$-bc^2\cos\alpha$	$-ac^2\cos\beta$	$-abc\cos\alpha\cos\beta$
α	$a^2A/2\sin\alpha$	$\frac{1}{4}b^2\sin 2\alpha$	$\frac{1}{4}c^2\sin 2\alpha$	$bc\sin\alpha$	$ac\sin\alpha\cos\gamma$	$ab\sin\alpha\cos\beta$
β	$\frac{1}{4}a^2\sin 2\beta$	$b^2B/2\sin\beta$	$\frac{1}{4}c^2\sin 2\beta$	$bc\sin\beta\cos\gamma$	$ac\sin\beta$	$ab\sin\beta\cos\alpha$
γ	$\frac{1}{4}a^2\sin 2\gamma$	$\frac{1}{4}b^2\sin 2\beta$	$c^2C/2\sin\gamma$	$bc\sin\gamma\cos\beta$	$ac\sin\gamma\cos\alpha$	$ab\sin\gamma$

A.7 Partial Derivatives of the Bragg Angle with Respect to the Elements of the Metric Tensor

Partial derivatives of the Bragg angle, θ_K, with respect to the six elements of $\boldsymbol{G}^*$ are indispensable to nonlinear least-squares methods using derivatives, *i.e.*, Gauss–Newton and modified Marquardt methods (see 4.1.1 and 4.1.2) in the case of RIETAN-FP. Let $\theta = \theta_K$, $x_1 = a^{*2}$, $x_2 = b^{*2}$,

$x_3 = c^{*2}$, $x_4 = b^*c^* \cos\alpha^*$, $x_5 = c^*a^* \cos\beta^*$, and $x_6 = a^*b^* \cos\gamma^*$ for simplicity. From Eqs. (A.26) and (A.28), we obtain

$$\sin^2\theta = \frac{\lambda^2}{4}\left(h^2x_1 + k^2x_2 + l^2x_3 + 2klx_4 + 2lhx_5 + 2hkx_6\right), \tag{A.32}$$

whose both sides are differentiated with respect to x_1 to afford

$$\begin{aligned} \frac{\partial}{\partial\theta}\left(\sin^2\theta\right)\frac{\partial\theta}{\partial x_1} &= \frac{\lambda^2}{4}h^2. \\ \therefore \frac{\partial\theta}{\partial x_1} &= \frac{\lambda^2h^2}{4\sin 2\theta} \\ &= \frac{X}{2}h^2 \end{aligned} \tag{A.33}$$

with

$$\begin{aligned} X &= \frac{\lambda^2}{2\sin 2\theta} \\ &= d^2\tan\theta. \end{aligned}$$

Likewise, the following two equations can be derived:

$$\begin{aligned} \frac{\partial\theta}{\partial x_2} &= \frac{\lambda^2k^2}{4\sin 2\theta} \\ &= \frac{X}{2}k^2, \end{aligned} \tag{A.34}$$

$$\begin{aligned} \frac{\partial\theta}{\partial x_3} &= \frac{\lambda^2l^2}{4\sin 2\theta} \\ &= \frac{X}{2}l^2. \end{aligned} \tag{A.35}$$

Differentiation of the both sides of Eq. (A.32) with respect to x_4 yields

$$\begin{aligned} \frac{\partial}{\partial\theta}\left(\sin^2\theta\right)\frac{\partial\theta}{\partial x_4} &= \frac{kl\lambda^2}{2}. \\ \therefore \frac{\partial\theta}{\partial x_4} &= \frac{\lambda^2kl}{2\sin 2\theta} \\ &= Xkl. \end{aligned} \tag{A.36}$$

Likewise, the following two equations can be derived:

$$\begin{aligned} \frac{\partial\theta}{\partial x_5} &= \frac{\lambda^2lh}{2\sin 2\theta} \\ &= Xlh, \end{aligned} \tag{A.37}$$

$$\begin{aligned} \frac{\partial\theta}{\partial x_6} &= \frac{\lambda^2hk}{2\sin 2\theta} \\ &= Xhk. \end{aligned} \tag{A.38}$$

If x_1 , x_2, x_3, x_4, x_5, and x_6 are represented by Y, the partial derivatives of the profile function is formulated as

$$\frac{\partial}{\partial Y}G(\Delta 2\theta_{iK}) = \frac{\partial}{\partial\theta}G(\Delta 2\theta_{iK})\frac{\partial\theta}{\partial Y}. \tag{A.39}$$

With Eq. (A.39) and the partial derivatives (A.33)–(A.38), the partial derivatives of the profile function, $G(\Delta 2\theta_{iK})$, with respect to x_1, x_2, x_3, x_4, x_5, and x_6 can easily be converted into those with respect to the lattice parameters of the direct cell, a, b, c, α, β, and γ.

A.8 Unit-Cell Volume

The determinant of $\boldsymbol{G}$ is

$$|\boldsymbol{G}| = a^2b^2c^2\left(1-\cos^2\alpha-\cos^2\beta-\cos^2\gamma+2\cos\alpha\cos\beta cos\gamma\right), \tag{A.40}$$

which is equal to V^2:

$$V = \sqrt{|\boldsymbol{G}|}. \tag{A.41}$$

V^* is equal to the reciprocal of V:

$$\begin{aligned} V^* &= \boldsymbol{a}^* \cdot \boldsymbol{b}^* \wedge \boldsymbol{c}^* \\ &= \frac{1}{V^3}(\boldsymbol{b}\wedge\boldsymbol{c})\cdot\left[(\boldsymbol{c}\wedge\boldsymbol{a})\wedge(\boldsymbol{a}\wedge\boldsymbol{b})\right] \\ &= \frac{1}{V^3}(\boldsymbol{b}\wedge\boldsymbol{c})\cdot\left[(\boldsymbol{c}\cdot\boldsymbol{a}\wedge\boldsymbol{b})\boldsymbol{a}\right] \\ &= \frac{1}{V} \end{aligned} \tag{A.42}$$

The standard uncertainty of V, $\sigma(V)$, is calculated from those of a, b, and c [238]:

$$\sigma(V) = \left[V^2\sum_{i=1}^{3}A_i^2 + \frac{(abc)^4}{V^2}\sum_{i=1}^{3}B_i^2\right]^{\frac{1}{2}} \tag{A.43}$$

with

$$\begin{aligned} A_1 &= \frac{\sigma(a)}{a}, & B_1 &= \sin\alpha\,(\cos\alpha-\cos\beta\cos\gamma)\,\sigma(\alpha), \\ A_2 &= \frac{\sigma(b)}{b}, & B_2 &= \sin\beta\,(\cos\beta-\cos\alpha\cos\gamma)\,\sigma(\beta), \\ A_3 &= \frac{\sigma(c)}{c}, & B_3 &= \sin\gamma\,(\cos\gamma-\cos\alpha\cos\beta)\,\sigma(\gamma). \end{aligned}$$

A.9 Interatomic Distance

The square of the interatomic distance, l_{12}, between atom 1 at (x_1, y_1, z_1) and atom 2 at (x_2, y_2, z_2) is given by

$$l_{12}^2 = \begin{pmatrix} x_1-x_2 & y_1-y_2 & y_1-y_2 \end{pmatrix}\boldsymbol{G}\begin{pmatrix} x_1-x_2 \\ y_1-y_2 \\ y_1-y_2 \end{pmatrix} \tag{A.44}$$

[240], which is transformed into

$$\begin{aligned} l_{12} =& \big[a^2(x_1-x_2)^2+b^2(y_1-y_2)^2+c^2(z_1-z_2)^2+2bc\cos\alpha(y_1-y_2)(z_1-z_2) \\ &+2ca\cos\beta(z_1-z_2)(x_1-x_2)+2ab\cos\gamma(x_1-x_2)(y_1-y_2)\big]^{\frac{1}{2}}. \end{aligned} \tag{A.45}$$

A.10 Bond Angle

The cosine of the bond angle, ϕ_{123}, for atom 1 at (x_1, y_1, z_1), atom 2 at (x_2, y_2, z_2), and atom 3 at (x_3, y_3, z_3) with an apex of atom 2 is calculated as below [240]:

$$\cos\phi_{123} = \frac{1}{l_{12}l_{32}}\begin{pmatrix} x_1-x_2 & y_1-y_2 & y_1-y_2 \end{pmatrix}\boldsymbol{G}\begin{pmatrix} x_3-x_2 \\ y_3-y_2 \\ y_3-y_2 \end{pmatrix}. \tag{A.46}$$

A.11 Lattice Conversion

Because of various reasons, the original unit cell need to be converted into another new unit cell. In this section, let us attach a prime to each physical quantity relevant to the new lattice. For example, the magnetic unit cell, MUC, described in 8.1 is required to calculate the magnetic-structure factor, $F(\boldsymbol{h}_K, \text{magn.})$, of the virtual phase composed of only magnetic atoms on the basis of the new lattice. Arrays $\boldsymbol{P}$ and $\boldsymbol{Q}$, which are, respectively, defined in Eqs. (8.1) and (8.4), are useful for this purpose.

With Eq. (A.1) to define the metric tensor, $\boldsymbol{G}$, of the direct lattice, the lattice dimensions of the new unit cell are obtainable from the elements of the metric tensor, $\boldsymbol{G}'$, of the new unit cell [170]:

$$\boldsymbol{G}' = \widetilde{\boldsymbol{P}} \cdot \boldsymbol{G} \cdot \boldsymbol{P}. \tag{A.47}$$

On the other hand, $\boldsymbol{G}^*$ can be converted into $\boldsymbol{G}^{*\prime}$ by utilizing the relation [170]

$$\boldsymbol{G}^{*\prime} = \boldsymbol{Q}\boldsymbol{G}^*\widetilde{\boldsymbol{Q}}. \tag{A.48}$$

A.12 Conversion of Isotropic Atomic Displacement Parameters into Anisotropic Ones

When isotropic thermal motion models are changed into anisotropic ones (see 3.5.2), anisotropic atomic displacement parameters are calculated with an approximation formula

$$\begin{aligned} \boldsymbol{\beta} &= \frac{B}{4}\boldsymbol{G}^* \\ &= \frac{B}{4}\begin{pmatrix} a^{*2} & a^*b^*\cos\gamma^* & a^*c^*\cos\beta^* \\ b^*a^*\cos\gamma^* & b^{*2} & b^*c^*\cos\alpha^* \\ c^*a^*\cos\beta^* & c^*b^*\cos\alpha^* & c^{*2} \end{pmatrix}. \end{aligned} \tag{A.49}$$

Appendix B

CALCULATION OF MAGNETIC STRUCTURE FACTORS FOR THREE SYSTEMS

Equations to calculate $\langle \cos^2 \eta \rangle$ for triclinic and monoclinic systems in Table 3.3 were derived by N. Yamada [80] of the University of Electro-Communications to implement them into an earlier version of RIETAN. In his formulation, $\langle \cos^2 \eta \rangle$ includes not angles between the magnetic moment and direct-lattice axes as in the hexagonal, rhombohedral, tetragonal, and orthorhombic systems but those between the magnetic moment and reciprocal-lattice ones, which simplifies $\langle \cos^2 \eta \rangle$ considerably.

B.1 Unit Vector along the Magnetic Moment

Let $\boldsymbol{e}^1$, $\boldsymbol{e}^2$, and $\boldsymbol{e}^3$ be the vectors for the reciprocal lattice, and $\boldsymbol{e}_1$, $\boldsymbol{e}_2$, and $\boldsymbol{e}_3$ those for the direct lattice. Then, vector $\boldsymbol{v}$ is presented by

$$\begin{aligned} \boldsymbol{v} &= v_1\boldsymbol{e}^1 + v_2\boldsymbol{e}^2 + v_3\boldsymbol{e}^3 \\ &= v^1\boldsymbol{e}_1 + v^2\boldsymbol{e}_2 + v^3\boldsymbol{e}_3, \end{aligned} \tag{B.1}$$

as **Fig. B.1** shows. Because

$$v_i = \boldsymbol{v} \cdot \boldsymbol{e}_i \tag{B.2}$$

and

$$v^j = \boldsymbol{v} \cdot \boldsymbol{e}^j, \tag{B.3}$$

$\boldsymbol{v}$ is represented by

$$\boldsymbol{v} = \left(\boldsymbol{v} \cdot \boldsymbol{e}^1\right) \boldsymbol{e}_1 + \left(\boldsymbol{v} \cdot \boldsymbol{e}^2\right) \boldsymbol{e}_2 + \left(\boldsymbol{v} \cdot \boldsymbol{e}^3\right) \boldsymbol{e}_3. \tag{B.4}$$

If $\boldsymbol{e}_1$, $\boldsymbol{e}_2$, and $\boldsymbol{e}_3$ are, respectively, regarded as $\boldsymbol{a}$, $\boldsymbol{b}$, and $\boldsymbol{c}$, the three vectors, $\boldsymbol{e}^1$, $\boldsymbol{e}^2$, and $\boldsymbol{e}^3$, for the direct cell are $\boldsymbol{a}^*$, $\boldsymbol{b}^*$, and $\boldsymbol{c}^*$, respectively. Therefore, the unit vector, $\boldsymbol{n}(h_0, k_0, l_0) \equiv \boldsymbol{n}$, along the spin (magnetic moment) direction is given by

$$\boldsymbol{n}(h_0, k_0, l_0) = (\boldsymbol{n} \cdot \boldsymbol{a}^*)\, \boldsymbol{a} + (\boldsymbol{n} \cdot \boldsymbol{b}^*)\, \boldsymbol{b} + (\boldsymbol{n} \cdot \boldsymbol{c}^*)\, \boldsymbol{c}. \tag{B.5}$$

Let φ_{a*}, φ_{b*}, and φ_{a*} be the angles defined in Table 3.3 for the monoclinic and triclinic systems, then

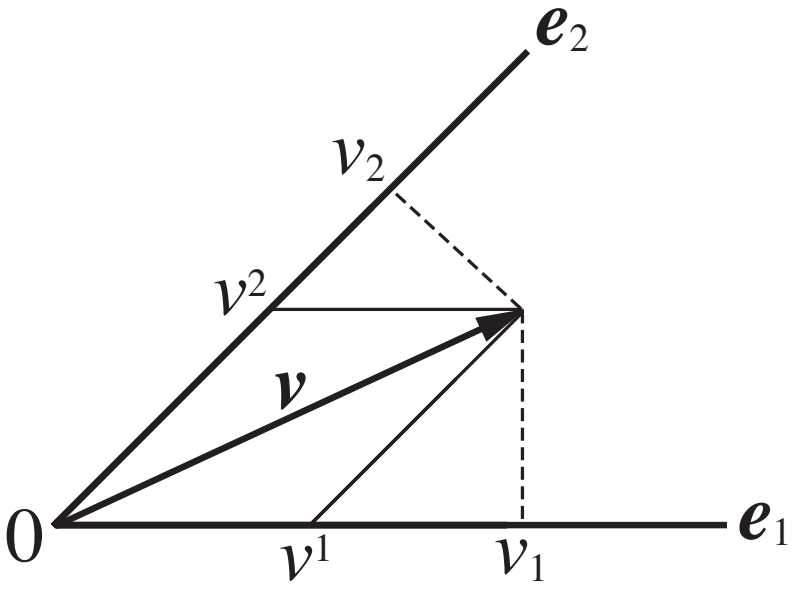

Figure B.1: Components of $\boldsymbol{v}$ along the $\boldsymbol{e}_1$ and $\boldsymbol{e}_2$ axes

$$\boldsymbol{n} \cdot \boldsymbol{a}^* = a^* \cos\varphi_{a*}, \tag{B.6}$$

$$\boldsymbol{n} \cdot \boldsymbol{b}^* = b^* \cos\varphi_{b*}, \tag{B.7}$$

$$\boldsymbol{n} \cdot \boldsymbol{b}^* = c^* \cos\varphi_{c*}. \tag{B.8}$$

Then, it follows that

$$\boldsymbol{n}(h_0, k_0, l_0) = a^* \cos\varphi_{a*}\boldsymbol{a} + b^* \cos\varphi_{b*}\boldsymbol{b} + c^* \cos\varphi_{c*}\boldsymbol{c}. \tag{B.9}$$

In what follows, $\cos^2\eta$ is calculated after conversion into the angles between the coordinate axes, $\boldsymbol{a}^*$, $\boldsymbol{b}^*$, $\boldsymbol{c}^*$, and the direction of the spin, $\boldsymbol{n}(h_0, k_0, l_0)$.

B.2 Triclinic

In the triclinic system,

$$\begin{aligned} \cos\eta &= \boldsymbol{n}(h,k,l) \cdot \boldsymbol{n}(h_0,k_0,l_0) \\ &= \big(ha^* \cos\varphi_{a*} + kb^* \cos\varphi_{b*} + lc^* \cos\varphi_{c*}\big)d, \end{aligned} \tag{B.10}$$

which is transformed into

$$\big\langle \cos^2\eta \big\rangle = \big(ha^* \cos\varphi_{a*} + kb^* \cos\varphi_{b*} + lc^* \cos\varphi_{c*}\big)d^2. \tag{B.11}$$

B.3 Monoclinic

Because hkl and $h\bar{k}l$ reflections are equivalent to each other in the monoclinic system (unique axis b),

$$\begin{aligned} \cos^2\eta &= d^2\Big[\big(ha^* \cos\varphi_{a*} + kb^* \cos\varphi_{b*} + lc^* \cos\varphi_{c*}\big)^2 \\ &\quad + \big(ha^* \cos\varphi_{a*} - kb^* \cos\varphi_{b*} + lc^* \cos\varphi_{c*}\big)^2\Big] \\ &= 2d^2\Big[\big(ha^* \cos\varphi_{a*} + lc^* \cos\varphi_{c*}\big)^2 + \big(kb^* \cos\varphi_{b*}\big)^2\Big], \end{aligned} \tag{B.12}$$

from which

$$\left\langle \cos^2 \eta \right\rangle = d^2 \Big[\left(ha^* \cos \varphi_{a^*} + lc^* \cos \varphi_{c^*} \right)^2 + \left(kb^* \cos \varphi_{b^*} \right)^2 \Big] \tag{B.13}$$

is derived.

B.4 Orthorhombic

Though $\left\langle \cos^2 \eta \right\rangle$ for the orthorhombic system was reported by Shirane [77], it will be derived below using Eq. (B.9). Because hkl $hk\bar{l}$, $h\bar{k}l$, and $\bar{h}kl$ reflections are equivalent to each other in the orthorhombic system,

$$\begin{aligned} \cos^2 \eta = d^2 \Big[& \left(ha^* \cos \varphi_{a^*} + kb^* \cos \varphi_{b^*} + lc^* \cos \varphi_{c^*} \right)^2 \\ & + \left(ha^* \cos \varphi_{a^*} + kb^* \cos \varphi_{b^*} - lc^* \cos \varphi_{c^*} \right)^2 \\ & + \left(ha^* \cos \varphi_{a^*} - kb^* \cos \varphi_{b^*} + lc^* \cos \varphi_{c^*} \right)^2 \\ & + \left(-ha^* \cos \varphi_{a^*} + kb^* \cos \varphi_{b^*} + lc^* \cos \varphi_{c^*} \right)^2 \Big] \\ = 4d^2 \big(& h^2 a^{*2} \cos^2 \varphi_{a^*} + k^2 b^{*2} \cos^2 \varphi_{b^*} + l^2 c^{*2} \cos^2 \varphi_{c^*} \big), \end{aligned} \tag{B.14}$$

which averages

$$\begin{aligned} \left\langle \cos^2 \eta \right\rangle &= d^2 \big(h^2 a^{*2} \cos^2 \varphi_{a^*} + k^2 b^{*2} \cos^2 \varphi_{b^*} + l^2 c^{*2} \cos^2 \varphi_{c^*} \big) \\ &= d^2 \big(h^2 a^{*2} \cos^2 \varphi_a + k^2 b^{*2} \cos^2 \varphi_b + l^2 c^{*2} \cos^2 \varphi_c \big) \end{aligned} \tag{B.15}$$

per reflection. Equation (B.15) corresponds to Eq. (14) in Ref. [77].

Appendix C

SEMI-EMPIRICAL EXPRESSIONS FOR ANISOTROPIC MICROSTRAIN BROADENING

C.1 Derivation of the Anisotropic Microstain Broadening

By substitution of s_K^2 for M_{hkl}, Eq. (A.28) can be rewritten as

$$M_{hkl} = h^2x_1 + k^2x_2 + l^2x_3 + 2klx_4 + 2lhx_5 + 2hkx_6. \tag{C.1}$$

Let us assume that x_i parameters ($i = 1 - 6$) have a Gaussian distribution characterized by a covariance matrix, $C_{ij} = \langle (x_i - \langle x_i \rangle)(x_j - \langle x_j \rangle) \rangle$, with $C_{ii} = \sigma^2(x_i)$ [97]. Because M_{hkl} is linear with respect to x_i, the variance of M_{hkl}, *i.e.*, the anisotropic microstrain broadening, Γ_a, is calculated by

$$\begin{aligned} \Gamma_\mathrm{a}^2 &= \sigma^2(M_{hkl}) \\ &= \sum_{i,j} C_{ij} \frac{\partial M}{\partial x_i} \frac{\partial M}{\partial x_j}. \end{aligned} \tag{C.2}$$

Given the individual partial derivatives, $\partial M/\partial x_1 = h^2$, $\partial M/\partial x_2 = k^2$, $\partial M/\partial x_3 = l^2$, $\partial M/\partial x_4 = kl$, $\partial M/\partial x_5 = lh$, and $\partial M/\partial x_6 = hk$, we obtain

$$\frac{\partial M}{\partial x_i} \frac{\partial M}{\partial x_j} = \begin{pmatrix} h^4 & h^2k^2 & h^2l^2 & h^2kl & h^3l & h^3k \\ h^2k^2 & k^4 & k^2l^2 & k^3l & hk^2l & hk^3 \\ h^2l^2 & k^2l^2 & l^4 & kl^3 & hl^3 & hkl^2 \\ h^2kl & k^3l & kl^3 & k^2l^2 & hkl^2 & hk^2l \\ h^3l & hk^2l & hl^3 & hkl^2 & h^2l^2 & h^2kl \\ h^3k & hk^3 & hkl^2 & hk^2l & h^2kl & h^2k^2 \end{pmatrix}. \tag{C.3}$$

Equation (C.2) can therefore be rearranged as

$$\Gamma_\mathrm{a}^2 = \sum_{HKL} S_{HKL} h^H k^K l^L \tag{C.4}$$

with terms S_{HKL} defined for $H + K + L = 4$. Thus, anisotropic microstrain broadening is represented by the S_{HKL} coefficients in the phenomenological model developed by Stephens [97] (see 3.9.3).

C.2 Anisotropic Microstrain Broadening in All the Laue Classes

There are 15 refinable S_{HKL} coefficients for the triclinic crystal system: S_{400}, S_{040}, S_{004}, S_{220}, S_{202}, S_{022}, S_{310}, S_{103}, S_{031}, S_{130}, S_{301}, S_{013}, S_{211}, S_{121}, and S_{112} [97]. On the other hand, Laue symmetry imposes restrictions on S_{HKL} coefficients in Laue classes other than $\bar{1}$ (triclinic), so that from 2 coefficients in the cubic crystal system to 15 coefficients in the triclinic one are needed to describe anisotropic macrostrain broadening.

In what follows, $\Gamma_{\rm a}^2$ in Eq. (3.74) [87] are represented as functions of S_{HKL} coefficients for all the Laue classes that can be used in RIETAN-FP without any standardization of crystal data (see Chap. 9). In hoge.ins for Rietveld or Le Bail analysis, coefficients which are not included in Eqs. (C.5)–(C.14) should be fixed at 0.0 with `ID(I)` = 0 (see Table S-6) though they are dummy parameters.

Triclinic ($\bar{1}$)

$$\begin{aligned}\Gamma_{\rm a}^2 = {} & S_{400}h^4 + S_{040}k^4 + S_{004}l^4 + 3(S_{220}h^2k^2 + S_{202}h^2l^2 + S_{022}k^2l^2) + \\ & 2(S_{310}h^3k + S_{103}hl^3 + S_{031}k^3l + S_{130}hk^3 + S_{301}h^3l + S_{013}kl^3) + \\ & 4(S_{211}h^2kl + S_{121}hk^2l + S_{112}hkl^2l)\end{aligned} \tag{C.5}$$

Monoclinic ($2/m$)

$$\begin{aligned}\Gamma_{\rm a}^2 = {} & S_{400}h^4 + S_{040}k^4 + S_{004}l^4 + 3(S_{220}h^2k^2 + S_{202}h^2l^2 + S_{022}k^2l^2) + \\ & 2(S_{301}h^3l + S_{103}hl^3) + 4S_{121}hk^2l\end{aligned} \tag{C.6}$$

Orthorhombic (mmm)

$$\Gamma_{\rm a}^2 = S_{400}h^4 + S_{040}k^4 + S_{004}l^4 + 3S_{220}h^2k^2 + S_{202}h^2l^2 + S_{022}k^2l^2) \tag{C.7}$$

Tetragonal ($4/m$)

$$\Gamma_{\rm a}^2 = S_{400}(h^4 + k^4) + S_{004}l^4 + 3S_{220}h^2k^2 + 3S_{202}(h^2l^2 + k^2l^2) + 2S_{310}(h^3k - hk^3) \tag{C.8}$$

Tetragonal ($4/mmm$)

$$\Gamma_{\rm a}^2 = S_{400}(h^4 + k^4) + S_{004}l^4 + 3S_{220}h^2k^2 + 3S_{202}(h^2l^2 + k^2l^2) \tag{C.9}$$

Trigonal ($\bar{3}$)

$$\begin{aligned}\Gamma_{\rm a}^2 = {} & S_{400}(h^4 + k^4 + 2h^3k + 2hk^3 + 3h^2k^2) + S_{004}l^4 + 3S_{202}(h^2l^2 + k^2l^2 + hkl^2) + \\ & S_{301}(2h^3l - 2k^3l - 6hk^2l) + 4S_{211}(h^2kl + hk^2l)\end{aligned} \tag{C.10}$$

Trigonal ($\bar{3}m1$)

$$\begin{aligned}\Gamma_{\rm a}^2 = {} & S_{400}(h^4 + k^4 + 3h^2k^2 + 2h^3k + 2hk^3) + S_{004}l^4 + 3S_{202}(h^2l^2 + k^2l^2 + hkl^2) + \\ & S_{301}(3h^2kl - 3hk^2l + 2h^3l - 2k^3l)\end{aligned} \tag{C.11}$$

Trigonal ($\bar{3}1m$)

$$\begin{aligned}\Gamma_{\mathrm{a}}^2 = {} & S_{400}(h^4 + k^4 + 3h^2k^2 + 2h^3k + 2hk^3) + S_{004}l^4 + 3S_{202}(h^2l^2 + k^2l^2 + hkl^2) + \\ & 4S_{211}(h^2kl + hk^2l)\end{aligned} \tag{C.12}$$

Hexagonal ($6/m$ and $6/mmm$)

$$\Gamma_{\mathrm{a}}^2 = S_{400}(h^4 + k^4 + 3h^2k^2 + 2h^3k + 2hk^3) + S_{004}l^4 + 3S_{202}(h^2l^2 + k^2l^2 + hkl^2) \tag{C.13}$$

Cubic ($m\bar{3}$ and $m\bar{3}m$)

$$\Gamma_{\mathrm{a}}^2 = S_{400}(h^4 + k^4 + l^4) + 3S_{220}(h^2k^2 + h^2l^2 + k^2l^2) \tag{C.14}$$

Appendix D

CALCULATIONS OF GEOMETRICAL PARAMETERS BY ORFFE

ORFFE developed by Busing, Martin, and Levy *et al.* [136] is used to calculate interatomic distances and bond angles from data recorded in text files, hoge.xyz, output by RIETAN-FP. With ORFFE, standard uncertainties of geometrical parameters are strictly calculated from both the diagonal and off-diagonal elements of the variance-covariance matrix. Tho original program of ORFFE has been extensively modified to obtain bond lengths and angles related to atoms in the asymmetric unit.

Though many functions including those related to thermal motion are available in ORFFE, three functions 201 (D.1), 002 (D.2), and 003 (D.3) written in fixed-column formats would be sufficient in nearly all structure refinements. Note that the formats of these two were changed from original ones in ORFFE. Instructions to use these two are also described in file hoge.ins. These two functions, if any, must be ordered as above.

For details of three integers, A, C, and S, described in D.1 and D.2, refer to an output file, hoge.dst or hoge.ffe, of ORFFE. In these files, values of site numbers A, translation numbers C, symmetry operation numbers S, and $1000C + S$ for all the geometrical parameter are also output.

D.1 Function 201

All distances (less than $l_{\max}$) between $A_{\max}$ atoms in the asymmetric unit and atoms in all asymmetric units, *i.e.*, all combinations of C and S.

Columns	Input data
1–5	201
6–10	$A_{\max}$, the number of sites in the asymmetric unit
26–30	The integer $10l_{\max}$.

The format of this line is (2I5,15X,I5); that is, the three integers 201, $A_{\max}$, and $10l_{\max}$ are right-justified with 5 columns, and '15X' means 15 spaces. If columns 26–30 are left blank, then

$l_{\max}$ is set at 4.0 Å. In hoge.xyz files, functions 201 must be always included, followed by optional functions 2 to calculate bond angles.

D.2 Function 002

Bond angle defined by atoms 1, 2, and 3.

Columns	Input data
1–5	002
6–10	A for atom 1
11–15	$1000C + S$ for atom 1
16–20	A for atom 2 (vertex)
21–25	$1000C + S$ for atom 2 (vertex)
26–30	A for atom 3
31–35	$1000C + S$ for atom 3

Of course, ‘ 2’ may be substituted for ‘002’. The format of this line is (7I5); that is, all of the seven integers are right-justified with 5 columns. Each atom designation consists of A and $1000C + S$.

D.3 Function 003

Dihedral angle between planes each defined by three atoms, that is, angle between normals to planes defined by atoms 1, 2 and 3, and atoms 4, 5 and 6, respectively. If right-hand fingers are curved so that they can pass successively through atoms 1, 2 and 3 then the thumb is in direction of normal. Sign of angle will be positive if this normal makes an acute angle with vector from atoms 4, 5 and 6.

Columns	Input data
1–5	003
6–10	A for atom 1
11–15	$1000C + S$ for atom 1
16–20	A for atom 2
21–25	$1000C + S$ for atom 2
26–30	A for atom 3
31–35	$1000C + S$ for atom 3
36–40	A for atom 4
41–45	$1000C + S$ for atom 4
46–50	A for atom 5
51–55	$1000C + S$ for atom 5
56–60	A for atom 6
61–65	$1000C + S$ for atom 6

Of course, ‘ 3’ may be substituted for ‘003’. The format of this line is (13I5); that is, all of the 13 integers are right-justified with 5 columns. Each atom designation consists of A and $1000C + S$ as is the case with function 002.

D.4 Automatic Generation of Functions 002

Instruction 002 has to be specified for each bond angle. It is very troublesome and mistakable to input three sets of A and $1000C + S$ per bond angle. With RIETAN-FP, we need not to input functions 2 in hoge.ins. At first, RIETAN-FP is executed after only 201 functions have been input in hoge.ins. Then, the resultant file, hoge.xyz, is dealt with ORFFE to update it. The file, hoge.xyz, updated contains functions 2 at its tail for all the combinations of two atom pairs (atoms 2–1 and atoms 2–3) whose interatomic distances have been calculated by giving 201 functions in hoge.ins. These functions 2 cover all the sites input in hoge.ins. When processing hoge.xyz updated in the above way by ORFFE, a series of bond angles is output after interatomic distances in hoge.dst (and hoge.ffe).

D.5 Calculation of Geometrical Parameters in the Simulation Mode

ORFFE may be executed even in the simulation mode (`NMODE = 1`), where standard uncertainties of geometrical parameters are set at zero, for convenience.

D.5.1 Single-phase simulation

Setting `NDA` at 1 as given below for the case of Fapatite.ins produces hoge.xyz, from which hoge.dst (and hoge.ffe) is output by ORFFE.

```
NDA = 0! No file is output which store ORFFE data.
NDA = 1! Filename.xyz for ORFFE is output for the first phase.
NDA = 1

If NDA > 0 then
# Input ORFFE functions as required and place '}' (+ comment) at the tail.
# Refer to the user's manual for ORFFE functions used frequently.  ORFFE
# functions must be input with a fixed column format; note not to set input
# data at erroneous positions.  When NDA > 0, hoge.xyz is output.  This file is
# used as an input file for ORFFE to calculate interatomic distances and bond
# angles.  ORFFE functions in hoge.xyz can be modified and/or added by the user.

ORFFE functions start {
# Note that the formats of ORFFE functions differ from original ones!
#        1         2         3         4         5         6         7         8
#2345678901234567890123456789012345678901234567890123456789012345678901234567890

# Function 201, FORMAT(2I5,15X,I5).  Output a list of interatomic distances for
# all the sites.  The second number is the number of sites, and the third integer
```

```
# is 10 X (maximum distance in Angstroms).
# Interatomic distances less than 3.1 angstroms are listed
  201    7                  31

# Function 002, FORMAT(7I5).  Calculate a bond angle.  Three sets of A and
# 1000*C + S (refer to the output of ORFFE) follow after function 002.  Automatic
# generation of functions 002 is highly recommended (see Appendix D.4).

} End of ORFFE functions.
# ORFFE functions can be modified and added by editing hoge.xyz directly.
end if
```

Note that simulation of powder diffraction patterns (`NMODE = 1`) is followed by calculation of interatomic distances and bond angles by ORFFE using hoge.xyz created by RIETAN-FP. Of course, no standard uncertainties of the geometrical parameters are output by ORFFE in this case.

Appendix E

lst2cif

E.1 A File Converter, lst2cif, to Create Crystallographic Information Files

The International Union of Crystallography (IUCr) strongly recommends to submit a crystallographic information file[1] (CIF) [241] on publication of every paper reporting results of structure analysis. Core CIF dictionary (coreCIF) v2.4.2[2] and Powder CIF dictionary v1.0.1[3] are available online from the Web site of IUCr. The definition and classification of CIF data for powder diffraction is described in "International Tables for Crystallography," Vol. G [242]. A utility program, lst2cif, to convert hoge.lst (the standard output of RIETAN-FP) and hoge.dst (the standard output of ORFFE [136]) into a CIF, hoge.cif, (**Fig. E.1**) is included in the distribution files for the RIETAN-VENUS package.

CIFs also serve to write papers reporting results of structure analyses. PublCIF[4] [243] makes it possible to convert hoge.cif and hoge.dst into hoge.pdf (Portable Document Format: PDF), hoge.html compatible with XML (Extensible Markup Language) 1.0, and hoge.rtf (Rich Text Format: RTF) which can be input and modified by Microsoft Word, OpenOffice.org,[5] and other word processors.

PublCIF also offers a very convenient feature of Online checkCIF, which can be select in the Tools menu.

E.2 Structure Parameters and Other Information on Crystallographic Sites

In the case of Fapatite.* included in the distribution files, structure parameters are output in hoge.cif as follows:

```
loop_
   _atom_site_label
   _atom_site_fract_x
```

[1] http://www.iucr.org/resources/cif
[2] http://www.iucr.org/___data/iucr/cifdic_html/1/cif_core.dic/index.html
[3] http://www.iucr.org/resources/cif/dictionaries/cif_pd
[4] http://journals.iucr.org/services/cif/publcif/
[5] http://www.openoffice.org/

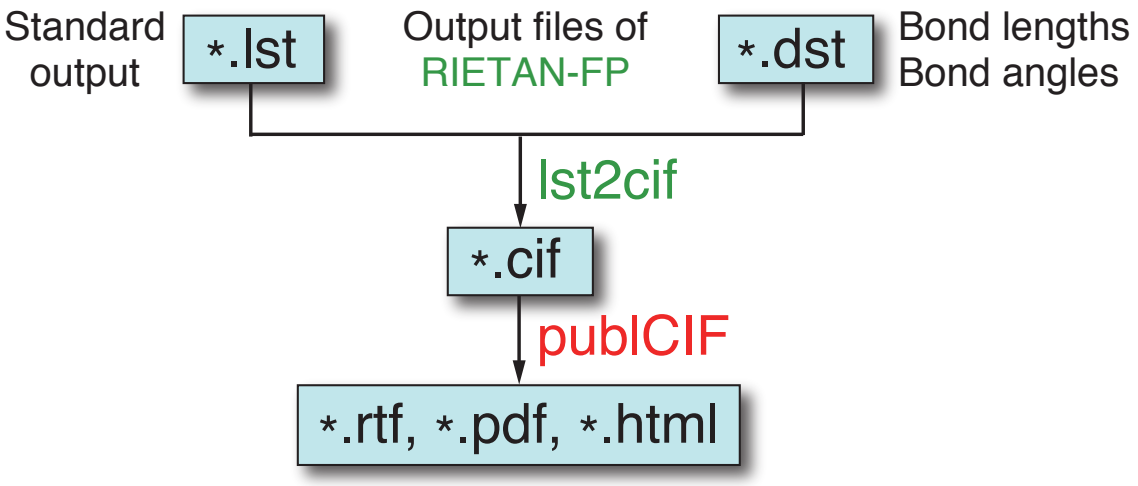

Figure E.1: Files input and output by lst2cif and publCIF

```
   _atom_site_fract_y
   _atom_site_fract_z
   _atom_site_occupancy
   _atom_site_symmetry_multiplicity
   _atom_site_Wyckoff_symbol
   _atom_site_adp_type
   _atom_site_U_iso_or_equiv
   _atom_site_type_symbol
O1      0.3242(3)   0.4854(3)   0.25        1          6 h Uiso  0.0094(9)  O
O2      0.5918(4)   0.4698(4)   0.25        1          6 h Uiso  0.0094(9)  O
O3      0.3392(3)   0.2573(3)   0.0698(3)   1         12 i Uiso  0.0106(6)  O
P       0.3973(2)   0.3679(2)   0.25        1          6 h Uiso  0.0070(3)  P
Ca1     0.33333     0.66667     0.0013(2)   1          4 f Uiso  0.0082(3)  Ca
Ca2     0.2418(1)  -0.0080(2)   0.25        1          6 h Uiso  0.0067(2)  Ca
F       0           0           0.25        1          2 a Uiso  0.018(1)   F
```

Nine data in each line must be self-evident from their definitions. Inclusion of

```
_atom_site_symmetry_multiplicity
_atom_site_Wyckoff_symbol
```

is highly significant. Only elemental names are output for `name_atom_site_type_symbol`.

On the use of lst2cif in solid solutions, no virtual chemical species (see 17.3.9) should be used because `atom_site_type_symbol` is simply extracted from `_atom_site_label`.The number of significant figures can be increased, *e.g.*, by changing `0.33333` into `0.333333` and `0.66667` into `0.666667`.

E.3 Geometrical Parameters

Lst2cif is capable of outputting symmetry codes for atoms related to geometrical parameters. The symmetry code of each atom site is represented by the symmetry-equivalent position number '`n`' plus the cell translation number '`klm`'. These numbers are combined to form a

single code '`n_klm`'. The first integer, `n`, denotes the symmetry operation applied to the coordinates stored in `_atom_site_- fract_x`, `_atom_site_fract_y`, and `_atom_site_fract_z`. It must match a number given in the identifier that uniquely labels each symmetry operation: `_space_group_symop_id`. Integers `k`, `l` and `m` refer to the translations that are subsequently applied to the symmetry-transformed coordinates to generate the atom used in calculating the bond. These translations (`x`, `y`, `z`) are related to (`k`, `l`, `m`) by the relations

```
k = 5 + x
l = 5 + y
m = 5 + z
```

Addition of `5` to the translations never produces negative numbers.

In the case of fluorapatite included in the distribution files, the following lines are output in the part of `#10. GEOMETRICAL PARAMETERS`:

```
loop_
   _geom_bond_atom_site_label_1
   _geom_bond_atom_site_label_2
   _geom_bond_distance
   _geom_bond_site_symmetry_1
   _geom_bond_site_symmetry_2
   _geom_bond_publ_flag
O1          P           1.561(3)      .    1_555  ?
O1          Ca1         2.383(2)      .    1_555  ?
O1          Ca1         2.383(2)      .   10_555  ?
O1          O3          2.535(3)      .    1_555  ?
O1          O3          2.535(3)      .   10_555  ?
.....
loop_
   _geom_angle_atom_site_label_1
   _geom_angle_atom_site_label_2
   _geom_angle_atom_site_label_3
   _geom_angle
   _geom_angle_site_symmetry_1
   _geom_angle_site_symmetry_2
   _geom_angle_site_symmetry_3
   _geom_angle_publ_flag
O3          P           O1          110.1(1)      1_555  .    1_555  ?
O3          P           O2          108.8(1)      1_555  .    1_555  ?
O1          P           O2          110.7(2)      1_555  .    1_555  ?
```

As illustrated above, one and two symmetry codes are given for interatomic distances and bond angles, respectively. Periods given for symmetry codes denote atoms in the asymmetric unit: `n_555`.

With publCIF [243], which is an application to edit and preview CIFs for publication, `n_klm`'s are automatically converted into another type of symmetry codes containing x, y, and z. PublCIF outputs geometrical parameters in the preprint window, converting (`k`, `l`, `m`) into another type of symmetry codes including x, y, and z. If `_geom_bond_publ_flag` or `_geom_angle_publ_flag` is changed from `?` to `yes` or `y`, and then `Acta C preprint` or `Acta E preprint` is selected in the `Preprint` menu, only geometrical parameters of the relevant lines are output in the preprint window.

Figure E.2 gives a part of an RTF file output for fluorapatite, whose Rietveld analysis from X-ray powder diffraction data is included in distribution files of RIETAN-FP, by publCIF in the Acta C preprint format and modified later with Microsoft Word. Unfortunately, superscripts representing numbers for symmetry codes do not increase one by one, starting from 1 in the current version of publCIF.

Crystal data

$Ca_5FO_{12}P_3$	V = 523.30 (1) Å^3
M_r = 504.30	Z = 2
Hexagonal, $P6_3/m$	Cu $K\alpha_1$, Cu $K\alpha_2$ radiation, λ = 1.540593, 1.544427 Å
a = 9.3690 (1) Å	T = 298 K
c = 6.88384 (6) Å	flat sheet with unknown dimensions

Data collection

Bragg-Brentano-type X-ray powder diffractometer	Scan method: step
Specimen mounting: flat plate	$2\theta_{min}$ = 15.00°, $2\theta_{max}$ = 130.00°, $2\theta_{step}$ = 0.02°
Data collection mode: reflection	

Refinement

R_p = 0.064	$R(F^2)$ = 0.01933
R_{wp} = 0.082	χ^2 = 2.161
R_{exp} = 0.056	5751 data points
R_{Bragg} = 0.038	44 parameters
$R(F)$ = 0.019	0 restraints

Table 1

Selected geometric parameters (Å, º)

P–O3	1.531 (2)	Ca2–F	2.3036 (9)
P–O1	1.561 (3)	Ca2–O3^{xiv}	2.334 (2)
P–O2	1.579 (3)	Ca2–O2^{xi}	2.344 (3)
Ca1–O1	2.383 (2)	Ca2–O3	2.506 (2)
Ca1–O2^{xii}	2.453 (2)	Ca2–O1^{xix}	2.667 (3)
Ca1–O3^{v}	2.824 (2)		
O3–P–O1	110.1 (1)	O1–P–O2	110.7 (2)
O3–P–O2	108.8 (1)		

Symmetry codes: (v) *x*–*y*, *x*, –*z*; (xi) –*y*+1, *x*–*y*, *z*; (xii) *x*–*y*, *x*, *z*–1/2; (xiv) *y*, –*x*+*y*, –*z*; (xix) –*x*+*y*, –*x*, *z*.

Figure E.2: Part of an RTF file obtained from a CIF of fluorapatite with publCIF

Datablock: I

Bond precision: P- O = 0.0028 A Wavelength=1.54443

Cell: a=9.3690(1) b=9.3690(1) c=6.88385(6)
alpha=90 beta=90 gamma=120

Temperature: 0 K

	Calculated	Reported
Volume	523.297(18)	523.301(9)
Space group	P 63/m	P 63/m
Hall group	-P 6c	-P 6c
Moiety formula	3(O4 P), F, 5(Ca)	?
Sum formula	Ca5 F O12 P3	Ca5 F O12 P3
Mr	504.31	504.30
Dx,g cm-3	3.201	3.201
Z	2	2
Mu (mm-1)	27.627	0.000
F000	500.0	500.0
F000'	506.98	

Figure E.3: Part of DATABLOCK I when checking Fapatite.cif by checkCIF/PLATON

E.4 Publication Check by checkCIF

E.4.1 Addition of data to hoge.cif

Program lst2cif allows us to output CIFs that pass severe tests by checkCIF[6] and checkCIF/PLATON[7] [244, 245] by adding a few data such as

- `_chemical_formula_moiety`
- `_pd_char_colour`
- `_cell_measurement_temperature`
- `_diffrn_ambient_temperature`

to eliminate alerts issued by checkCIF. A formula to be input for `_chemical_formula_moiety` is obtainable as 'Moiety formula' from the result of checking CIFs by checkCIF or checkCIF/PLATON. In the case of Fapatite.cif, it is '`3(O4 P), F, 5(Ca)`' (**Fig. E.3**). Chemical data are then recorded in Fapatite.cif as follows:

```
_chemical_name_systematic
; Fluorapatite
;
_chemical_name_common                  '?'
_chemical_formula_moiety               '3(O4 P), F, 5(Ca)'
_chemical_formula_structural           '?'
```

[6] http://checkcif.iucr.org/
[7] http://journals.iucr.org/services/cif/checkcif.html

```
_chemical_formula_analytical          '?'
_chemical_formula_sum                 'Ca5 F O12 P3'
_chemical_formula_weight              504.302
```

You must input `_chemical_formula_moiety` by yourself if checkCIF fails in giving the correct one. In such a case, obey the following general rules:

1. The order of elements within any group or moiety depends on whether carbon is present or not.
2. If carbon is present, the order should be: C, then H, then the other elements in alphabetical order of their symbol.
3. If C is not included, the elements are listed purely in the alphabetical order of their symbols.
4. Each moiety has to be separated with a comma, ',’.

In the current version of lst2cif, `_cell_formula_units_Z` is simply set at the minimum site multiplicity, which may differ from a value determined by checkCIF, particularly in organic compounds where molecules are connected with each other through hydrogen bonds. In such a case, change both `_chemical_formula_sum` and `_chemical_formula_weight` in addition to `_chemical_formula_weight` by yourself.

E.4.2 Temporary expedients to avoid unsuitable alerts

Unfortunately, the current version of checkCIF is far from perfect, outputting unsuitable alerts in most cases. Users of lst2cif have to overcome such troubles by themselves. For example, wavelengths of Cu $K\alpha$ radiation should be given as

```
loop_
   _diffrn_radiation_type
   _diffrn_radiation_wavelength
   _diffrn_radiation_wavelength_wt
'Cu K\a~1~'  1.540593  0.666667
'Cu K\a~2~'  1.544427  0.333333
```

Nevertheless, checkCIF/PLATON outputs the following unsuitable alert of level G if they remain unchanged:

```
Extra text has been found in the _diffrn_radiation_type field.
```

We are then obliged to replace the above lines with

```
loop_
   _diffrn_radiation_type
   _diffrn_radiation_wavelength
   _diffrn_radiation_wavelength_wt
'Cu K\a'     1.5418    1.0
#'Cu K\a~1~'  1.540593  0.666667
#'Cu K\a~2~'  1.544427  0.333333
```

Further, checkCIF/PLATON always outputs the following alert of level A:

```
Minimum (Negative) Residual Density .GE. 0 !!...       0.00 eA-3
```

even if the CIF was output by lst2cif from hoge.lst and hoge.dst, *i.e.*, results obtained by Rietveld refinement. This irrational alert can be eliminated by giving maximum and minimum difference electron densities as dummy data:

```
_refine_diff_density_max            0.1
_refine_diff_density_min            -0.1
```

Of course, these two lines have to be commented out after checking hoge.cif by checkCIF because they are false data.

C-level alerts, which arise from geometrical parameters calculated from fractional coordinates and lattice parameters in hoge.cif created by lst2cif, are often output by checkCIF/PLATON, for example,

```
PLAT731_ALERT_1_C Bond    Calc    3.029(5), Rep    3.028(2) ......          3 su-Ra
              O3   -O3      1.555   9.555                    #         33
PLAT731_ALERT_1_C Bond    Calc  2.3038(19), Rep   2.3036(9) ......          2 su-Ra
              F    -CA2     1.555   2.555                    #         57
```

Such unreasonable alerts result from deficiency in the number of significant figures and neglecting off-diagonal elements in the variance-convariance matrix. Two temporary expedients may be effective in taking steps to cope with such troubles:

1. Delete relevant lines if unnecessary,

2. Change geometrical parameters as indicated in the alerts, for convenience.

Acknowledgments

I wish to thank Ruben A. Dilanian for his dedication to a great deal of programming for the VENUS package (VICS, VEND, PRIMA, and ALBA), Erwin Parthé, a professor emeritus of Université de Genèva, for presenting me the source programs of STRUCTURE TIDY and LAZY PULVERIX, Koichi Momma of National Museum of Nature and Science for developing VESTA and Dysnomia and achieving the collaboration of RIETAN-FP–VESTA–ORFFE, Mohd. Roushown Ali of NIMS for preparation of constr_beta, and Takashi Ida of the Nogoya Institute of Technology for presenting the source code of TransmittanceCylinder012 to correct for absorption in the Debye–Scherrer geometry and collaboration on structure refinement giving consideration of particle statistics. Thanks are also due to Takuji Ikeda of AIST for his proposal of new features to be added to RIETAN-FP and his help in debugging RIETAN-FP.

I gratefully acknowledge those who developed TeXShop,[8] without which I could not write this long document containing many equations.

The development of RIETAN-FP has been financially supported by the quantum beam project of NIMS.

[8] http://www.uoregon.edu/~koch/texshop/texshop.html

Bibliography

[1] F. Izumi and K. Momma, *Solid State Phenom.*, **130**, 15 (2007).

[2] F. Izumi and K. Momma, *Bull. Ceram. Soc. Jpn.*, **43**, 902 (2008).

[3] F. Izumi, "The Rietveld Method," ed. by R. A. Young, Oxford University Press, Oxford (1995), Chap. 13.

[4] Y.-I. Kim and F. Izumi, *J. Ceram. Soc. Jpn.*, **102**, 401 (1994).

[5] F. Izumi and T. Ikeda, *Mater. Sci. Forum*, **321–324**, 198 (2000).

[6] F. Izumi and T. Ikeda, *J. Crystallogr. Soc. Jpn.*, **42**, 516 (2000).

[7] F. Izumi, "A Practical Guide to X-Ray Powder Analysis," 2nd ed., ed. by I. Nakai and F. Izumi, Asakura, Tokyo (2009), Chap. 7.

[8] F. Izumi and T. Ikeda, *J. Crystallogr. Soc. Jpn.*, **44**, 30 (2002).

[9] A. L. Bail, H. Duroy, and J. L. Fourquet, *Mater. Res. Bull.*, **23**, 447 (1988).

[10] H. M. Rietveld, *J. Appl. Crystallogr.*, **2**, 65 (1969).

[11] F. Izumi, S. Kumazawa, T. Ikeda, W.-Z. Hu, A. Yamamoto, and K. Oikawa, *Mater. Sci. Forum*, **378–381**, 59 (2001).

[12] F. Izumi and T. Ikeda, *Commission on Powder Diffraction, IUCr Newsletter*, No. 26, 7 (2001).

[13] F. Izumi and R. A. Dilanian, "Recent Research Developments in Physics," Vol. 3, Part II, Transworld Research Network, Trivandrum (2002), pp. 699–726.

[14] F. Izumi, *J. Ceram. Soc. Jpn.*, **111**, 617 (2003).

[15] F. Izumi, *Solid State Ionics*, **172**, 1 (2004).

[16] F. Izumi, *RADIOISOTOPES*, **59**, 191 (2010).

[17] F. Izumi and K. Momma, *IOP Conf. Ser.: Mater. Sci. Eng.*, **18**, 022001 (2011).

[18] H. Toraya, "The Rietveld Method," ed. by R. A. Young, Oxford University Press, Oxford (1995), Chap. 14.

[19] W. I. F. David and D. S. Sivia, *J. Appl. Crystallogr.*, **20**, 316 (1987).

[20] R. A. Dilanian and F. Izumi, "ALBA — a Fortran 90 Program to Determine 3D Patterson Functions from X-Ray and Neutron Diffraction Data by the Maximum-Entorpy Patterson Method," National Institute for Materials Science, Tsukuba (2005).

[21] F. Izumi, "Spectroscopy and Diffraction III," Vol. 11: the 5th Series of Chemistry, Maruzen, Tokyo (2006), pp. 220–223.

[22] A. Altomare, C. Cuocci, C. Giacovazzo, A. Moliterni, R. Rizzi, N. Corriero, and A. Falcicchio, *J. Appl. Crystallogr.*, **46**, 1231 (2013).

[23] K. Momma, T. Ikeda, A. A. Belik, and F. Izumi, *Powder Diffr.*, **28**, 184 (2013).

[24] V. F. Sears, "International Tables for Crystallography," Vol. C, 3rd ed., ed. by E. Prince, Kluwer, Dordrecht (2004), pp. 444–452.

[25] K. Momma and F. Izumi, *J. Appl. Crystallogr.*, **41**, 653 (2008).

[26] K. Momma and F. Izumi, *J. Appl. Crystallogr.*, **44**, 1272 (2011).

[27] D. E. Cox, "Synchrotron Radiation Crystallography," ed. by P. Coppens, Academic Press, London (1992), Chap. 9.

[28] F. Izumi, "Applicaions of Synchrotron Radiation to Materials Analysis," ed. by H. Saisho and Y. Gohshi, Elsevier (1996), Chap. 9.

[29] E. Prince, L. W. Finger, and J. H. Konnert, "Powder Diffraction: The Rietveld Method and the Two-Stage Method to Determine and Refine Crystal Structures from Powder Diffraction Data," Springer, Berlin (2006), pp. 52–53.

[30] A. A. Belik, F. Izumi, T. Ikeda, M. Okui, A. P. Malakho, V. A. Morozov, and B. I. Lazoryak, *J. Solid State Chem.*, **169**, 237 (2002).

[31] H. M. Rietveld, *Acta Crystallogr.*, **22**, 151 (1967).

[32] A. K. Cheetham and J. C. Taylor, *J. Solid State Chem.*, **21**, 253 (1977).

[33] G. Malmros and J. O. Thomas, *J. Appl. Crystallogr.*, **10**, 7 (1977).

[34] G. Will, "Powder Diffraction: The Rietveld Method and the Two-Stage Method to Determine and Refine Crystal Structures from Powder Diffraction Data," Springer, Berlin (2006).

[35] R. A. Young, E. Prince, and R. A. Sparks, *J. Appl. Crystallogr.*, **15**, 357 (1982).

[36] N. F. M. Henry and K. Lonsdale, eds., "International Tables for X-Ray Crystallography," Vol. I, Kynoch Press, Birmingham (1969), pp. 31–34.

[37] R. J. Hill and C. J. Howard, *J. Appl. Crystallogr.*, **20**, 467 (1987).

[38] D. L. Bish and S. A. Howard, *J. Appl. Crystallogr.*, **21**, 86 (1988).

[39] R. D. Deslattes, E. G. Kessler Jr, P. Indelicato, and E. Lindroth, "International Tables for Crystallography," Vol. C, 3rd ed., ed. by E. Prince, Kluwer, Dordrecht (2004), p. 203.

[40] G. Hölzer, M. Fritsch, M. Deutsch, J. Härtwig, and E. Förster, *Phys. Rev. A*, **56**, 4554 (1997).

[41] R. A. Young, A. C. Larson, and C. O. Paiva-Santos, "User's Guide to Program DBWS-9807a for Rietveld Analysis of X-Ray and Neutron Powder Diffraction Patterns," Georgia Institute of Technology, Atlanta (1999).

[42] C. J. Sparks, R. Kumar, E. D. Specht, P. Zschack, and G. E. Ice, *Adv. X-Ray Anal.*, **35**, 57 (1992).

[43] P. Suortti, *J. Appl. Crystallogr.*, **5**, 325 (1972).

[44] W. Pitschke, H. Hermann, and N. Mattern, *Powder Diffr.*, **8**, 74 (1993).

[45] W. Pitschke, N. Mattern, and H. Hermann, *Powder Diffr.*, **8**, 223 (1993).

[46] V. Sidey, *J. Appl. Crystallogr.*, **37**, 1013 (2004).

[47] E. N. Maslen, "International Tables for Crystallography," Vol. C, 3rd ed., ed. by E. Prince, Kluwer, Dordrecht (2004), pp. 600–602.

[48] T. Ida, *J. Appl. Crystallogr.*, **43**, 1124 (2010).

[49] G. Thorkildsen and H. B. Larsen, *Acta Crystallogr., Sect. A: Found. Crystallogr.*, **54**, 172 (1998).

[50] G. Thorkildsen and H. B. Larsen, *Acta Crystallogr., Sect. A: Found. Crystallogr.*, **54**, 186 (1998).

[51] C. W. Dwiggins, *Acta Crystallogr., Sect. A*, **31**, 146 (1975).

[52] W. Parrish and J. I. Langford, "International Tables for Crystallography," Vol. C, 3rd ed., ed. by E. Prince, Kluwer, Dordrecht (2004), pp. 42–79.

[53] C. Weidenthaler, R. X. Fischer, L. Abrams, and A. Hewat, *Acta Crystallogr., Sect. B: Struct. Sci.*, **53**, 429 (1997).

[54] A. Takenaka, "Structure Analysis," Vol. 6: the 3rd Series of Experimental Chemistry, Maruzen, Tokyo (1977), p. 202–204.

[55] D. Waasmaier and A. Kirfel, *Acta Crystallogr., Sect. A: Found. Crystallogr.*, **51**, 416 (1995).

[56] E. N. Maslen, A. G. Fox, and M. A. O'Keefe, "International Tables for Crystallography," Vol. C, 3rd ed., ed. by E. Prince, Kluwer, Dordrecht (2004), pp. 578–580.

[57] D. C. Creagh, "International Tables for Crystallography," Vol. C, 3rd ed., ed. by E. Prince, Kluwer, Dordrecht (2004), p. 241.

[58] Z. Berant, R. Moreh, and S. Kahane, *Phys. Lett. B*, **69**, 281 (1977).

[59] C. T. Chantler, *J. Phys. Chem. Ref. Data*, **24**, 71 (1995).

[60] D. C. Creagh, "International Tables for Crystallography," Vol. C, 3rd ed., ed. by E. Prince, Kluwer, Dordrecht (2004), pp. 255–257.

[61] B. L. Henke, E. M. Gullikson, and J. C. Davis, *At. Data Nucl. Data Tables*, **54**, 181 (1993).

[62] D. T. Cromer and D. A. Liberman, *Acta Crystallogr., Sect. A*, **37**, 267 (1981).

[63] P. K. Janert, "Gnuplot in Action," 2nd ed., Manning Pub. Co., Shelter Island (2016).

[64] Y. Xiao, F. Izumi, T. Graber, P. J. Viccaro, and D. E. Wittmer, *Powder Diffr.*, **18**, 32 (2003).

[65] V. K. Pecharsky and P. Y. Zavalij, "Fundamentals of Powder Diffraction and Structural Characterization of Materials," 2nd ed., Springer, New York (2009), pp. 218–220.

[66] K. Yvon, W. Jeitschko, and E. Parthé, *J. Appl. Crystallogr.*, **10**, 73 (1977).

[67] D. T. Cromer, "International Tables for X-Ray Crystallography," Vol. IV, Kynoch Press, Birmingham (1974), pp. 148–151.

[68] C. Giacovazzo, "Fundamentals of Crystallography," 3rd ed., ed. by C. Giacovazzo, Oxford University Press, Oxford (2011), p. 166.

[69] V. K. Pecharsky and P. Y. Zavalij, "Fundamentals of Powder Diffraction and Structural Characterization of Materials," 2nd ed., Springer, New York (2009), pp. 206–211.

[70] W. J. A. M. Peterse and J. H. Palm, *Acta Crystallogr.*, **20**, 147 (1966).

[71] E. Prince, L. W. Finger, and J. H. Konnert, "International Tables for Crystallography," Vol. C, 3rd ed., ed. by E. Prince, Kluwer, Dordrecht (2004), pp. 695–696.

[72] T. Hahn, ed., "International Tables for Crystallography," Vol. A, 5th ed., Kluwer, Dordrechi (2005).

[73] Y. Ohashi, "X-Ray Crystal Structure Analysis," Syôkabô, Tokyo (2005), pp. 103–104.

[74] T. Ozeki, "Spectroscopy and Diffraction III," Vol. 11: the 5th Series of Experimental Chemistry, Maruzen, Tokyo (2006), p. 161.

[75] G. E. Bacon, "Neutron Diffraction," 3rd ed., Clarendon Press, Oxford (1975), Chap. 8.

[76] K. Ohoyama, "Spectroscopy and Diffraction III," Vol. 11: the 5th Series of Experimental Chemistry, Maruzen, Tokyo (2006), Sect. 8.3.

[77] G. Shirane, *Acta Crystallogr.*, **12**, 282 (1959).

[78] E. H. Kisi and C. J. Howard, "Applications of Neutron Powder Diffraction," Oxford University Press, New York (2008), pp. 45–48.

[79] E. H. Kisi and C. J. Howard, "Applications of Neutron Powder Diffraction," Oxford University Press, New York (2008), pp. 260–262.

[80] N. Yamada, private communication (1995).

[81] P. J. Brown, "International Tables for Crystallography," Vol. C, 3rd ed., ed. by E. Prince, Kluwer, Dordrecht (2004), pp. 454–460.

[82] P. J. Brown, "International Tables for Crystallography," Vol. C, 3rd ed., ed. by E. Prince, Kluwer, Dordrecht (2004), p. 592.

[83] K. Yukino and R. Uno, *Jpn. J. Appl. Phys.*, **25**, 661 (1986).

[84] W. A. Dollase, *J. Appl. Crystallogr.*, **19**, 267 (1986).

[85] A. March, *Z. Kristallogr.*, **81**, 285 (1932).

[86] A. Altomare, M. C. Burla, C. Giacovazzo, A. Guagliardi, and A. G. G. Moliterni, *J. Appl. Crystallogr.*, **34**, 392 (2001).

[87] A. C. Larson and R. B. V. Dreele, "General Structure Analysis System (GSAS)," Report LAUR 86-748, Los Alamos National Laboratory, Los Alamos (2004).

[88] V. K. Pecharsky and P. Y. Zavalij, "Fundamentals of Powder Diffraction and Structural Characterization of Materials," 2nd ed., Kluwer, Boston (2009), pp. 197–198.

[89] M. Ahtee, M. Nurmela, P. Suortti, and M. Järvinen, *J. Appl. Crystallogr.*, **22**, 261 (1989).

[90] M. Järvinen, *J. Appl. Crystallogr.*, **26**, 525 (1993).

[91] E. H. Kisi and C. J. Howard, "Applications of Neutron Powder Diffraction," Oxford University Press, New York (2008), p. 166.

[92] S. A. Howard and K. D. Preston, "Modern Powder Diffraction," Vol. 20: Reviews in Mineralogy, ed. by D. L. Bish and J. E. Post, Mineral. Soc. Am., Washington, DC (1989), Chap. 8.

[93] M. M. Hall, Jr., V. G. Veeraraghavan, H. Rubin, and P. G. Winchell, *J. Appl. Crystallogr.*, **10**, 66 (1977).

[94] W. I. F. David and J. C. Matthewman, *J. Appl. Crystallogr.*, **18**, 461 (1985).

[95] G. Caglioti, A. Paoletti, and F. P. Ricci, *Nucl. Instrum. Methods*, **3**, 223 (1958).

[96] P. Thompson, D. E. Cox, and J. B. Hastings, *J. Appl. Crystallogr.*, **20**, 79 (1987).

[97] P. W. Stephens, *J. Appl. Crystallogr.*, **32**, 281 (1999).

[98] J.-F. Bérar and G. Baldinozzi, *J. Appl. Crystallogr.*, **26**, 128 (1993).

[99] C. J. Howard, *J. Appl. Crystallogr.*, **15**, 615 (1982).

[100] L. W. Finger, D. E. Cox, and A. P. Jephcoat, *J. Appl. Crystallogr.*, **27**, 892 (1994).

[101] B. van Laar and W. B. Yelon, *J. Appl. Crystallogr.*, **17**, 47 (1984).

[102] R. J. Papoular, *Mater. Sci. Forum*, **378–381**, 262 (2001).

[103] H. Toraya, *J. Appl. Crystallogr.*, **23**, 485 (1990).

[104] C. Dong, *J. Appl. Crystallogr.*, **32**, 838 (1999).

[105] F. Izumi, *J. Crystallogr. Soc. Jpn.*, **44**, 246 (2002).

[106] E. J. Sonneveld and J. W. Visser, *J. Appl. Crystallogr.*, **8**, 1 (1975).

[107] T. Roisnel and J. Rodríguez-Carvajal, *Mater. Sci. Forum*, **378–381**, 118 (2001).

[108] V. Favre-Nicolin and R. Cerny, *J. Appl. Crystallogr.*, **35**, 734 (2002).

[109] W. I. F. David and D. S. Sivia, *J. Appl. Crystallogr.*, **34**, 318 (2001).

[110] J. Rodríguez-Carvajal, *Phys. B (Amsterdam, Neth.)*, **192**, 55 (1993).

[111] J. C. Nash, "Compact Numerical Methods for Computers: Linear Algebra and Function Minimisation," 2nd ed., Adam Hilger, Bristol (1990), pp. 86–90.

[112] T. Nakagawa and Y. Oyanagi, "Recent Developments in Statistical Inference and Data Analysis," ed. by K. Matusita, North-Holland, Amsterdam (1980), p. 221.

[113] D. W. Marquardt, *J. Soc. Ind. Appl. Math.*, **11**, 431 (1963).

[114] R. Fletcher, "A Modified Marquardt Subroutine for Non-linear Least Squares," AERE-R6799, AERE Harwell, Harwell (1971).

[115] M. J. D. Powell, *Comput. J.*, **7**, 155 (1964).

[116] M. J. D. Powell, *Comput. J.*, **7**, 303 (1965).

[117] D. M. Himmelblau, "Applied Nonlinear Programming," McGraw-Hill, New York (1972), pp. 167–176.

[118] W. H. Press, S. A. Teukolsky, W. T. Vetterling, and B. P. Flannery, "Numerical Recipes in FORTRAN," 2nd ed., Cambridge University Press, New York (1994), Sect. 10.5.

[119] J. E. Post and D. L. Bish, "Modern Powder Diffraction," Vol. 20: Reviews in Mineralogy, ed. by D. L. Bish and J. E. Post, Mineral. Soc. Am., Washington, DC (1989), Chap. 9.

[120] H. G. Scott, *J. Appl. Crystallogr.*, **16**, 159 (1983).

[121] R. A. Young, "The Rietveld Method," ed. by R. A. Young, Oxford University Press, Oxford (1995), Chap. 1.

[122] C. Giacovazzo, "Fundamentals of Crystallography," 3rd ed., ed. by C. Giacovazzo, Oxford University Press, Oxford (2011), p. 128.

[123] Y. Idemoto, F. Izumi, Q. Huang, A. Santoro, M. Matsuzawa, and N. Koura, "High-Temperature Superconductors and Novel Inorganic Mateirals," NATO Science Series, 3. High Technology, Vol. 62, ed. by G. Van Tendeloo, E. V. Antipov, and S. N. Putilin, Kluwer, Dordrecht (1999), p. 129.

[124] R. J. Hill and H. D. Flack, *J. Appl. Crystallogr.*, **20**, 356 (1987).

[125] D. Schwarzenbach, S. C. Abrahams, H. D. Flack, W. Gonschorek, T. Hahn, K. Huml, R. E. Marsh, E. Prince, B. E. Robertson, J. S. Rollet, and A. J. C. Wilson, *Acta Crystallogr., Sect. A: Found. Crystallogr.*, **45**, 63 (1989).

[126] R. J. Hill and I. C. Madsen, *Powder Diffr.*, **2**, 146 (1987).

[127] D. E. Cox and R. J. Papoular, *Mater. Sci. Forum*, **228–231**, 233 (1996).

[128] T. Ohta, F. Izumi, K. Oikawa, and T. Kamiyama, *Phys. B (Amsterdam, Neth.)*, **234–236**, 1093 (1997).

[129] F. Izumi, A. Yamamoto, N. R. Khasanova, S. Kumazawa, W.-Z. Hu, and T. Kamiyama, *Phys. C (Amsterdam, Neth.)*, **335**, 239 (2000).

[130] G. S. Pawley, *J. Appl. Crystallogr.*, **14**, 357 (1981).

[131] A. A. Belik, F. Izumi, T. Ikeda, A. P. Malakho, and B. I. Lazoryak, *J. Mater. Chem.*, **12**, 3803 (2002).

[132] C. Baerlocher, "The Rietveld Method," ed. by R. A. Young, Oxford University Press, Oxford (1995), Chap. 10.

[133] C. Ferraris, "Fundamentals of Crystallography," 3rd ed., ed. by C. Giacovazzo, Oxford University Press, Oxford (2011), p. 545.

[134] J. B. Jones, *Acta Crystallogr., Sect. B: Struct. Sci.*, **24**, 355 (1968).

[135] J. Waser, *Acta Crystallogr.*, **16**, 1091 (1963).

[136] W. R. Busing, K. O. Martin, and H. A. Levy, "A FORTRAN Crystallographic Function and Error Program," Report ORNL-TM-306, Oak Ridge National Laboratory, Tennessee (1964).

[137] C. Giacovazzo, "Fundamentals of Crystallography," 3rd ed., ed. by C. Giacovazzo, Oxford University Press, Oxford (2011), p. 80.

[138] K. Momma and F. Izumi, *Ganseki Kobutsu Kagaku*, **39**, 136 (2010).

[139] K. Momma and F. Izumi, "VESTA: a Three-Dimensional Visualization System for Electronic and Structural Analysis," National Institute for Materials Science, Tsukuba (2010), Subsect. 9.8.2.

[140] Z.-Q. Liu, Q. Fang, W.-T. Yu, G. Xue, D.-X. Cao, and M.-H. Jiang, *Acta Crystallogr., Sect. C: Cryst. Struct. Commun.*, **58**, o445 (2002).

[141] R. E. Dinnebier, P. Bernatwicz, X. Helluy, A. Sebald, M. Wunschel, A. Fitch, and S. van Smaalen, *Acta Crystallogr., Sect. B: Struct. Sci.*, **58**, 52 (2002).

[142] A. Hönnerscheid, R. Dinnebier, and M. Jansen, *Acta Crystallogr., Sect. B: Struct. Sci.*, **58**, 482 (2002).

[143] M. Rakiah, J. Refebvre, O. Hernandez, W. van Beek, and M. Serpelloni, *J. Appl. Crystallogr.*, **37**, 766 (2004).

[144] A. Looijenga-Vos and M. J. Buerger, "International Tables for Crystallography," Vol. A, 5th ed., ed. by Th. Hahn, Kluwer, Dordrecht (2005), Part 3.

[145] T. J. B. Holland and S. A. T. Redfern, *Mineral. Mag.*, **61**, 65 (1997).

[146] A. Belsky, M. Hellenbrandt, V. L. Karen, and P. Luksch, *Acta Crystallogr., Sect. B: Struct. Sci.*, **58**, 364 (2002).

[147] W. I. F. David, K. Shankland, L. B. McCusker, and C. Baerlocher, eds., "Structure Determination from Powder Diffraction Data," Oxford University Press, Oxford (1992).

[148] "International Tables for Crystallography," Vol. C, 3rd ed., ed. by E. Prince, Kluwer, Dordrechi (2004), pp. 774–896.

[149] U. Müller, "Inorganic Structural Chemistry," 2nd ed., Wiley, Chichester (2006).

[150] B. E. Doublas and S.-M. Ho, "Structure and Chemistry of Crystalline Solids," Springer, New York (2006).

[151] R. D. Shannon, *Acta Crystallogr., Sect. A: Found. Crystallogr.*, **32**, 751 (1976).

[152] I. D. Brown and D. Altermatt, *Acta Crystallogr., Sect. B: Struct. Sci.*, **41**, 244 (1985).

[153] N. E. Brese and M. O'Keeffe, *Acta Crystallogr., Sect. B: Struct. Sci.*, **47**, 192 (1991).

[154] R. Hoppe, S. Voigt, H. Glaum, J. Kissel, H. P. Müller, and K. Bernet, *J. Less-Common Met.*, **156**, 105 (1989).

[155] C. Ferraris, "Fundamentals of Crystallography," 3rd ed., ed. by C. Giacovazzo, Oxford University Press, Oxford (2011), p. 535.

[156] M. Nespolo, G. Ferraris, and H. Ohashi, *Acta Crystallogr., Sect. B: Struct. Sci.*, **55**, 902 (1999).

[157] L. B. McCusker, R. B. V. Dreele, D. E. Cox, D. Louër, and P. Scardi, *J. Appl. Crystallogr.*, **32**, 36 (1999).

[158] "A Practical Guide to X-Ray Powder Analysis," 2nd ed., ed. by I. Nakai and F. Izumi, Asakura, Tokyo (2009), Chap. 7–11.

[159] V. K. Pecharsky and P. Y. Zavalij, "Fundamentals of Powder Diffraction and Structural Characterization of Materials," 2nd ed., Springer, New York (2009).

[160] D. C. Creagh and J. H. Hubbell, "International Tables for Crystallography," Vol. C, 3rd ed., ed. by E. Prince, Kluwer, Dordrecht (2004), pp. 220–236.

[161] J. H. Hubbell and S. M. Seltzer, "Tables of X-Ray Mass Attenuation Coefficients and Mass Energy-Absorption Coefficients (version 1.4)," National Institute of Standards and Technology, Gaithersburg (2004).

[162] H. P. Klug and L. E. Alexander, "X-Ray Diffraction Procedures," 2nd ed., Wiley, New York (1974), pp. 532–538.

[163] G. W. Brindley, *Philos. Mag.*, **36**, 347 (1945).

[164] K. Koopmans and G. D. Rieck, "International Tables for X-Ray Crystallography," Vol. III, Kynoch Press, Birmingham (1962), pp. 194–200.

[165] J. C. Taylor and C. E. Matulis, *J. Appl. Crystallogr.*, **24**, 14 (1991).

[166] E. H. Kisi and C. J. Howard, "Applications of Neutron Powder Diffraction," Oxford University Press, New York (2008), pp. 253–259.

[167] K. Ohoyama, *RADIOISOTOPES*, **59**, 477 (2010).

[168] A. A. Belik, S. Iikubo, K. Kodama, N. Igawa, S. Shamoto, S. Niitaka, M. Azuma, Y. Shimakawa, M. Takano, F. Izumi, and E. Takayama-Muromachi, *Chem. Mater.*, **18**, 798 (2006).

[169] L. M. Gelato and E. Parthé, *J. Appl. Crystallogr.*, **20**, 139 (1987).

[170] H. Arnold, "International Tables for Crystallography," Vol. A, 5th ed., ed. by Th. Hahn, Kluwer, Dordrecht (2002), Sect. 5.1.

[171] K. Momma and F. Izumi, "VESTA: a Three-Dimensional Visualization System for Electronic and Structural Analysis," National Institute for Materials Science, Tsukuba (2010), Sect. 6.2.

[172] E. Parthé and L. M. Gelato, *Acta Crystallogr., Sect. A: Found. Crystallogr.*, **40**, 169 (1984).

[173] P. Lightfoot, S. Pei, J. D. Jorgensen, Y. Yamada, T. Matsumoto, F. Izumi, and Y. Kodama, *Acta Crystallogr., Sect. C: Cryst. Struct. Commun.*, **47**, 1143 (1991).

[174] H. Burzlaff and H. Zimmermann, *Z. Krystallogr.*, **167**, 89 (1984).

[175] A. Altomare, M. C. Burla, G. Cascarano, C. Giacovazzo, A. Guagliardi, A. G. G. Moliterni, and G. Polidori, *J. Appl. Crystallogr.*, **28**, 842 (1995).

[176] M. Milanesio and D. Viterbo, "Fundamentals of Crystallography," 3rd ed., ed. by C. Giacovazzo, Oxford University Press, Oxford (2011), p. 419.

[177] V. K. Pecharsky and P. Y. Zavalij, "Fundamentals of Powder Diffraction and Structural Characterization of Materials," 2nd ed., Springer, New York (2009), pp. 510–512.

[178] A. Altomare, G. Cascarano, C. Giacovazzo, A. Guagliardi, M. C. Burla, G. Polidori, and M. Camalli, *J. Appl. Crystallogr.*, **27**, 435 (1994).

[179] L. Palatinus and G. Chapuis, *J. Appl. Crystallogr.*, **40**, 786 (2007).

[180] G. Oszlányi and A. Sütő, *Acta Crystallogr., Sect. A: Found. Crystallogr.*, **60**, 134 (2004).

[181] G. Oszlányi and A. Sütő, *Acta Crystallogr., Sect. A: Found. Crystallogr.*, **61**, 147 (2005).

[182] G. Oszlányi and A. Sütő, *Acta Crystallogr., Sect. A: Found. Crystallogr.*, **63**, 156 (2007).

[183] R. Jenkins and R. L. Snyder, "Introduction to X-ray Powder Diffractometry," Wiley, New York (1996), pp. 89–91.

[184] F. Izumi and T. Ikeda, *Annu. Rep., Adv. Ceram. Res. Center, Nagoya Inst. Technol.*, **3**, 33 (2014).

[185] A. C. Larson and R. B. V. Dreele, "General Structure Analysis System (GSAS)," Report LAUR 86-748, Los Alamos National Laboratory, Los Alamos (2004).

[186] G. K. Williamson and W. H. Hall, *Acta Metall.*, **1**, 22 (1953).

[187] N. C. Halder and C. N. J. Wagner, *Acta Crystallogr.*, **20**, 312 (1966).

[188] N. C. Halder and C. N. J. Wagner, *Adv. X-Ray Anal.*, **9**, 91 (1966).

[189] P. Scherrer, *Nachr. Ges. Wiss. Göttingen, Math.-Phys. Klasse*, **2**, 96 (1918).

[190] A. R. Stokes and A. J. C. Wilson, *Proc. Cambridge Philos. Soc.*, **40**, 197 (1944).

[191] A. R. Stokes and A. J. C. Wilson, *Proc. Phys. Soc. (London, U. K.)*, **56**, 174 (1944).

[192] D. Balzar, N. Audebrand, M. R. Daymond, A. Fitch, A. Hewat, J. I. Langford, A. L. Bail, D. Louër, O. Masson, C. N. McCowan, N. C. Popa, P. W. Stephens, and B. H. Toby, *J. Appl. Crystallogr.*, **42**, 1197 (2009).

[193] W. H. Hall, *Proc. Phys. Soc. A (London, U. K.)*, **10**, 741 (1949).

[194] E. H. Kisi and C. J. Howard, "Applications of Neutron Powder Diffraction," Oxford University Press, New York (2008), Chap. 9.

[195] T. Ida, S. Shimazaki, H. Hibino, and H. Toraya, *J. Appl. Crystallogr.*, **36**, 1107 (2003).

[196] N. Audebrand, J.-P. Auffrédic, and D. Louër, *Chem. Mater.*, **12**, 1791 (2000).

[197] R. W. Cheary and A. Coelho, *J. Appl. Crystallogr.*, **25**, 109 (1992).

[198] M. Sakata and M. Sato, *Acta Crystallogr., Sect. A: Found. Crystallogr.*, **46**, 263 (1990).

[199] M. Sakata, R. Mori, S. Kumazawa, M. Takata, and H. Toraya, *J. Appl. Crystallogr.*, **23**, 526 (1990).

[200] D. M. Collins, *Nature (London, U. K.)*, **298**, 49 (1982).

[201] E. T. Jaynes, *Phys. Rev.*, **106**, 620 (1957).

[202] M. Sakata, T. Uno, M. Takata, and C. J. Howard, *J. Appl. Crystallogr.*, **26**, 159 (1993).

[203] T. Sakurai, "X-Ray Analysis of Crystal Structures," Syôkabô, Tokyo (1978), pp. 232–233.

[204] M. Takata, E. Nishibori, and M. Sakata, *Z. Krystallogr.*, **216**, 71 (2001).

[205] S. Kumazawa, S. Yamamura, E. Nishibori, M. Takata, M. Sakata, F. Izumi, and Y. Ishii, *J. Phys. Chem. Solids*, **60**, 1407 (1999).

[206] T. Ikeda, F. Izumi, T. Kodaira, and T. Kamiyama, *Chem. Mater.*, **10**, 3996 (1998).

[207] T. Ikeda, Y. Akiyama, F. Izumi, Y. Kiyozumi, F. Mizukami, and T. Kodaira, *Chem. Mater.*, **13**, 1286 (2001).

[208] K. Takada, K. Fukuda, M. Osada, I. Nakai, F. Izumi, R. A. Dilanian, K. Kato, M. Takata, H. Sakurai, E. Takayama-Muromachi, and T. Sasaki, *J. Mater. Chem.*, **14**, 1448 (2004).

[209] F. Izumi, *Rigaku J.*, **36**, 18 (2005).

[210] F. Izumi and R. A. Dilanian, *Commission on Powder Diffraction, IUCr Newsletter*, No. 32, 59 (2005).

[211] F. Izumi and Y. Kawamura, *Bunseki Kagaku*, **55**, 391 (2006).

[212] R. A. Dilanian and F. Izumi, "VICS and VEND for Three-Dimensional Visualization of Crystal Structures and Electron/Nuclear Densities," National Institute for Materials Science, Tsukuba (2006).

[213] J. Smart, K. Hock, and S. Csomor, "Cross-Platform GUI Programming with wxWidgets," Prentice Hall, Upper Saddle River (2005).

[214] S. Kumazawa, M. Takata, and M. Sakata, *Acta Crystallogr., Sect. A: Found. Crystallogr.*, **51**, 47 (1995).

[215] S. F. Gull and J. Skilling, "Quantified Maximum Entropy, MemSys5 Users' Manual," Maximum Entropy Data Consultants Ltd., Suffolk (1999).

[216] J. Nocedal, *Math. Comp.*, **35**, 773 (1980).

[217] T. Ida, T. Goto, and H. Hibino, *J. Appl. Crystallogr.*, **42**, 597 (2009).

[218] T. Ida and F. Izumi, *J. Appl. Crystallogr.*, **44**, 921 (2011).

[219] T. Ida and F. Izumi, *Powder Diffr.*, **28**, 124 (2013).

[220] A. Antoniadis, J. Berruyer, and A. Filhol, *Acta Crystallogr., Sect. A: Found. Crystallogr.*, **46**, 692 (1990).

[221] S. van Smaalen, L. Palatinus, and M. Schneider, *Acta Crystallogr., Sect. A: Found. Crystallogr.*, **59**, 459 (2003).

[222] D. Louër and A. Boultif, *Powder Diffr.*, **29**, S7 (2014).

[223] S. R. Hall, F. H. Allen, and I. D. Brown, *Acta Crystallogr., Sect. A: Found. Crystallogr.*, **47**, 655 (1991).

[224] S. R. Hall, *Acta Crystallogr., Sect. A: Found. Crystallogr.*, **37**, 517 (1981).

[225] S. Adams, *Solid State Ionics*, **136–137**, 1351 (2000).

[226] S. Adams, *Acta Crystallogr., Sect. B: Struct. Sci.*, **57**, 278 (2001).

[227] S. Adams and R. P. Rao, *Phys. Status Solidi A*, **208**, 1746 (2011).

[228] F. Izumi, H. Koto, H. Sawa, J. Akimitsu, and H. Asano, *Phys. C (Amsterdam, Neth.)*, **160**, 235 (1989).

[229] R. F. Stewart, E. R. Davidson, and W. T. Simpson, *J. Chem. Phys.*, **42**, 281 (1999).

[230] J. B. Mann, Report LA-3961, Los Alamos National Laboratory, Los Alamos (1968).

[231] T. Ito, "Diffraction," Vol. 10: the 4th Series of Experimental Chemistry, Maruzen, Tokyo (1992), p. 182.

[232] H. Uekusa, "Spectroscopy and Diffraction III," Vol. 11: the 5th Series of Experimental Chemistry, Maruzen, Tokyo (2006), p. 140.

[233] K. Ohoyama, T. Kanouchi, K. Nemoto, M. Ohashi, T. Kajitani, and Y. Yamaguchi, *Jpn. J. Appl. Phys.*, **37**, 3319 (1998).

[234] R. A. Young, A. Sakthivel, T. S. Moss, and C. O. Paiva-Santos, *J. Appl. Crystallogr.*, **28**, 366 (1995).

[235] V. K. Pecharsky and P. Y. Zavalij, "Fundamentals of Powder Diffraction and Structural Characterization of Materials," 2nd ed., Springer, New York (2009), pp. 359–361.

[236] K. Momma and F. Izumi, "VESTA: a Three-Dimensional Visualization System for Electronic and Structural Analysis," National Institute for Materials Science, Tsukuba (2010), Sect. 12.2.

[237] V. K. Pecharsky and P. Y. Zavalij, "Fundamentals of Powder Diffraction and Structural Characterization of Materials," 2nd ed., Springer, New York (2009), p. 641.

[238] C. Giacovazzo, "Fundamentals of Crystallography," 3rd ed., ed. by C. Giacovazzo, Oxford University Press, Oxford (2011), Chap. 2.

[239] C. H. Kelsey, *Mineral. Mag.*, **33**, 809 (1964).

[240] T. Sakurai, "X-Ray Analysis of Crystal Structures," Syôkabô, Tokyo (1978), pp. 292–296.

[241] "International Tables for Crystallography," Vol. G: Definition and Exchange of Crystallographic Data, ed. by S. R. Hall and B. McMahon, Springer, Dordrecht (2006).

[242] B. H. Toby, "International Tables for Crystallography," Vol. G, ed. by S. Hall and B. McMahon, Springer (2005), pp. 117–130.

[243] S. P. Westrip, *J. Appl. Crystallogr.*, **43**, 920 (2010).

[244] A. L. Spek, *J. Appl. Crystallogr.*, **36**, 7 (2003).

[245] A. L. Spek, *Acta Crystallogr., Sect. D: Biol. Crystallogr.*, **65**, 148 (2009).